DEFORMATION CHARACTERISTICS OF CHANGING STRAIN PATHS ON HIGH FORMABILITY STEELS

by

ANASTASIA VRETTOU

A thesis submitted to the University of Birmingham for the degree of

DOCTOR OF PHILOSOPHY

School of Metallurgy and Materials

College of Engineering and Physical Sciences

University of Birmingham

March 2024

Preface

This dissertation is submitted for the degree of Doctor of Philosophy at the University of Birmingham. It describes the research carried out in the Department of Metallurgy and Materials Science between October 2019 and March 2024, under the supervision of Dr. David M. Collins. Except where reference is made to the work of others, the contents of this dissertation are entirely original and have not been a result of collaboration. No part of the work described here has been or is currently being submitted for the purpose of gaining academic qualification at this or any other institute of higher learning. This dissertation does not exceed 50,000 words in length.

Abstract

Understanding the mechanisms that govern deformation of metallic sheets is crucial for their forming applications, such as the manufacturing of structural vehicle components. This thesis focuses on the effect of strain path and Strain Path Changes (SPCs) that can influence the mechanical properties and microstructure of two high formability steels. A DX54 low carbon steel, and a TWIP steel are studied. Both alloys are used in the automotive industry, with the first having broad use due to its high ductility and low cost, while the second has a higher cost but exhibits exceptional work hardening and high ductility.

The effect of abrupt SPCs was examined on the DX54 low carbon steel via in-situ Synchrotron X-Ray Diffraction (SXRD) and ex-situ via Electron Backscatter Diffraction (EBSD). A two-step deformation process was used, including cold rolling followed by uniaxial tension. Both pre-strain direction and tensile directions as well as the pre-strain magnitude were varied. The role of texture changes and their association with microstructure development was examined. The deformation process resulted in a significant ductility loss for highly pre-strained specimens. The ductility decrease was more pronounced when SPCs were abrupt (i.e. a 90° change in the loading direction). Results also showed a large texture dependence of the mechanical properties and the microstructure evolution. This was an important result as prior studies had only considered the effect from a small number of grains and had underestimated the significance of texture.

An investigation of the TWIP steel behaviour under a variety of strain paths required the development of a biaxial testing device. A miniaturised testing setup was developed in Chapter 4, which allowed specimens to be subjected to near uniaxial, plane strain or equibiaxial strain paths. Such studies are seldom reported. Strain measurements were performed via Digital Image Correlation (DIC). The effect of non-proportional deformation was also examined for two, two-step processes: uniaxial pre-straining followed by equibiaxial tension and cold rolling followed by equib-

iaxial tension. Interrupted tests were conducted to facilitate microstructure examination via EBSD. Results highlighted the influence of strain path on microstructure evolution, with cold rolling leading to the highest Geometrically Necessary Dislocation (GND) density development and twin generation. Twin formation also showed notable grain orientation dependence, with the [011]||normal direction being the least favourable for twin formation.

Strain path sensitivity of the TWIP steel was additionally examined via in-situ neutron diffraction and ex-situ EBSD to provide microstructural information in the mesoscale. Five strain paths were examined, proportional and non-proportional incorporating uniaxial, and equibiaxial deformation states. Results from proportional strain paths showed that equibiaxial deformation led to higher dislocation densities and decreased twinning activity, due to the enhancement of the [011]||normal direction fibre, which is unfavourable for twinning. Furthermore, results indicated that whilst twin generation during equibiaxial deformation is limited compared to uniaxial deformation, twin growth is promoted for the former strain path.

Acknowledgements

I would like to acknowledge the University of Birmingham for funding my PhD studentship which made this research endeavour possible. I would also like to acknowledge ISIS Neutron and Muon source and Diamond Light Source, for funding experimental time at Paul Scherrer Institute and Diamond Light Source respectively.

This work would have not been possible without the support of my supervisor, Dr. David Collins, to whom I would like to express my sincere appreciation. Not only did he provide assistance during the course of this work, but he also played an important role in shaping my mindset as an experimental scientist. Additionally, I would like to thank my co-supervisor, Dr. Andrew Morris, for his insightful advice during the initial stages of my PhD, which facilitated my transition from physics to materials science.

A big part of this work was carried out at the Centre of Electron Microscopy at the UoB, so special thanks go to Dr Ludwig Schneider and Theresa Morris for their support. Additionally, this work would not have been the same without the contribution of Dr. Mary Taylor, who assisted with SEM work and Dr. Efthymios Polatidis for his contributions to result interpretation. Moreover, I would like to thank Dr. Hiroto Kitaguchi, Dr. Biao Cai, Dr. Thomas Connolley and Dr. Jan Capek, for their support during beamtime.

The person who significantly influenced and motivated me to pursue a PhD in experimental materials science was Dr. Emmanuel Syskakis, who, unfortunately, is no longer with us. I will forever be indebted to him for his profound impact on my academic journey.

The journey of my PhD would have been markedly different without the support of my amazing friends and colleagues. I could not be any more grateful to Anastassia, Marianna, David, Mel, Paraic, Dimitra, Kostas and Wakib whose friendship made the PhD experience unforgettable. I would also like to thank Dina, Peter, Francesco and Elena for all the beautiful moments we spent together (and the more to come).

Special “thanks” also goes to my colleagues James, Himanshu, and Jon, as well as all the people of 2B25, with whom I had the privilege to work with. Extra special thanks to Wakib and James for their support (and cooking), during beamtime.

At this point, I extend my utmost gratitude to those who have played a pivotal role in shaping my personal growth. To Thalia, my oldest friend, along with her beautiful newborn daughter, and to Avgoustinos, Eleni, Mandy, Danae and Nikos for their lifelong friendship. My heartfelt thanks also go to my mom, dad, and my beloved brother, Nikolas.

Finally, I reserve my deepest appreciation for Nikos, my partner and my true hero who stood by my side through the exciting and very challenging times of the past years. I would not have made it without him.

In the loving memory of my grandmas,

Anastasia and Dimitra

Contents

List of Figures

List of Tables

Chapter 1

Introduction

1.1 Steels for automotive applications

As we move towards an environmentally friendly transportation future, the automotive industry faces a challenge to significantly reduce and ultimately eliminate CO_2 emissions, making vehicle mass reduction necessary. Mass reduction directly improves energy efficiency, as the engine/motor power consumption can be reduced for the basic vehicle operations. The car body and chassis account for approximately 40% of the overall automobile mass [25], which underlines the importance of material selection on the environmental impact of the vehicle. In addition to low mass, the chassis materials must exhibit excellent drawability and deformation energy absorption in a case of collision; two factors of high importance in material selection. The current tendencies shown in Fig. 1.1 illustrate that vehicle weight has increased over time, as a result of design changes and technology additions. Hence, further efforts towards achieving excellent mechanical properties, and reducing the mass of materials used in a car body structure, is crucial.

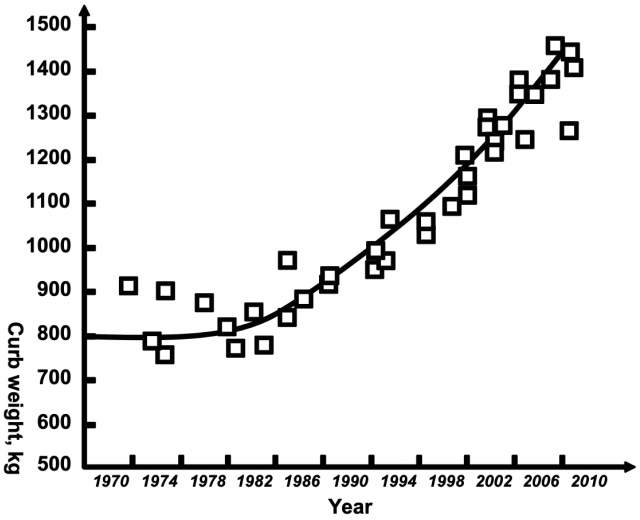

Figure 1.1: Increase of car weight in the EU [1].

Steel has been proven as an excellent material for automotive applications. It is a versatile alloy, as one can tune the composition and microstructure to control the mechanical properties, depending on the desired application. While the use of aluminium is attractive, as it can lead to a great reduction of the body structure weight, its low tensile strength is a significant drawback. Low carbon steel, has been widely used for the production of car body components since the 1920s [26], as it is a cheap and easy to form material. Due to the low carbon content, typically lower than 0.1 wt% [27] for a ferritic steel, it is characterised by high formability; this consists of relatively low Yield Strength (YS) and Ultimate Tensile Strength (UTS), while it can reach a high total elongation. In recent years, an increase in safety requirements as well as stricter environmental regulations have forced the automotive sector to develop and utilise alloys with higher strength, whilst maintaining high ductility. Since the 1970s, Dual-Phase (DP) steels have been increasingly used in car body structures. Their microstructure, including ferrite and martensite, resulting in increased ductility and high strength respectively, can lead to an high energy absorption and a UTS reaching 1200 MPa [28].

In recent decades, increasing attention has been given to TWinning Induced

Plasticity (TWIP) steels, which belong to the group of Advanced High Strength Steels (AHSS). TWIP steels (also called high-Mn steels) contain a large amount of Mn (≈12-25% [29]), and exhibit superior mechanical properties, by combining ultra high YS and UTS with high ductility, as shown in Fig. 1.2. They are also characterised by high work hardening rates, which further increases their ability to absorb energy during deformation and makes them ideal for automotive applications. Despite their superior properties, TWIP steels come with the main drawback of high cost. Alloying additions including the high Mn content results in an increased price compared to low carbon steels or aluminium alloys, making their use more limited.

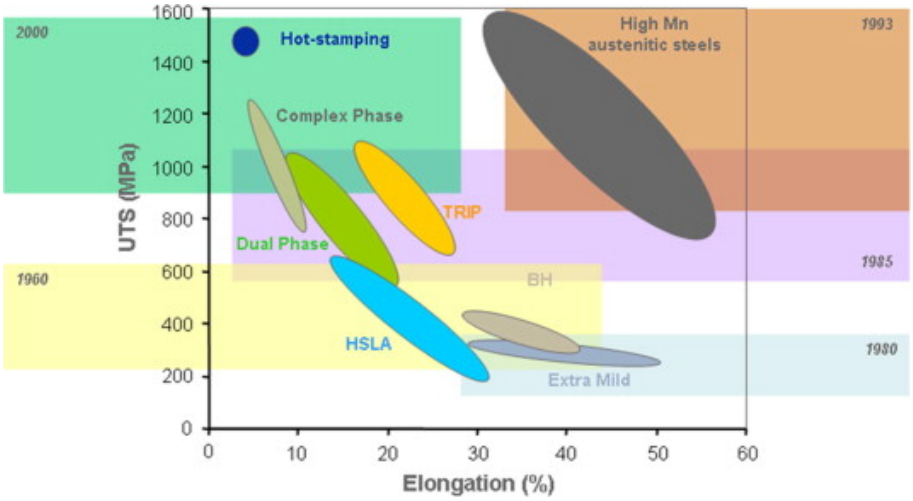

Figure 1.2: Ashby plot of automotive steels [2].

1.2 Strain path effect in sheet metal forming

Sheet metal forming or stamping is one of the most widely used processes in manufacturing. The term refers to the process where a metallic sheet with a uniform thickness is fabricated into different shapes by a punch or die. During stamping, the material undergoes biaxial deformation, where the deformation mode depends on the geometry of the die. The term *strain path* is used to describe the strain state (or more specifically the relationship between the *major* and *minor* strains) that

the material undergoes during deformation. Some examples of different strain paths developed during stamping of car body parts are shown in Fig. 1.3.

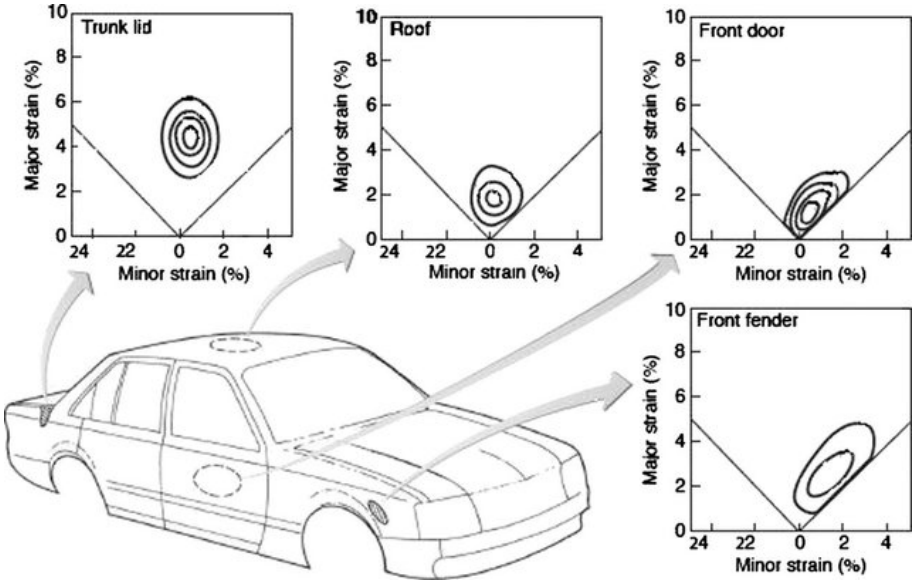

Figure 1.3: Major-minor strains developed during stamping for various car body parts [3].

Microstructure and texture strongly influence the strain path and consequently will be correlated to failure; this refers to the point where the material exhibits localised necking/thinning. Obtaining an understanding of the correlation between microstructure, texture and active deformation mechanisms with strain path will allow the prediction of failure via Finite Element Modelling (FEM). Additionally, it will assist the design of new alloys or processing methods, so that the final product (metallic sheet) satisfies the desirable properties for each application.

In addition to a strain path sensitivity investigation, the application of SPCs should also be considered. It is widely known that deformation history significantly influences the mechanical behaviour of the material. During stamping, an increment of the deforming material can undergo an SPC, as shown in Fig. 1.4. In this example [4], the process of hydroforming is simulated via FEM for an AA5182 alloy sheet. Following the green markers, it is observed that node 30138, which initially follows the *plane strain* condition (minor strain ≈ 0), at ≈ 0.09 major strain, shifts to the

equibiaxial condition (major strain ≈ minor strain). Furthermore, the reworkability is also desirable in many cases during manufacture, for example in the event of a fault occurring during forming. In such cases a process of re-shaping a component will inherently incorporate an SPC.

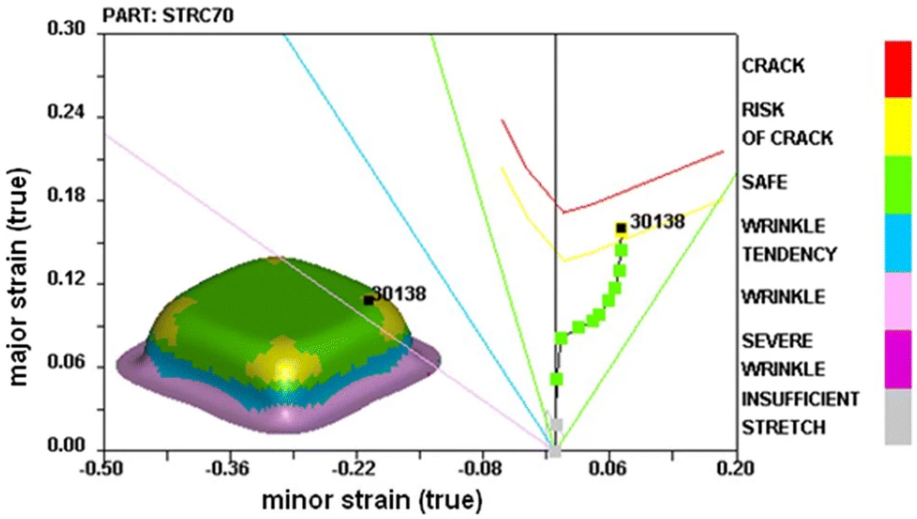

Figure 1.4: Node 30138 undergoes SPC during hydroforming process [4].

It has been shown for a low carbon steel [16], that a remarkable ductility improvement can occur after an SPC including pre-straining in uniaxial tension (the equivalent of the strain state in a conventional tensile test). Utilising this effect could potentially lead to significant enhancement of mechanical properties of alloys taken 'off-the-rack', without any further change in composition. Thus, understanding the SPC effect in commercially used alloys, whether this is beneficial or detrimental, is of great importance

1.3 Aim of this thesis

This thesis aspires to elucidate the deformation characteristics of steels exhibiting high formability when they are subjected a variety of strain paths. It has been previously shown that altering the deformation history of a low carbon steel [16] can

lead to a ductility increase. This outcome highlights that appropriate utilisation of material strain path sensitivity can potentially enhance its mechanical properties. However, in order to utilise this effect and gain predictability of strain paths which can be beneficial to ductility, one needs to obtain a better understanding of the load path effect on the microstructure. Within this thesis, the effect of strain path and SPCs is studied for two high formability steels: a low carbon ferritic steel and a high Mn TWIP steel. Material selection was carried out taking into account 1) the broad commercial use of these alloys, and 2) the ability to study deformation characteristics of two different crystal structures and facilitate comparisons between them.

First, a 'DX54' single phase, mild steel is examined under the application of abrupt and non-abrupt SPCs. The effects of SPCs on the microstructure of this material have been examined in the past in a variety of works [30, 31, 32, 33] focusing in mechanical properties and microstructure formations examined via TEM, however only a few studies have focused in the examination of the material response under SPCs in the mesoscale. In this work, the SPC effect is studied via a two-step deformation process including pre-straining via cold rolling followed by uniaxial tension. Emphasis is given to the role of texture development and the implications of rapid texture changes. For the examination, SXRD and EBSD techniques are used. Additionally, the simple structure and deformation characteristics of a well established material such as the DX54, can assist in the subsequent investigation of the microstructure and properties of a more complex and much less investigated TWIP steel.

Following the 'DX54' alloy examination via the aforementioned experimental methods, focus is given to the mechanical behaviour of a TWIP steel under proportional and non-proportional strain paths. Twinning mechanism under non-proportional processes has been seldom reported in the literature. First, a minia-

turised version of the punch testing method, a Marciniak test, is developed. The miniaturised test is then combined with Digital Image Correlation (DIC) to facilitate macroscopic strain measurements. Both proportional and non-proportional strain paths are studied. Microstructure of the deformed specimens is then examined via EBSD, to track changes in texture and twin development.

In the final part of this thesis, the same alloy is studied under non-proportional strain paths, in-situ, via neutron diffraction and ex-situ via EBSD. This methods allow a better understanding of the behaviour of this material, by combining information obtained in the microscale and the mesoscale.

Chapter 2

Literature review

The deformation mode, including the load direction and the deformation history, plays a definitive role on the microstructure and the deformation characteristics of a material. Deformation induced effects can lead to changes in the grain shapes and orientations, development of different dislocation substructures, shear bands, stacking faults, deformation twins or lead to phase transformations. All those effects ultimately control the macroscopic properties of the deforming material. The deformation history influence on the macroscopic properties of a material has been studied since the 1880s, when Johann Bauschinger [34] observed a decrease in the YS of specimens subjected to reverse loading. This phenomenon was attributed to a change in dislocation arrangement in the crystal, in which reverse-loading led to softening. Since then, it has been clear that understanding the role of loading conditions and deformation history related to the microstructure development and the mechanical properties is critical for engineering materials for forming applications.

In this chapter, the basic concepts regarding plastic deformation in polycrystalline Face Centered Cubic (FCC) and Body Centered Cubic (BCC) materials are

discussed, with a dedicated discussion of plastic deformation in steels. Plastic deformation refers to the irreversible effect of an applied load to the macroscopic and microscopic properties of a solid material. It is accommodated primarily by dislocation *slip* (or *glide*), while, depending on the intrinsic properties of the material, it can be also controlled by *twinning*, *deformation induced phase transformations* and *grain boundary sliding*. Here, dislocation glide and deformation twinning are discussed in detail as they control the behaviour of the alloys studied in this thesis.

2.1 Deformation via Dislocation Slip and Twinning

2.1.1 Dislocation slip

Dislocation slip refers to the motion of dislocations (line defects) on the plane containing both their *line* and the *Burgers* vector under the application of a local shear stress. A *slip system* is used to describe the geometry of slip. It is constituted by the *slip plane* and the *slip direction*, usually denoted as $\{hkl\}$ $\langle uvw \rangle$ (where hkl are the Miller indices, used to describe the slip plane and uvw the slip direction). In metallic systems, dislocation slip takes place on the planes with the highest atomic densities, on the one of the closed packed directions, as the high atomic density make slip in these directions energetically preferable. Hence, for FCC structures, slip takes place on one of the four symmetrically equivalent $\{111\}$ planes, each of which has three equivalent $\langle 110 \rangle$ directions (close packed directions for this structure). This leads in 12 slip systems in total.

The shortest path between two atomic positions in an FCC crystal is $\vec{b} = \frac{1}{2}\langle 110 \rangle$, which is also one of the translation vectors of this crystal structure. Hence, a dislocation which will glide along this direction, will leave behind a perfect crystal. Such

dislocation is characterised as a *perfect* dislocation. Fig. 2.1 summarises the stacking of {111} planes in an FCC crystal. During shearing of the lattice, it is expected that B planes glide along direction $\vec{b}$, so that an atom of plane B, moves to the next empty atomic position of plane B. However, such a movement would require a great amount of energy, as the energy barrier of the atoms of plane A shall be exceeded to allow such movement [5]. In contrast, one can notice from Fig. 2.1 that, a zig-zag movement along the path $\vec{c} \rightarrow \vec{d}$ is energetically preferable as shorter distances are covered during such movement. Such movement will split the perfect dislocation into two *partial dislocations*, a process described by the dissociation reaction:

$$\frac{1}{2}\langle 110\rangle \rightarrow \frac{1}{6}\langle 211\rangle + \frac{1}{6}\langle 12\bar{1}\rangle. \tag{2.1}$$

The first partial will leave behind a sequence of empty B atomic positions, as shown in Fig. 2.2, and a series of atoms in C positions. This interruption of the regular atomic sequence ABCABC..., which is now transformed into ABCA$^{\downarrow}$CABC..., leads to the formation of a *stacking fault*. A stacking fault is a planar defect in the stacking of atoms, mainly formed in FCC and HCP crystals, due to their high atomic density. Formation of stacking faults is associated with the Stacking Fault Energy (SFE), which is the energy required for the formation of a stacking fault. SFE is an intrinsic material property, which is influenced by the alloying elements, as will be described in later section.

In contrast to FCC crystals, which are characterised by slip on one of the {111} planes, more than one family of planes can accommodate slip in BCC crystals. At low temperatures ([35], slip takes place on one of the four {110} planes and one of the three $\langle 111\rangle$ directions, while at higher temperatures, slip can also occur on {112} and {123} planes. The slip systems of FCC and BCC crystals are summarised in Table 2.1.

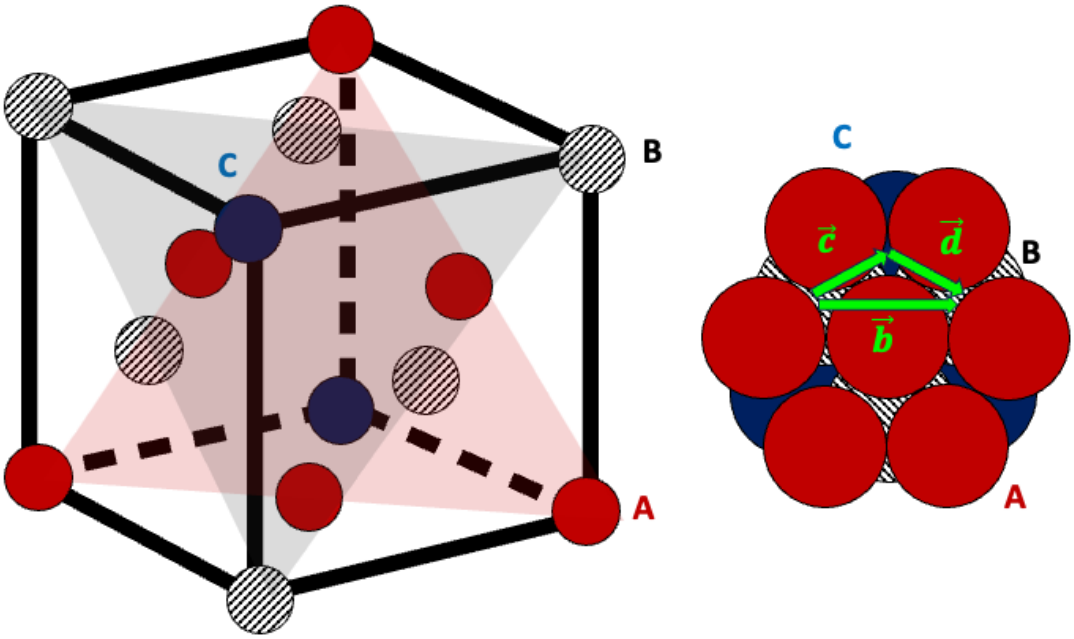

Figure 2.1: Stacking (left) and slip (right) of {111} planes on FCC crystals.

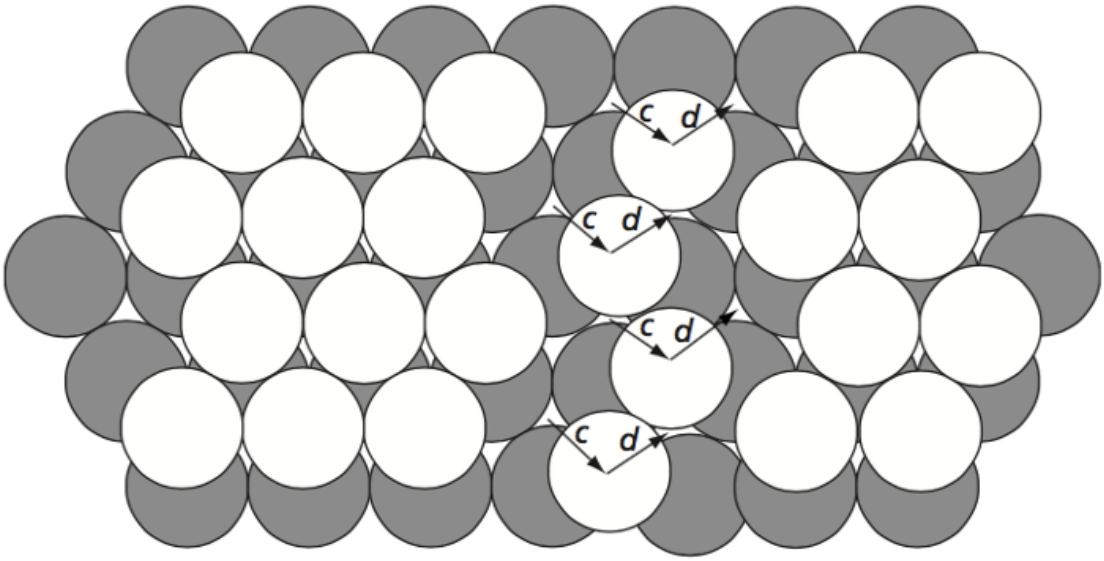

Figure 2.2: Partial dislocations formed in FCC, adapted from [5].

Structure	Slip systems
BCC	$12 \times \{110\}\langle 111\rangle$ $24 \times \{112\}\langle 111\rangle$ $12 \times \{123\}\langle 111\rangle$
FCC	$12 \times \{111\}\langle 110\rangle$

Table 2.1: Slip systems in BCC and FCC crystals.

Fig. 2.3 shows the geometry of slip in a single crystal, when a *uniaxial* load is applied. A uniaxial load is defined as the load applied in a single direction. In this example, slip can take place when the applied stress exceeds a critical value, known as the *Critical Resolved Shear Stress* (CRSS). In the case of uniaxial loading, the applied *Resolved Shear Stress* (RSS) can be calculated via Schmid's law:

$$\tau = \frac{F}{A} \cos\phi \cos\lambda \tag{2.2}$$

where τ is the RSS, F is the applied load, A is the cross-sectional area, ϕ the angle between the *slip plane normal* and the loading directions and λ is the angle between the slip direction and the loading direction. The quantity $\cos\phi\cos\lambda$ is called the *Schmid factor* and links the applied, macroscopic stress to the shear stresses applied to the slip system. From Eq. 2.2 and the geometrical relationship between ϕ and λ, it is seen that Schmid factor values are bounded between 0 and 0.5 (considering only the absolute values). A high value close to 0.5 indicates easier slip.

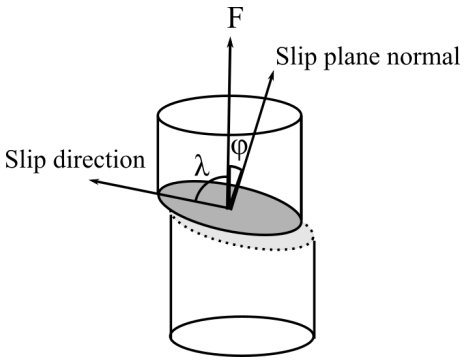

Figure 2.3: Geometry of slip in a single crystal.

The Schmid factor can be used as a parameter for predicting the activation of slip systems in a crystalline material, however, it is not always the case that the slip system with the highest Schmid factor is the one activated during plastic deformation. Schmid's law can be used to indicate the favourability of a particular slip system, but other factors can also influence the actual activation of slip in a polycrystal, including crystallographic texture, secondary deformation mechanisms such as

twinning or other effects which involve dislocation interactions with microstructure features [35] such as precipitates. These effects can influence dislocation mobility and therefore affect the slip system activation.

A major factor which is encountered in this thesis is the macroscopic stress state. Schmid's law assumes a uniaxial load applied on a single crystal, however, non-Schmid behaviour is encountered for different loading conditions, which leads to the activation of secondary slip systems (other than the Schmid-predicted one). An alternative method for predicting the ease of slip is via the Taylor factor, M [36]. The Taylor factor accounts for the individual grain orientations to predict the favourability of each orientation for deformation accommodation. Taylor's theory suggests that multi-slip takes place during deformation and predicts the activated slip systems using a *minimum work principle*. This means that the combination of active slip systems should be the one that minimises the energy required for slip. Assuming then that 1) same stress applied on the polycrystal is accommodated by each grain individually and 2) the shear stress, τ, for the activation of slip is the same for each slip system, one can then calculate the Taylor factor according to

$$M = \frac{\sigma}{\tau} \tag{2.3}$$

where σ is the applied, macroscopic stress [37].

2.1.2 Dislocations and plastic deformation

Plastic deformation in crystalline materials is accommodated by dislocation movement. Dislocations facilitate permanent changes in the atomic arrangement by allowing atomic planes to slip past each other. A simple visualisation of dislocation slip is shown in Fig. 2.4. In this figure an *edge* dislocation glides from left to right

while a shear stress τ is applied in the crystal. An edge dislocation is a type of line defect where the atomic plane abruptly terminates, resulting in a mismatch between the planes below and above the termination plane. To maintain atomic order below the plane where the dislocation terminates, the surrounding planes distort as shown in the figure.

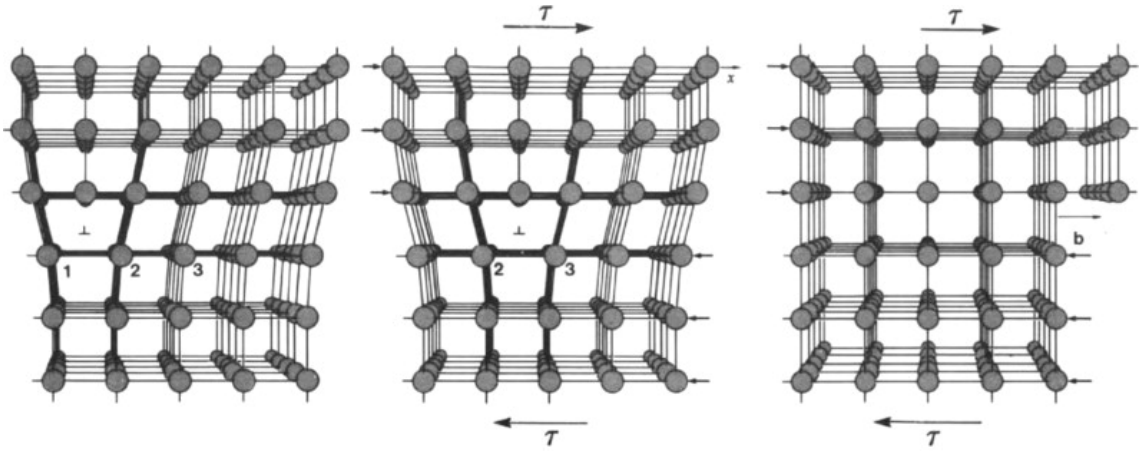

Figure 2.4: Movement of edge dislocation in a crystal under the application of a shear stress [6].

Depending on their distribution and accumulation, dislocations are characterised as *Geometrically Necessary Dislocations* (GNDs) or *Statistically Stored Dislocations* (SSDs). Bundles of dislocations of the same sign lead to a geometric effect in the crystal, where the lattice 'bends' to minimise the potential energy. Dislocations leading to the aforementioned lattice curvature are characterised as geometrically necessary or GNDs. In contrast, SSDs refer to bundles of dislocations of opposite signs, which cancel themselves out, and hence do not cause any significant geometric effect. Lattice curvature introduced by GNDs makes them easier to detect via an SEM, using techniques such us EBSD or Electron Channeling Contrast Imaging (ECCI), while observation of SSDs requires techniques of higher resolution such as TEM.

The concept of GNDs was introduced by Nye [38]. In his work he showed that various slip planes and their orthogonal trajectories are distorted into curved sur-

faces, and developed a method of correlating the lattice curvature with dislocation density. Nye introduced the dislocation tensor (second-rank tensor), which is used to characterise the dislocation network in a region within the crystal. Each dislocation tensor element, $\alpha_{i,j}$ (i, j=1-3) is linked to a curvature tensor element, $k_{i,j}$ via

$$\kappa_{ij} = \alpha_{ij} - \frac{1}{2}\delta_{ij}\alpha_{kk} \tag{2.4}$$

where the curvature tensor elements are $\kappa_{ij} = \mathrm{d}\theta_i/\mathrm{d}x_j$ and $\delta_{ij} = 1$ for $i = j$ or $\delta_{ij} = 0$ for $i \neq j$. Here, $\mathrm{d}\theta_i$ corresponds to the lattice rotations and $\mathrm{d}x_j$ the displacement vector. In this thesis, GND densities are used as an indicator of deformation accommodated within the crystal for a variety of strain states. A description of GND density measurement is given in a later section.

Dislocations play a significant role in the process of *work hardening*. Work hardening refers to the phenomenon where the flow stress is increased during deformation, which is closely related to the dislocation mobility and multiplication during deformation. Work hardening behaviour of a material is a result of several effects incorporating dislocation interactions. These include dislocation-dislocation interactions or interactions between dislocations and other obstacles such as grain or twin boundaries, precipitates, solute atoms (*dynamic strain aging*) or point defects.

According to Taylor's theory of dislocations [35], in a single crystal, the flow stress-strain relationship for two interacting dislocations of Burgers vector b is

$$\tau_d = \alpha G\sqrt{\frac{b}{x_i}}\varepsilon_d^{1/2} \tag{2.5}$$

where τ_d and ε_d are the flow stress and strain respectively, G is the shear modulus and α is a constant of order 10^{-1}. With x_i is denoted the dislocation *mean free path*, which is the distance a dislocation will cover until it is stopped by another disloca-

tion. The above description only assumes dislocation-dislocation interactions and, as expected for a polycrystal, stress-strain dependence deviates from this parabolic behaviour. Effects like dislocation pile-up at grain or twin boundaries lead to an increase in the work hardening rate. Similar is the effect of interactions between dislocations and precipitates or solute atoms. Contrariwise, interactions of dislocations can also lead to dislocation annihilation which will cause a decrease in the work hardening rate, an effect also known as *strain softening*.

2.1.3 Deformation twinning

In addition to dislocation slip, twinning is a deformation mechanism occurring in many materials that strongly influences the mechanical properties. Twinning refers to the abrupt reorientation of a portion of the crystal, so that the twinned region and the parent crystal form a specific orientation relationship between them. Major differences exist between twinning and dislocation slip. Crystal orientations above and below the slip plane are the same, while in twinning they are different. Slip incorporates movement of atoms in multiples of the atomic distance, while the atomic displacements in twinning are substantially lower than an atomic distance. Finally, slip takes place on planes that are many atomic distances apart while deformation twinning incorporates re-orientation of multiple, successive planes.

Twinning can form during an annealing process (annealing twins) or deformation (deformation twins). The morphology of annealing and deformation twins differs significantly. When observed metallographically, annealing twins often span large areas, typically measuring several micrometers, while deformation twins are significantly smaller and lenticular in shape. As this work focuses on the study of deformation characteristics of steels, only deformation twinning is discussed here.

Deformation twins in FCC crystals appear as a thin lamellar structure and have a thickness of a few hundreds of nanometers. Cahn [39] constructed a theory behind the crystallography of twinning, which is summarised here. Similar to dislocation slip, deformation twinning takes place when a shear stress applied to the crystal exceeds a minimum value; this is the *twinning stress*. When the twinning stress is reached, the crystal abruptly re-orients. It is characteristic of deformation twinning that the part of the crystal that re-orients will retain the crystal structure of the non-sheared, non rotated crystal. The unit cell and the atomic arrangement remain unchanged. In Cahn's theory it is shown that the only way this can happen is by finding three non-coplanar, rational lattice vectors in the initial, un-sheared state of the crystal, that will retain the same length and mutual angles after the application of the shear load. These planes are summarised in Fig. 2.5. K_1 represents the plane on which shear load is applied and remains undistorted. The second undistorted plane is designated with K_2 and with K_2' in its final, re-oriented state. The shear direction is shown with η_1 and lies on the shear plane, perpendicular to the K_1 plane. η_2 and η_2' lie on the twinned planes K_2 and K_2', respectively. These parameters are the *elements of twinning* and for FCC crystals are summarised in Table 2.2.

Two distinct results regarding the twinning geometry can be produced via the application of the shearing load. First, the twinned region can be produced via a 180° rotation of the twinned crystal around the K_1 plane normal. This example is shown in Fig. 2.5. Furthermore, the reflective symmetry between the K_2 and K_2' can be a result of a 180° rotation of the twinned region around η_1 (parallel to K_1). In both cases, the twinned and un-twinned regions are characterised by a reflective symmetry. In cubic crystals, both rotations will lead to the same final orientation relationships. In this case, the twins are called *compound twins*.

The atomic arrangement in a twinned FCC crystal is shown in Fig. 2.6. In the figure, a shear load is applied on the $[\bar{2}11]$ direction, resulting in an atomic displace-

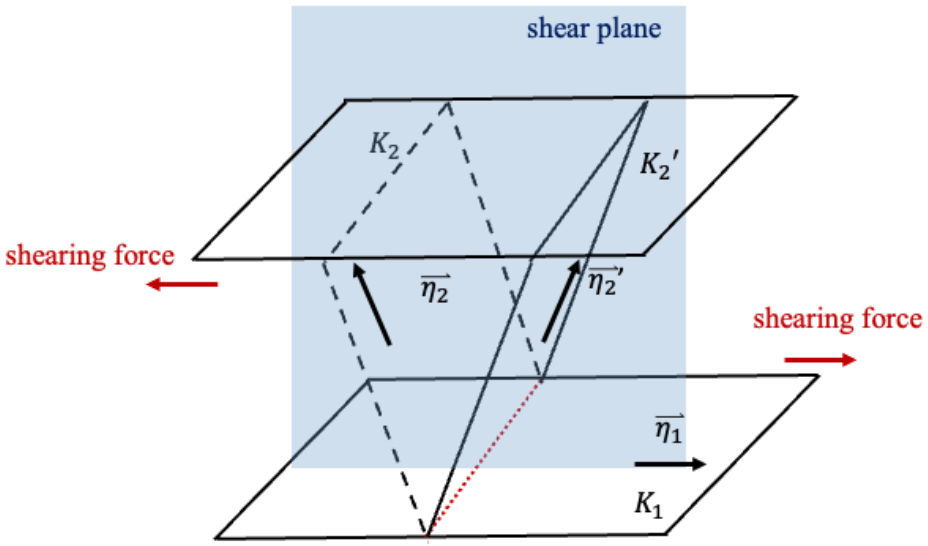

Figure 2.5: Deformation twinning elements of a sheared crystal. Diagram shows the direction of shearing load and how this results in re-orientation of the K_2 planes.

K_1	η_1	K_2	η_2	Twinning shear strain
$\{11\bar{1}\}$	$\langle 112\rangle$	$\{111\}$	$\langle 11\bar{2}\rangle$	$\sqrt{2}/2$

Table 2.2: Twinning elements in FCC crystals.

ment of $\alpha/\sqrt{6}$. This displacement of atoms interrupts the ABCABC... sequence and a stacking fault appears on one of the B planes, indicated with a solid red line. As load and co-ordinated displacement of atoms continues, the stacking fault grows, resulting in a 3 layer twin. The atomic sequence is now $...ABCAB\dot{A}\dot{C}\dot{B}CA...$ (right image). Three distinct regions are depicted in the last image, including the un-sheared matrix and the twin. The characteristic reflective symmetry between the twin and the matrix can be easily seen. In a twinned crystal, the twinning plane does not always coincide with the interface between the twin and the matrix, which is known as *twin boundary*. In the case where the twin boundary lies on the twinning plane, as in Fig. 2.7(a), the boundary is characterised as *coherent*. However, in many cases, the twin boundaries are not coincident with the twinning planes, and their formation involves the presence of dislocations as shown in Fig.2.7(b). The

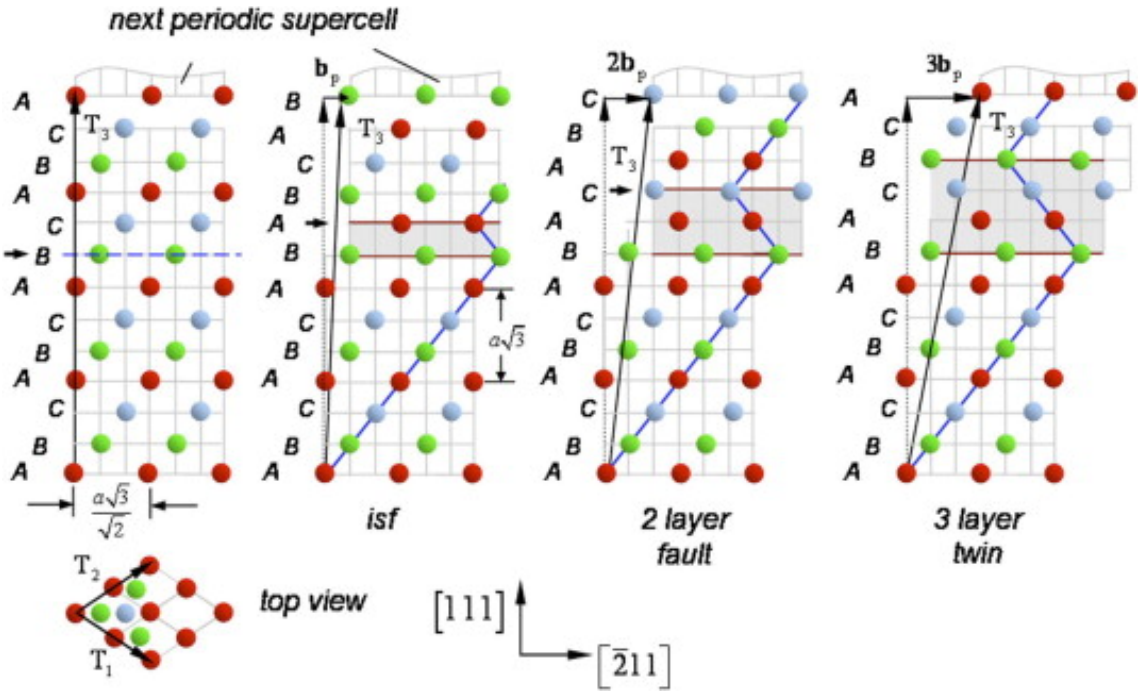

Figure 2.6: Twin formation in a sheared FCC crystal, obtained from [7].

latter are called *incoherent boundaries*.

2.2 The Iron-Carbon system

Steel is probably the most well known, studied and versatile metallic system. The phase diagram of the iron-carbon system which is shown in Fig. 2.8 reveals that depending on the processing and the alloying elements, numerous phases can occur, giving the alloy a number of desirable properties such as high ductility, exceptional strength, good weldability, corrosion resistance, machinability and hardness. The phase diagram shows the equilibrium between the different phases of steel including *austenite* (γ-iron), *ferrite* (α-iron), *cementite* (Fe_3C) and δ-iron. The present work focuses on deformation characteristics of high formability steels for automotive applications, hence the main focus of this section is devoted to low carbon and TWIP steels. Both alloy categories have exceptional ductility, however, their deformation

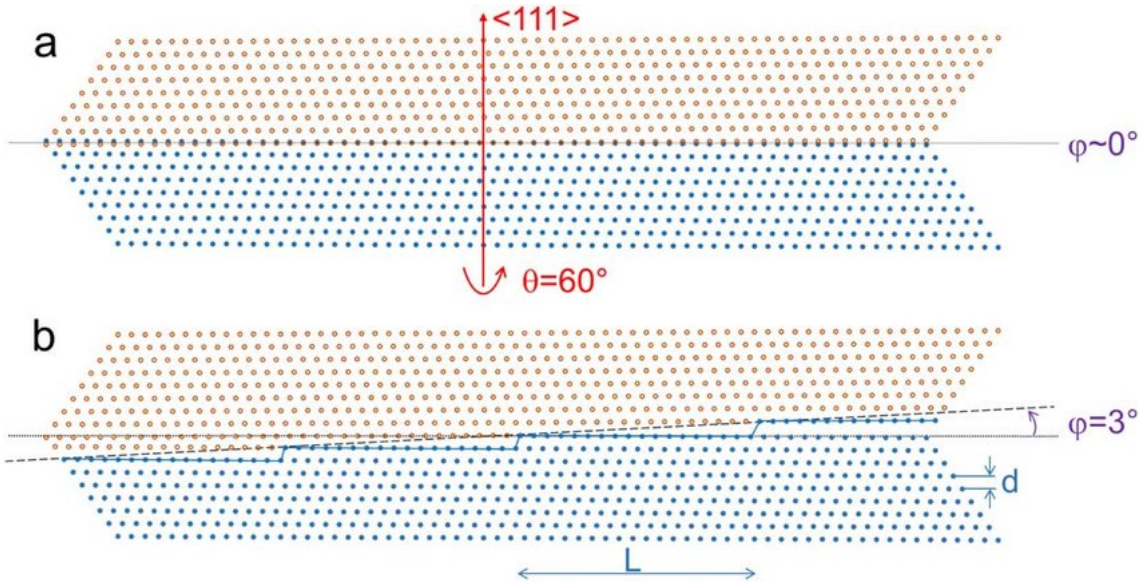

Figure 2.7: (a) Coherent and (b) incoherent twin boundaries [8].

mechanisms differ.

2.2.1 Ferritic steels

Low carbon steels contain a carbon content lower than approximately 0.1 wt% [27]. They are known for their high ductility as the low carbon content enhances dislocation mobility via decreasing potential dislocation pinning points [9]. This decrease in dislocation pinning points is also responsible for the relatively low yield strength (approximately 250 MPa) of these alloys.

Low carbon steels are usually characterised by a ferritic microstructure, which has a BCC crystal structure, and where C exists in the alloy in a solid solution form within the ferrite matrix, also known as α-iron. Low strength and high ductility of the ferritic phase makes low carbon steels excellent materials for forming applications. Cold rolling, is one of the most important processes in sheet metal forming, not only because it forms the raw material in an easy-to-use panel shape, but it also plays a definitive role in the *texture* development and hence the final mechanical

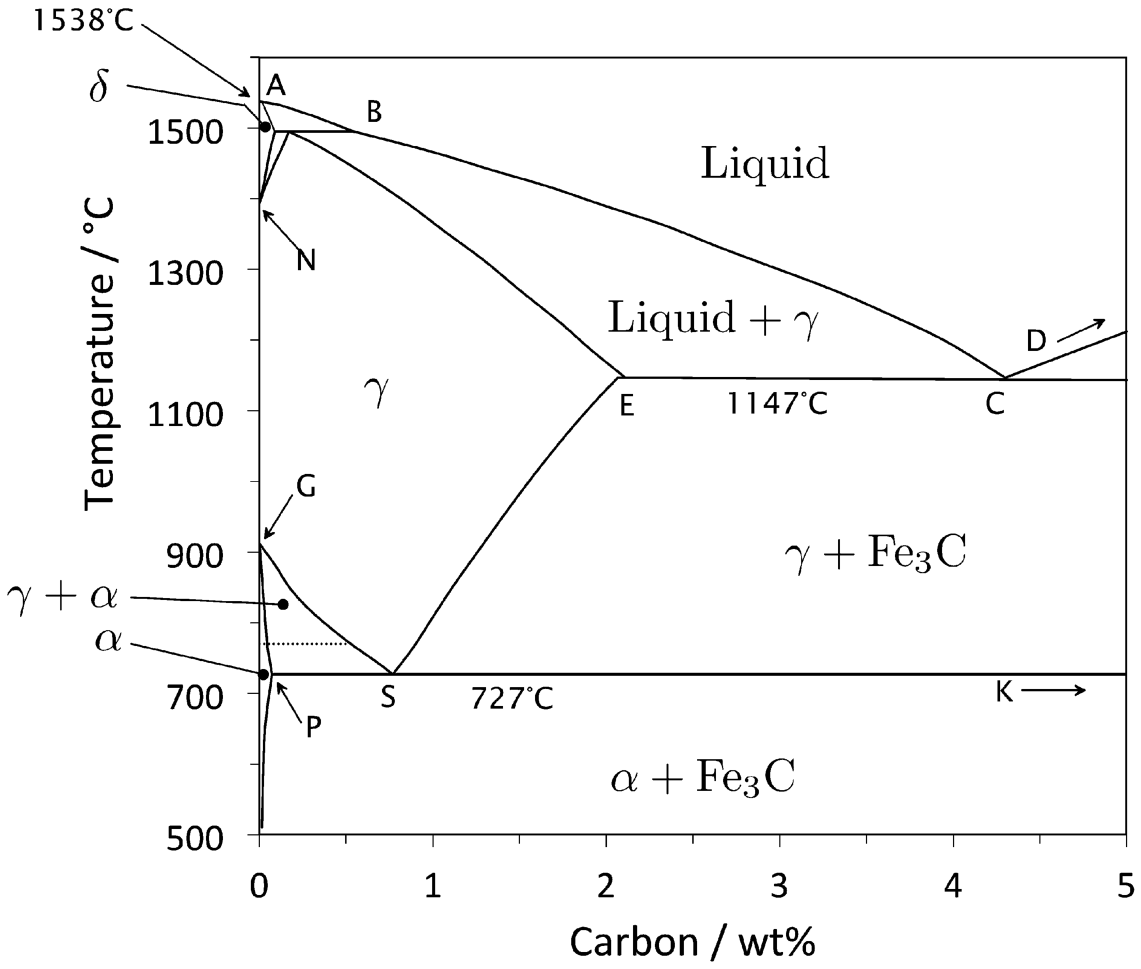

Figure 2.8: The iron-carbon phase diagram obtained from [9].

properties of the material.

The term texture refers to the preferred orientation of grains within a polycrystalline material, describing the statistical distribution of crystallographic orientations of the grains. To describe common textures obtained via cold rolling for the rest of this thesis, the RD, TD and ND notation is used, representing *rolling direction*, *transverse direction* and *normal direction*, respectively. As the names indicate, both RD and TD lie in the rolled sheet plane while the ND is normal to this plane. The most common textures [40] of ferritic steels are shown below:

- α-fibre running from $\{001\}\langle 110\rangle$ to $\{111\}\langle 110\rangle$, also known as RD-fibre

- γ-fibre running from $\{111\}\langle 110\rangle$ to $\{111\}\langle 112\rangle$, also known as ND-fibre

2.2.2 TWIP steels

TWIP steels are austenitic steels, with a Fe-Mn-C composition, which exhibit exceptional mechanical properties, combining high strength with ductility; as a result they are great candidates for automotive applications. Their excellent formability is attributed to the deformation twinning mechanism, promoted by the low SFE (15-45 $\mathrm{mJm^{-2}}$ [22]), which is strongly dependent on the Mn content (typically between 15-30% [22]). Low stacking fault energy increases the number of stacking faults in the crystal, which can act as twin nucleation points. The binary phase diagram of a Fe-Mn alloy is shown in Fig. 2.9. For low concentrations of Mn, the microstructure consists of α' and ε-martensite, while for medium concentrations, austenite and ε-martensite coexist. Finally, austenite alone is observed for Mn concentrations over 27%. To stabilise the microstructure and prevent phase transformations for Mn content $< 25\%$, addition of small amounts of C is required. In alloys with SFE $\leq$ 20 $\mathrm{mJm^{-2}}$ [41] formation of ε-martensite can occur under load, which is known as *TRansformation Induced Plasticity* (TRIP) effect. The Mn contribution to the SFE is non linear [22]. For low concentrations ($< 16\%$ at.), it decreases the SFE while for higher concentrations it increases the SFE and suppresses the $\gamma \rightarrow \varepsilon$ transformation.

In addition to Mn, the most common alloying elements in TWIP steels are Al and Si, as they act as stabilisers of the γ-phase, inhibiting a phase transformation occurring under load, from austenite to ε-martensite. It is known that an increase in Al content results in higher SFE [42] and suppresses the $\gamma \rightarrow \varepsilon$ transformation. The Al content can also affect twin formation. Chin et al. [43] explored the differences in twin generation in two TWIP steels, one containing Al and one not. Their study, utilising cup forming and tensile tests, revealed that Al addition led to an increased

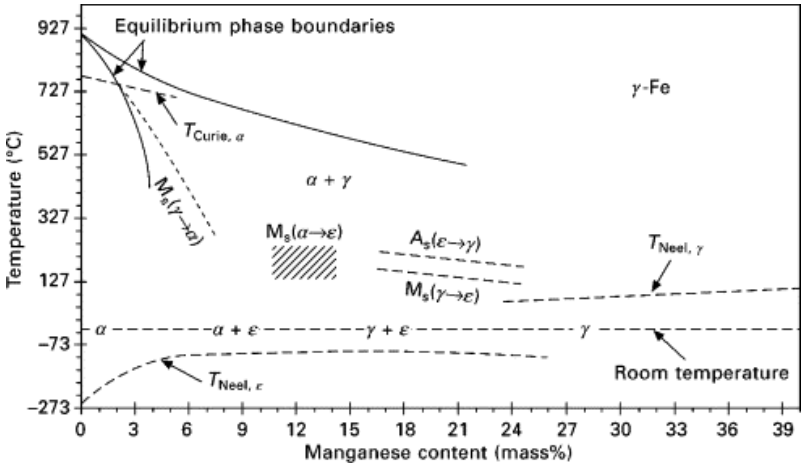

Figure 2.9: Binary phase diagram of a Fe-Mn steel [10].

SFE which they linked to a more homogeneous twin development in the TWIP steel with Al addition in comparison to an Al-free TWIP steel. The authors concluded that, whilst deformation twins were apparent in most of the grains in the TWIP steel including Al, the fraction of the twins in a the Al-free steel was higher. This result was further supported by the development of cracks in the Al-free TWIP steel, after cup forming, an effect attributed to the higher stress localisation of this alloy. Further studies [44, 42] also supported that increasing Al content increases the SFE and hence limits twin generation.

The addition of Si improves the overall strength of TWIP steels, via contributing to solid solution hardening as well as assisting the generation of deformation twins [45]. Experimental studies suggest that the SFE is decreased while increasing the Si content [46, 45], however, thermodynamic calculations [47] reveal a more complicated behaviour, where the SFE increases for low Si contents ($< 3\%$) and decreases for higher contents. The discrepancies between the calculated and the experimentally obtained SFE dependence on Si content, was attributed by [45] to a 'lack of Mn-Si and Si-C parameters' in the calculation.

TWIP steels are known for the very high strain hardening rates they exhibit, which are attributed to the high volume fraction of deformation twins generated

during deformation, as twins impede dislocation mobility. Twinning in TWIP steels is a result of the coordinated gliding of $\alpha_0/6\langle 121\rangle$ Shockley partial dislocations on the successive $\{1\bar{1}1\}$ planes (where α_0 is the lattice constant), which play the role of twinning planes [48]. This twinning mechanism was previously described in section 2.1.3. The twinned portion of the crystal and the un-twinned crystal form a 60° angle between them. The corresponding twin boundaries are also known as Σ_3 twin boundaries. Dislocation slip and twinning are competing deformation mechanisms and it is known that dislocation slip precedes deformation twinning [49, 50, 51], which is activated post-yield. Sub-yield twin formation was proposed by Rahman et al. [52], using X-ray diffraction broadening data in combination with elasto-plastic self consistent modelling, however, their findings were re-evaluated by Saleh and Gazder [53] and did not agree with their conclusions. A rapid increase in the work hardening rate post-yield is generally associated with generation of twin boundaries [54, 55, 56], while a saturation of twinning activity at high strains results in a decrease in the work hardening rate. While the above results highlight that the twinning mechanism is arguably crucial for the excellent work hardening of TWIP steels, it is known that dislocation slip remains the dominant deformation mechanism for this alloy family.

Similar to ferritic steels, it is important at this point to refer to the rolling textures forming in TWIP steels. SFE plays a critical role on the texture formation [22], with high SFE FCC materials being characterised by a Cu texture including Cu ($\{112\}\langle 111\rangle$), brass ($\{011\}\langle 211\rangle$) and S components ($\{123\}\langle 634\rangle$) in equal quantities. In contrast, TWIP steels which are characterised by low SFE, exhibit a brass texture comprised of a strong brass and a minor Goss component ($\{011\}\langle 100\rangle$) [40]. Brass texture is attributed to the simultaneous act of slip and deformation twinning hence is more prevalent in low SFE metals.

2.3 The strain path effect

The strain path effect refers to the influence of the deformation history on the mechanical and micromechanical properties of a material. The strain path defines a single or a series of strain states that a material undergoes while deforming. The terms of *major* and *minor* strain, often denoted as ε_1 and ε_2 respectively, are used to describe a strain path. Major strain refers to the maximum macroscopic strain the material undergoes while deforming, while the minor strain is perpendicular to the major strain. For the description of a strain path the ratio between ε_1 and ε_2 is often used, which is called *strain ratio*.

Strain paths can be represented as continuous lines in a two-dimensional plot, using the major and minor strains at the vertical and horizontal axes respectively. An example plot is shown in Fig. 2.10. In this example, three very common deformation states are shown, those of *uniaxial*, *plane* and *equibiaxial* strain states. Each state corresponds to a different strain ratio. For uniaxial strain, which is the deformation state encountered in a conventional tension test, the strain ratio is $\varepsilon_2/\varepsilon_1 = -1/2$. Plane strain, which is representative of cold rolling is described by $\varepsilon_2 = 0$. This means that the strain resulting from the material elongation equals the strain produced from its thickness reduction. Finally, for equibiaxial strain, $\varepsilon_2/\varepsilon_1 = 1$. Those three strain paths are extensively used within this thesis. In all the cases described above, the 'connection' between the initial, un-deformed state and the final state of a deforming material, is linear. Such strain paths are called *linear* or *proportional*. However, as was shown in Fig. 1.4, during stamping, changes in strain paths are encountered. In the case where an SPC takes place, then the strain path is called *non-linear* or *non-proportional*. For non-linear strain paths, the connection between the initial and the final deformation state of the material is non-continuous. A great proportion of this work is devoted to non-linear strain paths.

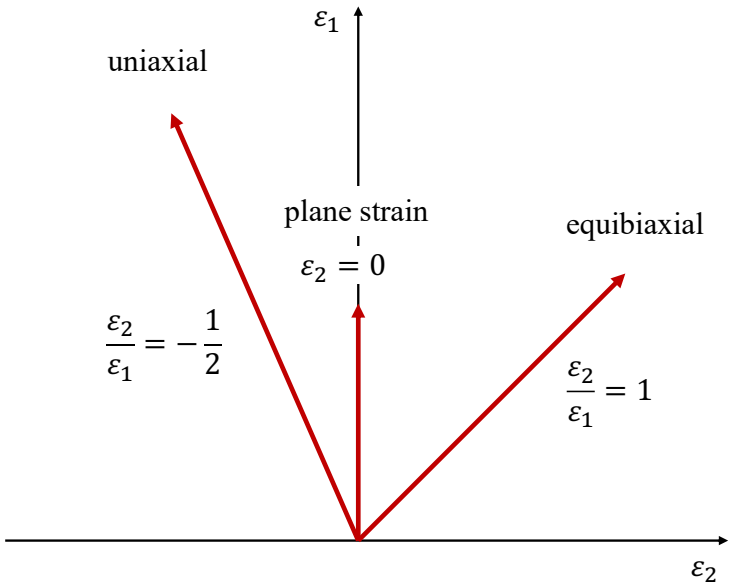

Figure 2.10: Common strain paths.

2.3.1 SPCs on low carbon steels

Due to its widespread use in metal forming, the properties of low carbon steel have been widely investigated in situations involving non-linear strain paths. Gosh and Backofen [57] were among the first studying the SPC effect on low carbon steels. In their work they subjected metallic sheets to a two-step deformation process, including pre-straining in different strain ratios and effective strains, followed by uniaxial loading. They recorded a notable dependence of the macroscopic material properties on the strain ratio, an increase in the YS after pre-straining, that was greater as the effective pre-strain increased, and an increase of strain hardening rate as the strain ratio of the biaxial pre-straining increased. A later work [58] investigating the effect of uniaxial and biaxial pre-straining on the same material, found that biaxial pre-straining resulted in a notable strength increase accompanied by a saturation of work hardening post-yielding, an effect described as *plastic instability*. This means that as the strain ratio increases, the material reached the strain of localised necking faster. In addition to the deformation state, the pre-straining direction was later

revealed [59] to play a significant role on the work hardening behaviour and the ductility of the material. The occurrence and the margin of unstable flow was found to depend significantly on the effective pre-strain and the loading direction, however, ductility was found to be affected once a critical amount of effective pre-strain was reached.

Microstructural effects of the above phenomena have been examined in detail via Transmission Electron Microscopy (TEM). Wilson and Bate [32] studied microstructure development in an IF-steel which underwent pre-straining via cold rolling followed by uniaxial tension an 0°, 45° and 90° to the rolling direction (RD). This way, they examined the *abruptness* of the SPC influence on the tensile properties of the material. It was found that for 90° pre-strain, and for increasing the effective pre-strain, the YS was increased and the ductility was significantly reduced when the effective pre-strain exceeded a specific level ($\approx 8\%$). The increase in the YS was associated with the development of dislocation cell walls during pre-straining, which can inhibit dislocation mobility during reloading. The drop in the hardening rate immediately after yielding, which was sharper as the effective pre-strain increased, was attributed to breaching the dislocation cell walls by micro-shear bands generated within newly activated slip systems. The same effect has also been observed for the same material, upon stress reversal processes [60]. In the latter, the drop in the work hardening rate was directly associated with interactions between deformation features forming during reloading within the dislocation cell walls, rather than modifications taking place at the pre-existing dislocation cell structures. Similar results regarding the rapid increase in the YS pre-straining and re-loading directions tend to be perpendicular, were obtained by Li et al [61]. In their work they attributed the high flow-stress anisotropy to the dislocation walls and the microbands formed during the pre-strain, while they suggested that the anisotropy effect cannot be influenced by texture modifications occurring from the different strain paths. Similar

results are backed up by a number of relevant studies [30, 31, 62, 33], highlighting the importance of deformation structures formed during pre-straining for the final work hardening behaviour and the strong influence of the initial and final loading directions to the mechanical properties.

In more recent years, studies increasingly have focused on modelling material behaviour under non-proportional deformation. Erinoso et al. [63] used a Crystal Plasticity Finite Element (CPFE) model to investigate the effects of a series of non-proportional strain paths on the dislocation distribution and the limit strains of a low carbon steel. Their findings indicated an increased ductility for uniaxial non-proportional strain paths in contrast to biaxial non-proportional strain paths, and a moderate influence of the pre-straining mode on the final dislocation distribution. Kitayama et al. [64] used a Visco-Plastic Self-Consistent (VPSC) model to describe the mechanical response of low carbon steels pre-strained in uniaxial tension and then sheared in different directions to the pre-strain direction. Their model was informed by crystallographic information incorporating dislocation annihilation post-SPC. Using similar formulations, Wen et al. [65] simulated the mechanical behaviour of a low carbon steel subjected to a tension-shear sequence. In both works, simulations managed to predict the experimentally obtained mechanical response with high accuracy.

As the computational simulations of the hardening behaviour under SPC gains increasing attention, experimental data to calibrate and/or validate VPSC and CPFE models are required. Even though low carbon steels are very popular alloys for non-proportional deformation investigation, fewer works have studied deformation characteristics of these alloys in the mesoscale. Collins et. al [16] used SXRD to map the lattice strains and texture changes of low carbon steel cruciform specimens, and observed a ductility improvement for strain paths incorporating uniaxial tension. The unexpected ductility increase was attributed to three main factors: 1)

a possible sheet orientation difference between the non-proportionally and the proportionally deformed specimen, 2) a difference in the strain rates developed during uniaxial tension of cruciform specimens vs Nakazima specimens and 3) an overestimation of the final strains by DIC. More details regarding experimental setups for biaxial deformation will be discussed in later section.

A ductility recovery combined with strength increase, of a pre-strained sheet has also been recorded for an IF-steel after asymmetric rolling [66]. Even though, as previously discussed, the cold rolling state is detrimental for the ductility of the material, it was observed that for a thickness reduction of 75%, strain localisation was delayed and the overall plasticity was improved, in comparison to lower thickness reductions. The authors attributed the enhanced strength and ductility to the refined grain and dislocation structures formed at high thickness reductions, which act as obstacles to crack propagation and decrease the size of the nucleating flaws.

The aforementioned results highlight the potential use of non-proportional deformation processes for mechanical properties enhancement. Fine tuning the material properties, however, requires further experimentation to provide insights regarding the material behaviour in the mesoscale (where the biggest lack of experimental information is observed). In the following sections, the strain path effect on TWIP steels is discussed and information regarding non-proportional deformation testing methods is given.

2.3.2 Strain path effect and TWIP steels

In contrast to low carbon steels, information regarding TWIP steels under non-proportional strain paths is limited. Thus, the current section does not only focus on TWIP steel behaviour but also includes information regarding the twinning mech-

anism on low SFE austenitic steels, under proportional and non-proportional strain paths.

Twinning activity assessment for austenitic steels under uniaxial and biaxial strain paths has been the objective of a number of studies. An increased number of deformation twins has been observed for biaxial paths over uniaxial strain paths for an AISI 316L stainless steel [67] and a TWIP steel [68]. Contradictory results were, however, obtained by a different study [69], which concluded that uniaxial strain path enhances twinning activity, while equibiaxial strain path is the least favourable for twin formation. This result is also supported by different studies [70, 71] on austenitic steels. Polatidis et al. [70], showed that the texture formed during equibiaxial loading of a 304 stainless steel is unfavourable for twin formation and twinning activity is impeded. The same study suggested that for biaxial deformation where twinning is unfavourable and cross slip is promoted, an increase in the α'-martensite nucleation cites is observed. According to a different work [71], focusing in the twinning activity in a TWIP and a TRIP steels subjected to uniaxial, plane strain and equibiaxial strain paths, it was shown that deformation twin generation was independent to the TRIP effect (formation of ε-martensite). Additionally, it was suggested that twinning activity is increased for the uniaxial strain path due to the favourable texture formed for this deformation process.

Formation of deformation twins has been proven to be strongly influenced by grain orientation and grain size. EBSD studies [72, 73, 74] on uniaxially deformed specimens have indicated that $\langle 111 \rangle \parallel$ tensile axis is the most favourable for twinning. It has been shown [73] that for low strains, twin generation follows a Schmid behaviour (the Shockley partial generating a mechanical twin is the one with the maximum Schmid factor) and is favourable for the $\langle 111 \rangle \parallel$tensile axis orientation. Young et al. [75] showed that if the CRSS for twinning is 15% higher than the CRSS for slip, then twinning becomes feasible only when multi-slip takes place. In-

stead of the Schmid factor, the Taylor factor can be also used to predict orientations favourable for twinning. Beladi et al. [74] found that for the early stages of plastic deformation, twinning occurs at grains with the highest Taylor factors, while grains with lower Taylor factors remained twin free. In the latter, deformation via slip was determined as the predominant deformation mechanism. The use of Taylor factor over the Schmid factor is thus best suited for metal subjected a complex deformation mode [76].

Regarding the effect of grain size, Bouaziz et al. [77] suggested that the twinning stress for a Fe-22%Mn-0.6%C TWIP steel is not influenced by the grain size, however, several studies have reported an decrease in the twinning activity for decreasing grain size in high Mn austenitic steels [73, 78, 79, 80]. It is empirically known that twinning stress dependence on the grain size, follows a Hall-Petch behaviour, $\sigma_{y,T} = \sigma_0 + k_T d^{-1/2}$, where $\sigma_{y,T}$ is the twinning stress, σ_0 and k_T are constants and d is the average grain size [81].

As discussed so far, it appears that combining two deformation mechanisms makes the investigation of mechanical properties of TWIP, or other austenitic steels more complex than ferritic steels. Only a few works have focused on the effect of SPCs on TWIP steels. Saleh et al. [82] examined the mechanical behaviour and the lattice strain evolution of a Fe–24Mn–3Al–2Si–1Ni–0.06C TWIP steel upon stress reversal (tension-compression cyclic loading) using neutron diffraction and elasto-plastic self-consistent modelling. Their findings indicated tension-compression asymmetry in the flow stress which was attributed to geometrical effect of the load path change rather than microstructural modifications upon stress reversals. McCormack et al. [83] were the first to directly observe twinning and de-twinning in a TWIP steel upon stress reversal. They also recorded a decrease in the twin formation during compression in respect to tension, an effect explained via Schmid's law, which indicates that twin systems active in tension, are not active during compression.

De-twinning was also observed in a later study [84] for a similar deformation process on a TWIP steel. In this study direct observation of twinning and de-twinning was carried out and it became apparent that de-twinning started at approximately the same stress required for twinning to initiate and not immediately after stress reversal. In this work, it was also found that deviations of the Schmid behaviour were observed in the activated twin systems, which were attributed to the heterogeneity of stress fields due to the stress reversal.

Except from stress reversal experiments, a few works have studied TWIP steels under SPCs using different types of test rigs. Pereira et al. [85] used a two-step tensile testing to study the effect of the pre-strain magnitude and deformation direction on the mechanical properties and microstructure on a Fe–18Mn–1.5Al–0.6C TWIP steel. A plateau in the flow stress was observed post yielding which was more prominent when re-loading was in the same direction as pre-straining. They found out that the plateau appearance was not due to possible strain rate variation during the experiment nor was significantly influenced by temperature. They finally linked this plateau to a rapid and localised formation of dislocations which had an insignificant effect in hardening. They also concluded that the appearance of twins occurs at intermediate strains (>10%) and with increasing strain, contributing to the hardening of this material. This study does not pinpoint the strain path making the twin formation more favourable. Another work [86] used unidirectional and reverse-loading during wire drawing of a Fe-17Mn-0.7C-1.5Cu (wt.%) TWIP steel to study texture and twin formation evolution. An increase in strength with simultaneous ductility loss was recorded in the case or reverse-loading correlated with an increase in the $\langle 111 \rangle \parallel$ ND fibre which is also favourable for twinning as previously discussed.

Via the above discussion is apparent that only a few studies exist in literature regarding the micromechanics of TWIP steels under SPCs, and almost all of those

results are obtained in the micro-scale (via SEM and TEM), while only one work [82] has been conducted to the best of the authors knowledge involving information at the mesoscale obtained via neutron diffraction. This is not surprising since studying biaxial deformation, especially in-situ, is non-trivial. In the following section, an overview of the experimental set-ups for investigation of properties of metallic sheets under biaxial deformation is provided.

2.4 Test rigs for biaxial deformation

This section focuses on experimental setups used to study biaxial deformation. The two most common testing categories are the punch-type tests and the cruciform-type tests. Strain path sensitivity of steels has been examined with both methods, although cruciform-type tests are more popular as SPCs can be explored. Details regarding the functionality and main works were such tests have been used for investigating steel formability, are provided here.

2.4.1 Punch tests and the Forming Limit Curve (FLC)

The investigation of the forming limit of metallic sheets under various deformation processes is of great importance for industrial applications. The conventional tension test can provide information about mechanical properties, but it does not investigate the significant strain path dependence of the resulting plastic strain developed under multiaxial loading. To overcome this difficulty one can use the Nakazima or Marciniak tests, where a hemispherical or flat punch respectively, is used to deform a metallic sheet, cut into various shapes, to control the stress development.

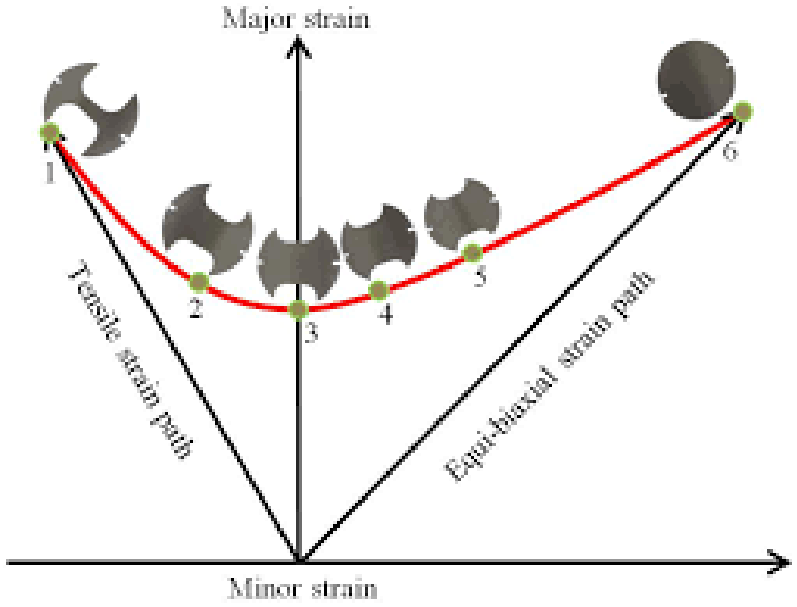

Figure 2.11: The Forming Limit Curve [11].

The most widely used type of test for examination of the formability of metallic sheets are the Nakazima and Marciniak tests. These tests are commonly used for determination of the forming limit, or in other words, the maximum strain level a material can reach, before strain localization occurs. The FLC was first introduced by Keeler [87] in 1963. A typical FLC is shown in Fig. 2.11, where the relationship between the major and minor strains is shown. The red line corresponds to the forming limit of the material; when this is exceeded, the material fails. Controlling the developing stresses is such tests is achieved via variation of the specimen design. Specimen with the narrowest gauge (No. 1 in Fig. 2.11) results in the uniaxial tension state, while the circular specimen (No. 6) corresponds to the equibiaxial tension state.

A typical FLC test rig geometry is shown in Fig. 2.12. In both Nakazima and Marciniak cases, specimen is clamped between a die and a blank holder, and is drawn by a hemispherical (Nakazima) or flat (Marciniak) punch, at a controlled rate. For strain measurement, the 3D DIC technique is used. The surface of the specimen is usually covered with a random black and white pattern (speckle pat-

tern). Throughout the deformation process, the speckle movement is recorded by a dual camera system, which is placed above the deforming specimen, and subsequently, with appropriate calibration, the measured displacements are transformed into strains.

Good lubrication between the punch and the specimen is a key factor controlling the developing principal strains and ensures that higher stretch levels are reached prior to the appearance of strain localization [88]. For this purpose, a polyethylene sheet is most commonly used, as it is considered to have excellent lubrication properties [88]. Additionally, minimising the friction effect assists the fracture of the blank to occur in the middle section opposed to the edges. To avoid friction development and fracture of the specimen at the edges of the flat punch instead of the middle, in the Marciniak test, an additional metallic sheet, with a central, circular hole, can be placed between the punch and the specimen, also called a *carrier blank* (Fig. 2.12), however, other methods have been reported in literature, leading to the same result. Deng and McGuire [89], developed a novel punch geometry, where a circular cut-off is located in the center of the flat punch surface, allowing a gap between the punch and the specimen. In contrast, Kong et al. [90] adjusted the specimen design, so that the thickness is reduced in the central area, while keeping the punch shape unmodified.

One of the main disadvantages of the punch-type test is that while monotonic loading can be easily applied via a punch test, investigating the effect of SPCs is difficult due to the geometry of the punch test setup. Nevertheless, there are some examples in literature that used the Marciniak test for SPC application. An Advanced High Strength Steel (AHSS) [91] was pre-strained via a flat punch under various deformation modes. Specimens were then prepared from the pre-strained sheets and were further deformed via tensile, stretch bending and hole expansion testing. In another studies [92, 93], focusing on the properties of a magnesium

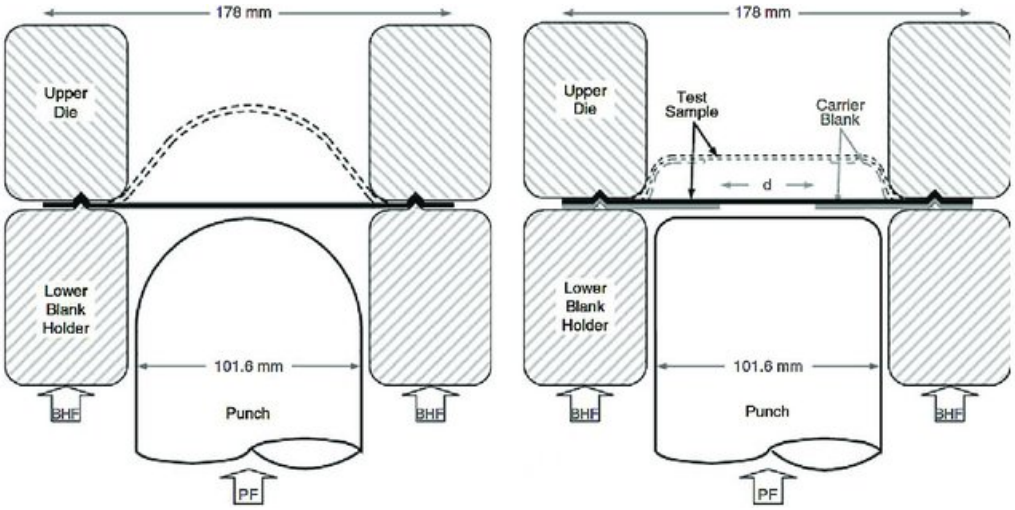

Figure 2.12: Nakazima (left) and Marciniak (right) test setup [12].

and aluminium alloys respectively under SPCs, Marciniak setup was used for pre-straining and miniaturised dog-bone specimens were cut from the punch-deformed area and were subjected to tensile testing.

Punch-type tests have been also used in some occasions for in-situ testing [94, 95, 96]. In those examples, an X-ray beam was probing behind the moving punch and the detectors for the diffracting beam were placed above the deforming specimens. While this method allows for in-situ measurements, the application of SPCs in-situ is prohibited, as further post processing would be required, as discussed in the previous paragraph. Application of SPCs during in-situ measurements have been facilitated by the cruciform-type tests, which are described in the next section.

2.4.2 Cruciform type tests

A more complicated specimen and test rig geometry characterises the cruciform type tests. For reference, a typical biaxial cruciform-type test rig is shown in Fig. 2.13a. As the name reveals, a cross-shaped specimen is loaded on a four-armed hydraulic rig. Depending on the rig, each of the arms can move independently providing

freedom on the application of a load state. Strain measurement is most commonly facilitated by 3D-DIC, where 2 cameras are located perpendicular to the deforming specimen surface, and record the displacements during loading. The main difference between the cruciform-type to the punch type tests, is that in the cruciform type, strain path is controlled by the loading conditions applied on the arms, while the specimen geometry does not vary between strain paths. A major advantage of the cruciform type test is that no post-processing is required for the applications of SPCs, in contrast to punch type tests.

The biggest disadvantage of the cross-shaped specimens is the strain localisation which happens far from the Region Of Interest (ROI), which is the area of uniform strain (central area), at the arms intersection points (see Fig. 2.13b). To avoid this effect several methods have been proposed in literature. Slits can be added at the arms area [13] to reduce stress concentrations, which can be also combined with central area thickness reduction, to assist stress concentrations to occur in the ROI [97]. In other designs, circular cut-outs have been also added, achieving fracture in the specimen centre [98]. In all cases, to achieve a specimen design to prevent strain localisation at the arm intersection areas, Finite Element Analysis (FEA) shall be consulted.

The ability to apply SPCs without the need for further specimen processing, which is unavoidable for punch type tests, has made the use of this test type for in-situ measurements attractive. Material characterisation in-situ during biaxial deformation applied on a cruciform specimen has been successfully conducted on steels, using X-ray [24, 16], neutron [99, 70, 100, 101, 102] and electron [103] diffraction. An example of a biaxial test setup for in-situ X-Ray diffraction study is shown in Fig. 2.14. In this figure, a cruciform specimen is biaxially loaded while an incident X-Ray beam is diffracted by the deforming specimen. The diffracted X-Rays are then collected in transmission onto a 2D detector, producing the characteristic for

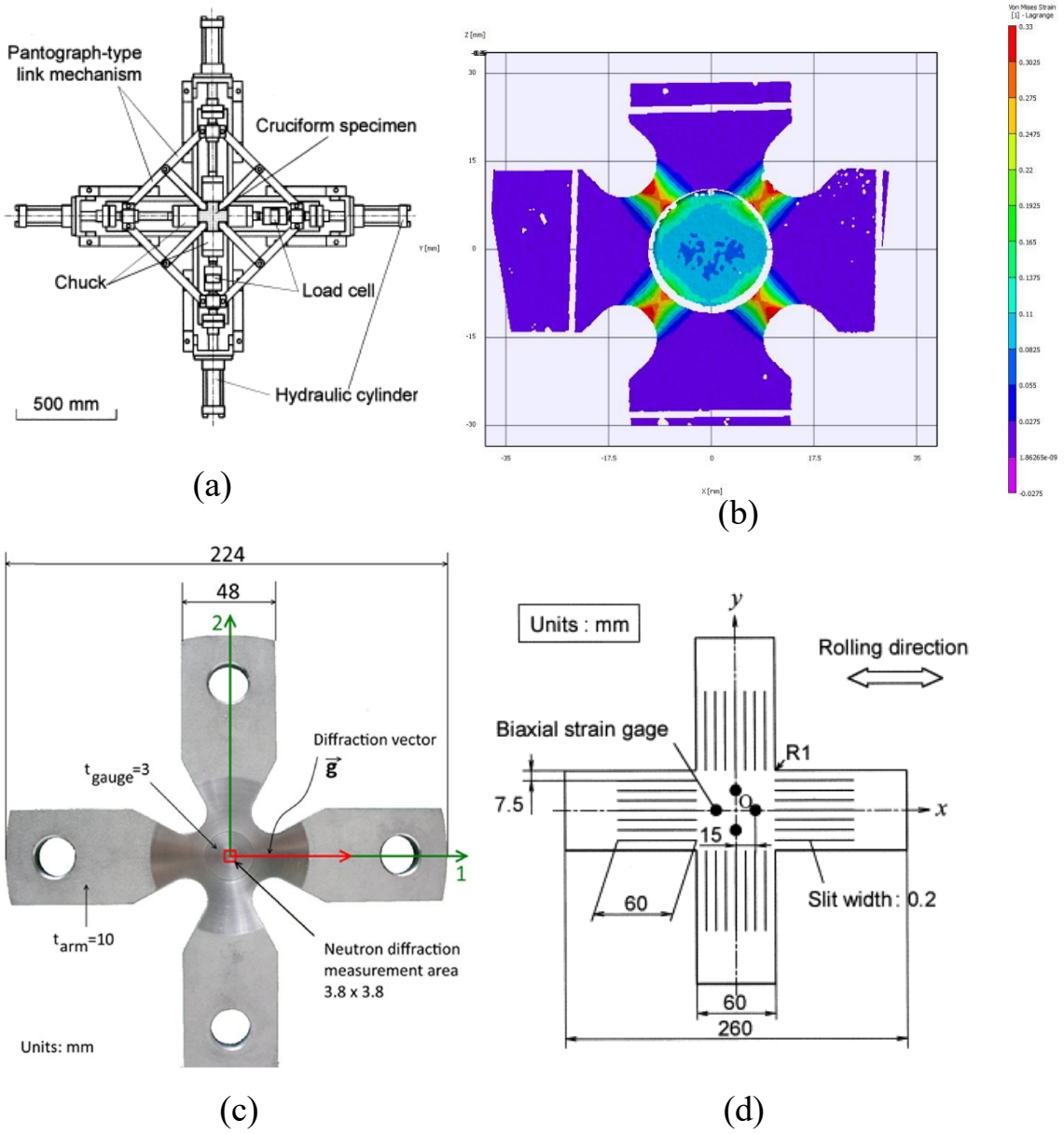

Figure 2.13: Biaxial testing: cruciform specimen design. (a) Biaxial test rig [13], (b) stress concentration areas [14], (c) circular cut-out design [15] and (d) arm slits design[13].

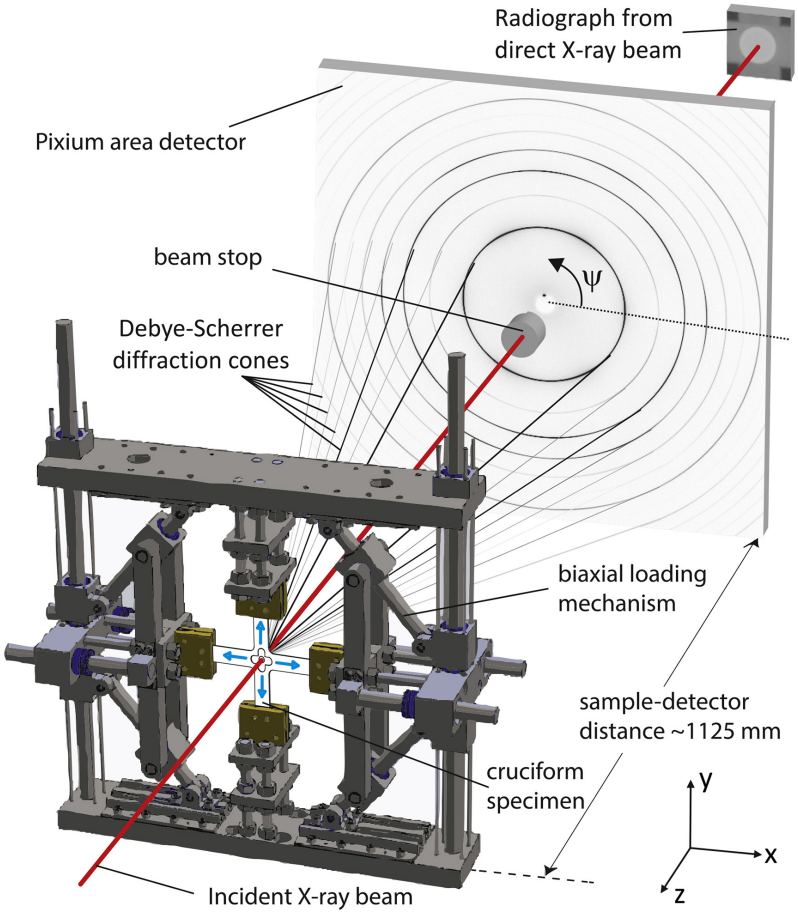

Figure 2.14: In-situ biaxial test rig, obtained from [16].

polycrystalline samples, Debye-Scherrer rings. As will be described in a later section 2.5, information obtained from the Debye-Scherrer rings can be used to study deformation characteristics of the deforming polycrystal.

2.4.3 The Small Punch Test (SPT)

The SPT is a biaxial testing method for evaluating the mechanical propertied of miniaturised specimens. It was first developed by Manahan [104], for the determination of the mechanical properties of irradiated specimens. The size of the tested specimens did not initially exceed the ones typically used for TEM ($3\,\text{mm} \times 0.25\,\text{mm}$), although nowadays, bigger specimens are also used, commonly having a diameter of

8 mm and thickness of 0.5 mm [17]. One of the main advantages of the SPT is that it allows the fabrication of multiple samples from just one component, which makes it a very attractive technique in comparison to the standard uniaxial tension test, particularly for cases where the volumes of the materials available are limited.

Although several test configurations have been reported in the literature [19], the typical test apparatus consists of the lower and upper dies, a hemispherical punch with diameter of 2.5 mm and a deflection measurement rod, as shown in Fig. 2.15. During testing, a specimen is tightly clamped between the dies and the punch moves at a constant rate (punch velocity range between 0.2 mm/min and 2 mm/min [17]), resulting in a compressive load on the specimen. Both the punch and rod displacements are measured, as does the punch load. The resulting plot is a *Load-Deflection* curve, from which the mechanical properties of the material can be estimated. In Fig.2.16 the typical load-deflection curve for a ductile material is shown. Areas (1) and (2) correspond to the elastic and the transition to plastic regimes respectively, while area (3) corresponds to the transition to the membrane stress region. In region (4), membrane stress is established, where the material undergoes the same normal stress everywhere throughout its thickness, until the maximum load is reached and the material is led to failure, at region (5).

Accurate estimation of the tensile properties via the SPT has been the objective of several works [105, 106, 107, 108]. The initial thickness of the specimen (t), predominantly, has a significant influence in the yield (σ_{YS}) and tensile (σ_{UTS}) strengths obtained. According to the ASTM International [17] the best estimation of those properties can be achieved via Eq. 2.6 and 2.7 by taking into account, not only the specimen thickness, but also the specimen deflection (u), during drawing. Two methods exist for the determination of the yield force (F_Y); the *two tangent* and *the parallel offset* methods [19]. According to the first method, the yield force corresponds to the point where two tangents, drawn from the elastic (1) and the

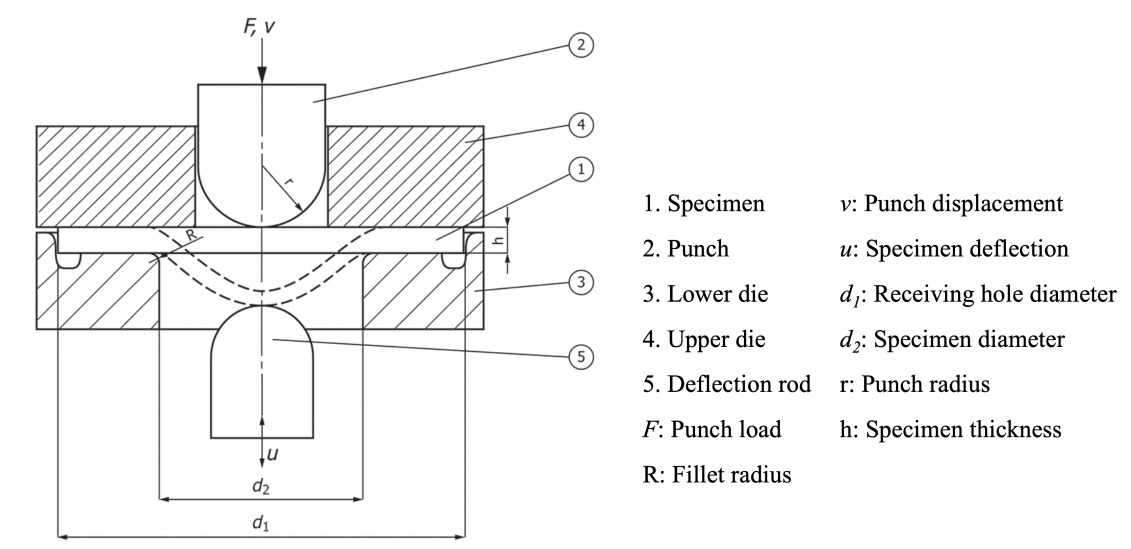

Figure 2.15: SPT geometry [17]

.

early plastic (2) regions respectively, intersect, as shown in Fig. 2.17. For the second method, a line is drawn parallel to the load-deflection curve at the elastic region (1), displaced by $t/10$ from that curve. The intersection with the parallel line and the original curve is the F_Y. The empirical parameter α can be then estimated by the correlation of the SPT results with the yield strength obtained for the same material from a conventional tensile test.

$$\sigma_{YS} = \alpha \frac{F_Y}{t^2} \tag{2.6}$$

Similarly, the ultimate tensile strength can be obtained using the maximum force reached during the test (F_{max}), assuming that necking occurs at this exact point. The empirical parameter β can be then calculated via the correlation of the data obtained from the SPT and pre-existing tensile data. In many cases, instead of the relationship 2.7, the Eq. 2.6 has been used, neglecting the effect of specimen thinning. However, Garcia et al. [106] suggested that the empirical parameter β' obtained from Eq. 2.8 show lower R^2 values and exhibit a high dependence on the

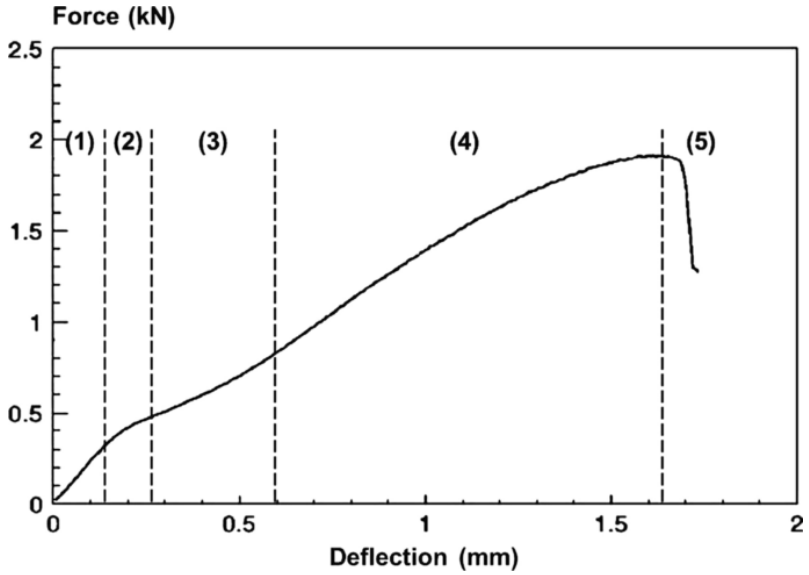

Figure 2.16: Typical load-deflection curve for ductile materials [18].

.

material tested.

$$\sigma_{UTS} = \beta \frac{F_{max}}{tu} \tag{2.7}$$

$$\sigma_{UTS} = \beta' \frac{F_{max}}{t^2} \tag{2.8}$$

In many setups, the deflection measurement rod does not exist. In those cases, the 'load-deflection' curve is replaced by the 'load-punch displacement' curve, and in Eq. 2.7, u is replaced by v, referring to the punch displacement. In this thesis, the latter plotting method is used.

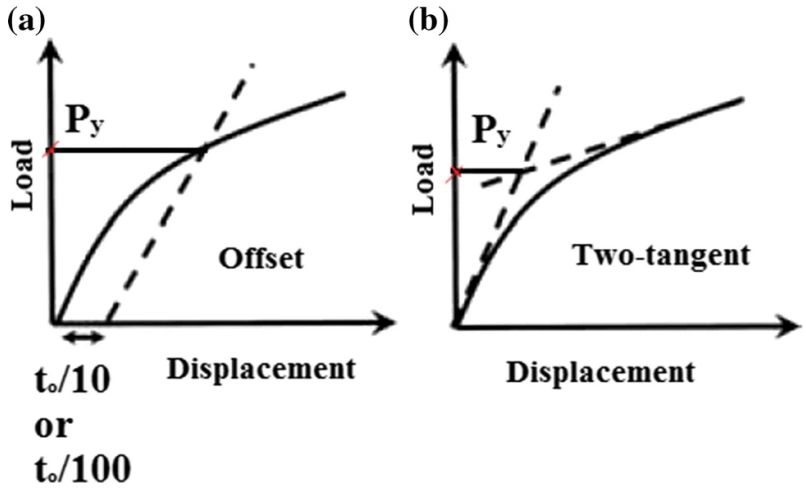

Figure 2.17: Determination of the yield force F_Y from the load-displacement (equivalent for load-deflection) curve [19].

.

2.5 Diffraction methods for deformation characterisation

X-ray, neutron and electron diffraction are essential tools used to characterise deformation in metals and other materials. The first two methods can provide insights of the material behaviour in the mesoscale, while the latter is used for characterisation in the subgrain level. Even though the principles behind the aforementioned methods are similar, the test setups and data format and post processing are significantly different. Thus, in this section, the information provided is separated in a) X-ray and neutron diffraction and b) electron, which are the three methods used extensively in this thesis.

2.5.1 X-ray and neutron diffraction

Quantities, such as lattice strains, texture formation, residual stresses, dislocation densities, average grain size or phase fractions of a deforming polycrystal can be

obtained via X-ray and neutron diffraction. One can work out the distances between diffracting crystallographic planes via Bragg's law:

$$n\lambda = 2d_{hkl}sin(\theta) \tag{2.9}$$

where n indicates the order of the diffracting plane, λ is the wavelength of radiation used, d_{hkl} is the distance between diffracting planes and θ is the diffraction angle. Deformation in the macroscale will lead to changes in the distances of crystallographic planes. In analogy to the macroscopic strain ε definition:

$$\varepsilon = \frac{L_f - L_i}{L_i} \tag{2.10}$$

where L_i and L_f the initial and final linear dimensions of a deforming material, the micro-strain or *lattice strain* can be defined as

$$\varepsilon_{hkl} = \frac{d_{hkl,f} - d_{khl,i}}{d_{hkl,i}} \tag{2.11}$$

where $d_{hkl,f}$ and $d_{hkl,i}$ are the initial (pre-deformation) and final distances of the crystallographic plane $\{hkl\}$. An example of lattice strain measurement configuration is given in Fig. 2.18. In this figure, a monochromatic X-ray beam is diffracted by a specimen under uniaxial tension. The result of diffraction is projected in a 2D detector and has the form of concentric circles also known as *Debye-Scherrer rings* or *diffraction rings*. Each one of the rings corresponds to a crystallographic plane. In a single crystal, where the beam is diffracted in only one direction, instead of rings the result would be just a spot. The ring shape is the result of diffraction by a polycrystal. From the distances between the rings one can obtain the spacing between the diffracting planes, d_{hkl}, from which the lattice strains can be then calculated as described in Eq. 3.9. Lattice strain depends on the direction of deformation and the crystallographic plane. Under tension, at the projection of the tensile axis, lattice

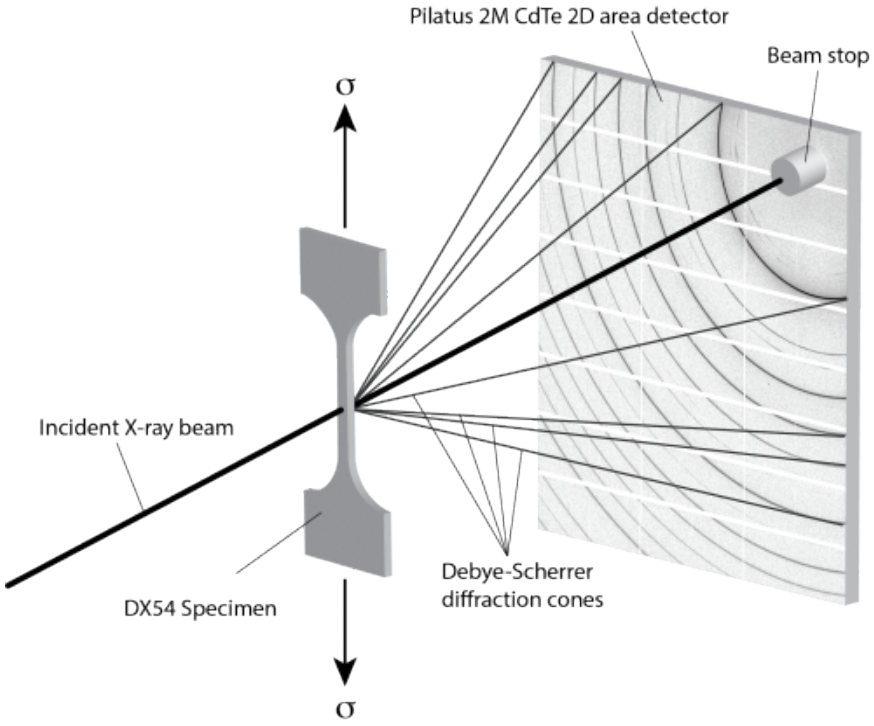

Figure 2.18: Transmission X-ray diffraction configuration during tensile testing, adapted from [20].

.

strain is positive, in analogy to the macroscopic strain. In contrast, in the transverse direction, where macroscopic strain is compressive, the lattice strain measured is negative. Additionally, deformation accommodated by the crystal is not similar for all planes. It is expected, that planes with the lowest atomic density, lead to higher lattice strains.

Crystallographic texture can be also obtained via neutron and X-ray diffraction. In a strongly textured material for example, where the a large fraction of grains is oriented in a specific orientation, the intensities of some of the planes will be higher than others, hence by measuring the intensity of the diffracted beam, one can obtain information about the texture. Finally, information regarding dislocation densities or average grain size can be obtained, using simple methods such us the Williamson-Hall method [109]. This method uses the *Full Width at Half Maximum* (FWHM), a parameter directly associated with dislocations and the crystalline size in the crys-

tal, to calculate dislocation densities and the average grain size. Direct calculation of dislocation densities is not an easy process and requires application of Fourier analysis of the peak profile. However, an indication of the amount of dislocations in the crystal can be provided via the *microstrain*, ε_m, which can be calculated via the Williamson-Hall method. According to Williamson-Hall model, the total broadening in the diffraction peaks is the sum of broadening due to crystalline size ($FWHM_D$), broadening due to strain ($FWHM_\varepsilon$) and instrumental broadening ($FWHM_{instr}$):

$$FWHM_{total} = FWHM_D + FWHM_{\varepsilon_m} + FWHM_{instr} \tag{2.12}$$

According to Scherrer equation:

$$FWHM_D = \frac{K\lambda}{D\cos(\theta)} \tag{2.13}$$

where K is a constant associated with the crystallite shape and often takes the value of 0.9 [110] and D is the crystallite size. The microstrain effect on the total broadening is defined by:

$$FWHM_{\varepsilon_m} = 4\varepsilon_m \tan(\theta) \tag{2.14}$$

By removing the effect of instrumental broadening from the diffraction peaks and by plotting the $FWHM\cos(\theta)/\lambda$ against $\sin(\theta)/\lambda$ one can then get the crystalline size and the microstrain via linear regression.

The discussed analysis can be applied to diffraction peaks obtained from both X-ray or neutron diffraction data. However, X-ray diffraction presents two main advantages compared to neutron diffraction. The biggest advantage is the time of data collection. A continuous flux of photons reaches the detector and allows capturing data at rates of diffraction pattern/second. In contrast, the collection

of neutrons during deformation is much slower and requires interruptions of the sample loading to allow collection of adequate particles to provide good statistical data. In addition, normally an X-ray detector can receive diffracted photons in a range of directions providing an obvious asset in texture examination, while for neutron diffraction setups, one or two detectors are typically placed in very specific directions in relation to the specimen, making this method less advantageous for texture investigation.

2.5.2 EBSD

Electron diffraction is usually utilised in an SEM or TEM to provide localised information about the crystal structure, texture and microstructure characteristics, phase identification, GND density calculation or strain fields at the subgrain level. TEM is normally used in cases where the features under examination require a very high resolution and it is not used within this thesis. Hence, this section is only devoted to EBSD.

As the name reveals, EBSD uses electrons that are backscattered from a well polished surface of a specimen, projected onto a phosphor detector. A typical EBSD setup within an SEM chamber is shown in Fig. 2.19a. Electron diffraction patterns comprise of bands, as shown in Fig. 2.19b, also known as Kikuchi bands. Each band corresponds to a crystallographic plane family while the band intersections correspond to crystal directions. The diffraction patterns obtained from a non-strained and 'ideal' grain should be exactly the same, and they should change at the grain boundaries, since the crystal orientations within a grain remain unchanged. In a deformed crystal, the existence of GNDs which results in lattice curvature, is reflected in small rotations of the Kikuchi bands. Those rotations are used to calculate the GND densities. More information on GND density calculation is provided in the

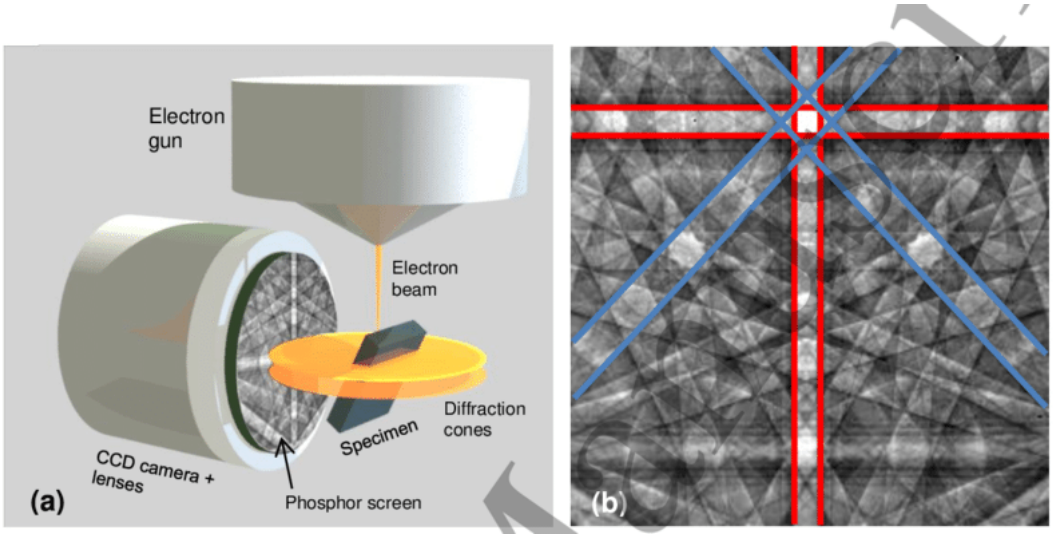

Figure 2.19: (a) EBSD setup and (b) backscattered electron diffraction pattern obtained from [21].

.

next chapter. As discussed earlier, GNDs are the only dislocation types observable via EBSD, while SSDs, which do not result in lattice curvature, are not directly measurable with this technique. Other parameters used for characterisation plastic deformation are the Grain Orientation Spread (GOS), the Grain Average Misorientation (GAM) or the Kernel Average Misorientation (KAM) which are parameters quantifying the misorientations in different positions within the grain, and which are associated with plastic deformation.

For implementing any analysis using EBSD, a method of defining *orientation* is required. This is done via the *Euler angles*, ϕ_1, Φ and ϕ_2. Those three angles are generally used to define a three-step rotation required to go from the coordinate system of a rigid body to a fixed coordinate system. Several conventions are used for such transformation, but in EBSD the most commonly used is the *Bunge convention* which includes the following rotation sequence: rotation around z-axis $\rightarrow$ rotation around x-axis $\rightarrow$ rotation around z-axis (also known as ZXZ). Bunge convention is used to represent a lattice orientation with respect to a fixed coordinate system. Hence, each pixel within an EBSD, or orientation map, is assigned a set of Euler

angles to describe its orientation.

EBSD is also used for texture measurements. One needs to be cautious of how representative the measurements are of the material, as EBSD can only provide information from a few hundred or thousand grains, in contrast to X-ray or neutron diffraction. To define the texture (or its absence) of a specimen with confidence requires large scanned areas with multiple grains per EBSD map and/or data collection from different specimen locations. For texture representation, *pole figures* or *inverse pole figures* are most commonly used. A pole figure is a stereographic projection of all the different orientations measured via EBSD. Examples of pole figures obtained from a Fe-18%Mn-0.6%C-1.5%Al TWIP steel are shown in Fig. 2.20. The presented pole figures reflect the existence of texture in the material, as specific crystallographic orientations have a higher density of diffracting grains. TWIP steels exhibit a mix of texture elements, as previously discussed, with the Goss and the Cu-type fibres being the most prominent. For reference, pole figures of a non-textured material would not have areas of high density of specific orientations.

2.6 Summary

At this point, the complex nature of deformation mechanisms under several modes of biaxial deformation has become apparent. In-depth understanding of deformation characteristics of TWIP steels under biaxial loading conditions, both proportional and non-proportional, is crucial for their use in sheet metal forming and relevant information has been reported in only a few works. The current work aspires to provide new insights on the strain path effect in TWIP steels. However, understanding the interplay between deformation mechanisms under complex loading paths is not straightforward. For that reason an steel alloy with a simpler microstructure is also

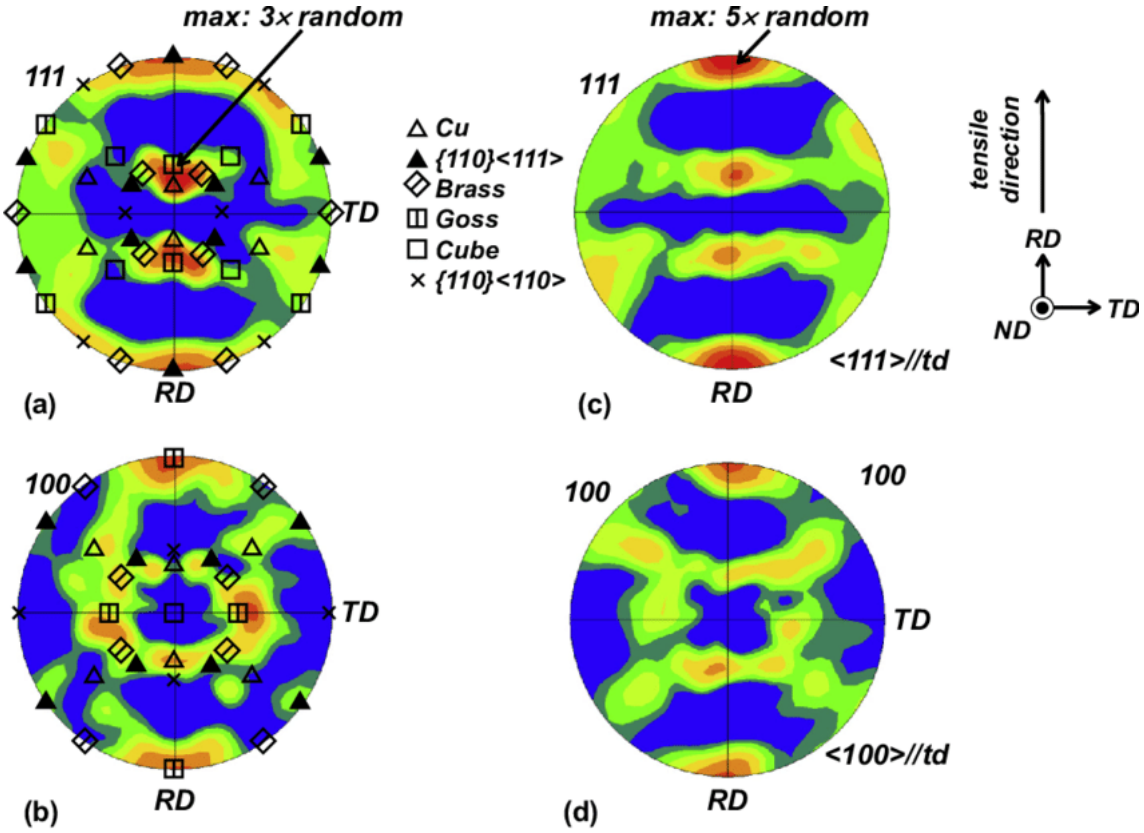

Figure 2.20: Examples of {111} and {100} pole figures showing common FCC fibres, obtained from a Fe-18%Mn-0.6%C-1.5%Al TWIP steel (obtained from [22]).

.

investigated in this thesis under non-proportional loading. DX54 alloy is a high formability steel which exhibits exceptional properties for forming applications and deforms via dislocation slip. As discussed earlier, the strain path effect on low carbon steels with similar properties have been investigated via mechanical testing and TEM. Whilst the effects of abrupt SPCs on microstructure are well known, a lack of information of the material behaviour in the mesoscale still exists. Additionally, less attention has been given in the effect of texture changes under SPCs, which is one of the objectives of this work. Finally, investigation of SPCs effect is non-trivial experimentally. Large specimens are required for biaxial testing which, considering the additional need for test repetitions, lead to a considerable material wastage. Part of this work is dedicated to developing a miniaturised version of the standard Marciniak test, which significantly reduces the material usage and also assists in avoiding steps of post processing that are otherwise required for post-mortem microstructure examination of deformed specimens. Its use for SPCs applications is also examined.

Chapter 3

Ductility loss in a mild steel under abrupt strain path changes

This chapter has been published as:

A. Vrettou, H. Kitaguchi, B. Cai, T. Connolley, D. M. Collins, Mechanisms controlling ductility loss from abrupt Strain Path Changes in a low carbon steel, *Materials Science and Engineering: A*, vol.843, p143091, 2022.

Author contribution to the above publication:

Anastasia Vrettou: Methodology, Data collection (EBSD), Data analysis, Writing – original draft. **Dr Hiroto Kitaguchi**: Data collection (SXRD), Writing – review and editing. **Dr Biao Cai**: Data collection (SXRD), Writing – review and editing. **Dr Thomas Connolley**: Data collection (SXRD), Resources, Writing – review and editing. **Dr David M. Collins**: Conceptualisation, Methodology, Supervision, Writing – editing and review, Funding acquisition.

3.1 Introduction

From the surveyed literature, it is apparent that understanding the effect of SPCs on the microstructure is of great importance for industrial applications, as it has been

systematically proved that they have a significant effect on the mechanical properties of many materials. Understanding how different deformation mechanisms develop at a variety of strain paths is necessary for such examination. Thus in this chapter, a material hardening only via dislocation glide, the DX54 steel, is used, to examine the effect of abrupt SPCs on the mechanical properties and microstructure.

DX54 is a low carbon, single phase steel grade. The response of steel grades with similar properties and microstructure has been investigated in the past via a variety of methods (see Section 2.3.1 for details). These investigations indicate the significance of the SPC effect on low carbon steels, especially when the changes applied are abrupt (e.g. perpendicular major strain directions). The vast majority of works on non-proportional deformation on similar alloys investigate microstructure via TEM, focusing more into deformation substructures (e.g. dislocation cells) evolution and less on effects of deformation in the mesoscale or texture evolution. In contrast, this work uses SXRD in combination with EBSD aiming to provide information on non-proportional deformation in the mesoscale. Here, the term mesoscale is used to refer to examination of deformation effects from a subgrain level up to the behaviour of several thousand grains. The benefit of such investigation is that it can be more useful for studying texture effects and also to provide global information about the material behaviour, in contrast with TEM where the effects studied are more localised.

In this chapter, the microscopic response of the DX54 steel is investigated, under the application of SPCs. A two-step deformation procedure is used, consisting of *pre-straining* by (1) cold rolling, followed by a subsequent (2) uniaxial tension. Deformation direction varies both in the first and the second deformation steps, and so does the pre-strain magnitude. This permits the examination of both deformation magnitude and direction effects on the microstructure. Microscopic response is examined *in-situ* via SXRD and *ex-situ* via EBSD.

3.2 Experimental

3.2.1 Material and the examined strain paths

Composition of the DX54 steel studied here is shown in Table 3.1. The material was received in the form of annealed and galvanised sheets, with an approximate thickness of 1 mm. Texture of the as-received sheet was obtained via EBSD. In Fig. 3.1 the EBSD map and the (110) and (111) pole figures are shown, obtained using a JEOl 7000 SEM, with a 25 kN voltage and 0.2 µm step size. The Initial Rolling Direction (IRD) and the Initial Transverse Direction (ITD) are indicated with arrows. The IRD and ITD terms will be used within this chapter, to distinguish the initial to the pre-strain rolling direction (which will be designated as RD). The material exhibits a strong γ-fibre texture, where $\{111\}$ planes are parallel to the sheet plane, which often characterizes BCC rolled steels [111]. The map shown here contains a relatively small number of grains, while as previously discussed, a large number of grains is required for accurate texture measurement, however measurements in other sheet locations led in a similar result. The average grain diameter was calculated via MTEX 5.6.0 [112], after removing all grains containing less than 5 pixels, and was found $\approx$14 µm.

Element	Fe	C	P	S	Mn
wt %	Balance	≤ 0.06	≤ 0.025	≤ 0.025	≤ 0.35

Table 3.1: Chemical composition of DX54 ferritic steel [24].

For non-proportional deformation study, specimens were deformed according to the process summarised in Fig. 3.2. This included pre-straining of the specimens using cold rolling (step 1), followed by uniaxial tension until fracture (step 2). Figure 3.2(a) represents the strain paths followed. Blue arrows indicate step 1 while red arrows correspond to step 2. Horizontal and vertical axes correspond to the strains

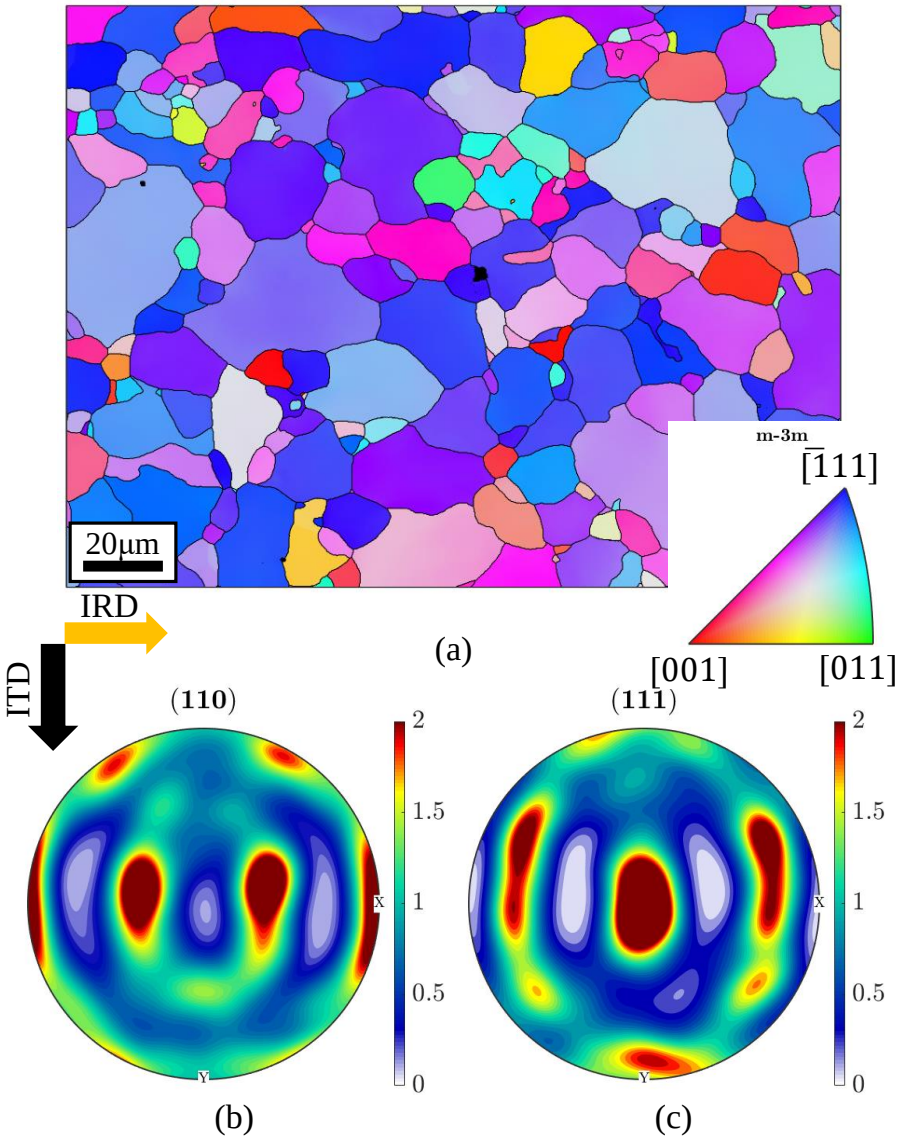

Figure 3.1: (a) EBSD map (z-axis out of plane) (b) (110) and (c) (111) pole figures for the as-received sheet. Rolling direction is indicated with yellow arrow.

developed parallel and perpendicular to the rolling direction of the as-received sheet respectively. Each pre-straining direction is linked to 4 distinct engineering pre-strain levels, $e_0 = 2, 4, 8$ and 14%. This means that during step 1, different sheets were subjected to cold rolling which results in four different thickness reductions. The corresponding effective pre-strains, designated here as ε_{1-4}, were calculated from

$$\varepsilon_n = \frac{\sqrt{2}}{3}\sqrt{(\varepsilon_x - \varepsilon_y)^2 + (\varepsilon_y - \varepsilon_z)^2 + (\varepsilon_z - \varepsilon_x)^2} \tag{3.1}$$

where ε_x, ε_y, ε_z are the true strains developed during the cold rolling stage, and n is an integer from 1-4. The calculated values of the effective pre-strains and the corresponding thickness reductions are summarized in Fig. 3.2b. For easiness, for the rest of this chapter, the engineering strain e_z calculated directly from the sheet thickness reduction is going to be used to describe each pre-strain.

Specimen manufacturing and the in-situ measurement process are summarised in Fig. 3.3. From the as-received sheet, a dog-bone specimen was fabricated via Electrical Discharge Machining (EDM), with the tensile direction perpendicular to the IRD. The remaining material was cut into 8 parts which were further rolled parallel or perpendicular to the IRD, as shown in Fig. 3.3a. This step corresponds to the material *pre-straining*. After step 1, from the rolled parts, dog-bone specimens were machined, parallel and perpendicular to the rolling direction of step 1. One dog-bone specimen was manufactured and tested for each pre-strained sheet. The gauge dimensions for the dog-bone specimens were $L \times w \times t$, where the gauge length was $L = 32\,\text{mm}$, the width was $w = 6\,\text{mm}$ and the thickness (t) depended on the thickness reduction due to rolling. Overall, 17 different strain paths were examined, 16 of which included an SPC.

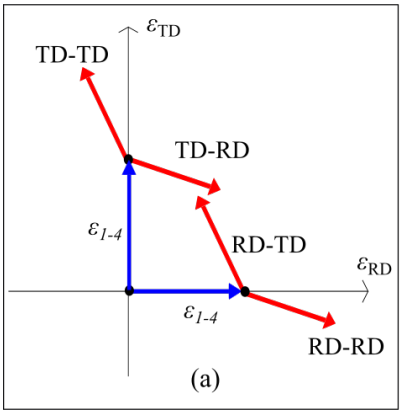

Annotation	Thickness reduction (mm)	Effective pre-strain (%)
ε_1	0.020	2.29
ε_2	0.038	4.53
ε_3	0.074	8.89
ε_4	0.123	15.13

(b)

Figure 3.2: (a) The strain paths studied. Blue arrows correspond to cold rolling (step 1) and red arrows to the subsequent uniaxial tesnion (step 2). (b) The effective pre-strains and corresponding annotations.

3.2.2 Ex-situ characterisation

The microstructure of the as-received, as well as the pre-strained sheets (prior to tensile testing), was examined via EBSD, using a JEOL-7000 field emission scanning electron microscope equipped with a Nordlys detector, with an effective resolution of 1344×1024 pixels^2. Specimens for EBSD examination were mechanically prepared with abrasive media including polishing with colloidal silica (0.04 µm particle size) for approximately 30 min. Map acquisition was carried out at a 20 mm working distance using a 25 kV accelerating voltage. Data were collected from an area of approximately 150 µm×150 µm, using 4×4 binning with exposure time 3.5 m s and a step size of 0.2 µm. Data were processed with the MTEX 5.6.0 [112] package using Matlab 2019b.

The GND density is used here as a parameter that quantifies sub-crystal deformation. GND densities were calculated via an MTEX integrated algorithm, based on the work of Pantleon [113]. According to Nye's definition [114], the dislocation tensor, is a 2nd rank tensor, which can be written as :

$$\alpha_{ij} = \sum_{t=1}^{N} b_i^t l_j^t \delta(\vec{x} - \vec{x^t}) \tag{3.2}$$

where $i, j, k = 1, 2, 3$, b is the Burgers vector, l is the line vector, $\vec{x}$ is the position vector and t corresponds to the dislocation system (N is the number of dislocation systems for the examined crystal structure). The calculation of α_{ij} depends on initially obtaining the curvature tensor elements, κ_{ij}, which are determined from the lattice curvatures, as

$$\kappa_{ij} = \frac{\partial \theta_i}{\partial x_j} \approx \frac{\Delta \theta_i}{\Delta x_j} \tag{3.3}$$

where θ is the rotation vector, which can be obtained from the orientation map, via the disorientations between neighbouring points. The dislocation tensor elements can be then calculated via the relationships [114]:

$$\alpha_{ij} = \kappa_{ji} - \delta_{ij}\kappa_{kk} \tag{3.4}$$

$$\kappa_{ij} = \alpha_{ji} - \frac{1}{2}\delta_{ij}\alpha_{kk} \tag{3.5}$$

The dislocation tensor can be re-written as

$$\alpha_{ij} = \sum_{t=1}^{N} b_i^t l_i^t \rho^t \tag{3.6}$$

where ρ^t are the dislocation densities for each one of the expected dislocation types for the examined structure. The ferritic steel in this study has a BCC structure, where slip occurs on the $\langle 111 \rangle$ direction and $\{110\}$, $\{112\}$ and $\{123\}$ slip planes [35]. In total, there are 52 different dislocation types, which include 12 $\{110\}\langle 1\bar{1}1 \rangle$, 12 $\{211\}\langle 1\bar{1}\bar{1} \rangle$ and 24 $\{123\}\langle 11\bar{1} \rangle$ edge dislocations and 4 $\langle 111 \rangle$ screw dislocations. The MTEX algorithm calculates the ρ^t values. In order to estimate the total GND density, ρ_{GND}, measured for the examined specimens, the distinct ρ values were

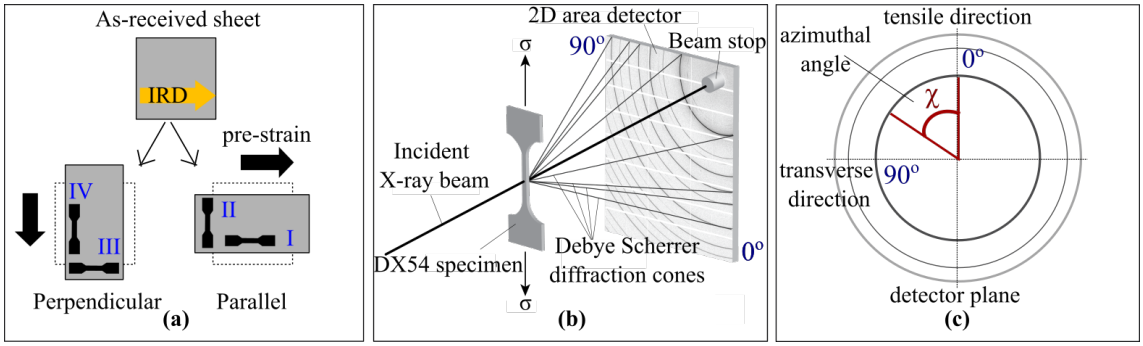

Figure 3.3: The experimental procedure summarized: (a) Pre-straining the specimens. The direction of the dog-bone specimens indicates the strain path followed. (I) corresponds to RD-RD, (II) to RD-TD, (III) to TD-RD and (IV) to TD-TD. (b) Schematic of the X-ray diffraction geometry during uniaxial loading. (c) Top view of the detector plane.

added, and the total GND density was calculated by:

$$\rho_{\mathrm{GND}} = \sum_{t=1}^{N} \left|\rho^{t}\right| \tag{3.7}$$

An additional algorithm was implemented in Matlab, based on the work of Jiang et al. [115], calculating the distance of each pixel within a grain, from the closest grain boundary. Grain boundaries (GBs) were divided into smaller segments and the 'Midpoint' of each segment was located, following an MTEX method [112]. The distance of each grain pixel from the closest segment 'Midpoint' was then calculated, as shown in Fig. 3.4 and plotted against the total absolute GND densities.

3.2.3 SXRD

Synchrotron X-ray diffraction patterns during uniaxial deformation were collected at Beamline I12, Diamond Light Source [116]. For tensile loading, an Instron 8801 Series uniaxial load frame, with maximum capacity of 100 kN, was used. One specimen was tested per strain path. Specimens were deformed at a rate of 3×10^{-3} mm/s. During tensile testing, the loading stage was vertically displaced opposite to the

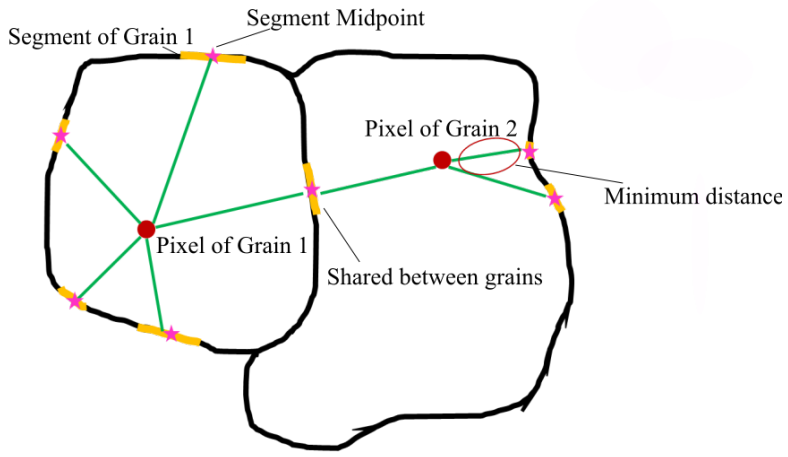

Figure 3.4: Determination of the minimum distance of each pixel from a grain segment midpoint.

crosshead displacement, at a rate 1.5×10^{-3} mm/s, in order to compensate for the specimen elongation and allow data collection from the same part of the deforming specimen. High energy X-rays were used in order to allow high precision of the peak position measurements. Patterns were collected at a rate of 1 pattern/s using the Pilatus 2M CdTe 2D area detector, characterized by a 1475×1679 pixel^2 active area with pixel size = 172×172 µm^2. The specimen-detector distance (= 1201.25 mm) as well as the beam energy (90.262 kV) were calibrated using a CeO_2 standard, as described in [117].

The described geometry, allowed data to be collected from only one quadrant of the Debye-Scherrer rings, as shown in Fig. 3.3b. This setup improves the angular resolution for each reflection (over the acquisition of full Debye-Scherrer rings), necessary to maximise the accuracy of the fitted peak positions. Whilst the line broadening shape of the collected reflections could be well described with fitting functions, the intrinsic instrumental broadening dominated over any sample broadening, and was thus not quantified in this study. Hereon, the angle between the tensile and the transverse directions will be called the azimuthal angle (see Fig. 3.3c). For all the presented measurements, the tensile axis was aligned parallel to the 0°. Strain measurement was derived from the crosshead displacement.

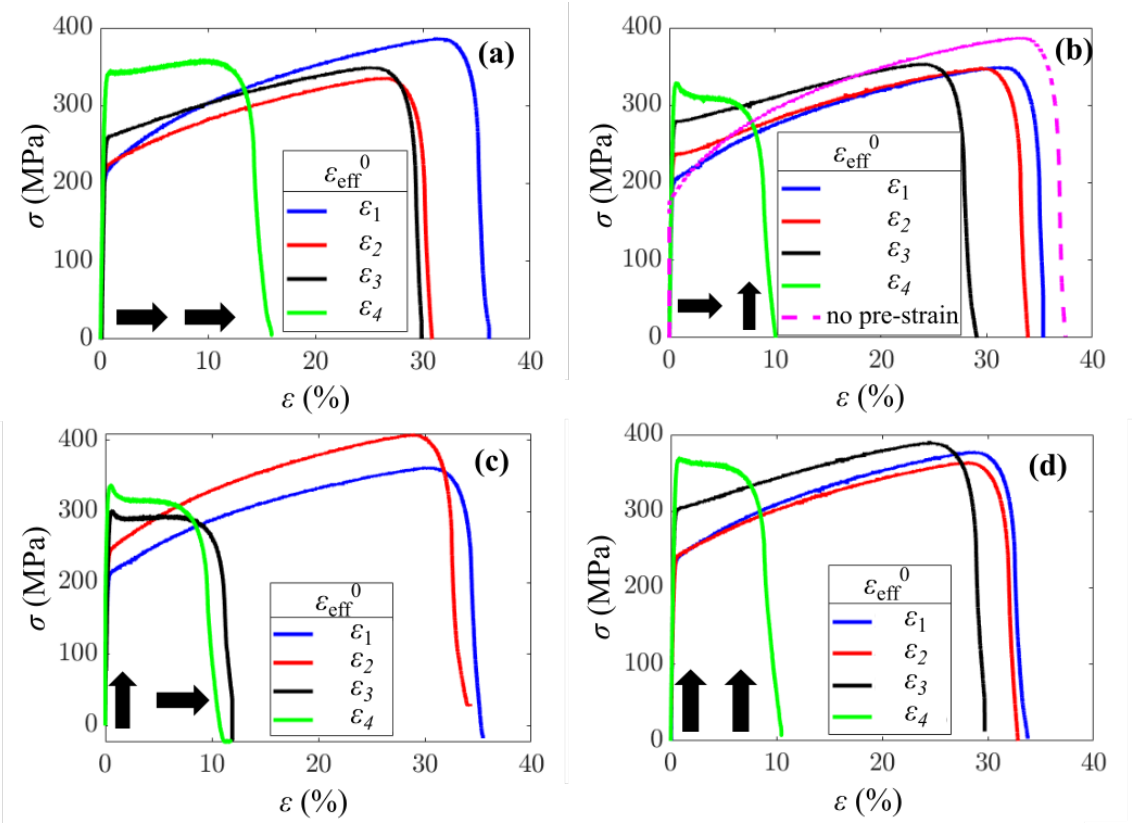

Figure 3.5: True stress-strain results obtained for the (a) RD-RD, (b) RD-TD, (c) TD-RD and (d) TD-TD strain paths, during uniaxial tensile testing. The arrows designate the directions of strain for each of the step in the strain paths. In the legends, true, effective pre-strain values are shown.

3.3 Results

3.3.1 Macroscopic stress and strain

The macroscopic uniaxial deformation behaviour of samples subjected to different levels of pre-strain are described here. The stress-strain curves, obtained during tensile testing, are shown in Fig. 3.5. Each one of the presented sub-figures corresponds to a different strain path, indicated with black arrows. The first arrow, designates the pre-straining direction with respect to the IRD and the second, the tensile direction. The legends include the true, effective pre-strain magnitudes.

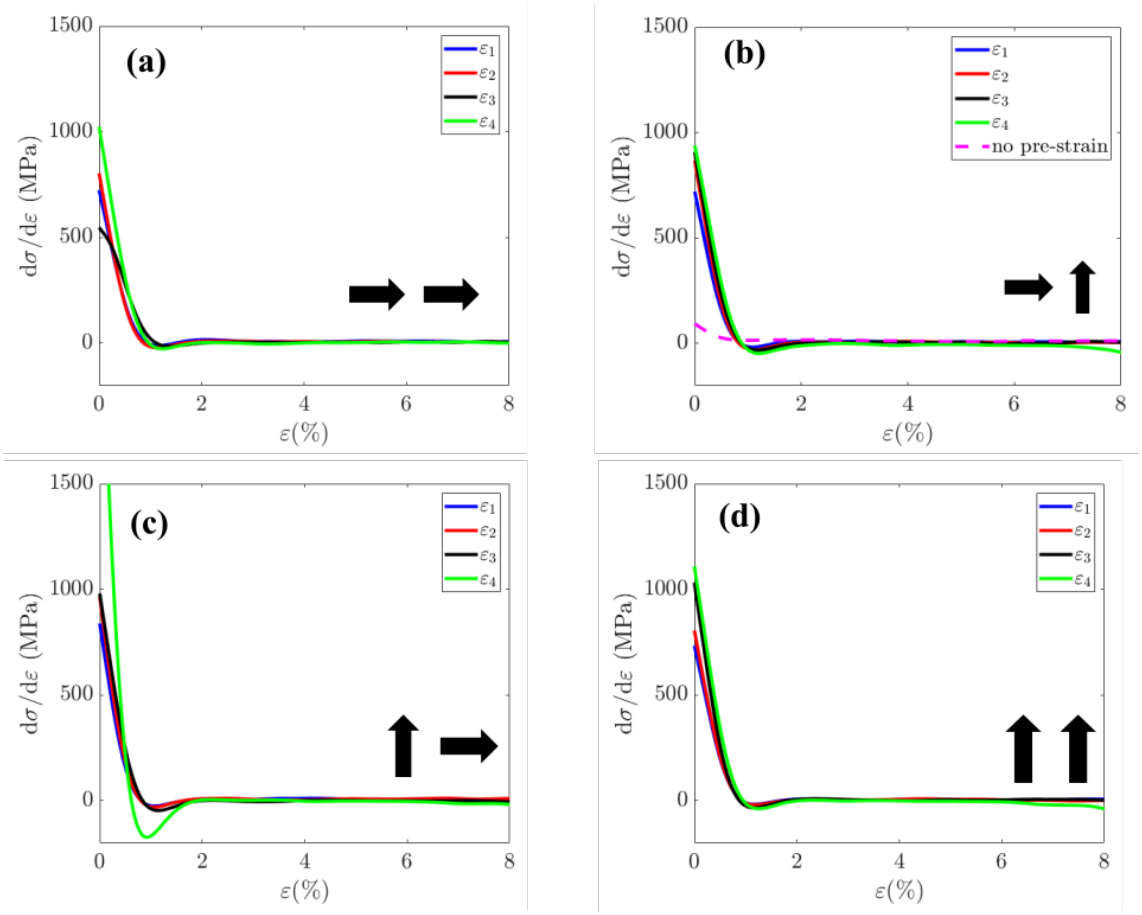

Figure 3.6: Work hardening curves for the (a) RD-RD, (b) RD-TD, (c) TD-RD and (d) TD-TD strain paths, during uniaxial tensile testing.

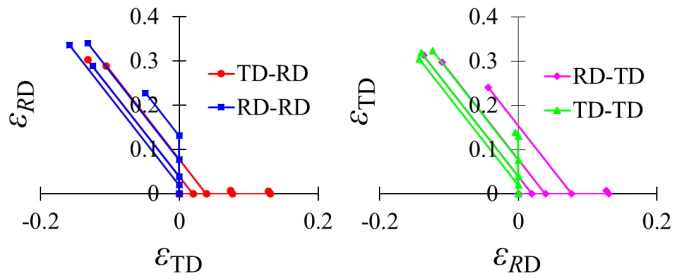

Figure 3.7: The forming limits of the specimens subjected to SPCs.

A small reduction in ductility along with a notable decrease in the UTS are apparent for the pre-strained specimens, in comparison with proportionally deformed one (Fig. 3.5b). However, increasing the pre-strain magnitude leads to an increased yield strength, a behaviour which is evident in all the examined strain paths, similar to the behaviour previously described by Doucet and Wagoner [118]. This increase is less significant for the RD-TD and TD-RD strain paths, and more important for the RD-RD and TD-TD ones. Although lower pre-strain magnitudes (ε_1 and ε_2) do not appear to severely influence the stress-strain relationship between the non pre-strained and the pre-strained specimens, increased pre-strain magnitude results, not only in a significant ductility reduction, but also has a significant stress-strain dependence. A characteristic work hardening stagnation is observed in all cases for a maximum pre-strain (ε_4) and for the TD-RD specimen, for both ε_3 and ε_4.

A strong dependence of the mechanical response of the material on the selected strain path, is manifested via specimens pre-strained to ε_4. For the RD-RD case (Fig. 3.5), a higher maximum strain is reached, in comparison with the rest of the strain paths. The work hardening rate is also positive in this case, after exhibiting a small transient early after yielding, allowing an extension of the plastic regime. In contrast, the TD-RD path leads to immediate necking which is followed by strain softening, not only for the specimen subjected to a maximum pre-strain, but also for the sample with a pre-strain ε_3. The sharp yield point observed in those specimens is also observed for the highly pre-strained ones, following the RD-TD and TD-TD strain paths. This characteristic point suggests that the corresponding specimens exceeded the strain for the onset of necking before uniaxial tensile testing during the pre-straining procedure. In addition to the stress-strain curves, the corresponding work hardening rate has been plotted, shown in Fig. 3.6. No significant differences are observed between each strain path, especially for the ε_1 and ε_2 pre-strains. However, pre-strain magnitude appears to influence the work hardening at early

stages of plastic deformation for the TD-RD strain path (Fig. 3.6c), with the ε_4, leading to a remarkably higher hardening rate at low macroscopic strains, compared to lower pre-strain values. Furthermore, pre-straining the specimens results has a remarkable increased hardening rate in comparison to the no pre-strain condition (Fig. 3.6).

In Fig. 3.7, the forming limits of all samples subjected to an SPC are shown. The axes of the presented diagrams are reversed in order to allow direct comparison between specimens with parallel tensile axes and perpendicular pre-strain directions. The points lying on the $\varepsilon_{\mathrm{RD}}$ and $\varepsilon_{\mathrm{TD}}$ axes correspond to the applied pre-strain magnitudes. Overall, the differences between specimens subjected to low pre-strains are insignificant. However, in both diagrams it is apparent that for strain paths that did not include an abrupt SPC (RD-RD and TD-TD), the strains when localised necking occurred are higher compared to examples that had abrupt SPCs (TD-RD and RD-TD). Between the 'uni-directional' strain paths, slightly decreased forming limits are observed for the TD-TD specimen compared to the RD-RD, a behaviour which is more obvious for highest pre-strains. The only exception to this tendency is the case of the ε_2 pre-strain. Between the RD-TD and TD-RD specimens, the latter appears to be the most detrimental for the specimen ductility, an effect that becomes obvious via the comparison of the specimens subjected to the ε_3 pre-strain.

It is important to note that the results discussed above are the outcomes of one tested specimen per strain path. This is due to the limited experimental time provided for in-situ investigations in synchrotron facilities. Hence, it is necessary to interpret these results qualitatively rather than quantitatively. However, the observed trends show a ductility decrease which is analogous to the pre-strain induced by cold rolling. Additionally, they indicate a premature strain softening for high pre-strain levels. These results are in good agreement with the existing literature on similar alloys [32, 118] and also are consistent for each strain path, which enhances

their validity.

3.3.2 Effects on texture

A correlation between the macroscopic response with changes in texture, is pursued in this work. This section describes alternations observed in the measured peak intensities for the different diffracting planes for the various deformation processes. Since there are no other effects observed for the examined material contributing to peak intensity changes (such as phase transformations), any changes in the peak intensities will be only attributed to texture changes. From the diffraction patterns collected during tensile deformation, changes in the peak intensities for the different diffracting planes were measured and used in order to obtain information about texture evolution. The normalised peak intensities were calculated, after background subtraction, via Equation 3.8

$$I_{\text{norm}} = \frac{I_{hkl}}{I_{\text{total}}} \tag{3.8}$$

where I_{norm} is the normalised intensity, I_{hkl} is the measured peak intensity corresponding to the $\{hkl\}$ reflection and I_{total} is the total measured (or integrated) intensity for each one of the collected patterns. Results obtained for the {110} and {200} reflections are presented here. The {110} peak intensity, which is the highest for the examined material, remains strong, irrespective of any texture change, which allows reliable fitting. In addition, the {200} peak showed substantial changes over time and between the different specimens, which highlights the importance of including this to the results section. In Fig. 3.8, normalised intensities of the {110} and {200} reflections are presented as a function of the azimuthal angle. The colour-bars for each one of the plots exhibited here, correspond to the macroscopic (true) strain or macrostrain developed during tensile testing. Zero macrostrain (which refers to the

start of the tensile test) is represented with a dark blue colour, while red corresponds to the maximum macrostrain reached for each one of the examined specimens (i.e. the strain at which the specimens fractured). The initial texture of the material is obtained from intensities at zero macrostrain. The texture configuration for the ε_1 and ε_4 pre-strain magnitudes is examined here.

As referred above, the {110} reflection exhibited the highest peak intensity for all the examined strain paths. Investigating the texture evolution of the ε_1 pre-strain specimen revealed that during uniaxial tension, the {110} peak intensity exhibited two maximums: one parallel to the tensile direction (0°) and another parallel to 60°. This distribution can be directly linked to the {110} pole figure (taken from the as-received sheet) presented in Fig. 3.8q, where a characteristic 6-fold symmetry is evident. The height of those maximums showed a variation depending on the examined strain path. For example, specimens pre-strained parallel to the IRD, had a similar peak intensity behaviour, as showed in Fig. 3.8a and 3.8b. For those specimens, the intensity was maximum parallel to the tensile direction (0°) and minimum at 30° and 90°. The second maximum, observed at 60°, was notably lower than the the one at 0°. In contrast, according to Fig. 3.8c and 3.8d, the peak intensity had the same magnitude at 0° and 60°, for specimens pre-strained perpendicular to the IRD. From the results described above, it was noted that the fraction of grains oriented with the {110} parallel to the specimen plane, was higher for specimens rolled perpendicular to the IRD. An increase in the {110} texture can assist the increased slip activity of those specimens, increasing their dislocation density, but inhibits further plasticity, due to dislocation build-up, when the strain path is changed.

Results presented in Fig. 3.8 showed that for the lowest pre-strain magnitude, no important differences were observed between specimens pre-strained in the same direction but were uniaxially loaded in perpendicular directions. It appeared that

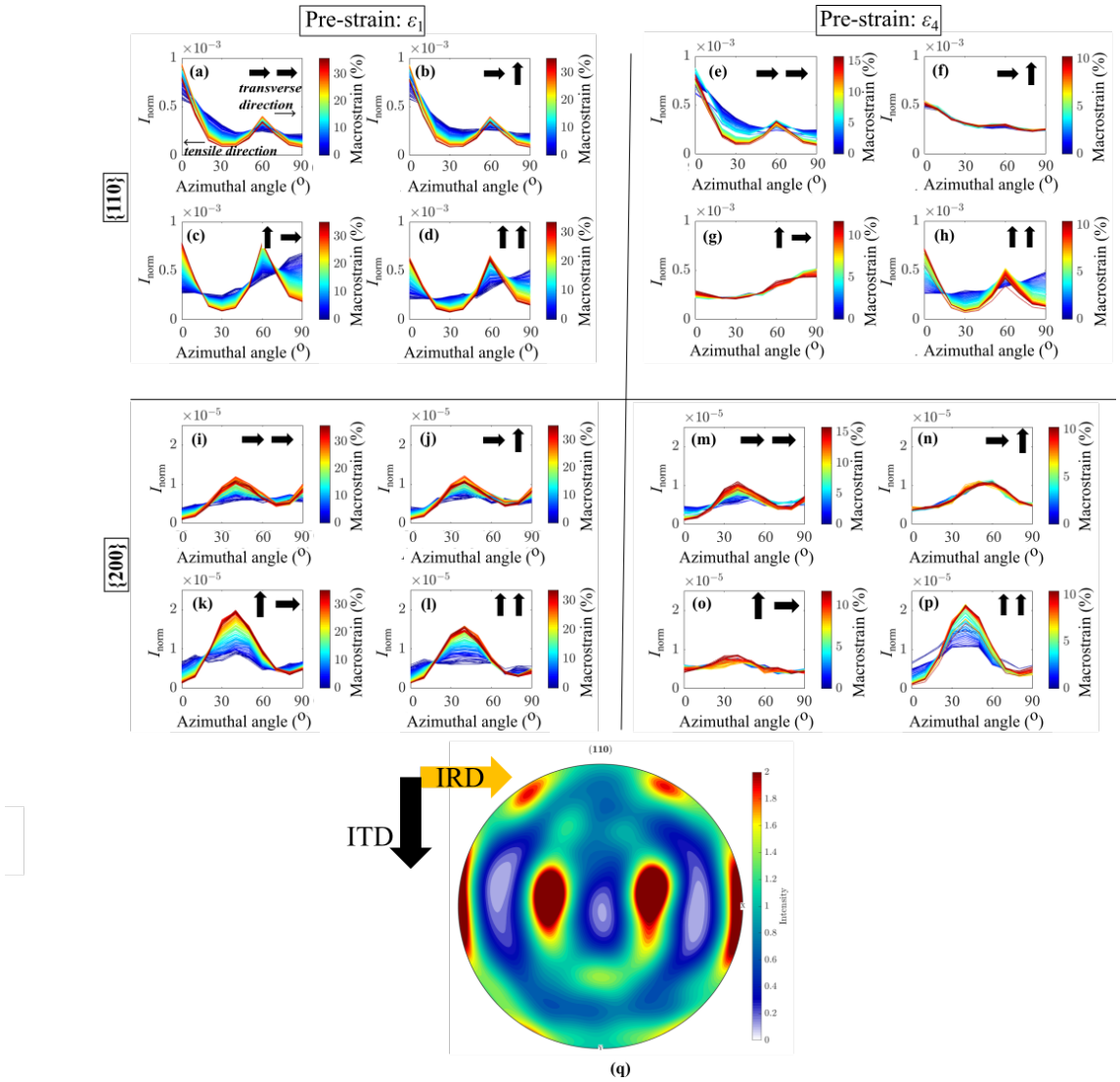

Figure 3.8: (a-p) Normalized peak- intensity for the {110} and {200} reflections for specimens subjected to ε_1 (min) and ε_4 (max) pre-strain. The strain path followed is indicated with black arrows. (q) 110 pole figure for the as-received specimen, indicating a characteristic 6-fold symmetry.

the tensile axis, had a weaker effect on the configured texture, than the pre-strain direction. However, for the maximum pre-strain magnitude (ε_4), important differences in the texture evolution were observed in specimens with the same pre-strain direction and perpendicular tensile directions. While texture appeared to change during tension for the RD-RD and TD-TD specimens, a stagnation was noted for the RD-TD and TD-RD specimens. This effect originates from the inability to record texture changes in specimens which had exhibited localised necking, while the beam was probing far from the neck region. More specifically, the incoming beam was probing at the specimen center, while post fracture optical inspection showed that the neck was far from this region for both specimens. Nevertheless, the appearance of this effect, underlined additionally to the results presented above, the important influence of the application of abrupt SPCs.

In Fig. 3.8, the {200} reflection peak intensity is also presented. From Fig. 3.8i and 3.8j it is manifested that this texture is enhanced at the directions where {110} texture is suppressed. A maximum of the peak intensity is exhibited at approximately 30°-40°, while a minimum is observed at 0°.

Similar tendencies as described for the {110} reflection are observed for the {200} reflection. For low pre-strain (ε_1), a similar configuration of the peak intensity is shown for specimens with the same pre-strain direction (Fig. 3.8i and 3.8j or Fig. 3.8k and 3.8l). In the case of rolling parallel to the IRD the maximum exhibited at the 40° is suppressed (Fig 3.8i and 3.8j) while, in contrast, it is importantly enhanced (Fig 3.8k and 3.8l for rolling perpendicular to the IRD.

An increased pre-strain magnitude (ε_4) results in the same texture stagnation observed for the {110} reflection. An important increase of the {200} intensity can be seen in Fig. 3.8p at 40°, in comparison with the specimen subjected to lower pre-strain (Fig. 3.8l). This increase, is accompanied by a small decrease of the

{110} intensity at 60° (see Fig. 3.8h). Overall, similar to what was described for the {110}-fibre, the {200} texture is slightly enhanced when pre-straining perpendicular to the IRD.

3.3.3 Lattice strain

Lattice strain is a quantity, characteristic of the compliance of the different diffracting planes to the external load application. Here, the behaviour of the lattice strain is examined as a function of the macrostrain. Its dependence on the azimuthal angle, is also investigated. Lattice strains for the individual grain families were calculated via Equation (3.9)

$$\varepsilon_{hkl} = \frac{d_{hkl} - d_{hkl,0}}{d_{hkl,0}} \tag{3.9}$$

where ε_{hkl} is the calculated lattice strain for the hkl reflection, d_{hkl} is the measured d-spacing and $d_{hkl,0}$ is undeformed, relaxed d-spacing obtained from the diffraction pattern for $\varepsilon_{hkl,0}$. This corresponds to the first diffraction pattern obtained for the pre-strained specimens immediately before uniaxial loading.

In Figure 3.9, the lattice strains of {110}, {200}, {211} and {310} planes are presented, as a function of the azimuthal angle, for three (true) macrostrain levels (4, 8 and 10.5%). It is observed that lattice strain was at a maximum when parallel to the tensile direction and at a minimum when parallel to the transverse direction. Only small differences were recorded between the different planes, concerning the angular distribution of lattice strains. In all cases, the highest magnitudes, as well as the greatest variations between tensile and transverse directions, were observed for the {200} planes.

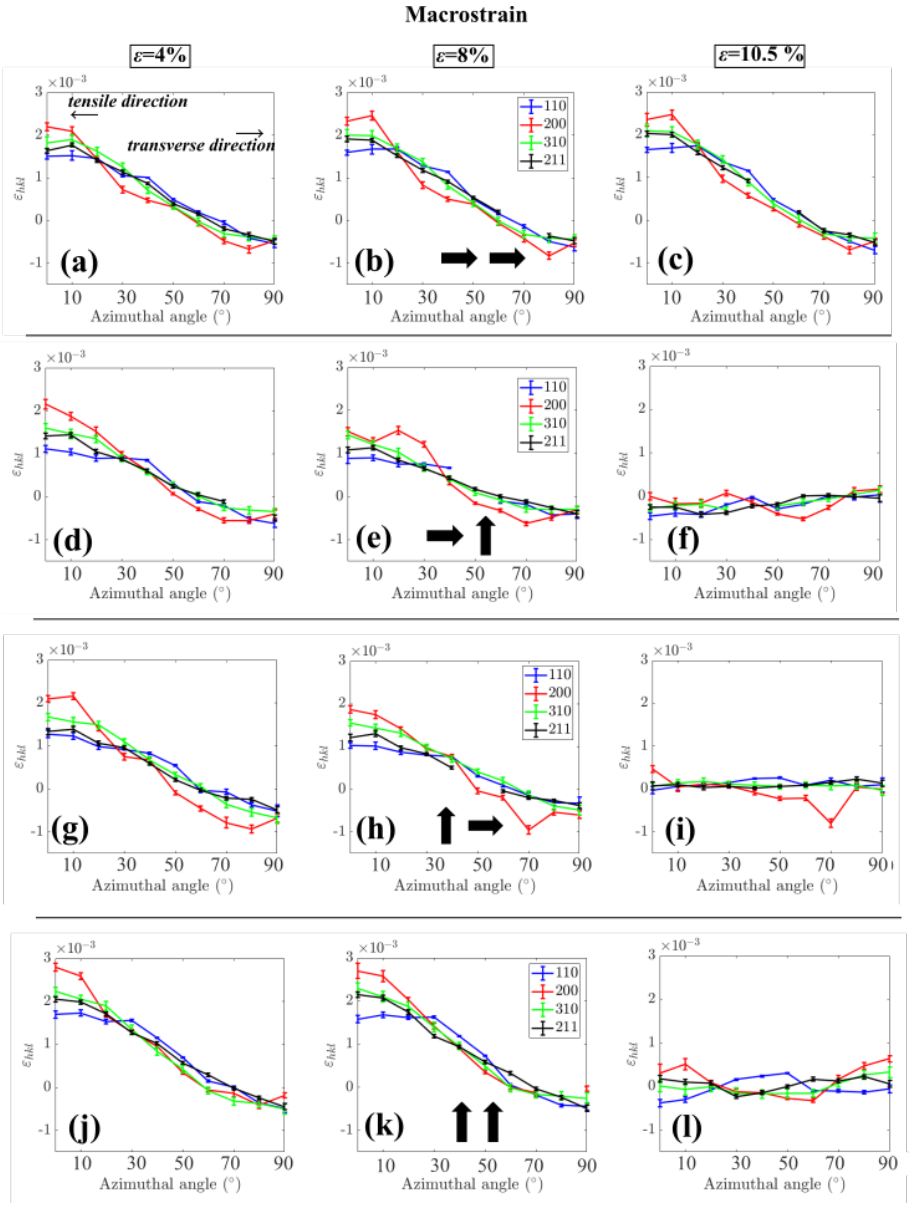

Figure 3.9: Lattice strain of the {110}, {200}, {211} and {310} reflections as a function of the azimuthal angle. Three macrostrain levels are shown (4, 8 and 10.5%). The strain path followed is indicated with black arrows

Between the 4% and 8% macrostrain levels, the lattice strain magnitude does not exhibit significant changes. A characteristic drop appears in the lattice strain for 10.5% the macrostrain, for the RD-TD, TD-RD and TD-TD strain paths (Figs. 3.9f, 3.9i and 3.9l). This indicates that the corresponding specimens are approaching their fracture strain level, highlighting the severe effect of the aforementioned strain paths on ductility.

The behaviour of the lattice strain with respect to the macrostrain, for the highly pre-strained specimens (ε_4) is displayed in Fig. 3.10. It is examined parallel to the tensile direction and transverse direction and is correlated with the macroscopic stress-strain response. As described earlier, it is evident that the {200} planes exhibit the highest lattice strain parallel to the tensile direction, for all the examined strain paths, which implies that those planes are the most compliant to deformation. In contrast, the {110} planes are characterized by the lowest lattice strains.

The relationship between the lattice strains presented here, and the macrostrain, displays unique characteristics between the different strain paths. It appears that, for unidirectionally deformed specimens (Fig. 3.10a and 3.10j), strain hardening is observed for all the different reflections. The {211} reflection for the RD-RD specimen, is the only exception, as the strain hardening rate is negative at low plastic strains which, however, alternates to positive at approximately 5% macrostrain.

In contrast, for the cross-deformed specimens (Fig. 3.10d and 3.10g), strain softening is observed from the early stages of plastic deformation. This behaviour can be directly associated with the macroscopic response of the corresponding specimens (Fig. 3.10f and 3.10i respectively), which fail immediately after exceeding the elastic region. In Fig. 3.10j, a particularly interesting behaviour is recorded. Positive hardening rates are apparent for all the examined lattice planes, which may appear contradictory to the macroscopic stress-strain behaviour shown in Fig. 3.10l. However, high hardening rates can be expected close to the necking area, under the presence of high, localised stresses.

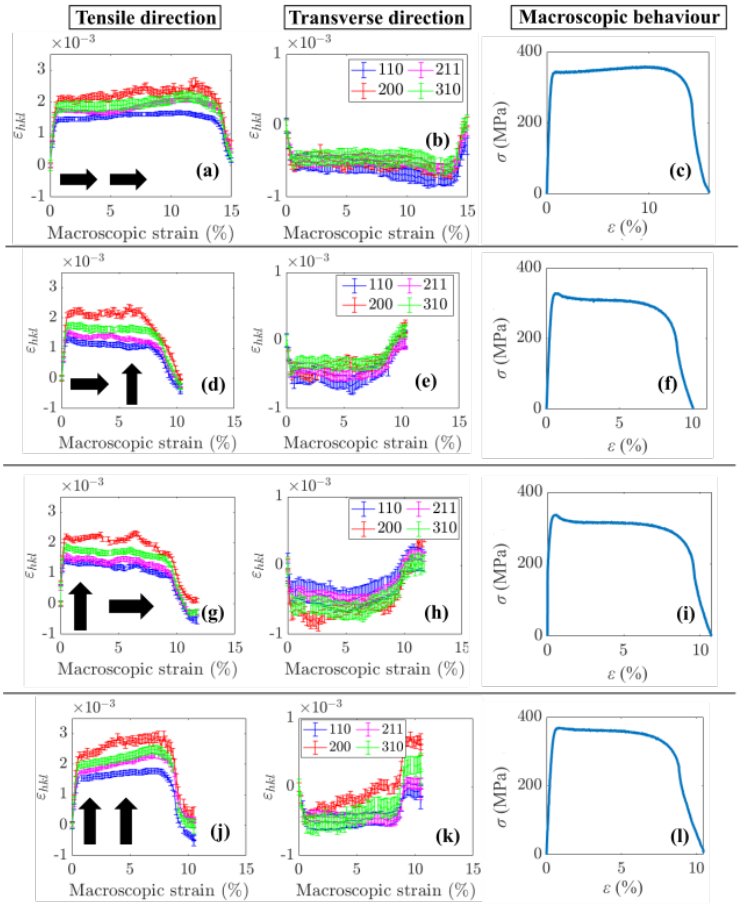

Figure 3.10: Lattice strain plotted against the macrostrain for highly pre-strained specimens (ε_4) and correlation with the macroscopic stress-strain behaviour. Plots refer to data collected parallel to the tensile and transverse direction.

3.3.4 EBSD results

The microstructure of the rolled specimens was examined via EBSD prior to uniaxial loading. All the examined specimens are characterized by a uniform microstructure and grain orientations, irrespective of the scanned area. Thus, information about texture could also be obtained via EBSD. GND maps reveal a great increase of the GND density for increasing pre-strain. More specifically, highly pre-strained specimens (ε_4) exhibit GND density of approximately an order of magnitude higher than the low pre-strained specimens (ε_1) or, as expected, of the as-received material. In addition, in both Fig. 3.11b and 3.11c, the recorded GND density is higher for

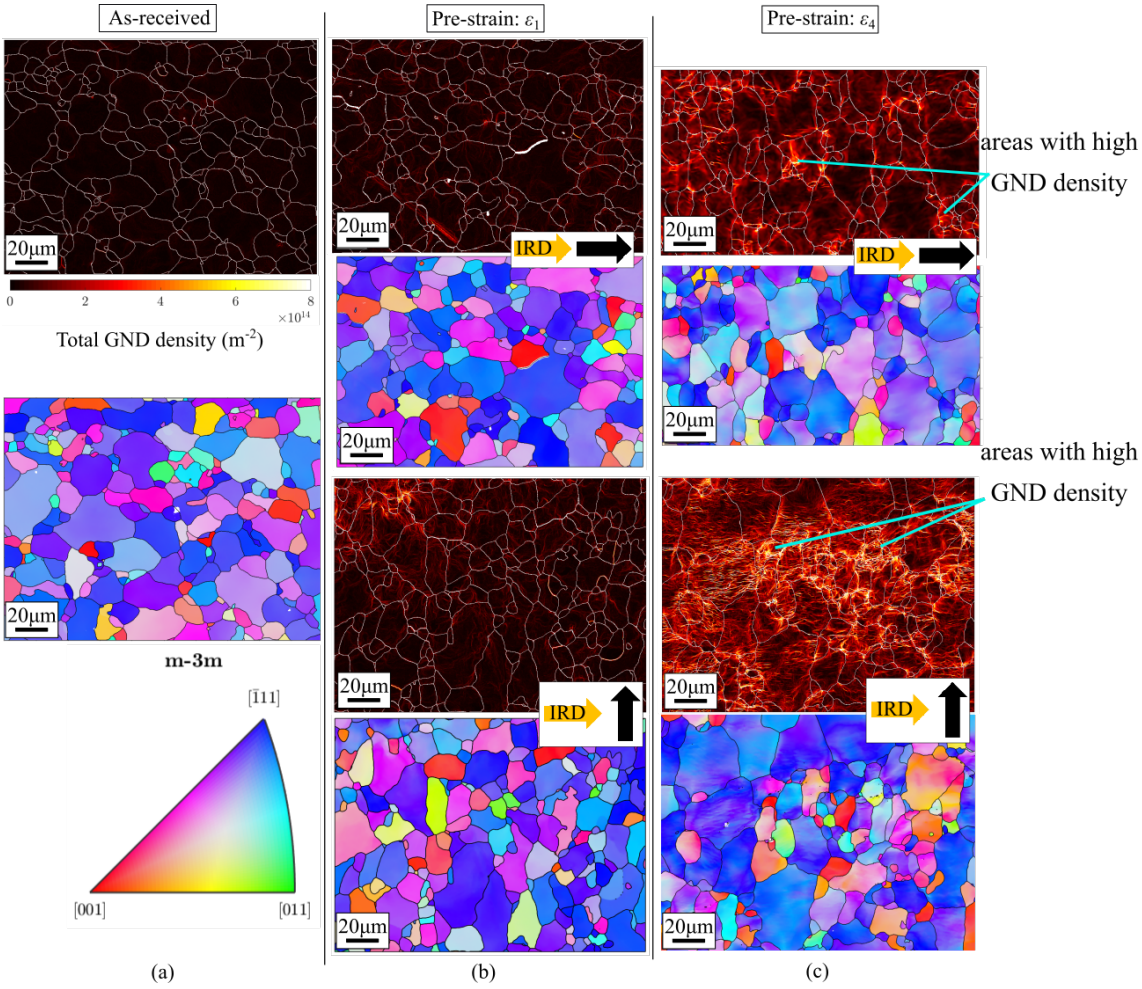

Figure 3.11: GND density, ρ_{GND}, maps and the corresponding Inverse Pole Figure (IPF) maps of specimens subjected to different levels and orthogonal directions of pre-strain. The yellow arrows indicate the IRD (rolling direction of the as received sheet) and the black arrows the pre-strain direction. The color-bar limits are the same for all the total GND density maps.

specimens rolled perpendicular to the IRD. This correlates to the immediate necking of those specimens after yielding, as shown in Fig. 3.10f and 3.10i. An increase in GND density reflects the re-orientation of lattice planes in order to accommodate changes in texture occurring during pre-straining. These changes are expected to be more significant when the rolling direction is changed with respect to the IRD, which explains the higher GND densities observed in the sample pre-strained perpendicular to the IRD.

A way to investigate whether a specific orientation leads to higher GND densities

is by plotting the Inverse Pole Figures (IPFs), indicating the GND density magnitude with different colours, using a colour map. In Fig. 3.12 the IPFs for the highly pre-strained specimens are presented. It is evident that the examined specimens are textured as a result of the cold rolling process, with the majority of grains aligned with the $\{\bar{1}11\}$ plane parallel to the sample surface, a texture common to rolled steels with a very low carbon content [119]. A greater orientation dispersion is observed for the cross-rolled specimens, showing a preferable lattice rotation, so that the $\{001\}$ planes are parallel to the sample surface. This is in agreement with the peak intensity results presented in Fig. 3.8k and 3.8l, confirming that cross-rolling leads to an increase of this specific texture. However, comparison between the colors of the individual orientations presented in the IPFs, demonstrates that, there is no significant correlation between the measured GND density and the lattice orientation.

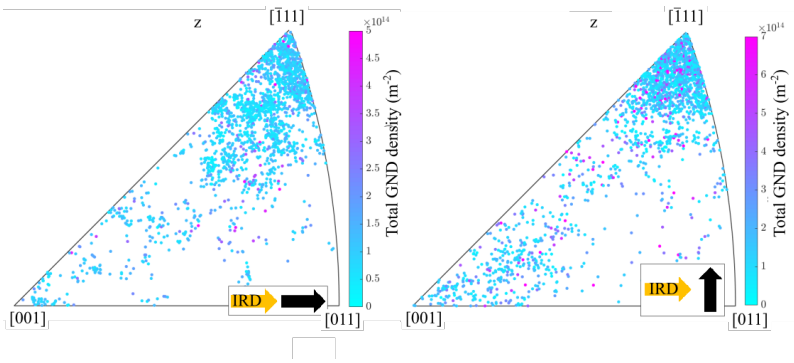

Figure 3.12: Inverse pole figures for highly pre-strained specimens, parallel (left) and perpendicular (right) to the IRD. The colour bar shows the total GND density magnitude.

3.4 Discussion

3.4.1 Strain hardening rates

By correlating the lattice strain with the macrostrain (Fig. 3.10), a variation upon the hardening rates of the examined planes and strain paths is evident. Clear differences were observed between rates of uni-directionally (RD-RD or TD-TD) and cross-deformed (RD-TD or TD-RD) specimens. These differences were examined for the tensile and transverse directions. A more detailed demonstration of the lattice strain hardening rate is shown in Fig. 3.13, where the hardening rate relationship with the azimuthal angle is examined. The effect of strain path, as well as the pre-strain magnitude are investigated for the {110} and {200} reflections. Data for only up to 5% (true) macrostrain are presented here, which aims to focus on early stages of plastic deformation. For increasing macrostrain (above 5%), the hardening rates remain practically unchanged.

Whilst the lattice strain (Fig. 3.9) clearly shows a maximum magnitude in the tensile direction, and minimum in the transverse direction, the distribution of the hardening rate between these respective directions is not uniform. For low pre-strain levels (ε_1), notable variation is observed for both of the examined sets of planes, leading to positive values in some directions (in most cases in the tensile or transverse direction) and negative in other directions. The variation is, however, reduced for an increased pre-strain (ε_4), leading to a suppression of the hardening rate in the directions for which it was initially positive. Concurrently, the hardening rate is abruptly decreased at approximately 50° for the {110} planes and at 40° for the {200} planes. The effect of strain path on the strain hardening distribution, is not so significant for the highly pre-strained specimens. Even though the macroscopic stress-strain relationship (Fig. 3.5) differs depending on the strain path, maximum

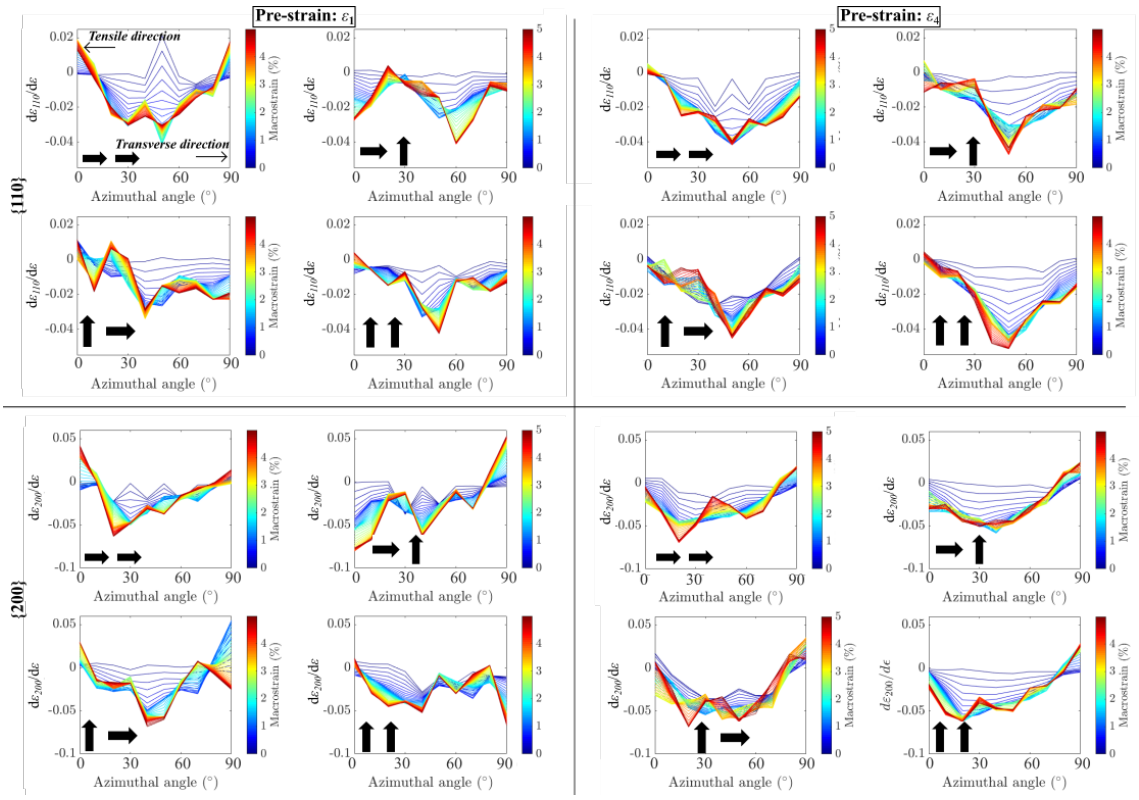

Figure 3.13: Lattice strain hardening of the {110} and {200} reflections as a function of the azimuthal angle, for low (ε_1) and high (ε_4) pre-strains.

pre-strain leads to either immediate necking (Figs. 3.5b, 3.5c, 3.5d) or to a work hardening instability (Fig. 3.5a) evident in low macrostrain levels. The above are directly expressed in a microscopic level by the lattice strain hardening rates.

3.4.2 GND distribution

Fig. 3.11c highlights possible differences between the GND distributions of the highly pre-strained (ε_4) specimens. It is evident that the dislocation structures are more prevalent far from the grain boundaries in the cross-rolled specimen in contrast with the uni-directionally rolled one. To assess whether this assumption is unambiguous, a quantification was made based on the work of Jiang et al. [115], as described in the Experimental section.

In Fig. 3.14 the relationship between the GND densities and the minimum distance of grain midpoints is shown. The different colours indicate the density of data points (or frequency), with red corresponding to high and blue to low density. A substantial difference in the total GND density magnitudes is apparent between the two specimens, which was also manifested in the GND density maps plotted in Fig. 3.11c. Whilst there is no obvious variation in the GND density distribution between the two specimens, it is evident that for the cross-rolled specimens (Fig12b), the frequency of high GND regions at distances far from the grain boundaries is greater than for rolling limited to one direction only (Fig12a). Higher densities are observed closer to the grain boundary segment midpoints and are gradually decreased for increasing distances. As expected, higher densities of points are characterized by lower GND densities.

3.4.3 Ductility reduction

From previous studies, combining mechanical testing with TEM examinations, it is known that abrupt SPCs including a pre-strain by rolling (or plane strain), result in several characteristics that confer early necking during subsequent deformation [32], and has been proven to be detrimental [118, 32], especially when the pre-strain and the second load directions are almost orthogonal. This effect is also generalised for other pre-straining or subsequent loading conditions [62, 120]. Dislocation walls, formed during the pre-straining, can be breached during the re-loading, resulting in an instant strain softening after yielding [121, 32]. This effect originates from the activation of new slip systems, which were only latent to the pre-strain procedure [62], and the formation of new dislocation structures corresponding to these systems, which interact destructively with the existing structures formed during pre-straining. The overall effect is the obstruction of further plastic deformation. However, there is

a significant texture effect too, observed in this work, which plays a significant role. The direction of the rolling pre-strain with respect to the initial rolling direction gives rise to very different GND densities, for samples reaching the same equivalent plastic strain (Fig 3.11c). Even for low levels of pre-strains (ε_1), this effect is evident (Fig 3.11b).

Whilst the results shown here indicate an independence of the total GND density from the grain orientation, it has been previously reported that the dislocation structures forming in each grain differ depending on the grain orientation [122]. This example focused on FCC crystal structures, exhibiting a grain orientation dependence on the formed dislocation structures, which controls the hardening observed between the different strain paths. This effect is not replicated in the BCC ferric steel studied. Instead, the texture effect dominates, with all grains rotating to orientations that confer easy slip during the pre-strain (Fig 3.11). Thus, the grain to grain dislocation density and structures are quite similar.

Along with the anticipated differences in dislocation structures generated in the different strain paths, texture evidently had the most significant effect on the formability of ferritic steel. The as received material is characterised by a strong gamma-fibre texture, as shown in Fig. 3.12, which is distinctly weakened when sheets are rolled perpendicular to the IRD. Conversely, the {001} texture is increased, which is known [119] to be detrimental for the ductility of the material. Texture formation during the rolling pre-strain step is of great importance in particular, and that can be understood by a comparison of the macroscopic stress-strain curves of RD-TD and TD-RD strain paths shown in Fig. 3.5b and 3.5c respectively. In the TD-RD specimen, immediate necking is observed even for approximately 8% pre-strain (ε_3), which is not the case for the other specimens subjected to an abrupt SPC (RD-TD). The former specimen, also exhibits the the highest increase of the {200} (equivalent to {001}) peak intensity during tensile loading.

To understand the total ductility attainable by BCC ferrite, it is clear that one must consider the abruptness of the strain path between the pre-strain and the initial rolling direction (in the as receive state). The strain to failure beyond the pre-strain is also influenced by the abruptness of the strain path. Any SPC that incurs a dramatic texture change must have significant grain reorientation, and evidently plasticity within all grains is increased to retain compatibility. Therefore, it is unambiguous that texture, for abrupt SPCs, controls the ductility reduction for a BCC ferritic steel. This work has significant implications to industrial practice: (1) a forming operation that changes the texture significantly from the prior processing, from the as received rolling direction, will decrease ductility dramatically. (2) If the manufactured forming operation experiences an abrupt strain path change, or the component experiences loading paths that differ from the processing history will result in premature fracture.

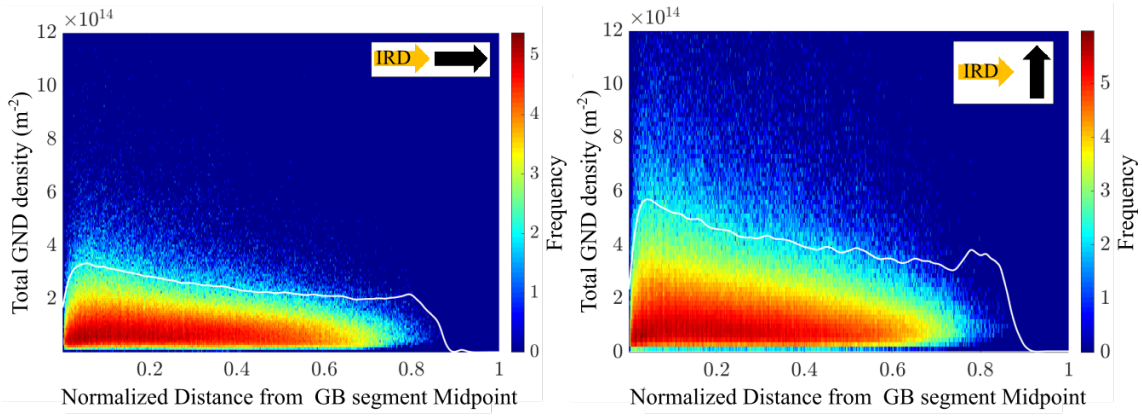

Figure 3.14: Total GND density distribution in respect with normalized distance from grain boundary segment midpoints, for specimens subjected to maximum pre-strain (ε_4). Highest frequencies are observed close to the grain boundaries. Colors indicate the densities of data points for a given distance/GND density. The white line corresponds to the level of 95% of the data.

3.5 Summary

In this chapter, the texture and microstructure evolution in a low carbon steel subjected to abrupt strain-path changes was studied. A significant ductility reduction was observed for specimens subjected to non-proportional strain paths, consisting of a rolling-uniaxial tension sequence. By increasing the pre-strain magnitude, the ductility reduction was even more significant, whilst for highly pre-strained specimens, plastic instability occurs immediately once the yield stress was reached. It was also found that the influence of pre-straining was more severe in the cases where abrupt SPCs were applied. For the corresponding specimens, strain softening was observed from the early stages of plastic deformation.

This effect was also reflected in the configured texture, as a saturation of the peak intensity change was recorded from in-situ synchrotron diffraction measurements. The texture configuration was remarkably influenced by the pre-strain direction, even for low pre-strain magnitudes. Texture evolution during uniaxial tension was less dependent on the tensile direction and was mainly influenced by the initial texture, configured during the pre-strain step. An increase of the {200} texture was observed when the rolling direction was perpendicular to the IRD.

An in-situ microstructure development investigation also revealed that lattice strain behaviour with respect to the macroscopic strain was highly dependent on the applied strain path. Work hardening behaviour showed similarities between uni-directional and cross directional deformation, respectively. The latter exhibits an abrupt decrease in most of the examined macroscopic directions (or azimuthal angles), for highly pre-strained specimens, resulting in a ductility reduction of those specimens.

Finally, ex-situ examination of the pre-strained specimens showed that deforma-

tion accommodated by the lattice, which is quantified here in terms of the GND density, is significantly increased for a high pre-strain. The GND density is higher for rolling perpendicular to the IRD and appears to be independent of the grain orientation. For the most abrupt strain path changes, structures of high dislocation density are present in intragranular regions after initial rolling which inhibits subsequent plastic deformation, giving immediate failure.

Chapter 4

A miniaturised testing method for strain path sensitivity evaluation

4.1 Introduction

The previous chapter revealed significant differences in the microstructure of a low carbon steel when subjected to a changing strain path. The results, which highlighted the significant strain path sensitivity of the examined material, motivate further investigation of microstructure development during other deformation processes. In contrast to low carbon steels, which have been used in industry for several decades, high-Mn steels have been investigated to a much less extent, especially their sensitivity to non-proportional strain paths. In this chapter, the development of a miniaturised test setup is presented, used to study the biaxial deformation behaviour of the DX54 and TWIP steels under proportional (for both alloys) and non-proportional (for the TWIP) strain paths. Greater importance is attached to the microstructure characteristics of the TWIP steel alloy, while the DX54 steel is

mainly used for the initial development and the evaluation of the miniaturised test results.

The development and the working principle of the miniaturised testing system are explained. This includes a description of the test rig, the strain measurement method along with initial predictions from finite element analysis. Subsequently, the microstructure and mechanical properties of the TWIP steel are investigated (the relevant information for the DX54 steel was included in the previous chapter). Results for the proportional strain paths are then described for both alloys and interrupted tests are conducted for the TWIP steel to examine the microstructure response to different strain paths. Interruptions were carried out at similar equivalent von Mises strains ($\varepsilon_{\mathrm{VM}} \approx 10 - 15\%$), allowing for comparison between the developed microstructures at intermediate strain levels. Such comparison aimed to investigate the interplay between dislocation slip and twinning mechanisms for the different deformation modes. Finally, results from non-proportional strain paths are presented. TWIP steel specimens were first subjected to a first deformation step using (a) cold rolling and (b) uniaxial tension, followed by a second deformation step using equibiaxial tension. Tests were carried out both up to fracture as well as up to $\varepsilon_{\mathrm{VM}} \approx 10\%$. This way, the effect of SPC on the microstructure could also be investigated and a direct comparison between proportional and non-proportional strain paths is allowed.

Element	Fe	C	Mn	Al	Si	V	Cr	Ni	Ti	Cu
wt %	Balance	$0.30 - 0.60$	19.06	1.07	0.25	0.13	2.10	0.06	0.03	0.05

Table 4.1: Chemical composition of the examined TWIP steel. Carbon content was provided by ThyssenKrupp as it could not be accurately measured in-house.

4.2 The examined material

4.2.1 Composition and microstructure

TWIP steel was received in the form of 2 mm thick, hot rolled sheets, manufactured by ThyssenKrupp. The composition was measured from 5 random areas of $30\times30\,\mu m^2$ via WDS. Specimens were mounted in conductive bakelite and were mechanically polished with diamond media with diameter 0.25 µm. WDS measurements were performed using a 20 kV accelerating voltage and a 14.90 nA beam current. A calibration of the elemental assignment was performed the day of the measurement. The composition is shown in Table 4.1. The carbon content measured was higher than the nominal values quoted from the manufacturing, likely due to SEM chamber and/or sample surface contamination, as well us the conductive bakelite. Hence, the weight percentage provided by the manufacturer for carbon is provided instead.

For the initial microstructure examination, EBSD was performed via a JEOL 7000 SEM. An area of approximately $350\times350\,\mu m^2$ was scanned using a 25 kV voltage and a stepsize of 0.6 µm. The working distance was set to 20 mm and the exposure time to 24.4 ms for 4×4 binning of the diffraction patterns. Fig. 4.1 shows the orientation map of the as-received material (left) as well as the parent grains vs annealing twins (right). Signs of retained deformation, originated from the hot rolling process, are observed in a few grains. Grain boundaries were defined at a misorientation angle of 5°. Setting a higher threshold, corresponding to high angle

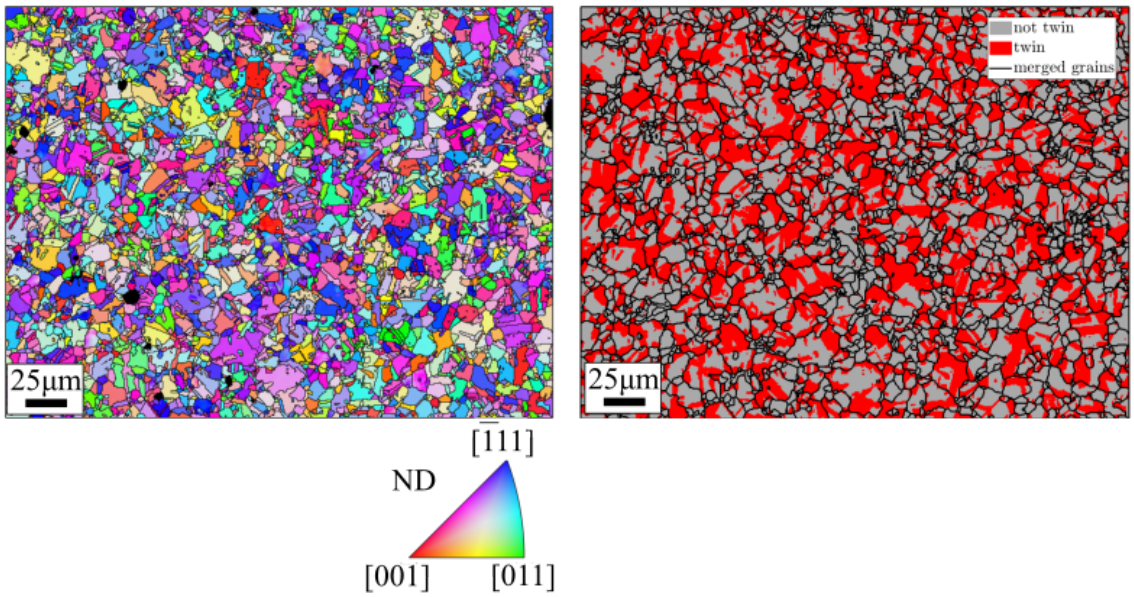

Figure 4.1: Orientation map (left) and the twinned areas (right) of the as-received material.

boundaries ($> 15°$) was found to omit some grain boundaries that were evident from the band contrast map, while it did not result in any substantial difference in the average grain size. For the average grain size calculation, distinction between the parent grains and the annealing twins was necessary. The average grain size was calculated after the parent grains were reconstructed, and was found to be 10.1 µm. while, the twinned area was estimated at approximately 38%.

The as-received material, is characterised by a weak texture, which is mix of copper-type and brass-type fibres. The corresponding pole figures are presented in Fig. 4.2. The inverse pole figure in Fig. 4.2b as well as the colour-bar limits indicate that the formed texture is notably weaker than the low carbon, BCC ferritic steel examined in the previous chapter. Therefore, it is expected that the effect of the rolling direction on the mechanical properties will be much less significant for the TWIP steel compared to the low carbon steel (DX54).

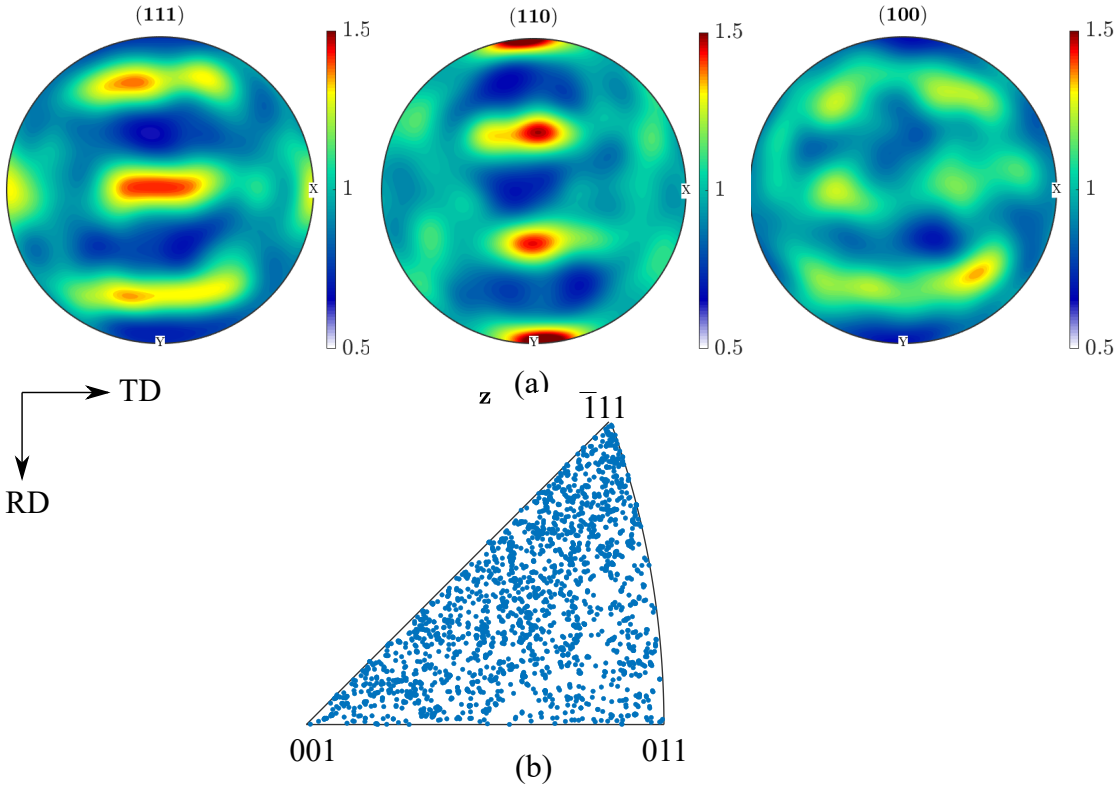

Figure 4.2: Pole figures (a) and inverse pole figure (b) for the as received material..

4.2.2 Tensile properties

Tensile properties of the TWIP steel were examined using an Instron 3367 tensile testing machine, with 30 kN load capacity. Dogbone-shaped specimens were cut perpendicular to the RD of the as-received sheet, via Electrical Discharge Machining (EDM) according to the ASTM standard [123] 'subsize' specimen size. A displacement rate of 0.025 mm/s was used, and the specimens deformed until fracture. Three tests were conducted to confirm the repeatability of the measurement. Engineering stress (s) and strain (e) were derived from the measured load-displacement values, according to

$$s = \frac{F}{A} \tag{4.1}$$

and

$$e = \frac{\Delta L}{L_0} \tag{4.2}$$

were F is the load applied to a cross-sectional area A, ΔL is the crosshead displacement and L_0 the initial gauge length of the specimens (here 25 mm). True stress (σ) and strain (ε) values were then calculated via

$$\varepsilon = \ln(1 + e) \tag{4.3}$$

and

$$\sigma = s(1 + e). \tag{4.4}$$

The true stress-strain results for the three specimens are shown in Fig. 4.3. Good repeatability was observed. An elongation measurement was obtained from the crosshead displacement; this method can lead to inaccuracies at low displacement levels due to the instrument compliance, hence the Young's modulus could not be accurately determined. The YS was obtained via the 0.2% offset method. The elastic, linear parts of the stress-strain curves were fitted via 1st degree polynomials and new, 'shifted' stress and strain values were determined using the slopes of the fitted curves (lines). Three values of the YS were then obtained from the intersection of the shifted curves with the measured curves, as shown in the inset of Fig. 4.3. A YS of 307 MPa, with a standard deviation of 13 MPa obtained from the average of the three values. This is a typical YS value for high-Mn steels, however, the decreased accuracy of the displacement measurement at low strains, leads to low accuracy in the obtained YS. A characteristic of TWIP steels is their very high UTS, here reaching 1648 MPa, along with a high total elongation (at UTS); 64.6%

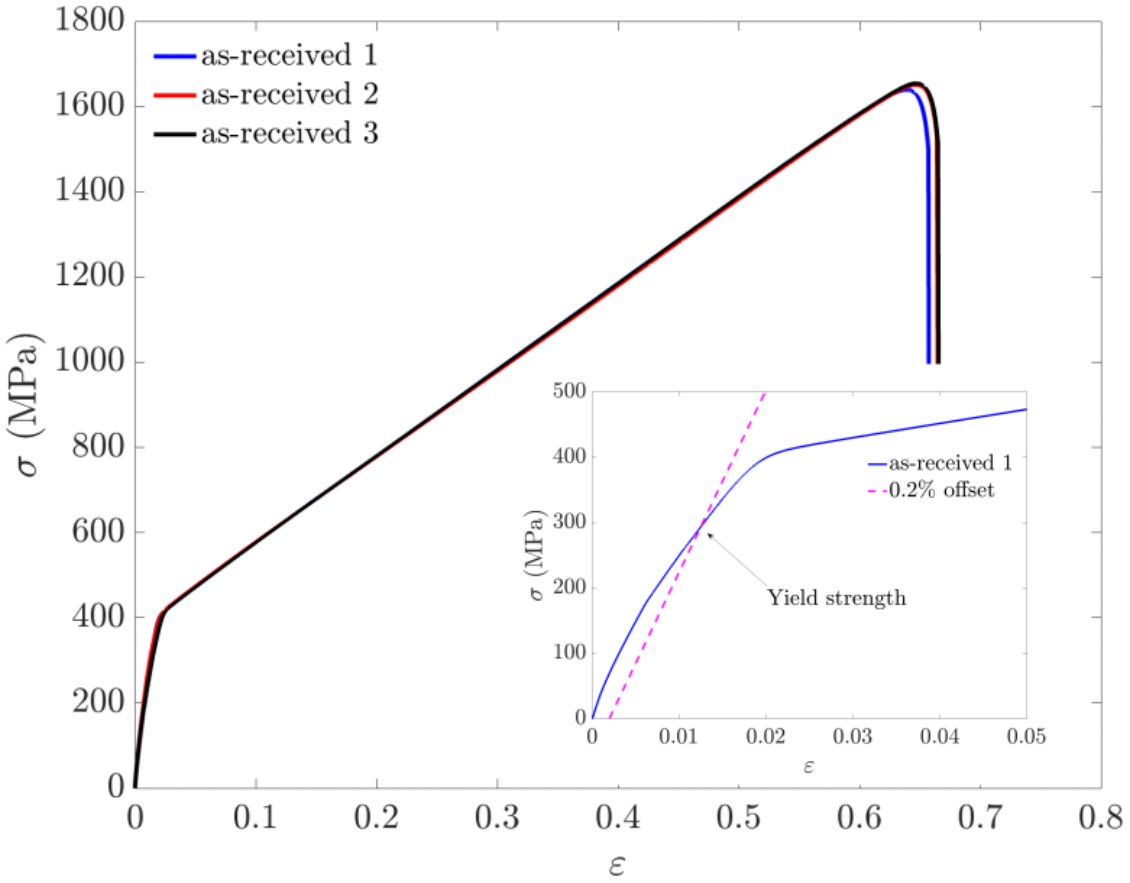

Figure 4.3: True stress vs strain curve for the as-received, TWIP steel. Inset illustrates the determination of YS according to the 0.2% offset method.

was recorded. Post-yielding, σ exhibits an almost linear dependence on ε, indicating a constant hardening rate of 2017 MPa.

4.3 Isochronous annealing

4.3.1 Microstructure and hardness

Miniaturised specimens used to investigate strain path sensitivity of the DX54 and TWIP steels were machined via mechanical milling to the geometries shown in Fig. 4.4b. This method results in residual stresses and a deformed microstructure, which

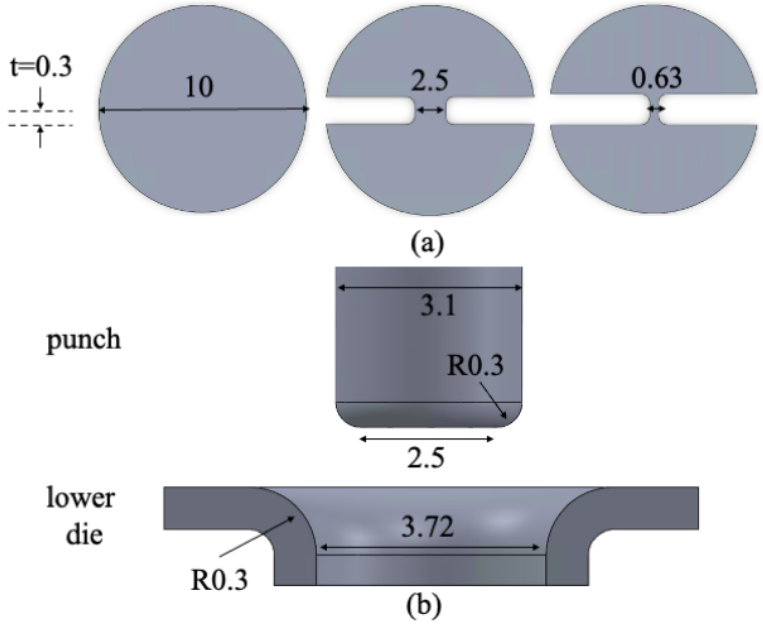

Figure 4.4: Dimensions in mm of (a) the flat punch and lower die and (b) the three specimen geometries, corresponding to equibiaxial, plane and uniaxial strain paths (left to right).

differs to the deformation induced by the miniaturised punch test. To remove machining induced deformation, annealing was used. DX54 specimens were annealed at 650°C for 2 hours according to [124], however, further investigation for suitable annealing conditions of the TWIP steel was needed. A strip of the examined material was initially rolled ||RD, up to 40% thickness reduction. Subsequently, four small specimens were cut from the rolled strip and were annealed for 30 mins in air at four different temperatures: 850, 900, 950 and 1000 °C. Post-annealing specimens were mechanically ground with abrasive media of 1 µm then etched with an acidic $FeCl_3$ solution containing 4 g $FeCl_3$, 20 ml HCl and 80 ml H_2O. Optical micrographs were next obtained with a ×20 magnification, as shown in Fig. 4.5. The as-received material is characterised by equiaxed grains with an average grain size of 11 µm, as calculated via the linear intercept method for three different areas of the specimen. A horizontal line was drawn per area and the intersections of the line with the grain boundaries were counted, as described in the ASTM E112-13 [125] (1 intersection with a grain boundary counts as 1, while an intersection occurring at the junction of

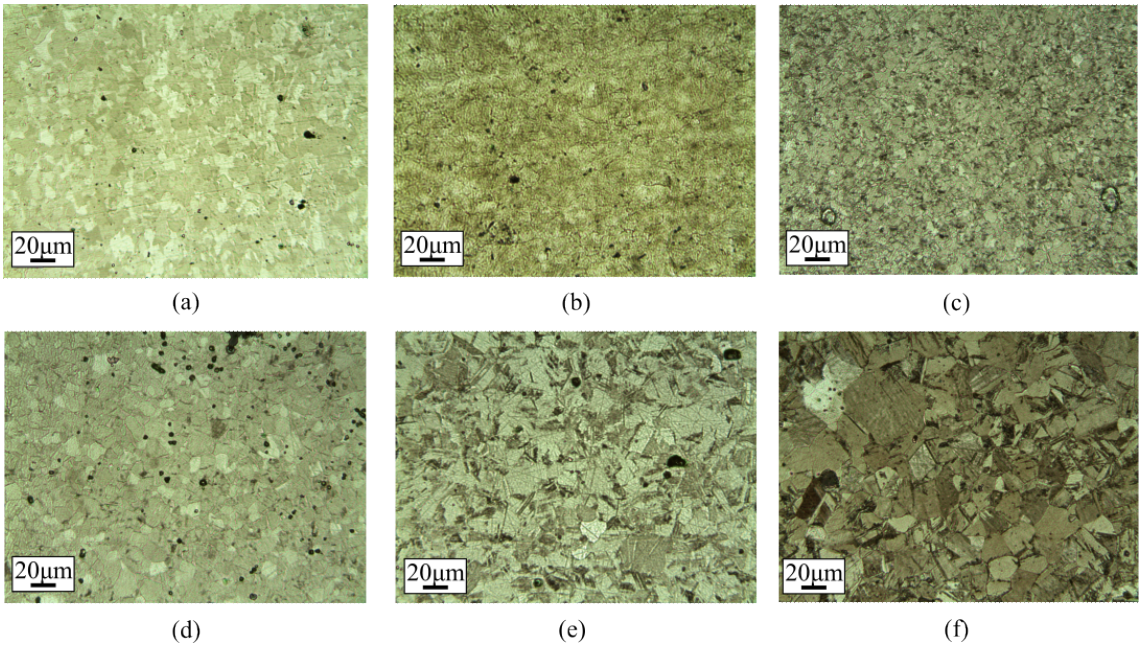

Figure 4.5: Optical micrographs obtained from the (a) as-received, (b) as-rolled and the annealed specimens at (c) 850, (d) 900, (e) 950 and (f) 1000 °C.

three grains counts as 1.5). Rolling of the specimen results in pancake-shaped grains and multiple deformation twins, as can be shown in Fig. 4.5b. Annealing at 850 and 900 °C did not show evidence of any microstructure changes against the as-received specimen. However, higher annealing temperatures led to substantial grain growth along with the formation of annealing twins.

Vicker's hardness testing was carried out to identify the recrystallisation temperature of the TWIP steel. Five indentations were conducted per specimen. Results presented in Fig. 4.6 indicate recrystallisation of the annealed specimens at 850°C, while it appears that hardness further decreases from 950°C and above. The hardness of the as-received material appears to be slightly higher than the one of the annealed specimens, despite its higher grain size in comparison to the one annealed at 850°C. Nevertheless, EBSD data presented in Fig. 4.1, showed some retained deformation in the as-received material which explains the slightly higher hardness. For the rest of the measurements presented in this chapter, annealing at 900°C for 30 min was used, as it leads to a fully recrystallised microstructure with a resulting

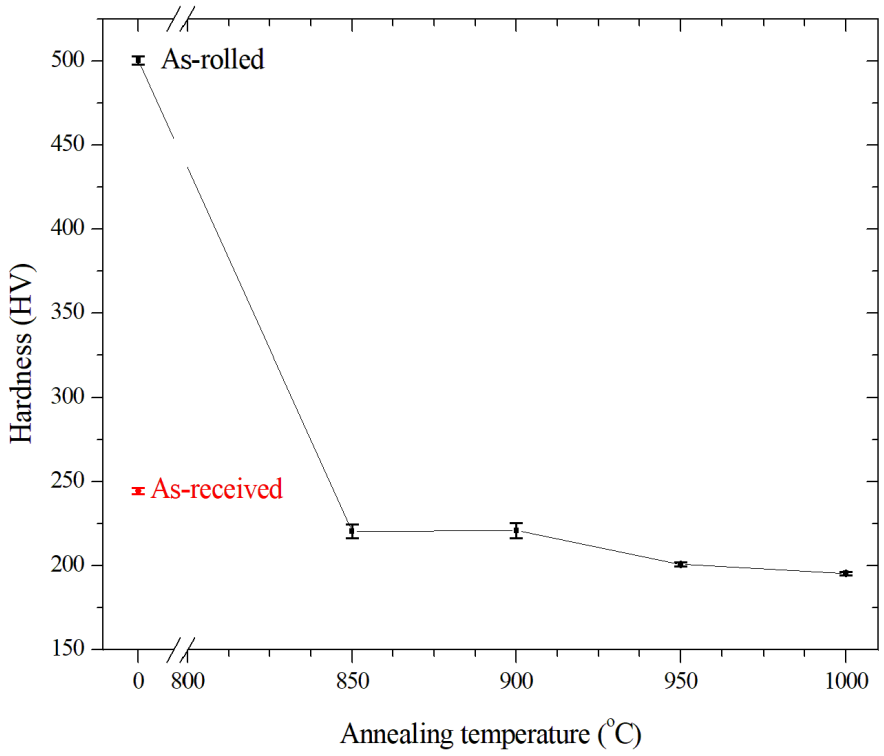

Figure 4.6: Vicker's hardness measurements of the as-received, as-rolled and annealed specimens. The error bars are the standard deviation for each measurement.

grain size comparable to the one of the as-received material.

4.3.2 Tensile properties

Three uniaxial tension tests were conducted for specimens annealed at 900°C, to obtain mechanical properties. The resulting true stress-strain curves are shown in Fig. 4.7. A decreased YS of 211 MPa was obtained compared to the as-received material, derived in a similar way to the one described in Section 4.2.2 , as a result of the increased grain size post-annealing. The higher grain size also led to a slightly increased tensile strain (ε=0.71). Contrariwise, the strain hardening rate and the UTS exhibited only an insignificant decrease (1910 and 1626 MPa, respectively).

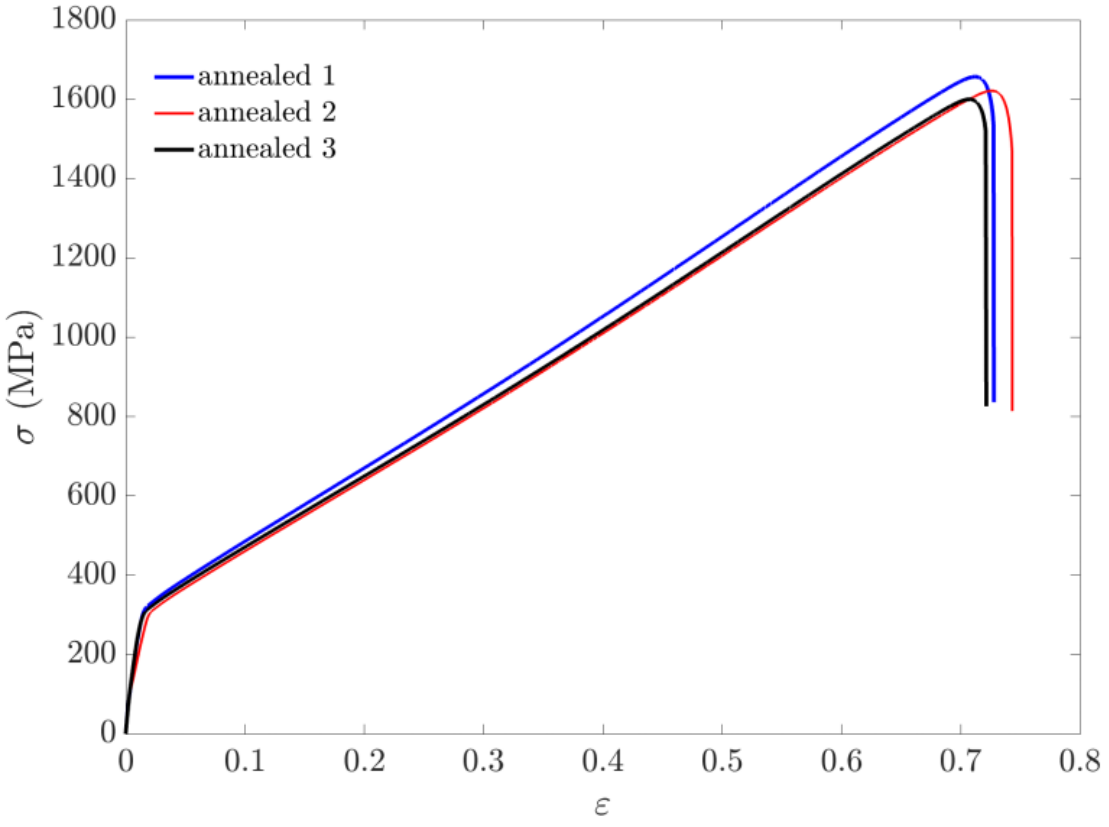

Figure 4.7: True stress vs strain curve for the TWIP steel annealed at 900°C for 30 mins.

Grain size is generally known to influence strain hardening behaviour [126, 127] of TWIP steels, both in terms of hardening rate as well as the developed hardening stages. However in the examined case, the difference in the grain size is so small that any variation in hardening behaviour is negligible. Such result can also indicate that deformation twin generation with increasing strain is not affected by the annealing process.

4.4 Miniaturised punch test

4.4.1 Finite Element Analysis

In order to investigate the micromechanical response of the examined material under a variety of strain paths, a miniaturised version of the typical Marciniak test [128] was newly developed; this consists of a flat punch with upper and lower dies. A diagram of the setup is shown in Fig. 4.4a. In the traditional Marciniak test setup, a *carrier blank* is also constrained between the specimen and the punch, to ensure that fracture will occur in the middle of the specimen, as it prevents strain localisation happening at the points where the edge of the flat punch applies pressure on the specimen. Obtaining the forming limit from a Marciniak test without using the carrier blank can lead to invalid results. However, obtaining the forming limit accurately is inherently not possible for this experimental setup, due to strain measurement errors occurring at high deformation levels. These effects will be discussed in Section 4.4.3. Additionally, designing miniaturised carrier blanks for a variety of miniaturised specimens is time inefficient and thus it was decided to avoid its use for the scope of this work. Three distinct strain paths, corresponding to equibiaxial, plane strain and uniaxial tension, were achieved via deforming specimens with constant diameter and thickness of 10 mm and 0.3 mm respectively, and varying gauge widths. Dimensions of the punch, lower die and the miniaturised specimens are summarised in Fig. 4.4.

Deformation processes were simulated in Abaqus 2017, using the geometric characteristics of the miniaturised test. For simplicity, only the specimen and the flat punch were included in the model. The specimen was simulated as a three-dimensional deformable solid and was assigned material properties for the annealed TWIP steel, obtained from the uniaxial tension test (Fig. 4.7), to define its plastic

behaviour. The Young's modulus was set to 200 GPa and the Poisson's ratio to 0.3. The flat punch was simulated as a three-dimensional analytical rigid object. Such objects can be described in Abaqus via an analytical function and do not need to be meshed. During deformation, the punch and specimen which are in contact, undergo substantial friction forces, even when PTFE foil is used. Thus, contact between the punch surface and the specimen surface was defined as contact with friction, characterised by a friction coefficient of 0.04, according to [129] (static friction coefficient between steel and PTFE). The deformable region of the specimen was assigned a mesh with a global mesh size of 0.15 length units for the plane strain and equibiaxial specimens, while a finer mesh of 0.10 length unit was assigned to the uniaxial specimen to compensate for the narrow gauge and to improve accuracy. As specimens have a thickness of 0.3 mm, through the thickness mesh size was decreased to 0.03 for increased accuracy. The element type was defined as a 3D cubic, with 1 integration point in the centre of the cube (C3D8R). For simulation purposes, it was assumed that the specimen is tightly clamped between the two dies, and encastre boundary conditions were assigned to the outer, non-deformable regions of the specimen. In reality, a small clearance exists between the specimen and the dies, allowing a small amount of material flow, thus it is expected that the simulated through-thickness strains will be higher than the actual ones.

The punch movement was simulated as a smooth displacement step with an amplitude of 2 mm. This means that the displacement increases linearly with time. In the SPT experiments described in this chapter, the actual punch speed was set to 0.02 mm/s, thus the total simulated time (*time period*) would be 100 s. Such time period is not only computationally expensive, but in our case, unfeasible, as it leads to element distortion errors. A time increment of the total time period, ΔT must

follow the condition

$$\Delta T \leq \min\left(L^{el}\sqrt{\frac{\rho}{\lambda + 2\mu}} \right) \tag{4.5}$$

where L^{el} is associated with the element size, ρ is the material density and λ and μ are the Lamé coefficients. For a fine mesh, as is adopted here, it is obvious that the number of time increments is extremely high (higher than 2×10^6), which led to computational errors. To assist with the simulation time for this quasi-static process, the total deformation process was assumed to be completed in total time of 10 s. This is expected to introduce small deviations in the results compared to the real material behaviour, since rate sensitivity of an FCC material is well known [130]. However, it is not expected to affect the resulting strain paths, which is the main objective of the current simulation. From Eq. 4.5 it is shown that the time increment is also proportional to the density of the material. To further help with the total simulation time, a virtual increase of density can be applied to increase the time increment; a process known as *mass scaling*. Semi-automatic mass scaling, of a factor of 10^6 was defined here.

Strain paths as calculated from the above analysis are shown in Fig. 4.8. Forming limit strains were defined at the point where the second derivative vs time of the equivalent plastic strain hits its maximum value. It is observed that a uniaxial strain path can accommodate significantly higher deformation in comparison to the other two strain paths. This is a well known result for this type of test. The use of a carrier blank with a flat punch can extend the maximum strain by preventing strain localisation at the edges of the specimen. However, in the setup used in this work, a carrier blank was not used, thus lower limit strains were expected.

A change in the strain path, which is often observed in experimental FLCs, can be seen at $\varepsilon_1 \approx 0.8$. Non-linearity most commonly occurs in the Nakazima test where

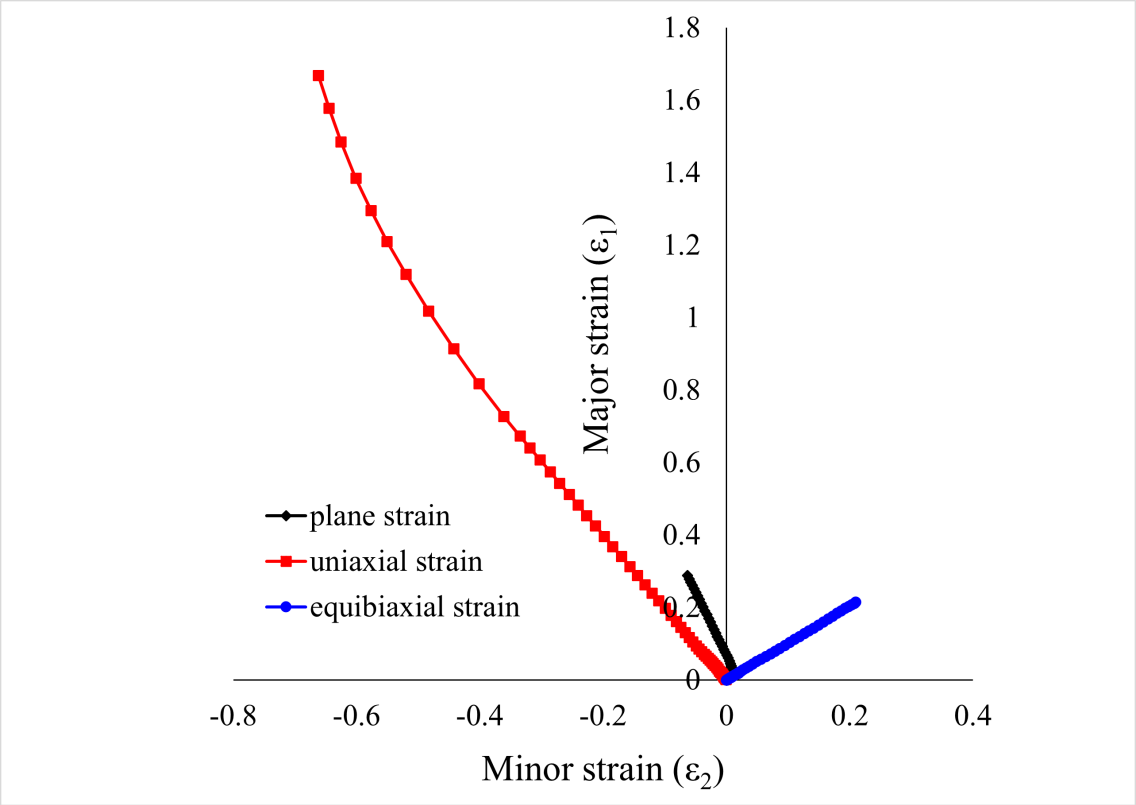

Figure 4.8: Strain paths as calculated via finite element analysis.

the punch is hemispherical, however, non linearity is also observed when using a flat punch [131]. An abrupt SPC is also observed in the path representing plane strain, at $\varepsilon_1 \approx 0.05$. Post SPC, the strain path deviates from the plane strain condition, which can explain the higher forming limit of this path in comparison to the equibiaxial strain. Usually, plane strain condition is the most detrimental for the formability of the material, whilst in our case the equibiaxial strain appears to result in the lower forming limit. It is important to highlight at this point that deviations from the typical forming limits and major-minor strain relationships can be a result of the following: (a) any anisotropy inherent in the examined material was ignored during simulations, (b) grain size and anisotropic properties effects become more prevalent in specimens of a miniaturised size and (c) choosing to avoid the use of a carrier blank results in strain localisation and fracture at the edges of the punch and not in the middle, which is the main weakness of this method regarding investigation of the forming limit.

4.4.2 Experimental setup

The miniaturised test rig described in the previous section, was designed as an auxiliary fitment onto an Instron 3345 tensile testing machine with a load capacity of 5 kN. The flat punch was fitted into the load cell, which in turn is fixed to the loadframe crosshead, allowed vertical movement. The dies were fixed (constrained) at the base of the instrument. In a typical Marciniak test, strains can be measured via DIC, from the deforming surface of a 'patterned' specimen. Most commonly, a stochastic black and white speckle pattern is applied onto the specimen surface, facilitating the tracking of displacements when loaded; however a periodic, circular pattern can be also used. A set of two cameras is usually placed above the specimen surface, allowing in and out-of-plane displacement measurements.

In cases where such geometry cannot be used, a right angle prism mirror can be placed under the test piece, and an image/video can be recorded through the mirror surface, as described in [132, 133, 134]. In this study, the latter geometry was used and is shown in Fig. 4.9. At the top of the image, the flat punch attached on the Instron crosshead can be seen. The specimen, which cannot be directly observed is clamped between the two dies. Below, a Thorlabs silver coated right angle prism mirror is placed normal to the specimen surface. A video of the deforming surface was recorded via a Thorlabs CMOS camera equipped with a 12× magnification zoom lens (left), and the image of the deforming specimen can be seen in the screen (right).

4.4.3 Strain measurement

As described above, displacement measurements were facilitated via recording video from a single camera. The data collected, were then processed using the Ncorr v1.2

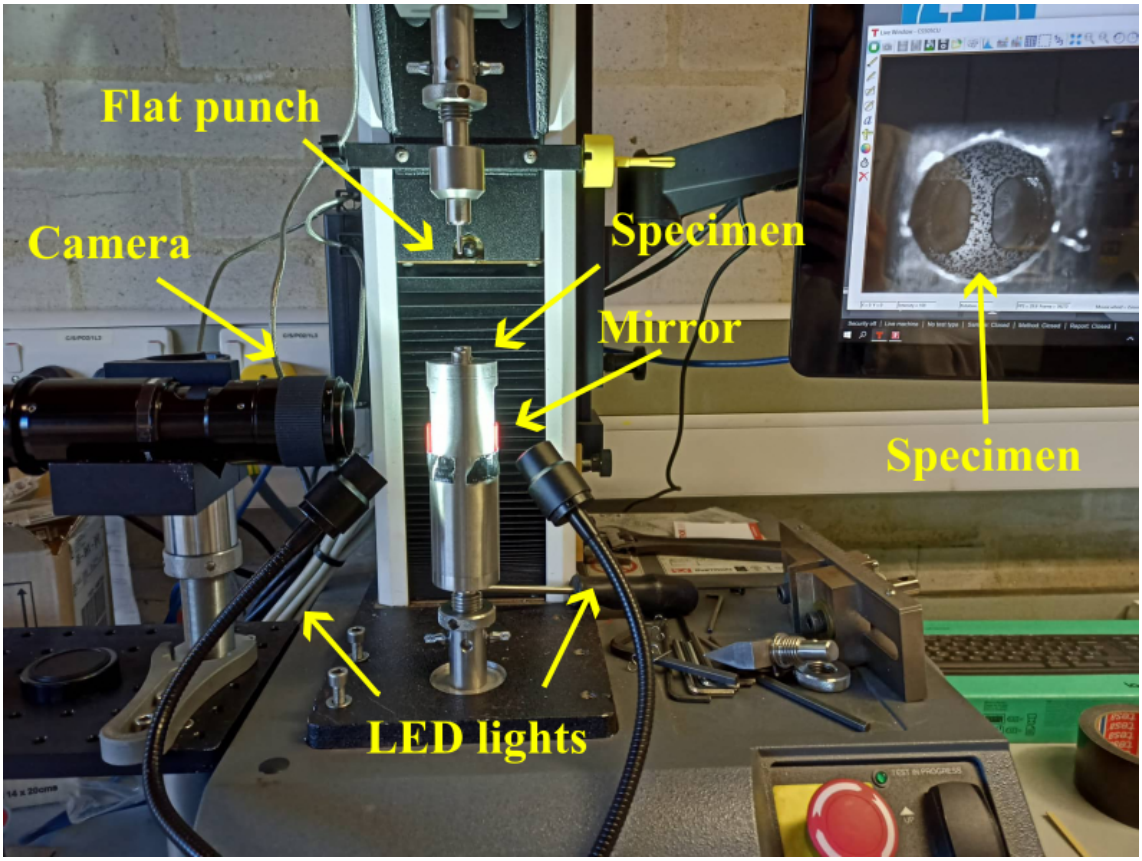

Figure 4.9: Experimental setup.

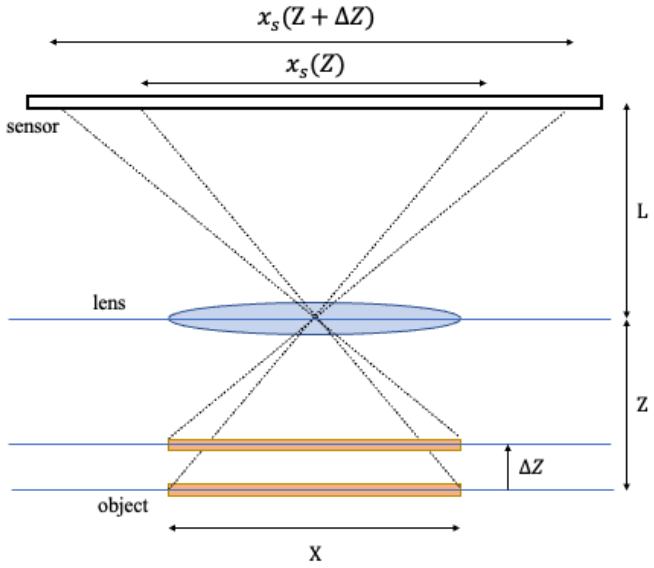

Figure 4.10: Out of plane displacement effect as recorded by a single camera.

software [135], which was executed via Matlab 2021a [136].

A key challenge encountered with the setup used here was to account for errors arising from out-of-plane displacements. This is a well known effect, which has been quantified by Sutton et. al. [137]; eliminating such artefacts is a significant advantage of 3D-DIC over 2D-DIC. However, it has been recently discussed [138] that for a Marciniak-type test, where the out-of-plane deformation is conducted with a flat punch, these errors are systematic, and can be easily subtracted from the measured strains. The systematic error, as explained by Sutton et. al. [137], can be calculated using the pinhole camera concept, summarised in Fig. 4.10. The image of an object in the camera sensor has a size indicated from the coordinates x_s and y_s, calculated by:

$$x_s(Z) = \frac{L}{Z}X, y_s(Z) = \frac{L}{Z}Y \tag{4.6}$$

where X and Y are the coordinates indicating the real object size, L is the focal length and Z is the distance between the object and the lens. For a ΔZ displacement of

the object towards the camera lens , the new object size in the sensor plane is:

$$x_s(Z+\Delta Z) = \frac{\mathrm{L}}{Z+\Delta Z}X, y_s(Z+\Delta Z) = \frac{L}{Z+\Delta Z}Y \tag{4.7}$$

which can be re-written as

$$x_s(Z+\Delta Z) = \frac{L}{Z(1+\frac{\Delta Z}{Z})}X, y_s(Z+\Delta Z) = \frac{L}{Z(1+\frac{\Delta Z}{Z})}Y. \tag{4.8}$$

By keeping the first two terms of $\left(1+\frac{\Delta Z}{Z}\right)^{-1}$ Taylor expansion, we can re-write

$$x_s(Z+\Delta Z) = \frac{L}{Z}X\left(1-\frac{\Delta Z}{Z}\right),\ y_s(Z) = \frac{L}{Z}Y\left(1-\frac{\Delta Z}{Z}\right) \tag{4.9}$$

We can therefore calculate the *virtual displacements*, originated in the enlargement of the object due to its out-plane-movement through

$$U(\Delta Z) = -\frac{\Delta Z}{Z}LX = -\frac{\Delta Z}{Z}x_s,\ V(\Delta Z) = -\frac{\Delta Z}{Z}LY = -\frac{\Delta Z}{Z}y_s \tag{4.10}$$

where U and V are the displacements on the x and y axes respectively. From the subset displacement, Ncorr calculates the Green-Lagrange strain elements according to:

$$\varepsilon_{xx} = \frac{1}{2}\left[2\frac{\partial U}{\partial x_s} + \left(\frac{\partial U}{\partial x_s}\right)^2 + \left(\frac{\partial V}{\partial x_s}\right)^2\right] \tag{4.11}$$

$$\varepsilon_{yy} = \frac{1}{2}\left[2\frac{\partial V}{\partial y_s} + \left(\frac{\partial V}{\partial y_s}\right)^2 + \left(\frac{\partial U}{\partial y_s}\right)^2\right] \tag{4.12}$$

and

$$\varepsilon_{xy} = \frac{1}{2}\left[\frac{\partial V}{\partial x_s} + \frac{\partial U}{\partial y_s} + \frac{\partial U}{\partial x_s}\frac{\partial U}{\partial y_s} + \frac{\partial V}{\partial x_s}\frac{\partial V}{\partial y_s}\right] \tag{4.13}$$

From equations 4.10, 4.11, 4.12 and 4.13, one can easily calculate the *virtual strains*

$$\delta\varepsilon_{xx} = \delta\varepsilon_{yy} \approx -\frac{\Delta Z}{Z}, \delta\varepsilon_{xy} = 0. \tag{4.14}$$

For the above calculation it can be safely assumed that the terms $\frac{1}{2}(\partial U(\Delta Z)/\partial x_s)^2$ and $\frac{1}{2}(\partial V(\Delta Z)/\partial y_s)^2$ are very small and can be ignored.

For an approaching object, ΔZ is a negative value, thus the virtual strain is a positive number; hence the measured strain is slightly larger than the real strain produced from deformation. One can correct this strain via subtracting the $\delta\varepsilon_{xx}$ and $\delta\varepsilon_{yy}$ from the measured strain. As expected from Eq. 4.14, in-plane virtual strains linearly increase with punch displacement. This behaviour is illustrated in Fig. 4.14. According to [138], post-subtraction it was found that the deviations between the 2D and the 3D-DIC measured strains were small. Additionally, putting into consideration the significant increase in the cost of the 3D-DIC camera systems, it was decided that for the scope of this work, aiming to investigate the microstructural effects of different strain paths, those deviations were acceptable and thus 2D-DIC was used.

It is important to highlight at this point that the above correction cannot be applied for images collected out-of-focus. The camera used here does not have an auto-focus mode, thus strains could be accurately measured only for a punch displacement equal to the *depth of field*, a parameter dependent on the zoom lens and the magnification used. For the measurements presented in this thesis, minimum magnification was used to allow higher depth of field, hence a larger region of accurately measured strains, and additionally provide a large enough field of view. For these settings, the depth of field was 1.39 mm. It was found that the high ductility of the examined material led to fracture at higher punch displacements, which makes

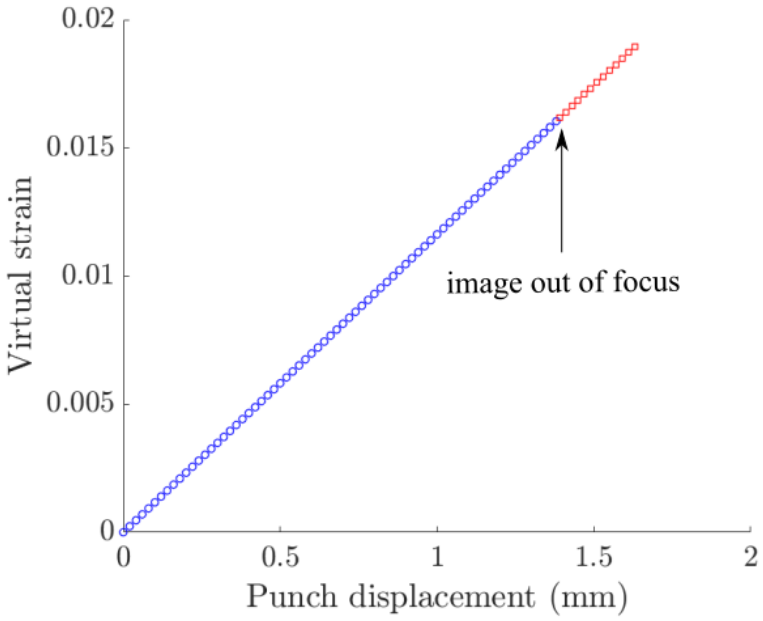

Figure 4.11: Virtual strain caused by the out-of-plane displacement as a function of the punch displacement. Focal length of the camera used here is 1.39 mm, thus beyond this value, image gets out of focus. Strains measured via out-of-focus images are not accurate.

the accurate determination of the forming limit impossible for this setup.

4.4.4 Through-the-thickness strain calculation

A measurement of the out-of-plane strain is not possible with DIC, however, as FEA predicted for the experiment setup in this study, it cannot be ignored. To calculate the out-of-plane strain element the following assumptions are made: (1) the volume is conserved during deformation, (2) the out-of-plane shear strain elements are small and can be ignored. The principal strains are defined as

$$\epsilon_i = \frac{\Delta L}{L_0} \tag{4.15}$$

where i =1,2,3, L and L_0 are the length and the initial length prior to deformation, respectively. Assuming that the volume V is conserved then:

$$\frac{V_f}{V_0} = \frac{\Delta L_x + L_{x,0}}{L_{x,0}} \frac{\Delta L_y + L_{y,0}}{L_{y,0}} \frac{\Delta L_z + L_{z,0}}{L_{z,0}} = 1 \tag{4.16}$$

where V_0 and V_f stand for the initial and final volume, respectively. From 4.15 and 4.16:

$$1 = (1 + \epsilon_1)(1 + \epsilon_2)(1 + \epsilon_3) \tag{4.17}$$

or

$$\epsilon_3 = -\frac{\epsilon_1 + \epsilon_2 + \epsilon_1\epsilon_2}{1 + \epsilon_1 + \epsilon_2 + \epsilon_1\epsilon_2} \tag{4.18}$$

Ncorr calculates the Lagrangian tensor elements through displacements. The strain tensor is written as:

$$\varepsilon = \begin{vmatrix} \varepsilon_{xx} & \varepsilon_{xy} & \varepsilon_{xz} \\ \varepsilon_{yx} & \varepsilon_{yy} & \varepsilon_{zz} \\ \varepsilon_{zx} & \varepsilon_{zy} & \varepsilon_{zz} \end{vmatrix} \tag{4.19}$$

Using assumption (2) and the fact that the tensor is symmetric, the expression is rewriten:

$$\varepsilon = \begin{vmatrix} \varepsilon_{xx} & \varepsilon_{xy} & 0 \\ \varepsilon_{xy} & \varepsilon_{yy} & 0 \\ 0 & 0 & \varepsilon_{zz} \end{vmatrix} \tag{4.20}$$

Irrespective to the strain tensor definition, the principal strains $\epsilon_1, \epsilon_2, \epsilon_3$ are the

eigenvalues of the tensor. This way one can calculate them as follows:

$$\det(\boldsymbol{\varepsilon} - \lambda \boldsymbol{I}) = 0 \Rightarrow \begin{vmatrix} \varepsilon_{xx} - \lambda & \varepsilon_{xy} & 0 \\ \varepsilon_{xy} & \varepsilon_{yy} - \lambda & 0 \\ 0 & 0 & \varepsilon_{zz} - \lambda \end{vmatrix} = 0 \tag{4.21}$$

$$\Rightarrow (\varepsilon_{zz} - \lambda) \begin{vmatrix} \varepsilon_{xx} - \lambda & \varepsilon_{xy} \\ \varepsilon_{xy} & \varepsilon_{yy} - \lambda \end{vmatrix} = 0 \tag{4.22}$$

$$\Rightarrow \lambda_3 \equiv \epsilon_3 = \varepsilon_{zz} \tag{4.23}$$

and

$$\lambda^2 - \lambda \left(\varepsilon_{xx} + \varepsilon_{yy}\right) + \varepsilon_{xx}\varepsilon_{yy} - \varepsilon_{xy}^2 \tag{4.24}$$

so

$$\lambda_{1,2} \equiv \epsilon_{1,2} = \frac{\varepsilon_{xx} + \varepsilon_{yy}}{2} \pm \frac{1}{2}\sqrt{(\varepsilon_{xx} - \varepsilon_{yy})^2 + 4\varepsilon_{xy}^2} \tag{4.25}$$

A value for ϵ_3 is then calculated from 4.18 and 4.25. The Von Mises strain can be then obtained from:

$$\varepsilon_{\mathrm{VM}} = \frac{\sqrt{2}}{3}\sqrt{(\epsilon_1 - \epsilon_2)^2 + (\epsilon_2 - \epsilon_3)^2 + (\epsilon_3 - \epsilon_1)^2} \tag{4.26}$$

4.5 Proportional strain paths

4.5.1 Specimen preparation

Proportional strain paths corresponding to 1) uniaxial tension, 2) plane strain and 3) equibiaxial tension conditions were first examined. The specimen preparation for miniaturised punch test incorporated three main stages: a) encapsulation prior to heat treatment to prevent oxide development on the specimen surface, b) annealing which removes any residual stresses caused by machining and c) polishing and painting prior to testing.

First, specimens were wrapped in Mo-foil and were encapsulated together with a small Ti piece in SiO_2 tubes. Both Mo and Ti contribute in the absorption O_2 from the specimen environment during annealing. Tubes were evacuated down to a final air pressure of approximately 10^{-2}Pa and were back-filled with Ar gas. Subsequently, the DX54 specimens were annealed for 120 min at 650°C and the TWIP specimens for 30 min at 900°C, and were then air-cooled inside the SiO_2 tube. The process for an appropriate annealing temperature determination for the TWIP steel has been described in Section 4.3. A similar investigation was not conducted for the DX54 steel; the annealing temperature was determined from a prior study [124]. Post-annealing, one side of the specimens was polished with a 3 µm diamond particle solution to reduce surface roughness while the other side remained untouched to assist paint adhesion. Prior to painting, three thickness measurements were carried out per specimen, using a micrometer placed at the central part of each specimen. A thin layer of matt white, acrylic spray paint was used to cover specimen surfaces, and was left to dry in room temperature for a minimum of 30 mins. Afterwards, the white surface was covered with a random speckle pattern, using an airbrush, which helps to reduce the speckle size and increases the displacement measurement

accuracy. In some instances, paint was de-laminated during deformation. It was generally observed that painting on the same day of the test reduced this problem, however, other parameters such as the temperature and humidity of the environment also influence the quality of the paint.

The specimen and punch lubrication have a great impact on the measured load, hence initial friction (load measured at the beginning of deformation) was recorded at every measurement. A small misalignment between the top part (where the punch is adjusted) and the bottom part of the available Instron tensile testing machine, led to an increase of the measured friction, because punch was in contact with the sides of the upper die at all times. The 'Specimen-punch' and 'die-punch' contribution to the overall friction cannot be distinguished. However, to reduce the friction, three pieces of PTFE foil with a thickness of 0.1 µm were placed between the punch and specimen surface along with a graphite-based lubricant which was applied onto the punch peripheral and the upper die walls.

4.5.2 Evaluation of the test using the DX54 steel

The scope of this section is to assess the functionality of the miniaturised Marciniak test using the DX54 alloy. Three strain paths were examined: the (a) uniaxial, (b) plane strain and (c) equibiaxial ones. Three specimens were subjected to plastic deformation up to fracture for each strain path to assess the result repeatability including the accuracy of the estimated forming limits. A 1.2 mm/min punch displacement rate was used in all cases and a 40% load drop from its maximum value terminated each test. Similar measurement parameters are used throughout this chapter. A video was recorded at a rate of approximately 14 frames per second, using an image binning of 2×2, resulting in an image resolution of 1232×1024 pixels^2. The punch displacement rate was set to 1.2 mm/min. To reduce the time required

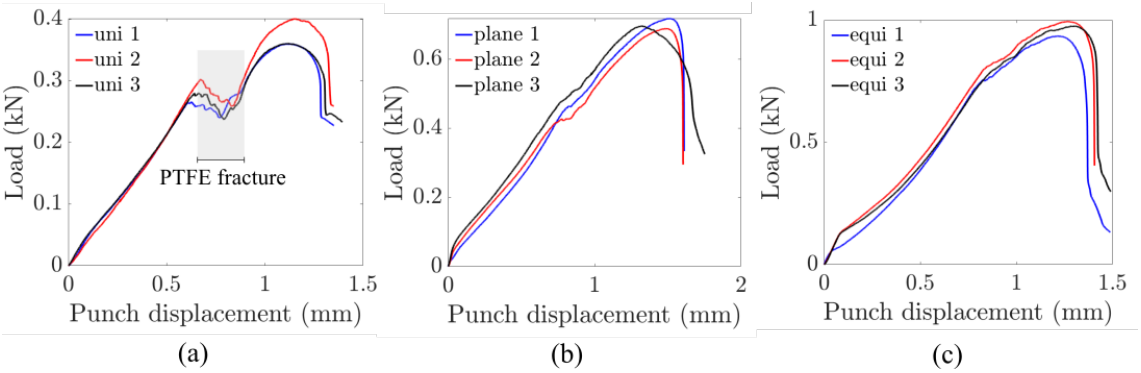

Figure 4.12: Load-punch displacement curves for (a) uniaxial, (b) plane and (c) equibiaxial strain specimens.

for strain calculation via Ncorr, 1 out of the 14 frames was extracted from the video, resulting in a frame rate of 1 image per second.

The load vs punch displacement results obtained for the aforementioned strain paths for the DX54 alloy are presented in Fig. 4.12. Results show good repeatability regarding the total punch displacement to fracture and the maximum load. Prior to reaching the maximum load, serrations were observed in all the examined specimens, however they are more obvious for the uniaxial strain one. This is due to the overall low loads recorded for the uniaxial case. Serrations look similar to the 'pop-ins' described in [17], which are correlated with crack initiation in brittle specimens. In our case however, they do not occur due to crack generations, but correspond to the fracture point of the PTFE foil placed between the specimen and the punch, and cannot be subtracted from the measured curves. Nevertheless, they are not expected to interfere with the result repeatability.

The shape of the curves looks similar to the typical load-displacement curve shape for small punch testing (see Fig. 2.16). The equibiaxial specimens clearly follow this typical behaviour; the linear, elastic part of the curve is observed at low displacements, followed by the transition to the plastic deformation regime. The latter, gives its place to the transition to membrane stress region and finally to the

establishment of membrane stress and then failure (drop from the maximum load). The transition to membrane stress region is less obvious for the uniaxial and plane strain specimens.

During loading, deformation of the specimen surface was recorded. The resulting strains were calculated using the Ncorr software. For the reference image, a Region Of Interest (ROI) was drawn to coincide with the specimen shape. A subset radius was set to 30 and a subset spacing to 3, for all measurements. These parameters were empirical and were all chosen so that the computational time does not make the processing inefficient but also, does not cause noisy displacement data. Those parameters were the same for all specimens. 50 iterations were carried out during the correlation process. Post correlation, the displacements were calculated. Noisy data occurring almost exclusively at high punch displacements were removed from the displacement (and thus strain) calculation, by decreasing the *correlation coefficient cutoff* parameter, to appropriate values for each measurement (not the same value was used every time). Strains were calculated according to the Green-Lagrange definition, provided in Eq. 4.11, 4.12 and 4.13.

Fig. 4.13 shows the ε_{yy} vs ε_{xx} measurements for uniaxial, plane and equibiaxial strain specimens. Results show very good repeatability, especially at low strains, while some deviations are observed at $\varepsilon_y > 0.20$ for the uniaxial strain path. As discussed previously, regarding load-punch displacement results shown in Fig. 4.12a, the uniaxial strain path is expected to lead in higher deviations due to the small specimen gauge, resulting in more prevalent grain size influence on the mechanical properties. Strain ratio $\frac{\varepsilon_{xx}}{\varepsilon_{yy}}$ of the equibiaxial strain path is ≈ 1 as expected. Plane strain path exhibits the simulation predicted SPC at $\varepsilon_{yy} \approx 0.05$ and post-SPC the minor strain ε_{xx} becomes ≈ 0, as expected. The uniaxial strain path is non linear, and an SPC is observed at $\varepsilon_{yy} \approx 0.10$. This non-linearity results in a strain ratio of $\approx -\frac{1}{4}$ instead of the $-\frac{1}{2}$, a result also predicted via FEA (see Fig. 4.8, and is also

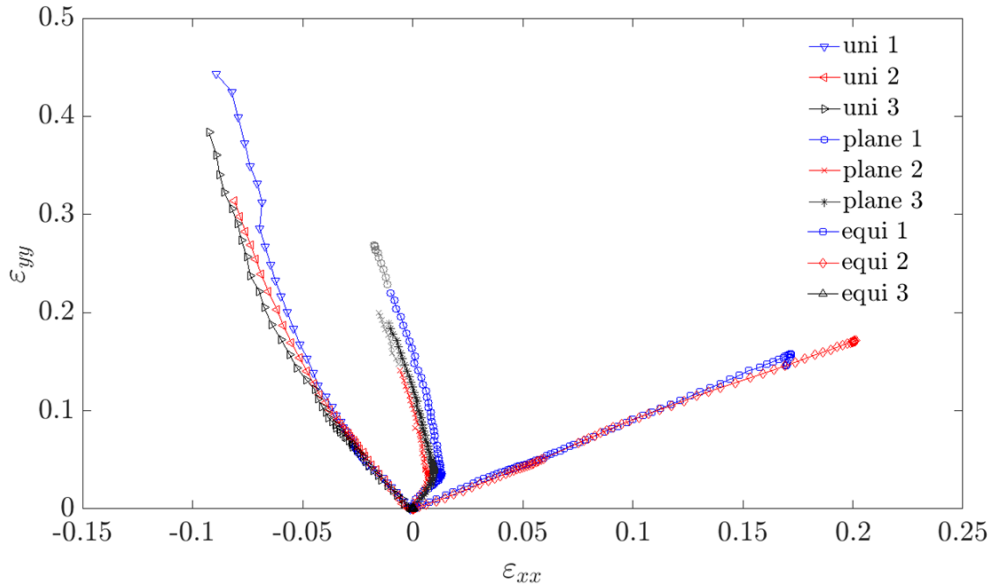

Figure 4.13: ε_{yy} vs ε_{xx} curves for DX54 specimens representative of uniaxial (left), plane (middle) and equibiaxial (right) strain paths. Gray data-points correspond to strains measured from out-of-focus images.

reported in the literature [131].

4.5.3 TWIP steel proportional strain paths

Following the tests conducted on the DX54 steel, and after good repeatability was confirmed, examination of the mechanical properties of the TWIP steel using the SPT took place. Specimen preparation and measurement conditions were identical to the ones described in the previous section. In Fig. 4.14, load-displacement data for all strain paths are presented. For equibiaxial and plane strain conditions, results obtained show good repeatability, with the punch displacement at fracture being approximately similar for all specimens per strain path and the measured loads differing only insignificantly in the case of equibiaxial tension. Contrariwise, load-displacement curves for specimens corresponding to the uniaxial tension state (Fig. 4.14c), exhibit major differences, which are more obvious at high displacements;

however the shape of the curves remains the same, indicating similar work hardening behaviour. It is apparent that specimen 'uni 1' is characterised by lower loads in comparison to the other two specimens. As discussed earlier, the small gauge of the uniaxial strain path can lead to deviations of the resulting load-displacement behaviour. It appears that this effect is more prominent on the TWIP steel specimens compared to the DX54 steel, though there is no apparent microstructural evidence behind this result. TWIP steel examined here, has a lower grain size than the DX54 steel, thus the deviations in the load-displacement behaviour cannot be explained through microstructure, an investigation of the specimen geometry is therefore necessary.

The thicknesses of the specimens were measured with a micrometer. At least 3 measurements were conducted per specimen. From the measurements it was found that the thicknesses of the deformed specimens differ only slightly, with the specimen 'uni 1' being 10 µm thinner than the other two specimens. In Fig. 4.15 gauge widths in pixels, of uniaxial tension specimens of Fig. 4.14 are shown. An increase in specimen width is directly linked to an increase in the applied load, as expected, which highlights that a slight change in the geometric characteristics will lead in big discrepancies in the mechanical behaviour in miniaturised specimens. Those discrepancies are not significant for bigger gauge widths (or for the disks which are used in the standard SPT), however as the width is decreased, they become more permanent. This is the main disadvantage in the use of miniaturised specimens over the standard Marciniak test, where a punch diameter of 100 mm is employed.

It is highlighted that the punch displacement at fracture, Fig. 4.14, is not an indicator of ductility when the specimens geometries (and hence the strain paths) under comparison differ. For example, plane strain specimens fracture at approximately 2 mm punch travel, while the uniaxial tension ones, at 1.5 mm, however, strain measurements presented below, show that the ductility of the uniaxial ten-

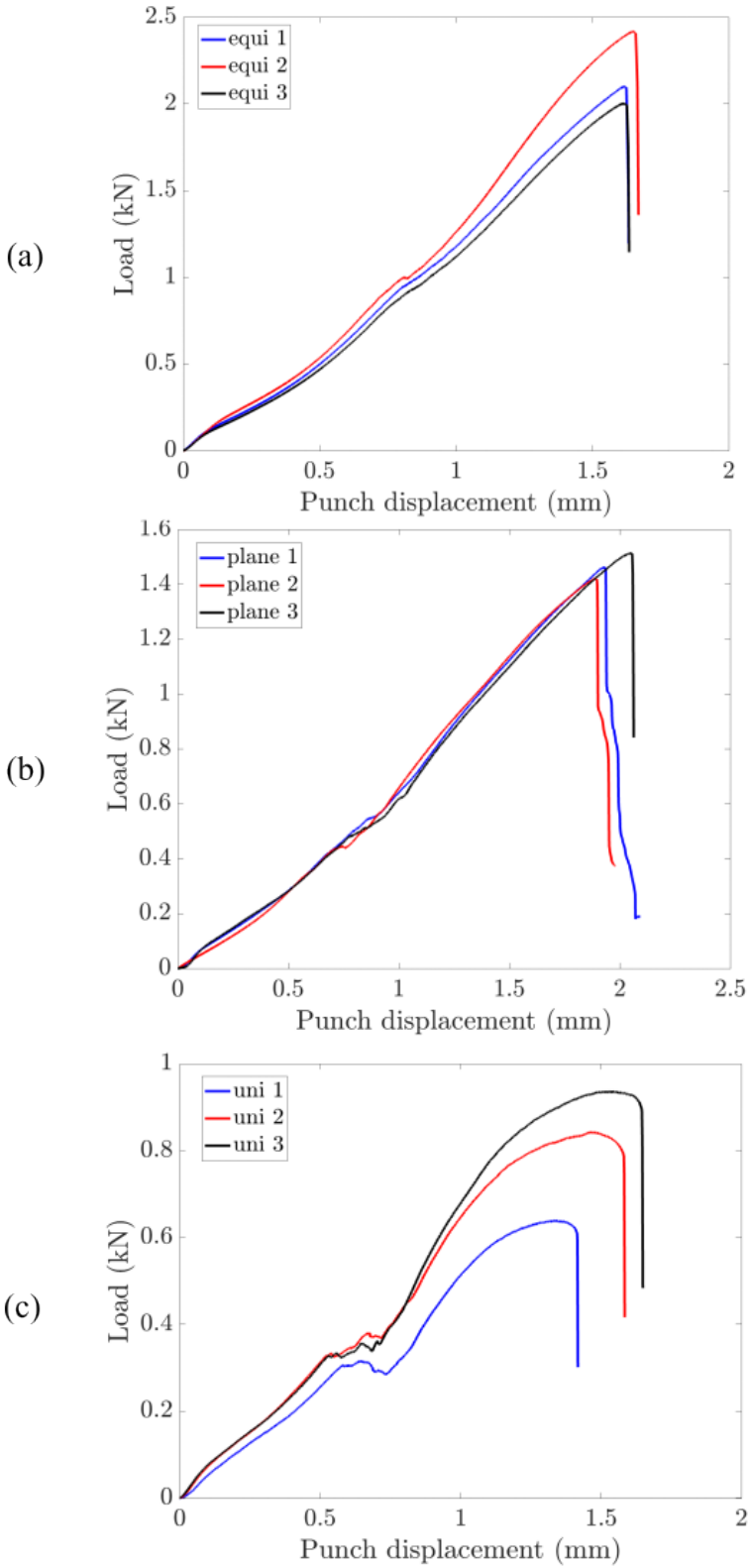

Figure 4.14: Load- punch displacement curves for (a) equibiaxial, (b) plane and (c) uniaxial strain specimens.

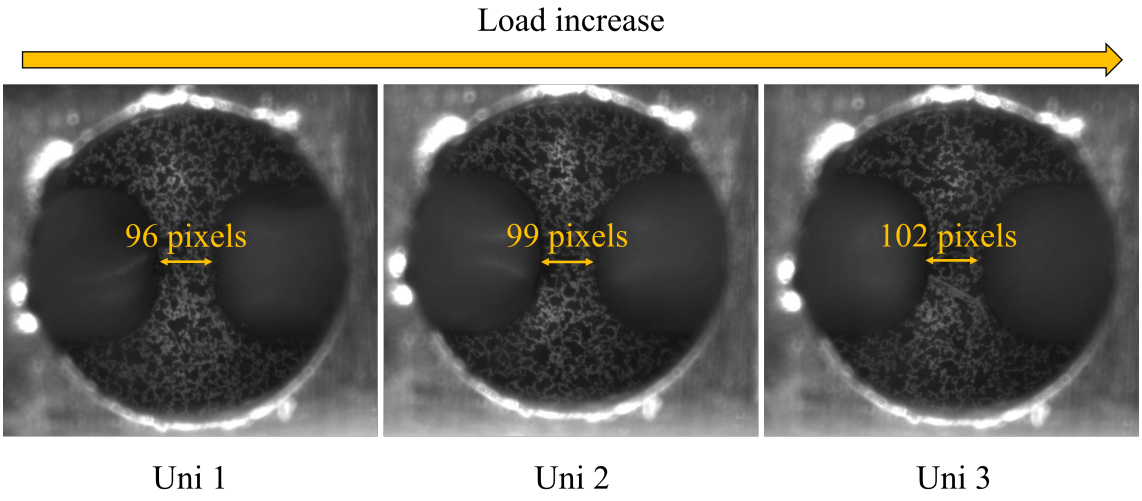

Figure 4.15: Gauge width comparison in pixels, for uniaxial SPT specimens.

sion specimens, is substantially higher that the one of plane strain, as expected.

Using the same strain measurement method described earlier in this chapter, the major vs minor strain behaviour was obtained and is presented in Fig. 4.16. Strain paths, which are directly related to the specimen geometry, exhibit big similarities with the ones presented in Fig. 4.13. Non-linearity effects are observed in uniaxial and plane strain paths, while an almost perfect linear behaviour is observed in equibiaxial specimens. A small exception is specimen 'equi 3', which exhibits a subtle SPC at a major strain of approximately 5%. This is potentially related to a small slide or distortion of the specimen during loading, which is not easily observable in the recorded video but is pictured in the data. Experimental results are compared with the simulation results, discussed in Section 4.4.1. A perfect overlap of the simulated with the experimental data is observed for the equibiaxial strain path, while the simulation deviates from the experiment for the uniaxial and plane strain paths. Those deviations become apparent as the strain increases (for the uniaxial case above 8% and for the plane above 5% major strains), whilst at lower strains the data is in agreement.

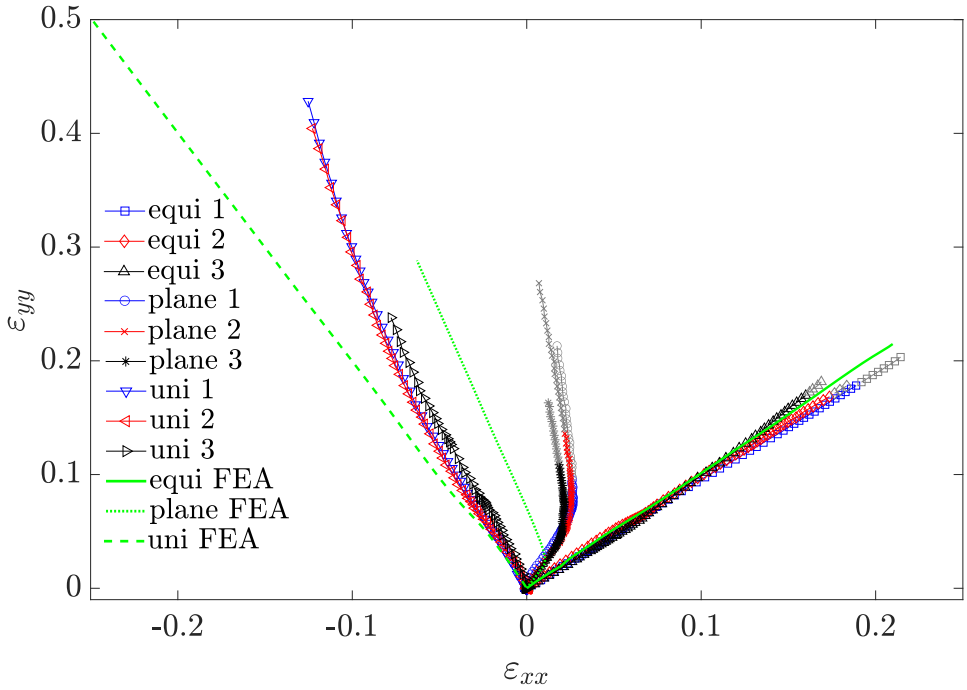

Figure 4.16: Strain paths obtained from biaxial deformation of TWIP steel specimens. Gray data-points correspond to strains measured from out-of-focus images.

It is highlighted that the simulation results did not take into account inherent anisotropy in the mechanical properties of this material or the strain rate sensitivity and were only conducted as an approximation to indicate the geometrical characteristics of the test pieces and the test rig. Non-linearity effects in the simulated results are also revealed, for the plane strain state at lower strains than the experimental results, and for higher strains for the uniaxial strain case. This indicates that the simulation predicts the experimental results well regarding the geometrical characteristics of the test, however it needs to be informed by microstructural characteristics and strain sensitivity to improve its accuracy.

The results discussed above show that the miniaturised Marciniak type test works well regarding the application of different strain paths and can be used as a quick method of deforming ductile materials in different strain states, and examine the strain path sensitivity. Results showed an overall good repeatability, in spite of the specimen small size, which allows predictability of the load vs displacement relationship and thus permits the execution of interrupted tests to investigate microstructure at elevated strains. Such investigation took place and is discussed in the rest of this chapter.

Miniaturised specimens present an additional significant advantage over the standard sized ones; they allow the application of SPCs. This chapter ends by discussing the results obtained from specimens initially subjected to (1) cold rolling and (2) uniaxial tension, and then cut from the rectangular deformed area and loaded with the flat punch in equibiaxial tension. Such examination is impossible in a lab scale, using the conventional Nakazima or Marciniak tests.

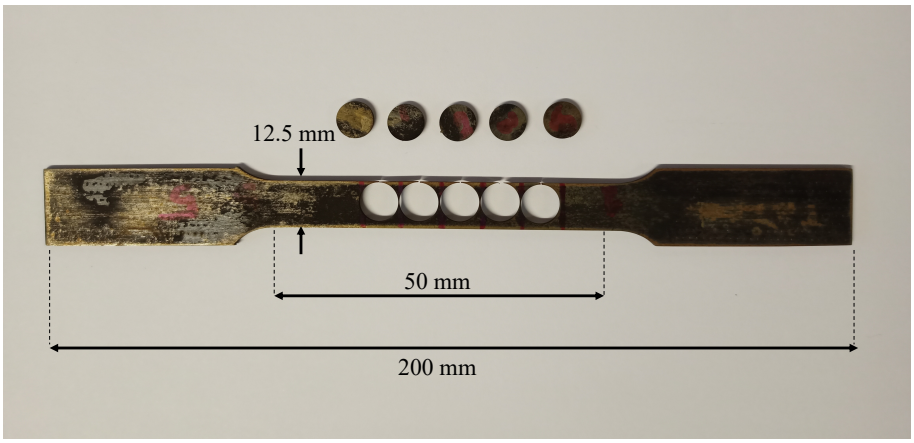

Figure 4.17: SPT specimens cut from a deformed dog-bone specimen

4.6 Non-proportional strain paths

After the functionality of the in-house built miniaturised testing method was confirmed, two non-proportional strain paths were studied: (a) cold rolling up to 15% strain followed by equibiaxial tension and (b) uniaxial tension up to 14% strain followed by equibiaxial tension. Prior to any deformation, specimens were annealed at 900°C for 30 mins, to achieve similar initial microstructure to the rest of the SPT samples. Subsequently, a rectangular sheet was cold rolled perpendicular to the RD, up to e_0=15% and a dog-bone specimen was loaded perpendicular to the RD using an Instron 3367 tensile testing machine with a load capacity of 30 kN, up to e_0=14%. From the pre-deformed specimens, disks with diameter of 10 mm were cut via EDM, as shown in Fig. 4.17. The disks were then mechanically ground down to a thickness of 0.3 mm.

Three specimens were tested for the uniaxial and two for the rolling pre-strain conditions. The corresponding load-displacement curves are presented in Fig. 4.18. Cold rolling (see Fig. 4.18a) resulted in a significant increase in the yield strength in comparison to the proportional equibiaxial loading (here referring to the behaviour

of the yield strength and not its actual value-in reality only the force at the transition from elastic to plastic deformation can be accessed from the current data). The ultimate tensile strength also increased while the overall ductility was decreased. A change in the hardening behaviour can additionally be observed, for punch displacements of approximately 0.2-1 mm, where the curvature of the load-displacement curve notably decreases.

A uniaxial pre-strain effect (Fig. 4.18b appears to be less significant regarding the yield strength and the hardening behaviour, although a decrease in the curvature of the load-displacement curve is also observed, however, is less distinct than the rolling pre-strain case. YS as well as the overall strength is slightly increased in comparison to the proportional equibiaxial loading. Ductility is also decreased, with the final displacement being approximately the same to the one of the rolling pre-strain condition. Those results indicate that uniaxial pre-strain is overall more catastrophic for the mechanical properties of the material than the rolling pre-strain. This is an uncommon result, since the forming limit for the plane strain (similar to the deformation via rolling) is consistently lower than the uniaxial strain path for this TWIP steel. Any discrepancies in the grain size or the thickness of the specimens were also ruled out via microstructure examinations and specimen thickness measurements respectively. In the previous chapter the effect of SPC abruptness was discussed. Results showed that for a mild steel, where only dislocation slip was active, abrupt SPCs had a significantly negative impact on the mechanical properties of the material, which was also apparent in the microstructure. Uniaxial $\rightarrow$ equibiaxial SPC is more abrupt than the rolling $\rightarrow$ equibiaxial one, which may be one factor for deteriorating the mechanical performance. However, further microstructure examination reported at the end of this chapter, is required to support this statement.

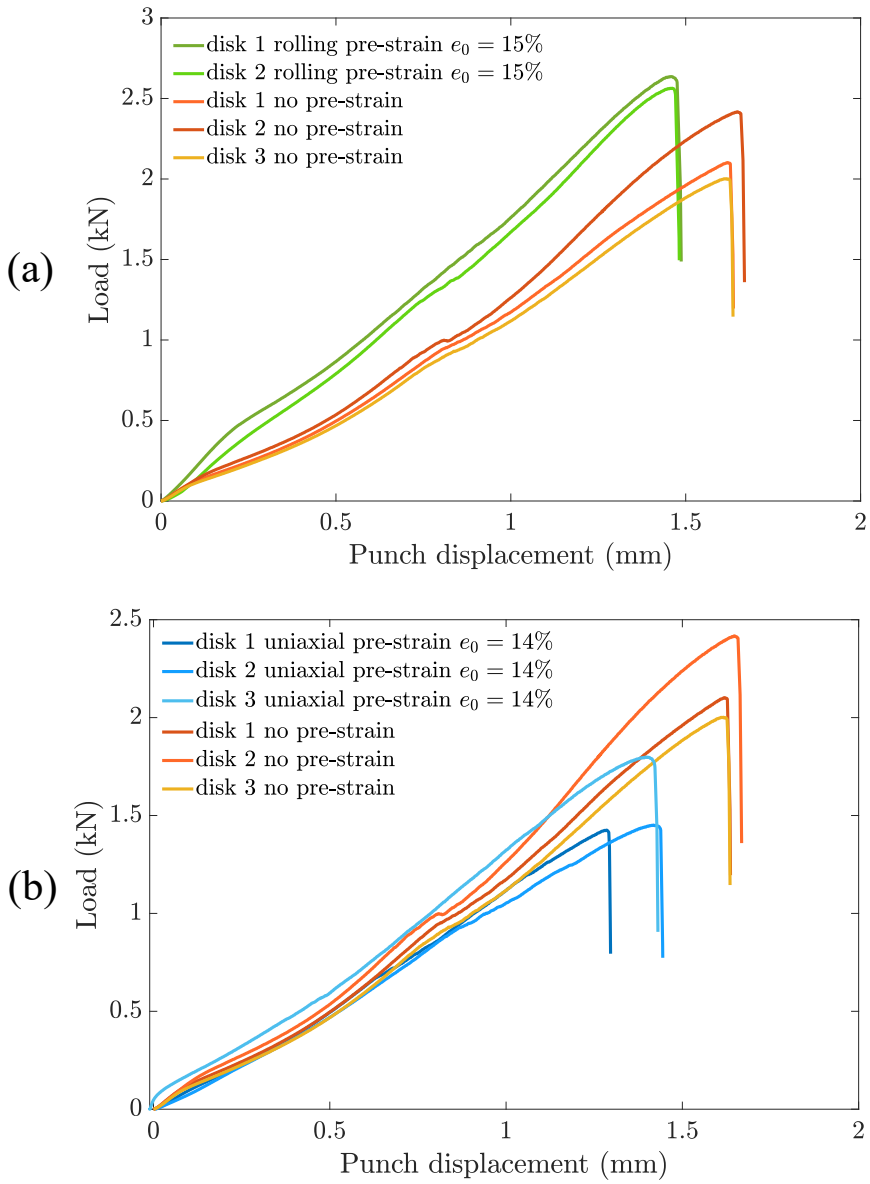

Figure 4.18: Load displacement curves of (a) rolling and (b) uniaxially pre-strained vs non-pre-strained specimens.

Table 4.2: Interrupted tests (proportional and non-proportional) conducted for microstructure examination. Final von Mises strain **excludes the pre-strains** in the case of non-proportional strain paths.

No	Type	Strain path	Pre-strain %	Final von Mises strain %
I	proportional	uni	-	8.43
II	proportional	plane	-	9.99
III	proportional	equi	-	15.25
IV	non-proportional	plane→equi	15	16.72 (failure)
V	non-proportional	uni→equi	14	10.72

4.7 Interrupted tests

In this section, the microstructure of specimens subjected to similar levels of equivalent strain, following different deformation routes, are discussed. The von Mises equivalent strain is used to refer to the 'amount of deformation' for each strain path, as defined by Equation 5.1. Strain paths as well as the equivalent von Mises strain for each one of the specimens are shown in Fig. 4.19 and are summarised in Table 4.2. A 'jump' between the failure and the second to failure data points is observed for the cold rolling → equibiaxial strain path (blue curve). This abrupt increase in the measured strains is due to a 'freeze' in the recorded video with some frames lost (and hence datapoints) prior to specimen rupture. For convenience, from now on, the strain paths will be referred at with Latin numerals (see first column of Table 4.2. In the case of non-proportional paths, the letter 'i' will be used to designate the pre-straining step, and the letter 'f' the final deformation step. Specimen deformed according to path IV, reached failure at the final strain. Microstructures for the remaining specimens were examined prior to failure.

Specimen preparation for EBSD measurements within an SEM included the following steps: first, the deformed specimens were affixed with silver paint mixed with super glue, onto cubes of the same material. These were then mounted together in a polymer (acrylic) media. Mounted specimens were mechanically ground

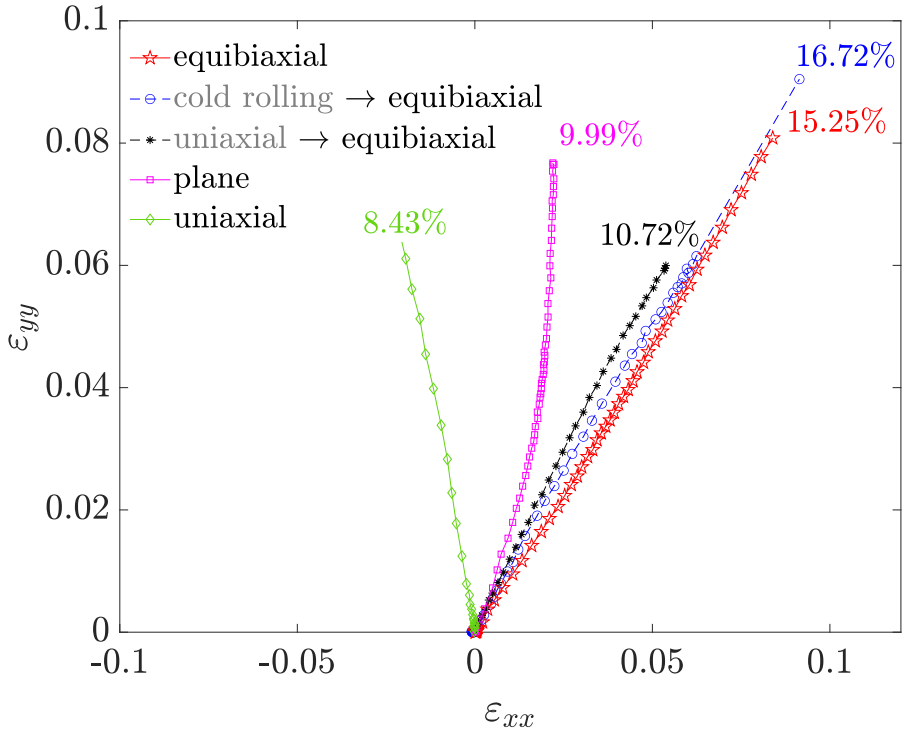

Figure 4.19: Major vs minor strain curves for interrupted tests conducted at various strain paths and equivalent strain levels. Dashed curves correspond to the second deformation step of non-linear strain paths. Equivalent von Mises strain reached, is designated for each curve.

and polished with coloidal silica for approximately 45 mins. Before removing from the polisher, the specimens were cleaned on the polishing disk with running water for approximately 15 mins. Subsequently, the mounted specimens were affixed (using silver paint and super glue) onto aluminum stubs. For suitable conductivity, the surface of the acrylic was completely covered with silver paint; this substantially increases the area of the specimen touching the SEM stage, and prevents charging.

Results obtained from EBSD highlight the strain path sensitivity of the examined material. In Fig. 4.20, the microstructures of strain paths III and IV are compared, in terms of grain orientation and band contrast. Band contrast is used in the current Section, to identify the formation of deformation twin boundaries. Strain path IV incorporates two deformation steps: a pre-straining via rolling (Fig. 4.20,b,e) and a reloading equibiaxially (Fig. 4.20c,f). It is easily observed that intragranular curvature, demonstrated via colour gradients in the orientation maps, is significantly higher in the cold rolled specimen (Fig. 4.20b) in comparison to the equibiaxially deformed one (Fig. 4.20a), for the approximately the same amount of equivalent strain ($\varepsilon_{\mathrm{VM}} \approx 15\%$). Additionally, from the band contrast maps, a few thin deformation twins appear for the equibiaxial case, preferably in grains oriented with $\langle\bar{1}12\rangle$ ||ND (ND is specimen plane normal) and $\langle\bar{1}13\rangle$ ||ND (magenta colour) plane. In contrast, twinning activity appears to be notably higher for the rolled specimen, with multiple grain orientations leading to deformation twin generation. Twins in this case are also wider and can be easily spotted in the orientation map.

Non-proportional loading incorporating rolling followed by equibiaxial tension, results in a highly deformed microstructure, as it can be seen in Fig. 4.20,c,f. The overall band contrast is substantially lower, all grains demonstrate high intragranular curvature and notable thickening of the deformation twins is observed. Twinning here is also promoted in grain orientations in which for the previous deformation step, it was not preferable (for example grains oriented with planes between $\langle\bar{1}11\rangle$ ||ND

and ⟨011⟩ ‖ND - ‘blue grains’).

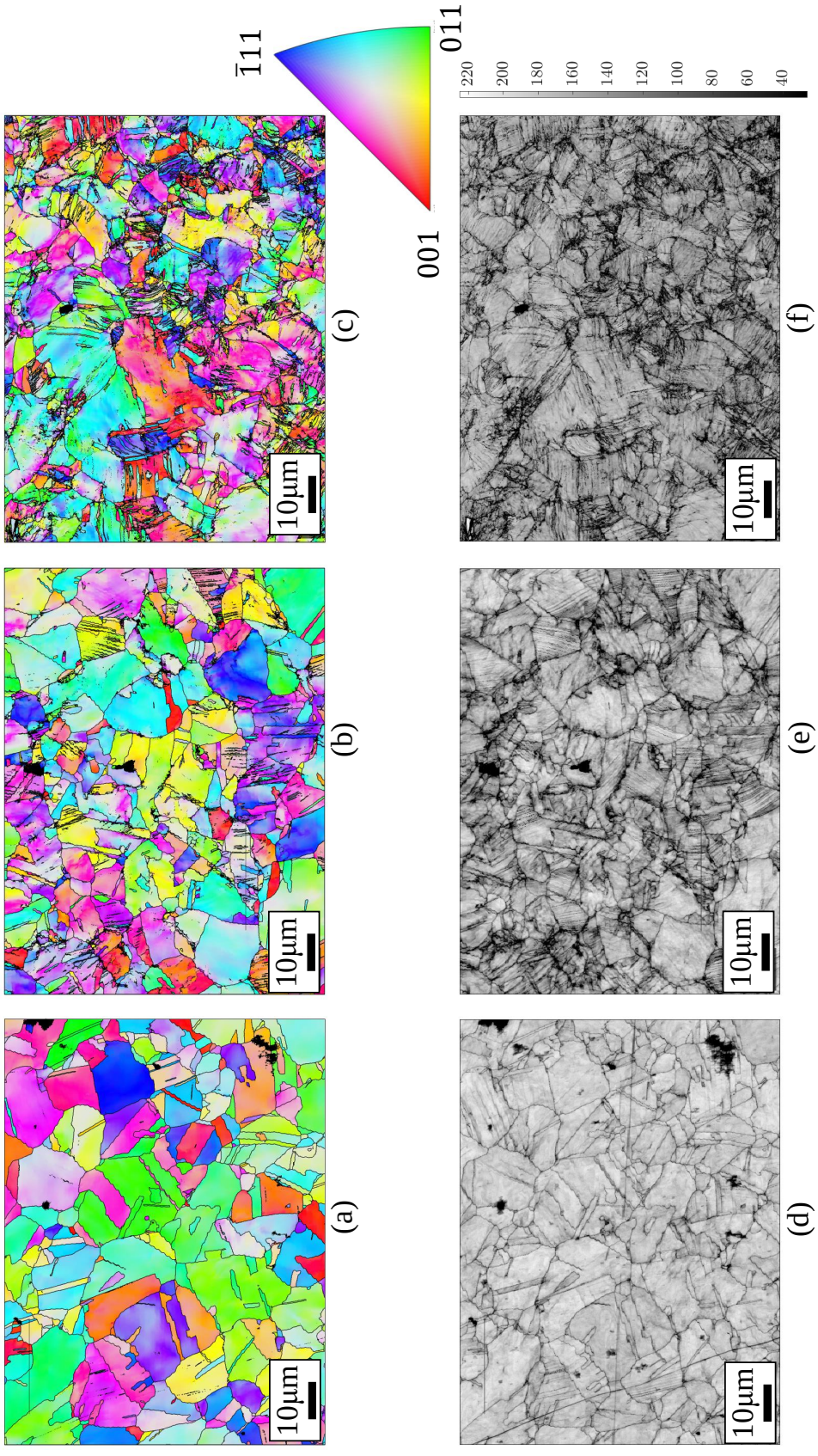

Figure 4.20: Orientation and band contrast maps for strain paths: (a,d) III, (b,e) IVi and (c,f) IV. Colour-bar limits are the same for all band contrast maps.

Band contrast is used here as an indicator of high deformation, as high intragranular curvature, or deformation twinning, can result in an overall lower band contrast per grain. The relationship between band contrast and grain orientation is examined in Fig. 4.21, for the strain paths III, IVi and IV, where the inverse pole figures are plotted, and a colour-map is used to indicate the band contrast values. A higher band contrast (better electron image quality) can indicate less deformed microstructure and vice versa. Colour-map limits are the same for all the examined strain paths.

Equibiaxial deformation up to $\varepsilon_{\mathrm{VM}} \approx 15\%$ (Fig. 4.21a) resulted in an overall high band contrast and a slight increase in the fraction of grains with $\langle 011 \rangle \parallel \mathrm{ND}$. However, reliable conclusions about texture cannot be made from such a small number of grains. This uniformly distributed high band contrast indicates low deformation within the grains. Contrariwise, for a similar equivalent strain, strain path IVi (Fig. 4.21b) leads to higher band contrast for specific grain orientations, indicating that those orientations (shown with red circles in figure), do not accommodate a large amount of deformation. This means that those orientations are characterised by lower GND accumulation and/or limited twinning activity. A change in the strain path, which is in this case plane strain (equivalent to cold rolling) to equibiaxial, completely eliminates this effect and results in an overall low band contrast, regardless the orientation. This uniformity in the low band contrast can be directly associated to the failure of the corresponding specimen, as no grain orientation can further accommodate plastic deformation.

Specimens deformed according to strain paths I and II (near uniaxial and plane strain respectively) were also examined, at a lower level of equivalent strain ($\varepsilon_{\mathrm{VM}} \approx 10\%$). Microstructures of the aforementioned strain paths are shown in Fig. 4.22. One can easily observe that, in comparison to the maps of Fig. 4.21, twinning activity is significantly lower and band contrast is notably higher. Higher intragranular

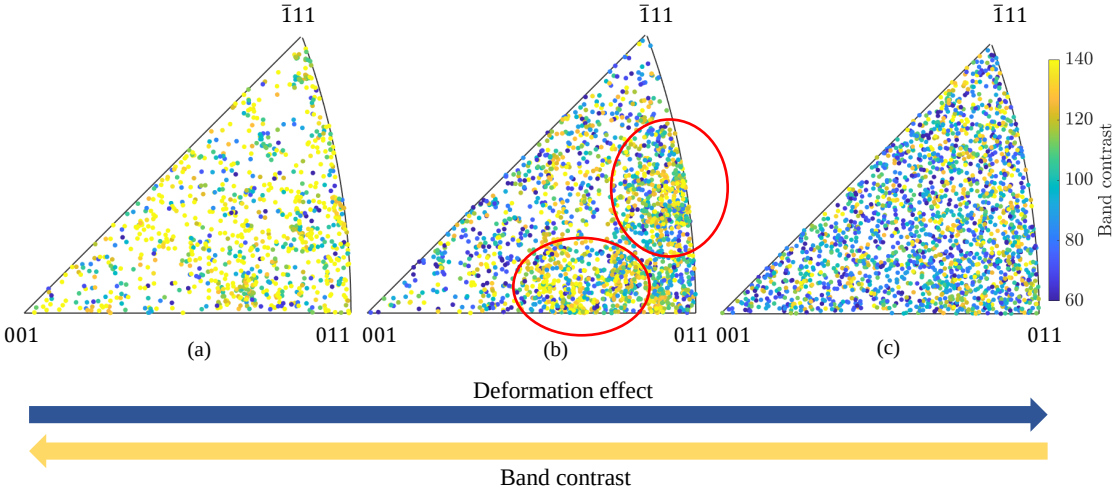

Figure 4.21: Grain orientation vs band contrast for strain path (a,d) III, (b,e) IVi and (c,f) IV. Designated are areas with high band contrast, indicating less deformed grains.

curvature is observed in the case of plane strain, evidently observed as a colour gradient within some grains (Fig. 4.22). Almost no deformation in the microstructure is observed in the uniaxial case. Grain Orientation Spread (GOS) was used to make this result clearer. GOS for each pixel is calculated from the average of misorientation angles to the grain mean orientation, and is an indicator of a deformed microstructure by pointing out grains with high intragranular curvature. It can be observed that in the case of plane strain, the GOS is much higher than the uniaxial case, for most grains (see Fig. 4.22f and 4.22e respectively).

As discussed above, very few deformation twins can be observed in the band contrast maps for strain paths I and II (Fig. 4.22c and 4.22d) in comparison to maps obtained for strain paths III, IV and V, which were shown earlier. Mechanical twins are indicated with red arrows. It is expected, however, that twinning occurs much earlier in plastic deformation, but the available resolution is not high enough to allow their clear observation. An increasing strain, results in thickening of the twins

and therefore makes their observation much easier. Additionally, slight charging of the specimens, impeded clear twin observation. For example, plane strain (Fig. 4.22c) results to twinning some grains (top-right) which appears to be very dull in the band contrast map. Overall, slightly more deformation twins are formed during plane strain than uniaxial deformation.

The effect of SPCs is also presented in Fig. 4.23 in terms of GND density and band contrast, where the microstructures of non-proportional strain paths are presented. The first rows include maps obtained from the rolling $\rightarrow$ equibiaxial strain path, and the second from the uniaxial $\rightarrow$ equibiaxial strain path. From the first deformation step (column 1), it is seen that the effect of cold rolling on the microstructure is more significant in the cold rolling case compared to the uniaxial case. GND densities are notably higher for the first compared to the latter, and multiple deformation twins are observed. Fewer deformation twins can be seen for the uniaxial pre strain. Such microstructure differences can explain the increased YS recorded during re-loading, in the case of the rolling pre-strain, compared to the uniaxial pre-strain (see Fig. 4.18). High GND densities are observed at grain boundaries as well as the middle of the grains in the cold rolling case, while in the uniaxial case they are localised closer to the grain boundaries.

During the second deformation step, the effect of SPC becomes apparent. For rolling pre-strain, deformation twinning occurs in all grains and GND density increases significantly. All grains are saturated with GNDs, an indication that no further deformation can be accommodated; thus the specimen fractures. For the uniaxially pre-strained specimen, twinning activity increases significantly during the second deformation step, even though the final equivalent strain is lower than the rolling pre-strain case ($\approx$ 10% vs $\approx$ 15% respectively). In contrast with the rolling pre-strain, uniaxial pre-strain leads to localisation of high GND density in some grains, while the rest of the grains exhibit relatively low GND density (see

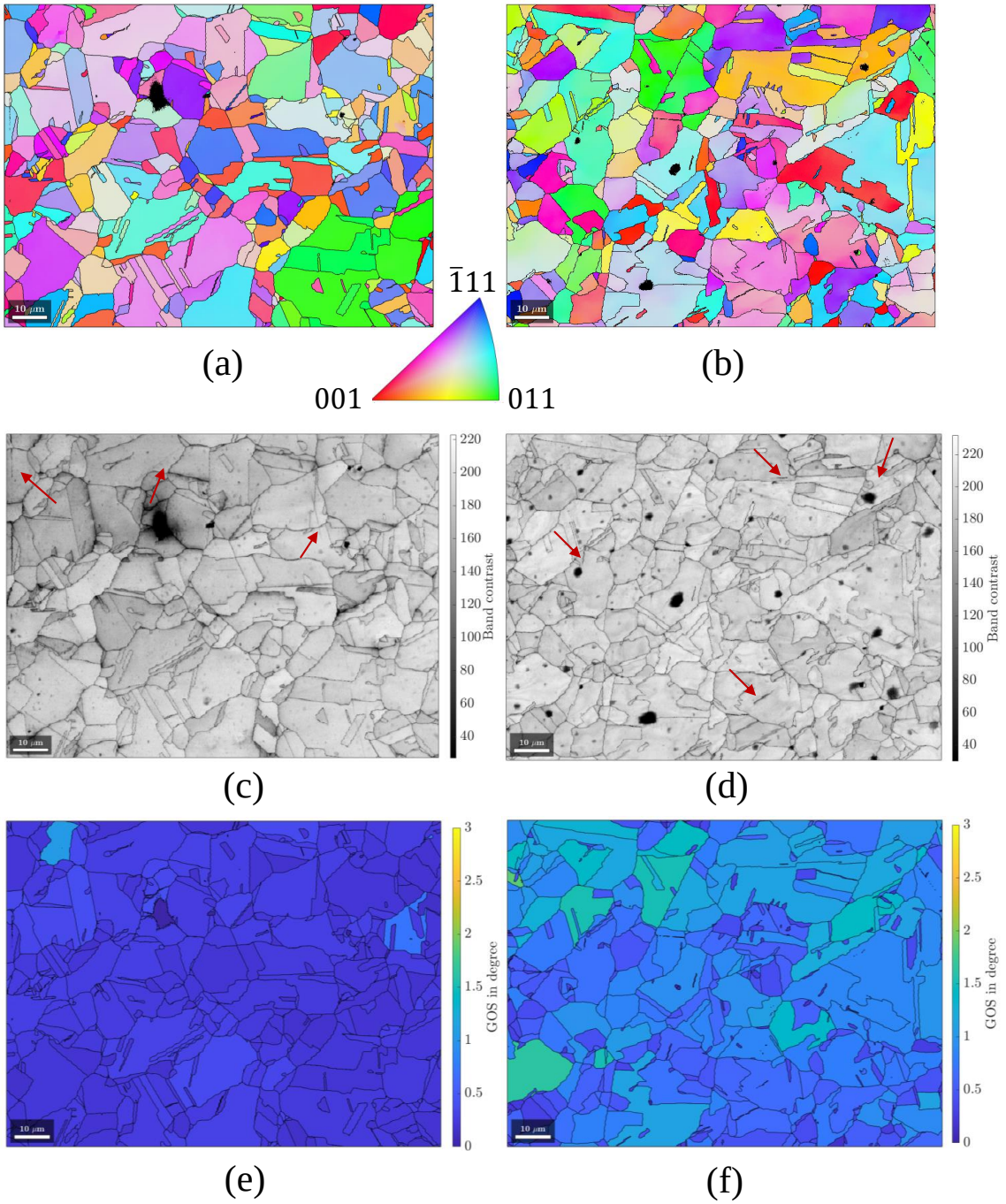

Figure 4.22: Orientation, band contrast and GOS maps for specimens subjected to strain paths I (a,c,e) and II (b,d,f). A few deformation twins are observed, indicated in the band contrast maps, with red arrows.

Fig.4.23h).

4.8 Discussion

4.8.1 Miniaturised testing setup

The primary benefit of employing a miniaturised biaxial testing setup resides in the reduced volume of material used for biaxial testing. This can reduce both the cost and material waste. The small size of the specimens can also facilitate non-proportional deformation examination, something that is more difficult when using 200 mm sized specimens (especially when the SPC incorporates uniaxial pre-strain). Additionally, its adaptability within the uniaxial tensile rig makes it a very attractive option for use in a smaller scale lab environment in contrast to the standard sized Marciniak test which is more suited for industrial scale applications. Also, the small diameter of the specimens makes the deformation to SEM process faster, as no machining of specimens is required, as part of the sample preparation for SEM examination.

Despite the numerous advantages associated with the utilisation of a miniaturized test setup, it has been demonstrated to entail certain drawbacks. The smaller specimen gauge and the low thickness means that mechanical behaviour is the result of only a few hundreds of grains, which can lead to high deviations especially for uniaxial tension specimens. Additionally, any deviations from the nominal specimen geometries, introduced from machining, have a large effect on strain development during deformation. Consequently, equibiaxial deformation specimens have exhibited superior repeatability compared to uniaxial ones.

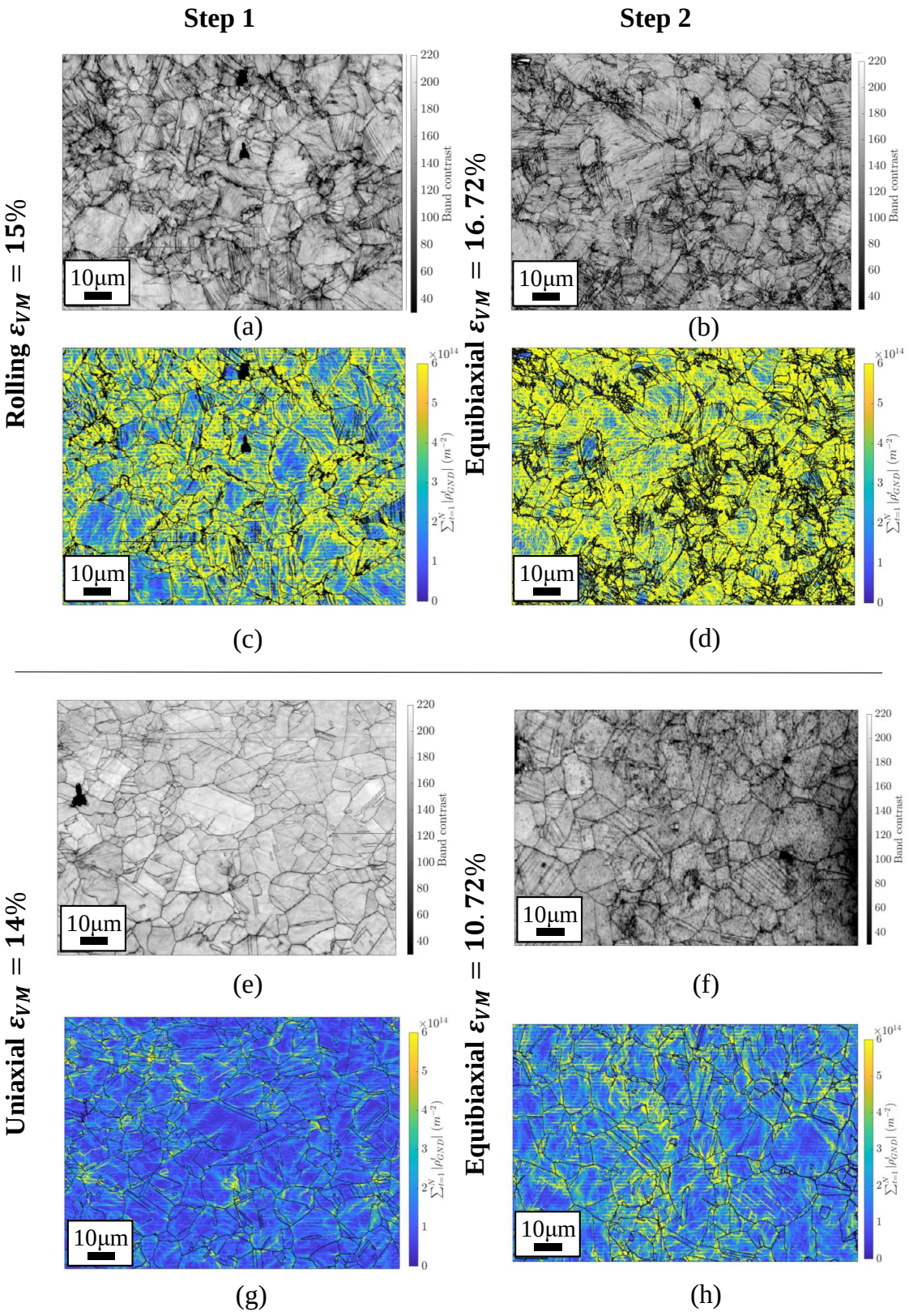

Figure 4.23: Band contrast and GND maps for non proportional equibiaxial loading. (a-d) Rolling pre-strain with $\varepsilon_{\mathrm{VM}} = 15\%$ and (e-h) uniaxial pre-strain with $\varepsilon_{\mathrm{VM}} = 14\%$.

Another weakness of the testing setup showcased within this chapter is the use of a single camera for capturing specimen deformation. A single camera system does not account for out-of-plane deformation, thus any curvature within the specimen surface would lead to inaccuracies in the measured strains. Additionally, the system used in this study, does not have the ability to auto-focus. The correction method proposed by [138] to compensate for the magnification effect occurring during out-of-plane movement, is only valid as long as the image remains out of focus. Here the camera depth of field was 1.39 mm, so we were limited to accepting strain measurements only within a punch displacement range of 0 to1.39 mm.

4.8.2 Microstructure and mechanical behaviour under SPCs

Fig. 4.20 revealed a strong dependence of twin formation on strain path and grain orientation. Equibiaxial deformation, which led to multiple grains aligned with [011] ‖ND, limited twin formation in comparison to cold rolling (equivalent to plane strain) condition. Twin formation for equibiaxial deformation is inhibited for the aforementioned grain orientations, while it is enhanced during cold rolling, where the fraction of [011] ‖ND orientations is limited. An increase of the [011] ‖ND fibre during equibiaxial deformation [68, 70] or uniaxial compression [139] has been previously reported and correlated with a decrease in twinning activity. The present results are thus in good agreement with the previous observations.

From the EBSD maps of Fig. 4.20 it is not obvious whether the rolling → equibiaxial SPC enhanced deformation twinning. Most of the grains during both rolling and the subsequent equibiaxial deformation contain multiple deformation twins. Interestingly, twin growth is promoted after the SPC (twins are notably bigger in after the SPC) and twin boundaries appear ‘distorted’. This twin ‘distortion’ has been previously attributed [140] to interactions of twins with dislocation substructures,

after a SPC introduced by multi-axial forging. Given that equibiaxial deformation does not promote twinning, it is possible that twins shown in Fig. 4.20c and 4.20f are already formed during the rolling pre-straining step.

A significant increase in the GND densities was recorded after the aforementioned SPC (see Fig. 4.23d) which could further support the above argument. In contrast to rolling pre-strain, uniaxial pre-strain did not introduce many GNDs (Fig. 4.23g). Additionally, only a few deformation twins were observed during uniaxial pre-strain (Fig. 4.23e) in contrast to rolling pre-strain. Information about discrepancies of twinning between uniaxial and plane strain deformation on TWIP steels is very limited. In a work from Lü et al. [141] a higher fraction of deformation twins was observed for uniaxial tension in comparison to plane strain which is not in good agreement with the results presented here. It appears that for the uniaxial $\rightarrow$ equibiaxial strain path twinning is promoted during the second deformation step, which is a peculiar result, given that it is known that equibiaxial deformation inhibits twin formation. However, given that GND densities measured for uniaxial deformation are also low, it is expected that the shear stress accommodated by the lattice may not be adequate to promote deformation twinning during the first deformation step, but as strain increases, many twins are generated during the second deformation step. As twins are generated during the second deformation step, and as GND densities remain relatively low (at least lower than for rolling pre-strain), twin boundaries do not show any distortion like the one observed for the rolling$\rightarrow$equibiaxial strain path.

According to Fig. 4.18, an increase in the yield strength with a simultaneous decrease in ductility in comparison to proportional equibiaxial deformation, was observed for the second deformation step of the rolling $\rightarrow$ equibiaxial strain path. Microstructure examination revealed a high twinning and GND activity after pre-straining via rolling, which can explain the overall increased strength of the cor-

responding specimen. The significant increase in GND density for $\varepsilon_{\mathrm{VM}} = 16.72\%$, which was globally high for all grain orientations, can explain the early fracture of the pre-strained compared to non-pre-strained specimen. On the other hand, uniaxial pre-straining does not introduce a remarkable influence in the yield strength, however, it results in important ductility and UTS reductions, which cannot be explained by the microstructure evolution. As shown in the previous chapter, high GND accumulation far from the grain boundaries can indicate early fracture of the specimens. In this case, GND densities are mostly still localised close to the grain boundaries and are, in general, remarkably lower than the GND densities measured for the rolling pre-strained specimens. One possible reason could be the stress localisation at a subgrain level, introduced due to the more abrupt SPC (uniaxial to equibiaxial rather than cold rolling to equibiaxial). However, this argument cannot be supported by the present data and further investigation is required to explain this effect.

4.9 Summary

In this chapter a miniaturised version of the standard Marciniak test was developed to facilitate biaxial loading with simultaneous DIC measurements via a single camera. Specimens of different geometries were fabricated from DX54 and TWIP steel sheets. Results from the measured strains follow the typical major vs minor strain behaviour expected for the specimen geometries used, however, effects of non-linearity in the strain paths examined, were more pronounced for the miniaturised test rig in comparison to the standard-sized test rig. Good repeatability of the load-displacement measurements was observed. Highest deviations were observed for the uniaxial specimens, which were attributed to a small number of grains in the narrow gauge width.

The miniaturised setup used here presented the following limitations: specimen deformation is limited to low strains due to 1) loss of focus after a 1.39 mm displacement of the specimen surface and 2) strain localisation occurred far from the central area of the specimens. Additionally, microstructure examination was proven challenging using the mounting method described earlier, as charging of the specimens impeded a good observation of fine features like deformation twins. This was taken into account before any result interpretation.

Interrupted tests were conducted on TWIP steel specimens subjected to proportional (uniaxial, plane and equibiaxial) strain paths and non-proportional strain paths (rolling $\rightarrow$ equibiaxial and uniaxial $\rightarrow$ equibiaxial). Microstructure examination was conducted via EBSD, where the different characteristics of each one of the deformed specimens were revealed. Cold rolling at $\varepsilon_{\mathrm{VM}} = 15\%$ resulted in a highly deformed microstructure characterised by high GND densities, low band contrast and the formation of multiple deformation twins. Twinning activity appeared to be the highest during cold rolling followed by the uniaxial and equibiaxial strain paths. [011] ‖ND appeared to be the least favourable for twin formation. After a rolling $\rightarrow$ equibiaxial SPC, twins formed during the first deformation step exhibited considerable growth and distortion. Distortion was associated with twin-dislocation substructure interactions. The same effect was not apparent for a uniaxial pre-strain.

Chapter 5

Non-proportional loading effect on a TWIP steel studied via neutron diffraction

This chapter is the result of collaborative work. Individual contributions are listed below:

Anastasia Vrettou: Methodology, Data collection (in-situ neutron diffraction and EBSD), Data analysis, **Dr James Ball**: Data collection (in-situ neutron diffraction), **Mohammed (Wakib) Said**: Data collection (in-situ neutron diffraction), **Dr Jan Capek**: Data collection (in-situ neutron diffraction), **Dr Efthymios Polatidis**: Data collection (in-situ neutron diffraction), **Dr David Collins**: Conceptualisation, Supervision, Funding acquisition

5.1 Introduction

In the previous chapter, the effects of strain path and SPCs on the mechanical properties and microstructure of a high Mn TWIP steel were examined, via a com-

bination of the modified SPT and EBSD. A notable strain path dependence of the microstructure to the macroscopic response was observed, which was further influenced by the SPC abruptness. In this chapter, the same alloy was examined via in-situ time-of-flight neutron diffraction in order to facilitate further, in-depth investigation of the microstructure evolution during proportional and non-proportional strain paths. This investigation included examination of the lattice strains, normalised peak intensity changes and peak broadening evolution in-situ, where data were collected from a probed volume covering thousands of grains. Post-mortem, the final microstructure was further investigated via EBSD, which allowed localised information about the microstructure to be obtained.

5.2 Experimental process

5.2.1 The examined material

The same alloy used in the previous chapter was examined here via neutron diffraction. A hot-rolled plate of the TWIP steel, with thickness of 10 mm, provided by ThyssenKupp, was used. To confirm the similarity of the composition with the thinner plates used in the previous chapter, specimens from the thick plate were measured using WDS on a JEOL 7000 FEG SEM. The conditions replicated those described in Section 4.2.1(20 kV voltage and 14.9 nA beam current). Results shown in Table 5.1 confirm a high similarity between the two plates.

The microstructure of the thick plate was examined via EBSD on the same SEM, using a 30 kV voltage. The EBSP binning was set to 4×4 and the step-size to 0.6 µm. An average grain size of 15.94 µm, was obtained using the method described in Section 5.1.1. This is very close to the 14.76 µm grain size obtained

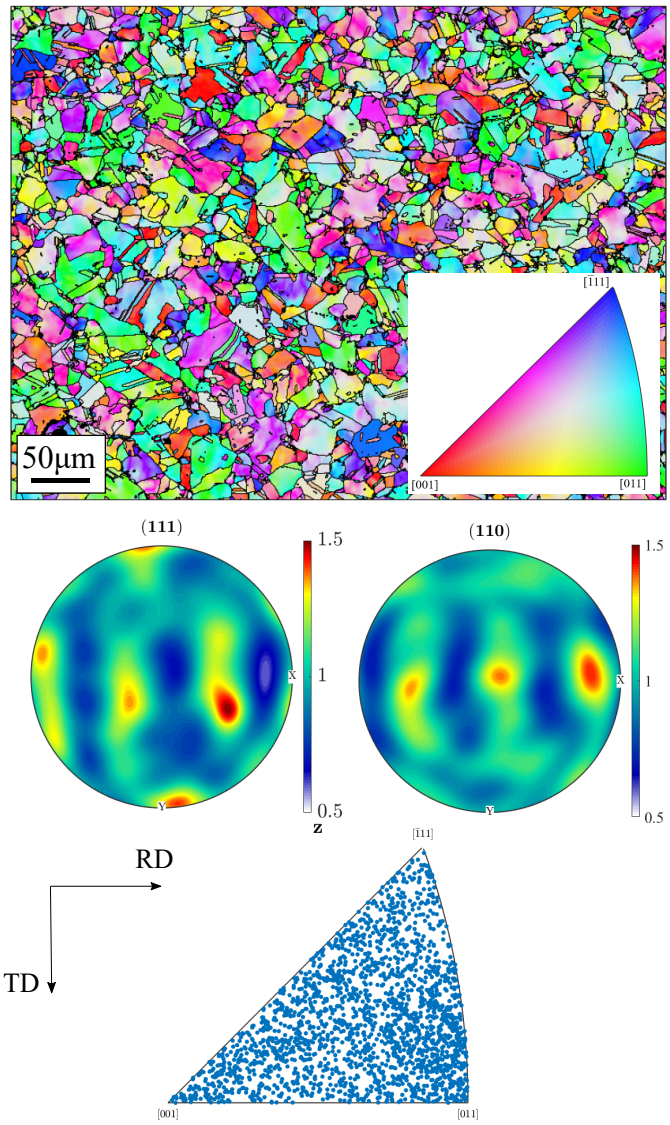

Figure 5.1: Z-axis orientation map (top), (111) and (110) pole figures (middle) and z-axis inverse pole figure (bottom). RD and TD lie on specimen plane.

Element	Fe	C	Mn	Al	Si	V	Cr	Ni	Ti	Cu
wt. %	Balance	$0.30 - 0.60$	19.15	1.08	0.46	0.02	2.55	0.31	0.1	0.06

Table 5.1: Chemical composition of the examined TWIP steel. The carbon content was provided by ThyssenKrupp as it could not be accurately measured in-house.

post-annealing at 900°C (conditions for the SPT specimens), hence a comparison between the mechanical properties of specimens from the two chapters is valid. The as-received material possesses a very weak Brass-type texture ($\{110\}\langle 1\bar{1}2\rangle$), as shown in Fig. 5.1. The orientation map shows some signs of deformation, observed as colour gradients within the grains, in the orientation map. This is expected from the prior hot-rolling process during the plate manufacturing.

The as-received TWIP steel sheet was cut into cruciform shaped specimens with a water jet machine, using a geometry specifically designed for POLDI biaxial load frame[23]. Specimen geometry is shown in Fig. 5.2. It is common that such shape results in the development of high strain concentrations at the corners between the arms and the central area, instead of the specimen center. To compensate for this effect, the central thickness of the specimens is reduced to locally reduce the cross sectional area, thereby creating a region of highest stress in the specimen gauge. Here, thickness of the central area, was reduced to 2 mm. A lower thickness than the one proposed by [23] was used, allowing for high strains to be reached in the central area of the specimens. This is particularly necessary due to the high work hardening rate of the examined material. However, thinner samples reduces the probed volume from which scattered neutrons / time unit can obtain data, thus high collection times were required to obtain suitable signal to noise ratios.

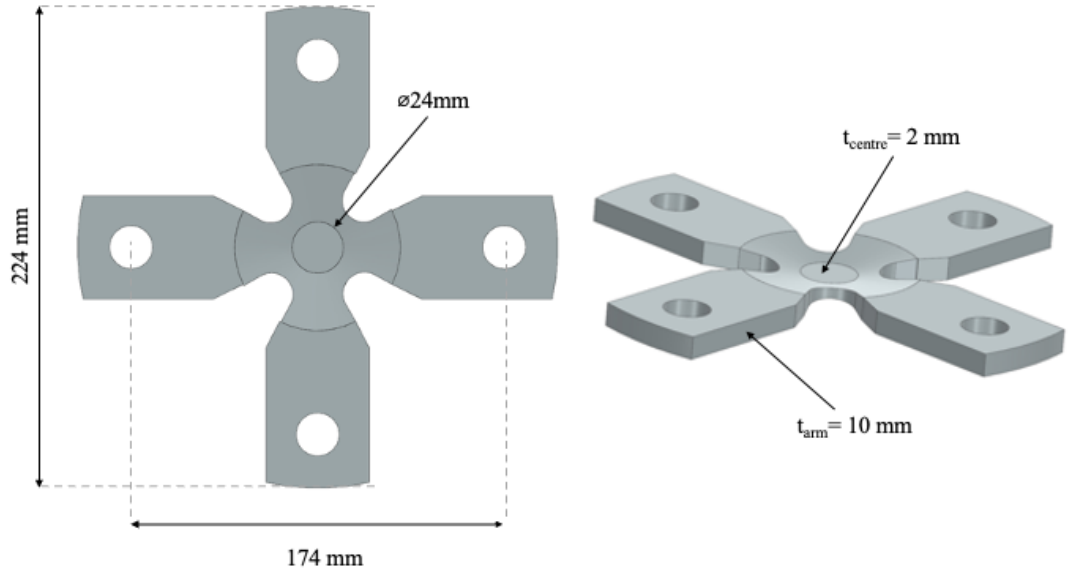

Figure 5.2: Cruciform specimens designed for the POLDI biaxial load frame.

5.2.2 In-situ TOF neutron diffraction and strain measurement

Neutron diffraction experiments were performed at the Pulse Overlap Diffractometer (POLDI), which is part of the Swiss Spallation Neutron Source (SINQ) at PSI, Switzerland. The experimental setup is presented in Fig. 5.5. The test rig includes four main parts: a biaxial load frame, a dual optical camera system, the incident beam and the detector. The biaxial load frame, manufactured be Zwick, has a load capacity of $F_{1,\max}$ =100 kN on the vertical axis and a load capacity of $F_{2,\max}$ =50 kN on the horizontal axis. The detector was fixed at a 45° to the specimen plane and at 90° to the incoming beam. The Aramis dual camera system facilitates 3D-strain field measurements. During in-situ deformation, specimens were subjected to interrupted loading at a rate of 40 N/s. The acquisition time for each diffraction pattern was 23 min, at predefined load intervals, during which the load was held constant. The incident beam had a cross-section of $3.8 \times 3.8\,\mathrm{mm}^2$ and was normal to the central specimen area. Specimens were spray-painted in a black and white stochastic pattern, as described in the previous chapter. Two cameras were placed at approximately ±15° to the sample plane normal; images were used to calculate

strain components along the specimen plane, from the central area of the specimen (area probed by the beam) at a rate of 1 frame/s. The accumulated plastic strain, or Von Mises strain, was automatically calculated via the Aramis GOM software according to

$$\varepsilon_{\mathrm{VM}} = \overline{\varepsilon_{\mathrm{p}}} = \int \sqrt{\frac{2}{3} \mathrm{d}\varepsilon_{ij}^{\mathrm{p}} \mathrm{d}\varepsilon_{ij}^{\mathrm{p}}} \tag{5.1}$$

where $\varepsilon_{ij}^{\mathrm{p}}$ are the 3-dimensional strain tensor elements $(i, j = 1, 2, 3)$. From the calculated data, the mean average Von Mises strain ($\varepsilon_{\mathrm{VM}}$) was used.

Strain measurement data presented in this chapter were directly provided from the GOM software. Whilst using a non-contact measurement method eliminates displacement measurement deviations due to the instrument compliance to deformation, DIC can introduce different types of errors. Camera positioning and lens distortion can 'distort' the specimen surface images and result in displacement measurement deviations. These deviations can be minimised by frequently conducting appropriate calibration of the optical system. For example, for the experiments described in this chapter, the optical system was re-calibrated when there was any possible movement of the camera or lights during specimen loading. Additionally, the lighting itself can be source of error in the optical measurement, as a less bright surface can obstruct accurate measurement of the specimen surface displacements. Between the measurements described here, any contact with the lighting system was avoided to obtain consistent strain measurements. Finally, specimen surface preparation is also crucial in DIC measurements. While spray painting the specimen surface with black spots, which are ideally randomly distributed on a white background, areas of high or low spot density can occur. Nevertheless, Von Mises strains presented here are averaged within the captured region of interest to eliminate these effects.

Paint quality and painted surface roughness play a crucial role in the successful strain measurement. One problem encountered during these experiments was the delamination of the spray paint at high strains. At high levels of deformation cracking of the paint resulted in unreliable strain measurements, thus data obtained in-situ and presented here against strain, are in most cases up to the maximum strain measured with accuracy. However, to estimate the maximum strain reached during deformation, the knowledge of which is necessary for ex-situ result interpretation (EBSD measurements), an approximation method was used. Here, the first and last images of the recorded video were extracted. Images were imported to the Ncorr software, and ε_{xx}, ε_{yy} and ε_{xy} strains were re-calculated, within a circular region of interest. Fig. 5.3 shows the strain distribution for a painted surface that is full of cracks. Far from the cracks, the strain distribution is uniform and corresponds to the 'real' strain of the specimen. To obtain an approximate value for the actual strain of the specimen, a histogram with 10 bins was plotted to summarise the ε_{xx} distribution (see Fig. 5.4). Only strain data obtained from the bin with the maximum number of occurrences was then used for the average strain calculation. The Von Mises strain was then calculated as described in Section 4.4.4. The same process was repeated for the second camera. Differences between the strains from the two cameras were negligible. The final average Von Mises strain was then calculated from the Von Mises strains obtained for the two cameras:

$$\varepsilon_{\mathrm{VM}} = \frac{\varepsilon_{\mathrm{VM,left}} + \varepsilon_{\mathrm{VM,right}}}{2} \tag{5.2}$$

where $\varepsilon_{\mathrm{VM,left}}$ and $\varepsilon_{\mathrm{VM,right}}$ are the strains for the left and right cameras respectively.

The main disadvantage of this method is that, even though strains developed here are in-plane, so a 2D deformation analysis software is safe to use, the slightly angled view of the specimen surface is expected to result in a magnification error, similar to the one described in the previous chapter. A similar compensation to the one

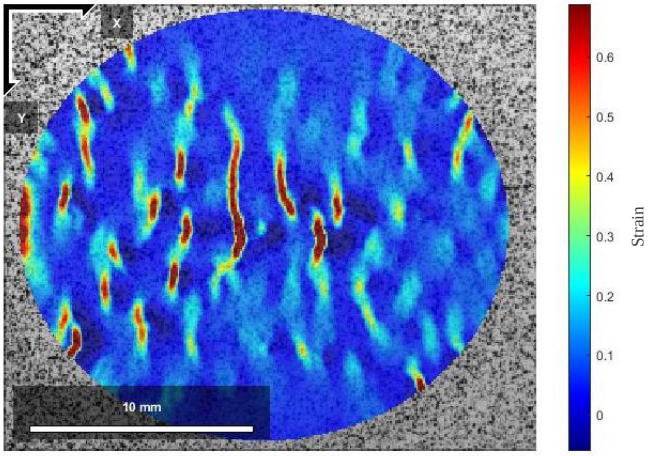

Figure 5.3: ε_{xx} measured via Ncorr for a deformed specimen. Areas of high strain are originated in cracks on the paint and not in the deformed specimen.

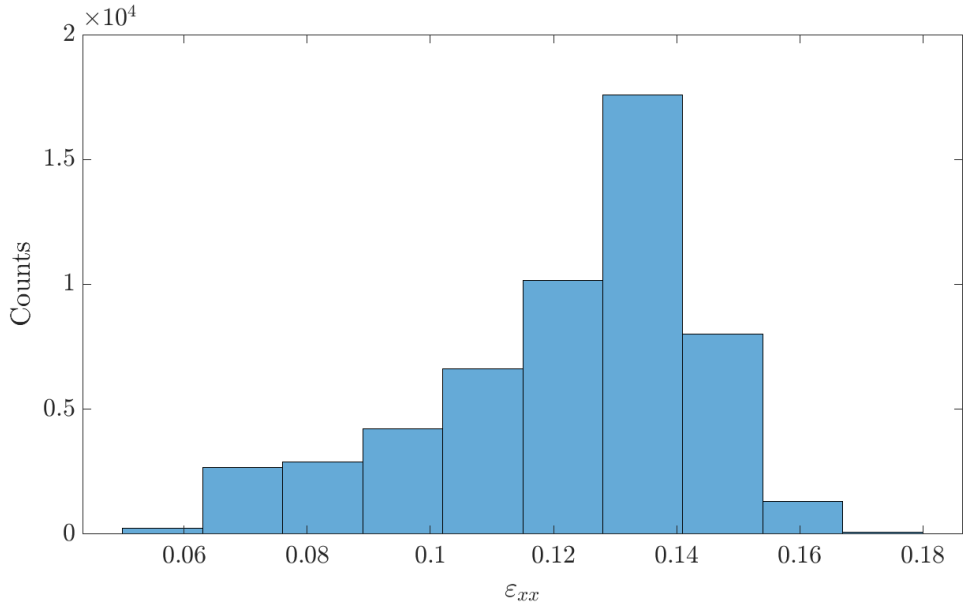

Figure 5.4: Histogram of ε_{xx} as measured from a single camera of the Aramis system.

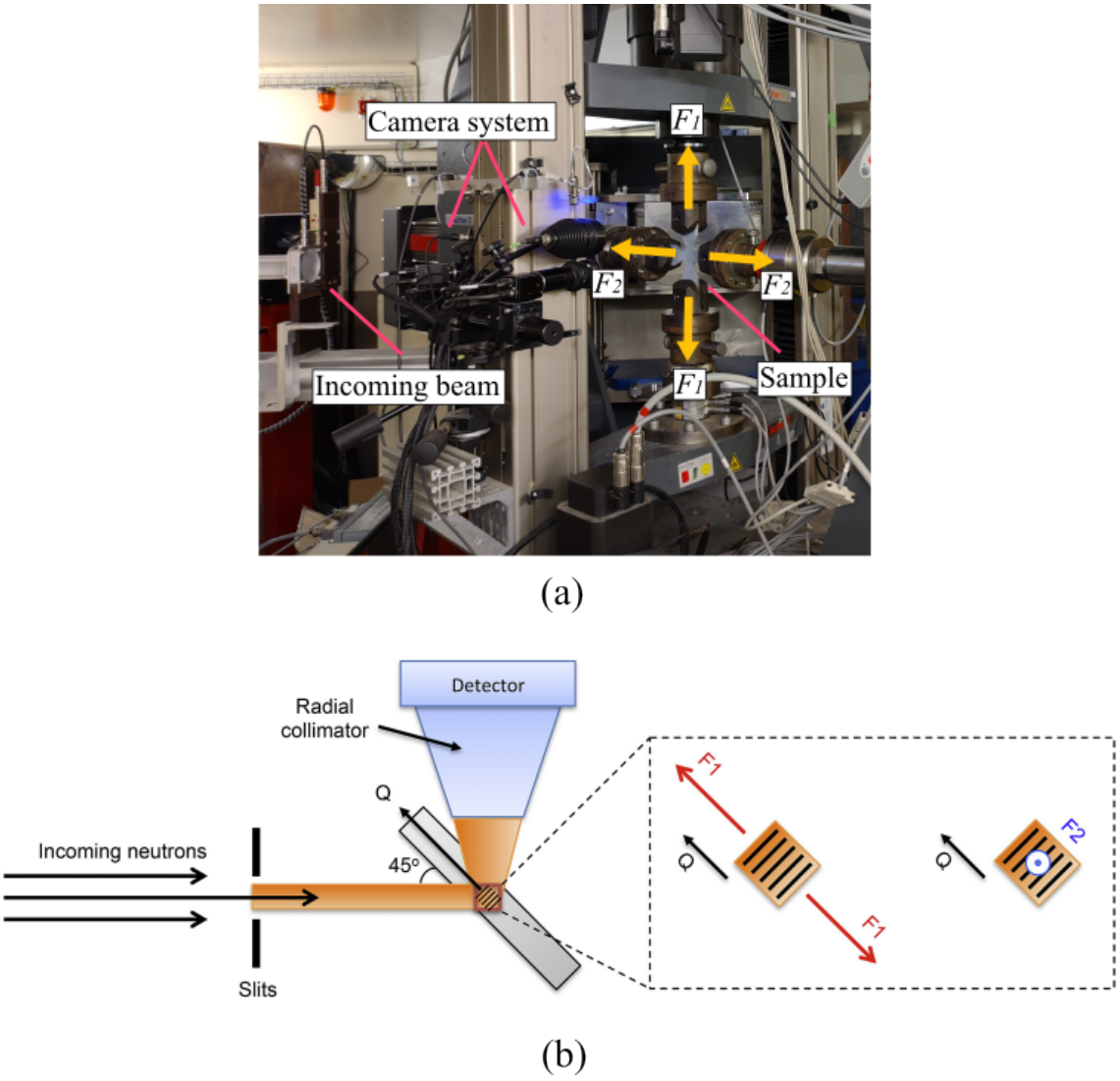

Figure 5.5: Experimental setup at POLDI. (a) Biaxial load frame and dual-camera DIC system. (b) Geometry of the diffracting beam and sample [23].

described in the previous chapter was not possible, since the distance between the cameras and the specimen could not be obtained with high accuracy. However, due to the small size of the area captured, and the high distance between the specimen and the cameras, the error is expected to be small, and for this examination, it can be ignored.

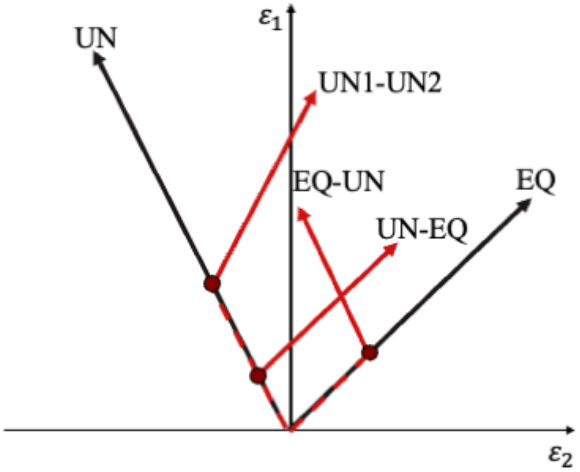

Abbreviation	Process
UN	Uniaxial tension
EQ	Equibiaxial tension
UN-EQ	Uniaxial up to $\varepsilon_{VM} = 1.73\% \rightarrow$ equibiaxial
EQ-UN	Equibiaxial up to $\varepsilon_{VM} = 3.19\% \rightarrow$ uniaxial
UN1-UN2	Uniaxial F1 up to $\varepsilon_{VM} = 3.83\% \rightarrow$ uniaxial F2

Figure 5.6: Strain paths followed for the TOF neutron diffraction experiment. Black is used to illustrate proportional, and red for non-proportional strain paths. Dashed lines correspond to the pre-straining step, which was performed ex-situ.

5.2.3 Strain paths examined

Deformation processes studied in this chapter include proportional and non proportional strain paths. For non proportional strain paths, two deformation steps were used. A microstructure examination was conducted in-situ during the second (final) deformation step, and ex-situ, after completion of the deformation process. Due to the high strength of the material studied, and the limited load capacity of the biaxial load frame, mechanical behaviour and the effect on microstructure were studied at the early stages of plastic deformation, up to approximately 10% equivalent strain. Fig. 5.6 summarises the strain paths used for this experiment. Non-proportional strain paths are designated with red lines, and proportional deformation with black lines. Dashed lines are used to designate the pre-strain step. During the pre-strain, no neutrons were collected to reduce the overall measurement time.

5.2.4 Ex-situ EBSD

The resulting microstructure for all the examined specimens was examined ex-situ via EBSD. Square samples of approximately $15 \times 15\,\mathrm{mm}^2$ were cut from the specimen gauge section, and then mounted in conductive bakelite. The samples were then mechanically ground and polished for approximately 45 min with colloidal silica. For the EBSD data a JEOl 7000 FEG SEM was used. Data were collected at a 70° angle, using a voltage of 25 kV and a 0.12 µm step size. For the diffraction pattern collection, a 4×4 binning and a 10.5 ms exposure time were used. In all cases, specimens were probed normal to the deformation plane (plane of load application).

5.3 In-situ neutron diffraction

5.3.1 Load-strain dependence

The load-strain results measured via DIC are presented here. Fig. 5.7 shows the load-Von Mises strain relationships for all the examined strain paths. Pre-strain values were added to the strains shown here. Curves are grouped so that results from all in-situ uniaxial (Fig. 5.7a) and in-situ equibiaxial (Fig. 5.7b) strain paths are presented in the same plot, to directly compare the effect of pre-strain on the macroscopic mechanical properties. From Fig. 5.7a it is observed that the effect of equibiaxial pre-strain on the resulting load-strain curve (EQ-UN) is far more significant compared to the effect of uniaxial pre-strain on perpendicular direction (UN F1 - UN F2). A slight increase in the yield load is recorded for the EQ-UN strain path, followed by a notable increase in the work hardening rate compared to the corresponding proportional strain path. In contrast, the yield load and work

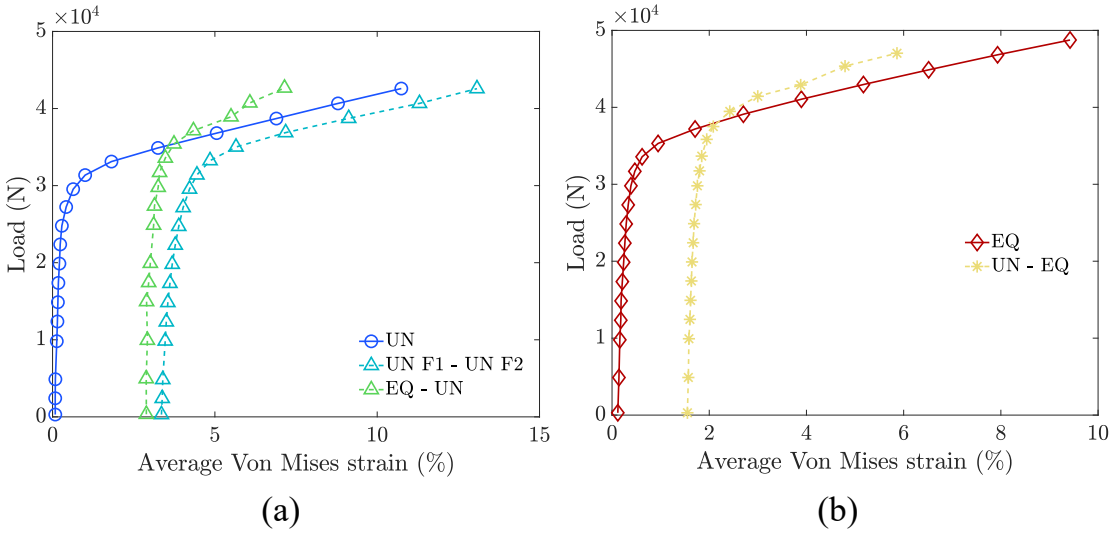

Figure 5.7: Load-average Von Mises strain curves for all the examined strain paths. Only the second deformation step is shown, during which neutron collection took place. In (a) uniaxial strain paths (proportional with solid and non-proportional with dashed lines) and in (b) equibiaxial strain paths are shown. Pre-strain is added to the strain values.

hardening rate of the UN F1 - UN F2 strain path are approximately the same to the UN strain path, indicating that uniaxial pre-strain with a 90° change in the loading axis, has almost no effect in the macroscopic material properties. This can be associated to the abruptness of the SPC, which in case of UN F1 - UN F2 is less significant in comparison to EQ-UN.

In Fig. 5.7b, results from the EQ and UN-EQ strain paths are shown. Comparing the proportional strain paths (EQ vs UN), it is observed that the EQ strain path is characterised by higher yield load and work hardening rate compared to the UN strain path. In contrast to the UN F1- UN F2 strain path, it is observed that the uniaxial pre-strain notably influences the yield strength and work hardening rate of the subsequent equibiaxial loading, even though the pre-strain for the UN-EQ path is lower than the one of the UN F1 - UN F2 path. Further microstructure examination is expected to reveal the mechanisms behind this macroscopic effect.

5.3.2 Effects of deformation in the diffraction patterns

Neutron diffraction patterns were saved in the format of intensity (neutron counts) vs scattering vectors (Q), and were processed using the software MATLAB 2021a. The evolution of the diffraction patterns for increasing strain is shown in in Fig. 5.8 and 5.9, for proportional uniaxial (UN) and equibiaxial (EQ) strain paths, respectively. The normalised intensity is shown here, which has been calculated by dividing the absolute values with the sum of all counts per measurement step. An effect of deformation is evident for both strain paths. As strain increases, the reflections shift towards lower Q, indicating an increase in the lattice spacing d ($Q \propto d^{-1}$). Additionally, an increase in the peak width is observed as strain increases, indicative of an increase in the dislocation density and the deformation twinning generation rate. Finally, peak intensity gradually changes, as a result of texture formation during deformation.

Austenitic steels, in addition to dislocation glide and deformation twinning, often exhibit a martensitic transformation during deformation. The examined material does not show any signs of phase transformation up to $\varepsilon_{\mathrm{VM}} \approx 10\%$, however, even if a small fraction ε-martensite was formed during deformation, the instrument resolution was inadequate for its detection. EBSD measurements also did not indicate martensitic transformation in deformed specimens. Hence, only slip and twinning are accounted for in the microstructure effects discussed in the rest of this chapter.

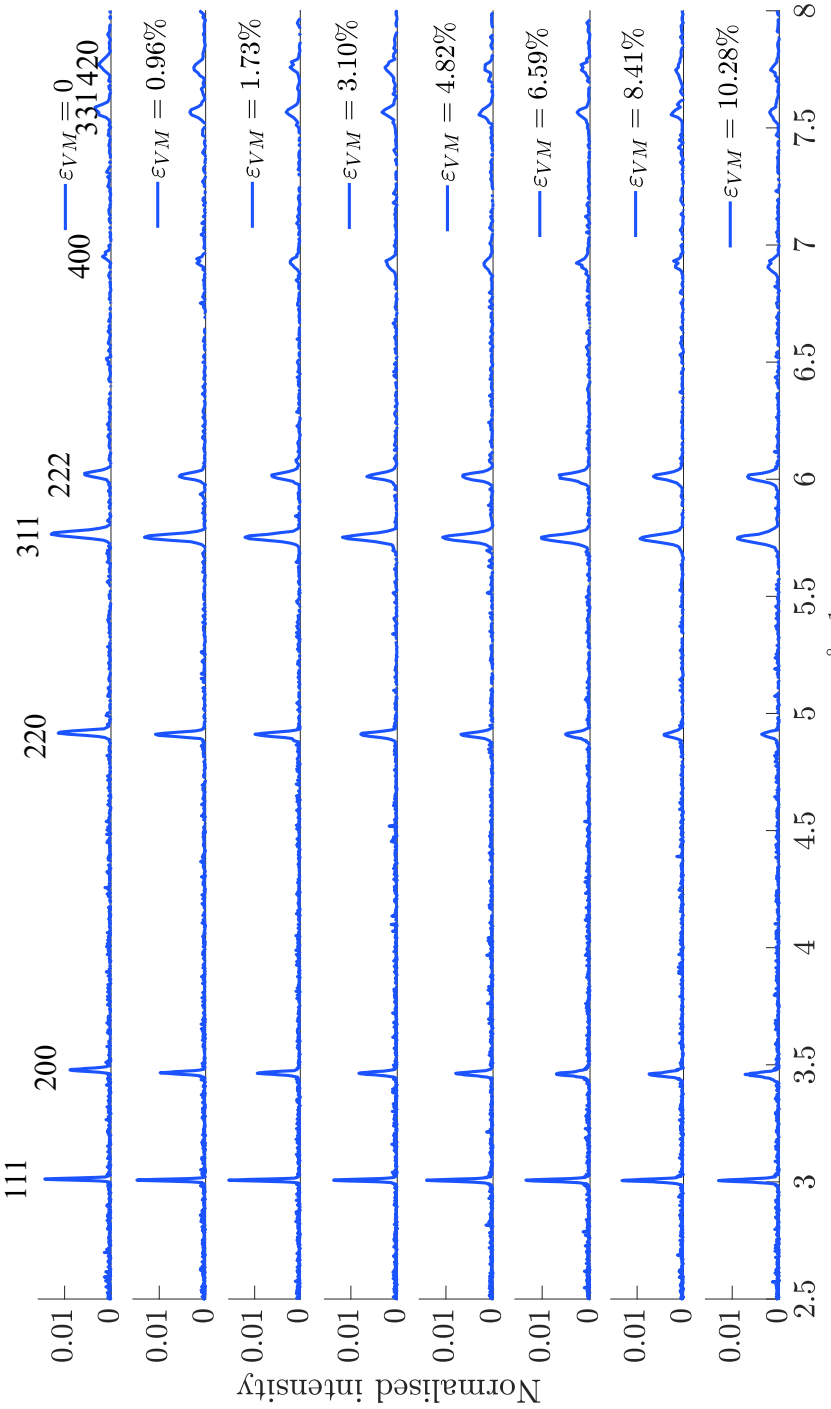

Figure 5.8: Diffraction patterns at increasing strains for UN strain path.

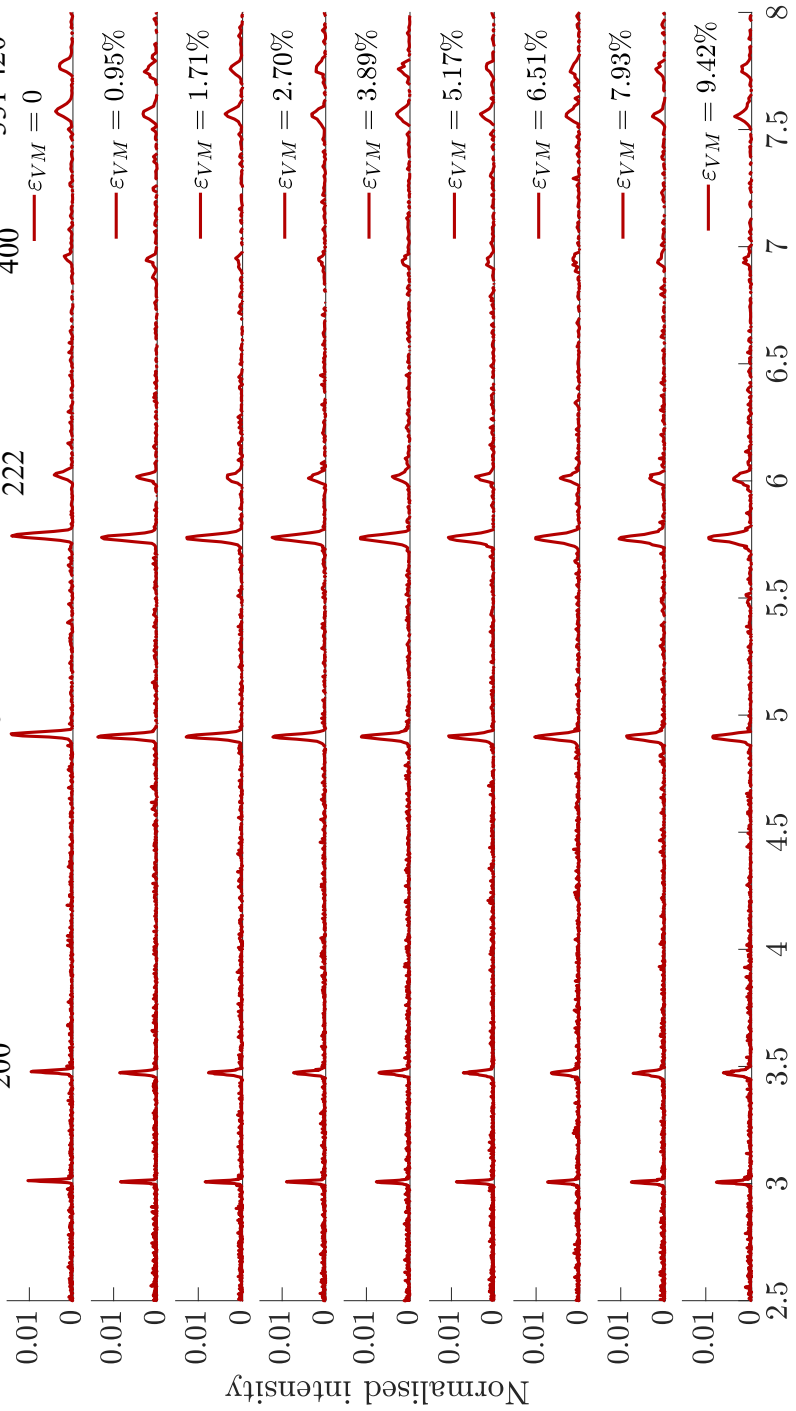

Figure 5.9: Diffraction patterns at increasing strains for UN strain path

5.3.3 Lattice strain

In Fig. 5.10 the lattice strains obtained from the first four diffraction peaks are presented ({111}, {200}, {220} & {311}) for all the examined strain paths. Peaks for higher scattering vectors were ignored as their low intensity and the high background signal prohibited accurate fitting (i.e. high errors were obtained). It is expected that the lattice strains will behave similarly for equivalent planes (e.g. {200} and {400}). Similar to the results presented in Chapter 3, {200} planes are characterised by the highest lattice strains during in-situ uniaxial deformation (Fig. 5.10 a-d), due to their lowest atomic density. In contrast, {111} planes appear to be the least compliant to deformation for all uniaxial strain paths, exhibiting the lowest lattice strain values. Hardening rates for the ε_{111} and ε_{200} are higher than those of ε_{311} and ε_{220}. The latter, exhibits a saturation post-yielding for both the proportional and non-proportional strain paths, where the final deformation step was uniaxial tension.

In agreement with the macroscopic load-strain dependence, the 90° change in the loading direction of the UN F1 - UN F2 strain path, has a weak effect on the lattice vs macroscopic strain relationship. The most notable differences post SPC are seen for the ε_{200}, which is decreased after uniaxial pre-straining, while ε_{220} is only slightly increased. Equibiaxial pre-strain led in all cases to an increase in the lattice strain, however, only the {200} and {311} planes exhibited hardening during the second deformation step, while the other planes resist any further deformation; the lattice strain remains either constant or decreases.

The aforementioned trends differ for equibiaxial deformation (Fig. 5.10). ε_{111}, ε_{200} and ε_{311} are lower than ε_{220}, however, they exhibit higher hardening rates. Uniaxial pre-straining results in a notable increase of ε_{200} and ε_{311} while ε_{111} and ε_{220} remain almost unchanged. Hardening of the latter replicates the behaviour

of proportional equibiaxial deformation, showing an increase post-yielding while ε_{200} and ε_{311} exhibit a rapid decrease, followed by a stagnation in the hardening rate, indicating competing effects of deformation mechanisms taking place after pre-straining.

5.3.4 Peak broadening and intensity changes

In addition to peak shifts linked to changes in the lattice strains during deformation, an increase in the peak broadening is also apparent, illustrating an increase of defects. The peak broadening effect was studied here in terms of FWHM evolution during deformation. In Fig. 5.11 the FWHM vs average Von Mises strain behaviour is presented, for all strain paths. Very distinct differences are shown, especially between uniaxial and equibiaxial strain paths. Uniaxial proportional deformation (UN) resulted in an almost linear increase of the FWHM in respect with $\varepsilon_{\mathrm{VM}}$ for {111}, {200} and {311} planes (Fig. 5.11a,b,d). In contrast, FWHM of the {220} planes, slightly increases post yielding and it soon saturates, at $\varepsilon_{\mathrm{VM}} \approx 5.5\%$. An increase in the FWHM can reflect both the increase in dislocation densities as well as deformation twin generation. However, as twin growth is promoted, and the twin size increases, the mean free path of dislocations decreases and the FWHM is reduced [52]. A saturation in the FWHM of the {111} and {220} planes, is recorded for the EQ strain path, while the {200} and {311} planes show a monotonic increase. This effect could indicate a faster twin growth during equibiaxial in comparison to uniaxial deformation.

To examine discripancies between dislocation densities and twinning for the uniaxial and equibiaxial strain paths, the modified Williamson-Hall plot was used. According to the Williamson-Hall theory, line profile broadening is a combination of broadening originated by the pollycrystalline solid, inversely proportional to the

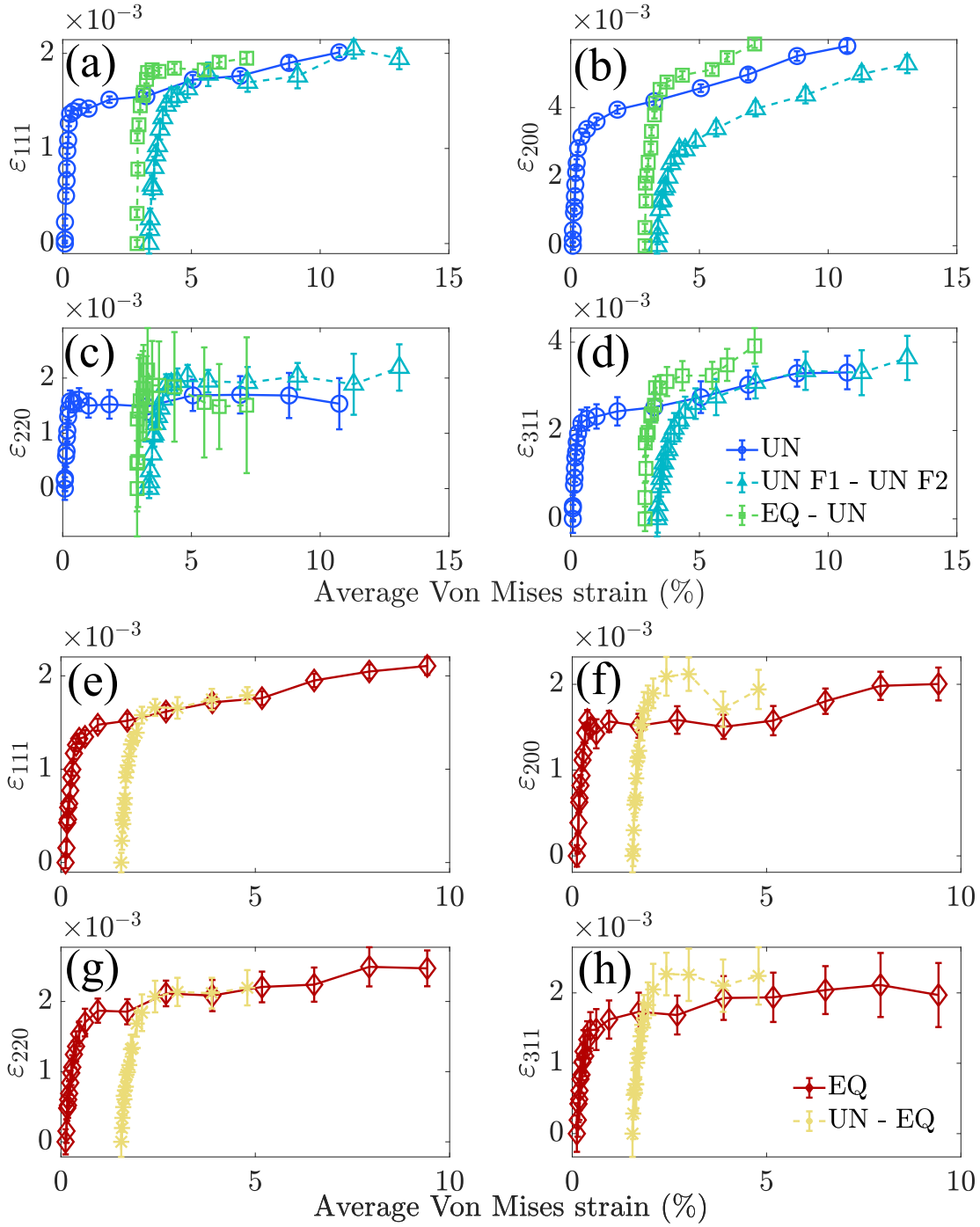

Figure 5.10: Lattice strains as calculated from the first four diffraction peaks vs the average Von Mises strain. Results presented here were obtained from (a-d) uniaxial and (e-h) equibiaxial strain paths, both proportional (solid line) and non proportional (dashed line).

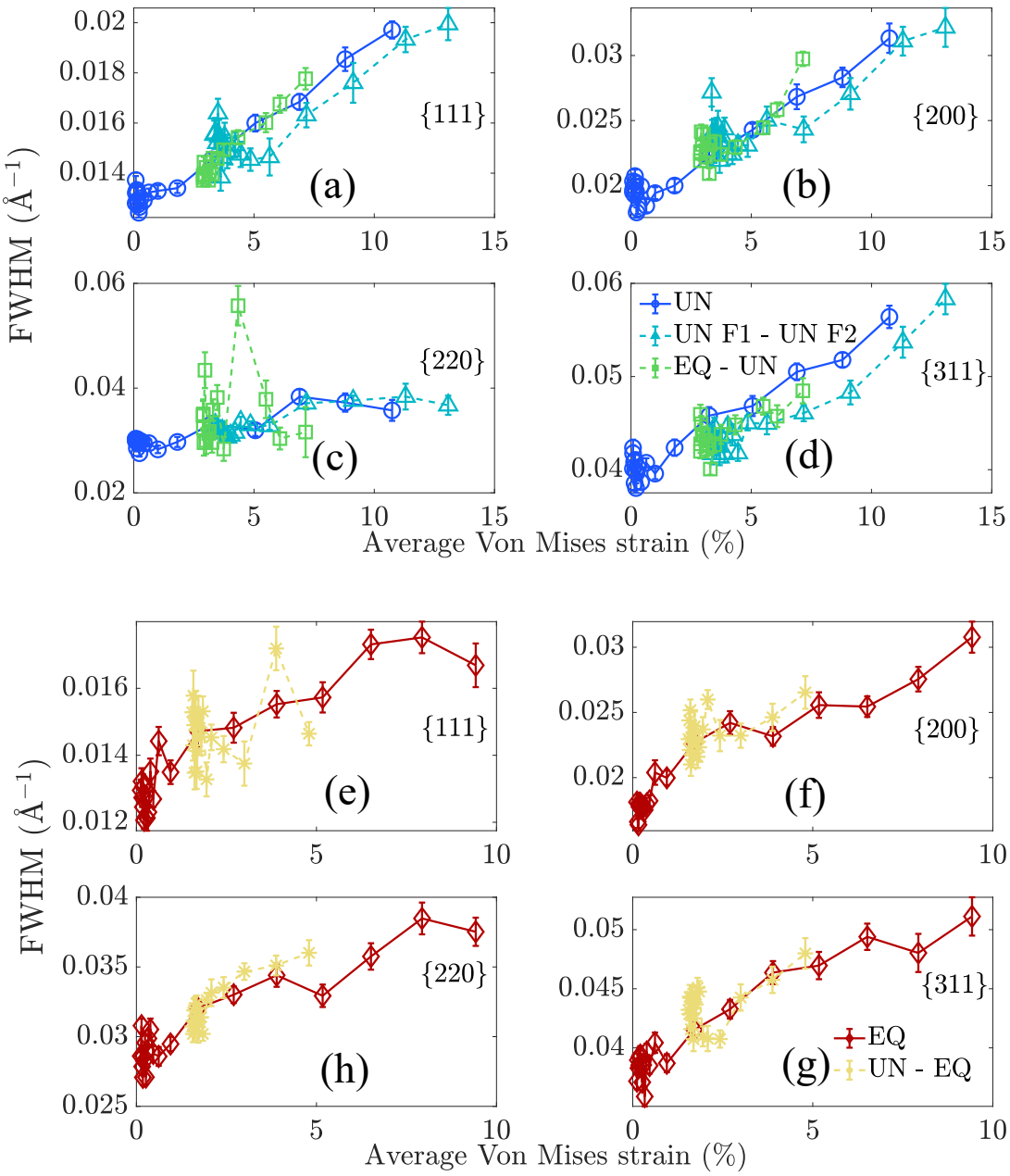

Figure 5.11: FWHM as calculated from the first four diffraction peaks vs the average Von Mises strain. Results presented here were obtained from (a-d) uniaxial and (e-h) equibiaxial strain paths, both proportional (solid line) and non proportional.

average grain size and to the dislocation induced strain field. Simply:

$$\text{FWHM} = \frac{0.9}{D} + \Delta Q_\rho \tag{5.3}$$

where 0.9 is a constant used for cubic crystal structures, D is the average grain size and ΔQ_ρ is the dislocation induced broadening. Equation 5.3 assumes that the instrument induced broadening has been subtracted from the measured FWHM. Ungar and Borbley [142] reached to the following expression via calculating the dislocation induced broadening:

$$\text{FWHM} = \frac{0.9}{D} + A\left(\frac{\pi b^2}{2}\right)^{1/2}\rho^{1/2}(Q\bar{C}^{1/2}) + A^* S^{1/2}\left(\frac{\pi b^2}{4}\right)^{1/2}(Q\bar{C}^{1/2})^2 \tag{5.4}$$

where A and A^* are coefficients related to the dislocation arrangement, and can be only obtained via Fourier analysis, b is the Burgers vector and $\bar{C}$ is the average contrast factor for dislocations. S is a correlation factor related to "two-particle correlations" [142], in the 'sea' of dislocations in the material. An approximation of this value is the variance of dislocation density: $S^* = \langle \rho^{*2} \rangle - \langle \rho^* \rangle^2$.

Ungar and Borbley [143] also calculated contribution of stacking faults and twinning to broadening. By taking into account this contribution, Equation 5.4 can be re-written as

$$\text{FWHM} - \beta' W(Q) = 0.9/D + (\pi A b^2/2)^{1/2}\rho^{1/2}(Q\bar{C}^{1/2}) + \mathcal{O}(Q\bar{C}^{1/2})^2 \tag{5.5}$$

where β' is related to the density of stacking faults and twins, and $W(Q) \propto \sqrt{h^2 + k^2 + l^2}$, where h, k, l are the Miller indices of each diffracting plane.

Using equations 5.4 and 5.5, discrepancies between the strain paths examined here can be investigated. At first, calculation of the contrast factors for the examined material is required. The contrast factors were calculated using the method

$\bar{C}_{111}$	$\bar{C}_{111}$	$\bar{C}_{111}$	$\bar{C}_{111}$
0.1124	0.2365	0.1434	0.1781

Table 5.2: Average contrast factors as calculated for the {111}, {200}, {220} and {311} planes.

described in [144]. According to the aforementioned method, the average contrast factors for the individual reflections for a cubic crystal are dependent on the Miller indices and the elastic constants of the material. The average contrast factor for each diffracting plane can be calculated from

$$\bar{C} = \bar{C}_{h00}(1 - qH^2) \tag{5.6}$$

where

$$q = \alpha^*[1 - \exp(-A_i/b^*)] + cA_i + d^* \tag{5.7}$$

and

$$H^2 = \frac{h^2k^2 + k^2l^2 + h^2l^2}{h^2 + k^2 + l^2} \tag{5.8}$$

The constants a^*, b^*, c and d^* as well as $\bar{C}_{h00}$ were obtained from [144]. The elastic constant ratio, $c_{12}/c_{44} \approx 1$ and the elastic anisotropy $A_i \approx 2$ values were used, obtained from [145], where the above values were calculated for a Fe-18Mn-1.5Al-0.6C alloy, a TWIP steel with a similar composition to the one for the TWIP steel examined in this work. An equal contribution for edge and screw dislocations in broadening was assumed and the contrast factors obtained are shown in Table 5.2.

Via the calculations described above, the modified Williamson-Hall plot was constructed at $\varepsilon_{\mathrm{VM}} = 10.74\%$ for UN and $\varepsilon_{\mathrm{VM}} = 9.42\%$ for EQ strain paths, shown in Fig. 5.12. To remove the effect of instrumental broadening, the vertical axis includes

the values of $\Delta\text{FWHM} = \text{FWHM}_{\varepsilon_{\text{VM}}=0.1} - \text{FWHM}_{\varepsilon_{\text{VM}}=0}$, which represents the difference between the FWHM value at the *unloaded* state subtracted by the FWHM at $\varepsilon_{\text{VM}} \approx 10\%$. From Fig. 5.12a it can be seen that the overall broadening of EQ strain path is higher than the UN one. Considerable scattering is observed, impeding a good parabolic fitting of the experimental data. For reference, the FWHM of a Si powder standard used for calibration of the instrument is also plotted in Fig. 5.12b, revealing the parabolic relationship between the FWHM and Q. A similar parabolic plot is expected for the modified W-H plot, however the instrument settings at the time of the experiments, resulted in high instrument broadening, and only qualitative comparisons can be made using the current experimental data. However, regardless the scattering, the FWHM for the EQ strain path is consistently higher than UN, indicating an increased number of defects for the same strain path.

In addition to broadening, diffraction peak fitting can provide information about texture changes via peak intensity changes. The integrated peak intensity results are presented here, in Fig. 5.13. Results are plotted in the form of integrated intensity changes to remove any discrepancies in the initial texture of the specimens. In contrast to data obtained from X-ray diffraction, information obtained using neutron diffraction is limited to a single macroscopic direction, defined by the scattering angle of the neutrons. The integrated intensity is presented as a function of average Von Mises strain in Fig. 5.13. A rapid increase in the {111} and {200} peak intensities are observed for UN strain path, accompanied by a rapid decrease in the {220} peak intensity, while {311} intensities remain almost unchanged. No significant effects in the peak intensity change are observed after pre-straining for Fig. 5.13a-d. UN F1 - UN F2 strain path, results in a similar trend in peak intensity changes as UN strain path, highlighting that uniaxial pre-straining at 90° does not influence the microstructure development during the second deformation step. This result was also highlighted by broadening and lattice strains for the same strain path.

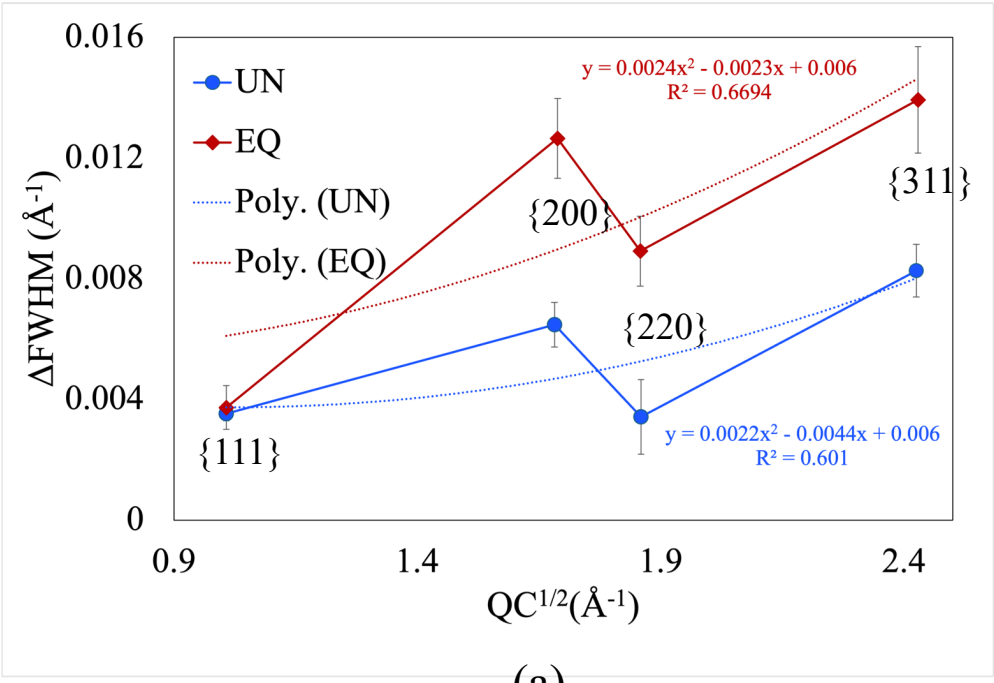

Figure 5.12: (a) Modified Williamson-Hall plot for proportional uniaxial and equibiaxial strain paths, as obtained at $\varepsilon_{VM} = 10.74\%$ and $\varepsilon_{\mathrm{VM}} = 9.42\%$ respectively. (b)FWHM as a function of Q for an Si-standard.

Contrariwise, equibiaxial pre-straning (EQ-UN strain path) leads to increased {111} and {200} peak intensity changes, whilst the {220} shows a distinctive decrease.

Changes in the peak intensities during equibiaxial deformation are notably lower than uniaxial deformation, nevertheless the trends are similar. The {111} peak intensity increases while {220} decreases. Due to scatter in the data, no trends are evident for the {200} and {311} peaks. A uniaxial pre-strain is seen to most strongly influences the {111} and {220}, with little influence on the {200} and {311} peaks.

5.4 Ex-situ characterisation via EBSD

In-situ characterisation offers valuable information regarding the microstructure development for the bulk material. In this section, the microstructure of the deformed specimens was examined ex-situ via EBSD. Localised information regarding the grain orientations, GND structures and twinning development is provided. The resulting interpretation accounts for any dissimilar final strains of the specimens. In all cases, the middle area of the cross-shaped specimens is observed.

A method of final von Mises strain approximation for specimens were in-situ DIC was not possible due to paint delamination, as described in Section 5.2.2. To assist the reader, the final equivalent strain values as calculated via this method, are summarised in Table 5.3. The pre-strain values are excluded from the calculation.

Figure 5.14 includes the orientation and the band contrast maps of the UN, UN F1-UN F2 and EQ-UN strain paths. In all cases, high intragranular deformation is observed, exhibited as colour gradients in the orientation maps. In addition, multiple fine deformation twins can be seen, which are easier to distinguish in the band contrast maps. For the examined strain levels ($\varepsilon_{\mathrm{VM}}$=12.8% for the UN, 11.9%

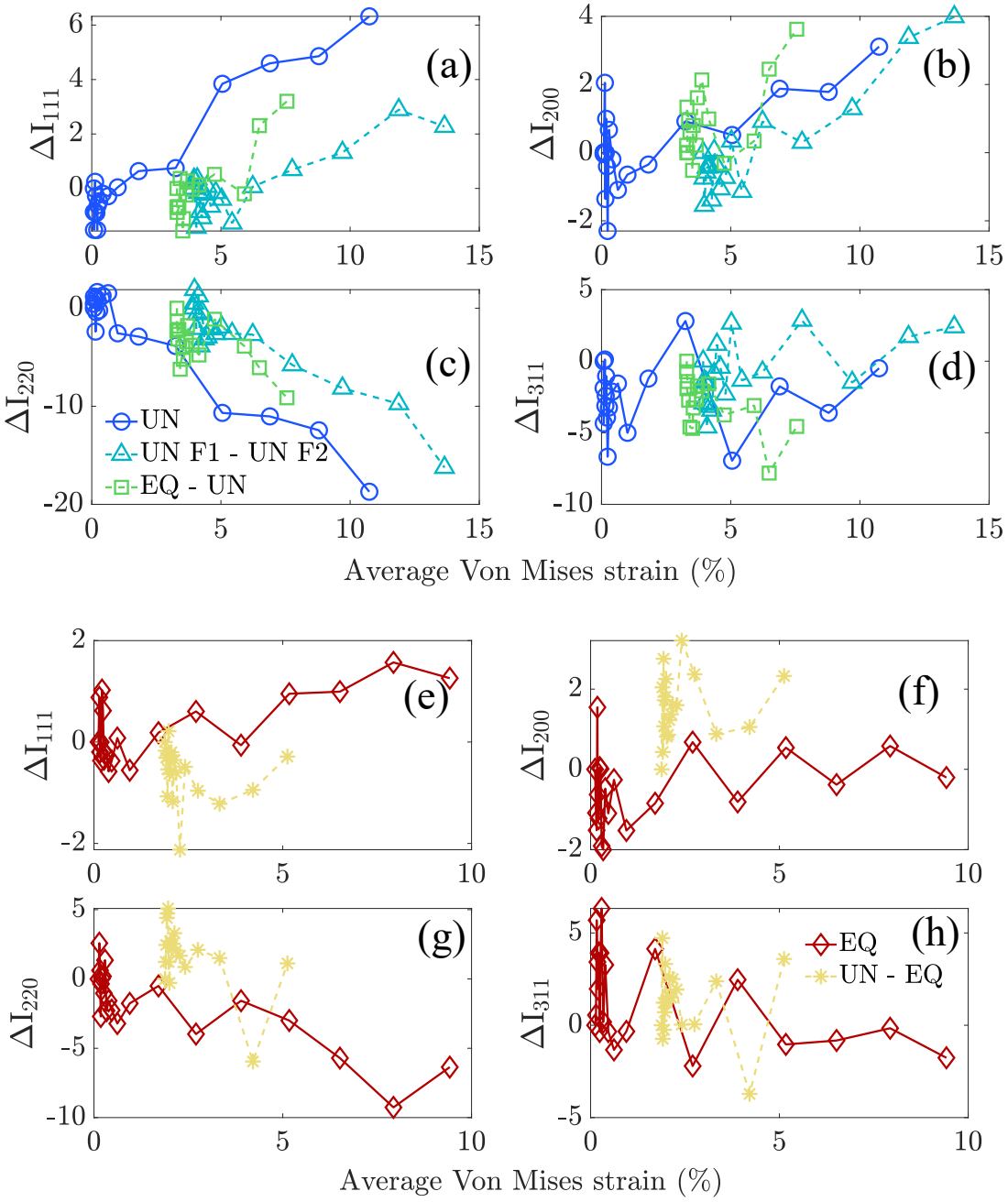

Figure 5.13: Integrated intensity change for (a-d) uniaxial in-situ and (e-h) equibiaxial in-situ strain paths.

Strain path	ε_{VM}
UN	12.81 %
UN F1-UN F2	11.92 %
EQ-UN	6.89 %
EQ	8.71 %
UN-EQ	7.10 %

Table 5.3: Equivalent strains as calculated using the approximation method described in section 5.2.2

for the UN F1-UN F2 and 6.9% for the EQ-UN strain paths) multiple twins have formed in almost all grains in the corresponding maps, and no grain orientation stands out as most favourable for twin formation. In the case of equibiaxial prestraining (Fig. 5.14e-f), fewer deformation twins are observed. One of the reasons behind this result may be the lower ε_{VM} reached for the corresponding specimen in comparison to the other two. However, the twins generated for this strain path, appear to be thicker than the ones for the UN and UN F1-UN F2 strain paths, which could indicate that twin growth is more rapid for equibiaxial deformation.

Microstructures of the specimens deformed following the EQ and UN-EQ strain paths, are shown in Fig. 5.15. Deformation twinning appears to be less significant for these strain paths compared to the UN, UN F1-UN F2 and EQ-UN ones, and some orientations, such us the [011]||sample plane normal (or ND), appear to be much less favourable for twinning in comparison to others. For example, grains orientated with [001]||ND, include multiple deformation twins. This indicates that twin orientation dependence is more significant for equibiaxial deformation than for uniaxial deformation. Additionally, twins formed for equibiaxial deformation (Fig. 5.15a-b) are thicker than the ones for uniaxial deformation (Fig. 5.14a-b), an effect also observed for the EQ-UN strain path.

Neutron data collected from only one macroscopic direction (one detector available) are not advantageous for texture evolution investigation. Hence, EBSD was

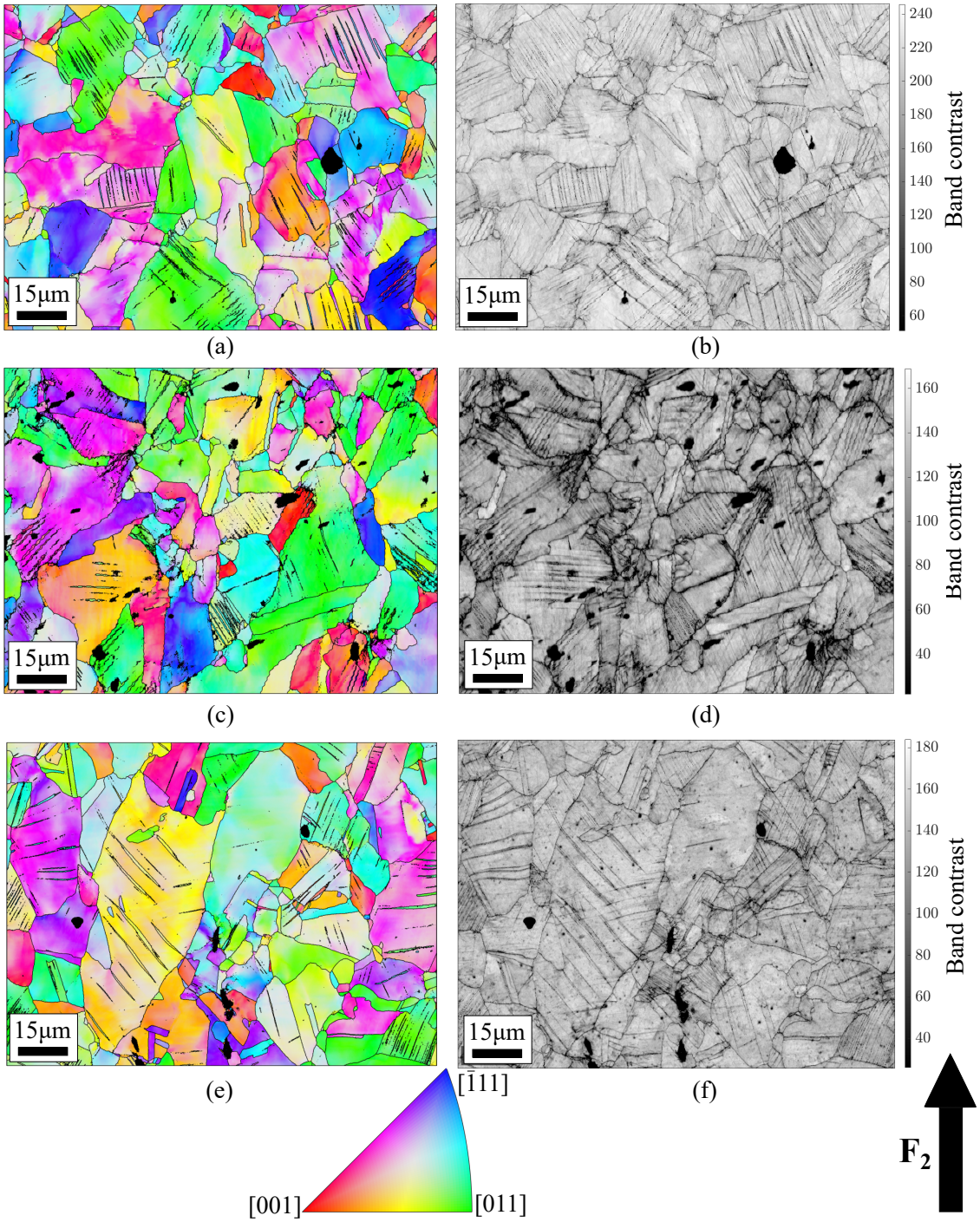

Figure 5.14: Orientation maps (z-axis||normal direction) and band contrast maps for in-situ uniaxial strain paths: (a,b) UN at $\varepsilon_{VM} = 12.8\%$, (c,d) UN1-UN2 at $\varepsilon_{\mathrm{VM}} = 11.9\%$ and (e,f) EQ-UN at $\varepsilon_{\mathrm{VM}} = 6.9\%$. Loading direction is indicated at the bottom left of the figure. Von Mises strain refers to the strain developed during the second deformation step, for the non-proportional strain paths.

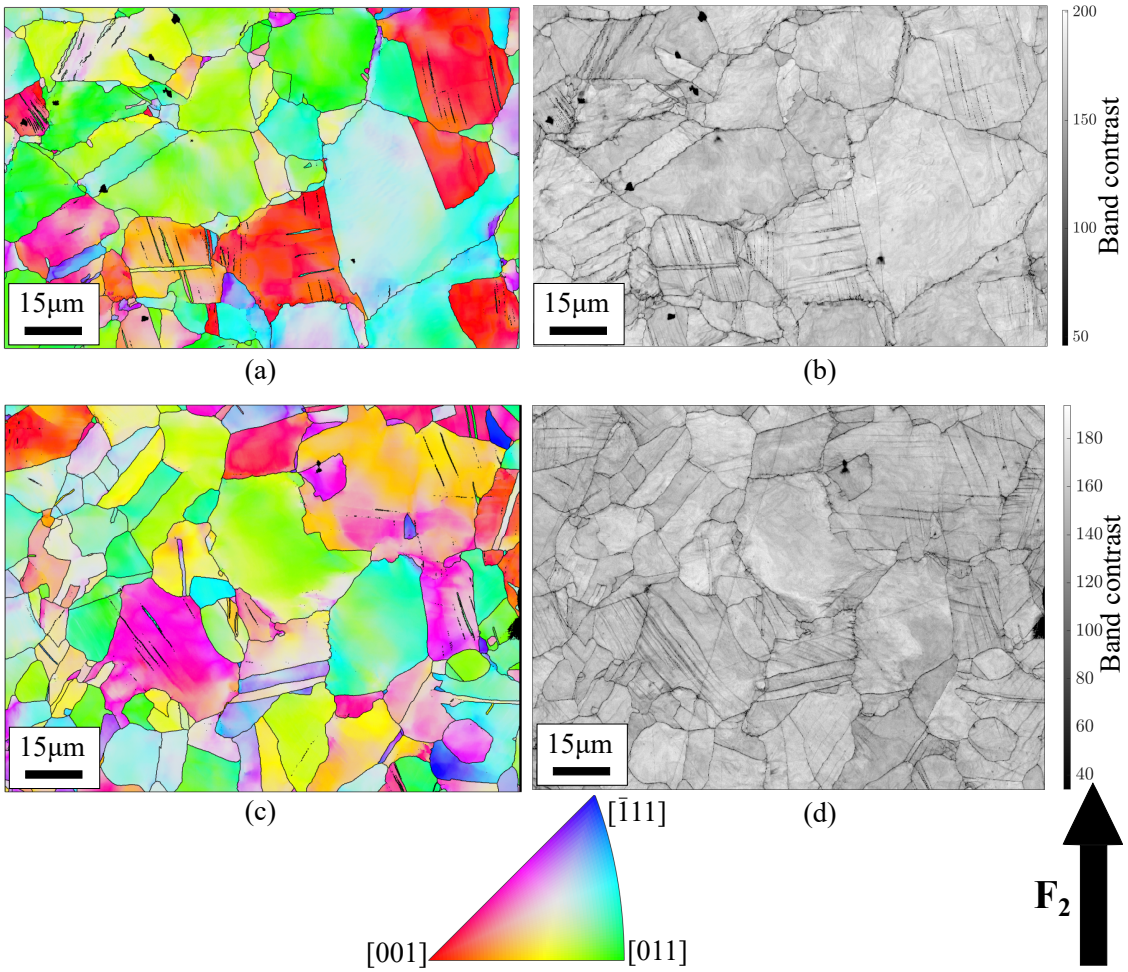

Figure 5.15: Orientation maps (z-axis‖normal direction) and band contrast maps for in-situ equibiaxial strain paths: (a,b) EQ at $\varepsilon_{\mathrm{VM}} = 8.7\%$, (c,d) UN-EQ at $\varepsilon_{\mathrm{VM}} = 7.1\%$. Loading direction of the pre-straining step is indicated at the bottom left of the figure. The von Mises strain refers to the strain developed during the second deformation step, for the non proportional strain path.

used to obtain texture information post-loading. Even though initial texture of specimens appeared to be quite weak, to account for any discrepancies between initial textures of the specimens both the initial and the final textures were examined per specimen. As stated earlier, texture investigation requires hundreds of grains within a scanned area. Since the areas shown in Fig. 5.14 and 5.15 are quite small, additional maps from areas of $\approx 400 \times 400\,\mu m^2$ were captured using a step size of $0.6\,\mu m$. To obtain this measurements, the beam was focused at the exact same regions of interest as per Fig. 5.14 and 5.15, but were zoomed out. The rest of measurement settings were maintained the same, as described in the experimental section.

In Fig. 5.16, the inverse pole figures for the UN, EQ, UN-EQ and EQ-UN strain paths are presented for both the initial (prior to loading) and the deformed state. For the non-proportional strain paths, UN-EQ and EQ-UN, only the final state was examined (no microstructure and texture information is available after the pre-straining step). The minimum and maximum values, as shown by the colour scale, are the same for all plots. Discrepancies between initial textures of the examined specimens may appear dramatic, however it should be highlighted that the maximum limit of 1.5 is very low, and is an indicator of a very weak texture. The final texture post-loading appears to be completely independent of the initial texture, a result that is more obvious for the EQ-UN strain path. Uniaxial deformation results in a strong pole at the [011]||ND direction, with [013]||ND and [012]||ND directions being also favourable for a small fraction of grains. In contrast, EQ loading leads to a clear increase of grains where [011]||ND. In cases where a SPC was incorporated (Fig. 5.16e-f and g-h) an increased spread of the grain orientations is observed. The spread is more obvious for the UN-EQ strain path compared to the EQ-UN one. The texture for the UN-EQ strain path and the texture formed after uniaxial deformation are in agreement. The EQ-UN strain path leads to a characteristic strengthening of the [011] pole, with a spread of orientations close to the [012] and $[\bar{1}35]$ poles. This

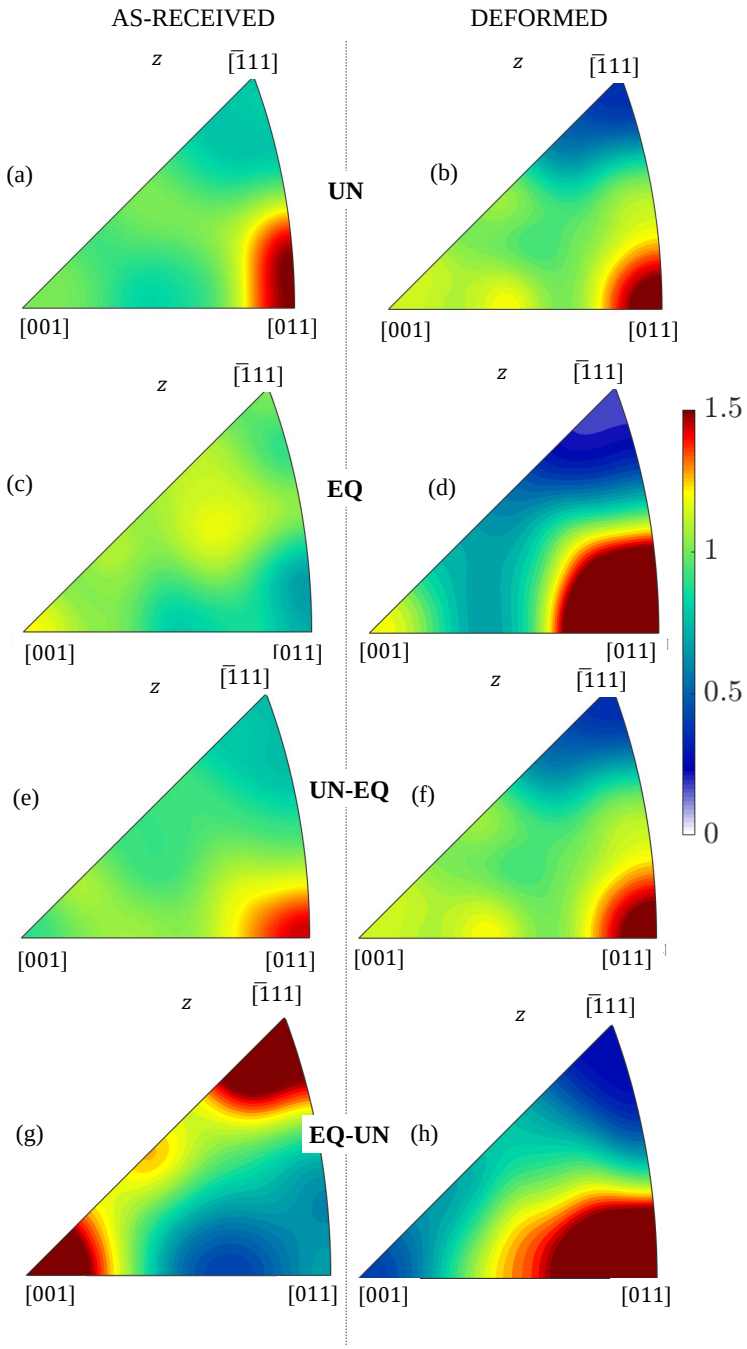

Figure 5.16: Inverse pole figures (ND) obtained for the initial (left column) and the deformed state (right column) for (a,b) UN, (c,d) EQ, (e,f) UN-EQ and (g,h) EQ-UN strain paths.

spread resembles a mixture of uniaxial and equibiaxial proportional textures. The above results indicate that texture changes during uniaxial deformation are more significant than equibiaxial deformation, a result that aligns with the peak intensity change data summarised in Fig. 5.13.

Microstructure characteristics of the deformed specimens were examined ex-situ in terms of GND density development. Fig. 5.17 and Fig. 5.18 show the GND densities obtained from uniaxial and equibiaxial (proportional and non-proportional) strain paths respectively. It is evident that the GND densities are overall higher for uniaxial strain paths (Fig. 5.17), however, it should be highlighted that the equivalent strains for the UN and UN F1 - UN F2 strain paths are substantially higher than the rest of strain paths (≈12% for uniaxial opposed to ≈7-8% for equibiaxial). Additionally, in those two cases, high GND densities are detected in the intragranular area, while for the rest of strain paths, high GND densities are found primarily close to the grain boundaries. Between the uniaxial strain paths, it is clear that in the cases of UN and UN F1 - UN F2 strain paths, the distribution of dislocation substructures are uniform, while for the EQ-UN path, a distinct area of high GND density is apparent in the middle of the map, indicating that an abrupt SPC can lead to more localised deformation characteristics.

Maps shown in Figs. 5.17 and Fig. 5.18 do not reveal any unquestionable dependence of twin nucleation sites and GND density, although in some grains a preferential twin generation at areas of lower GND density is observed (grains shown in circles). In many cases, especially for the UN and UN F1- UN F2 strain paths, where the equivalent strain is higher, dislocations appear to cross twin boundaries, indicating that the energy barriers imposed by the twin boundaries, are not adequate to impede dislocation movements, an effect that has previously been observed for a TWIP steel at similar strain levels [56].

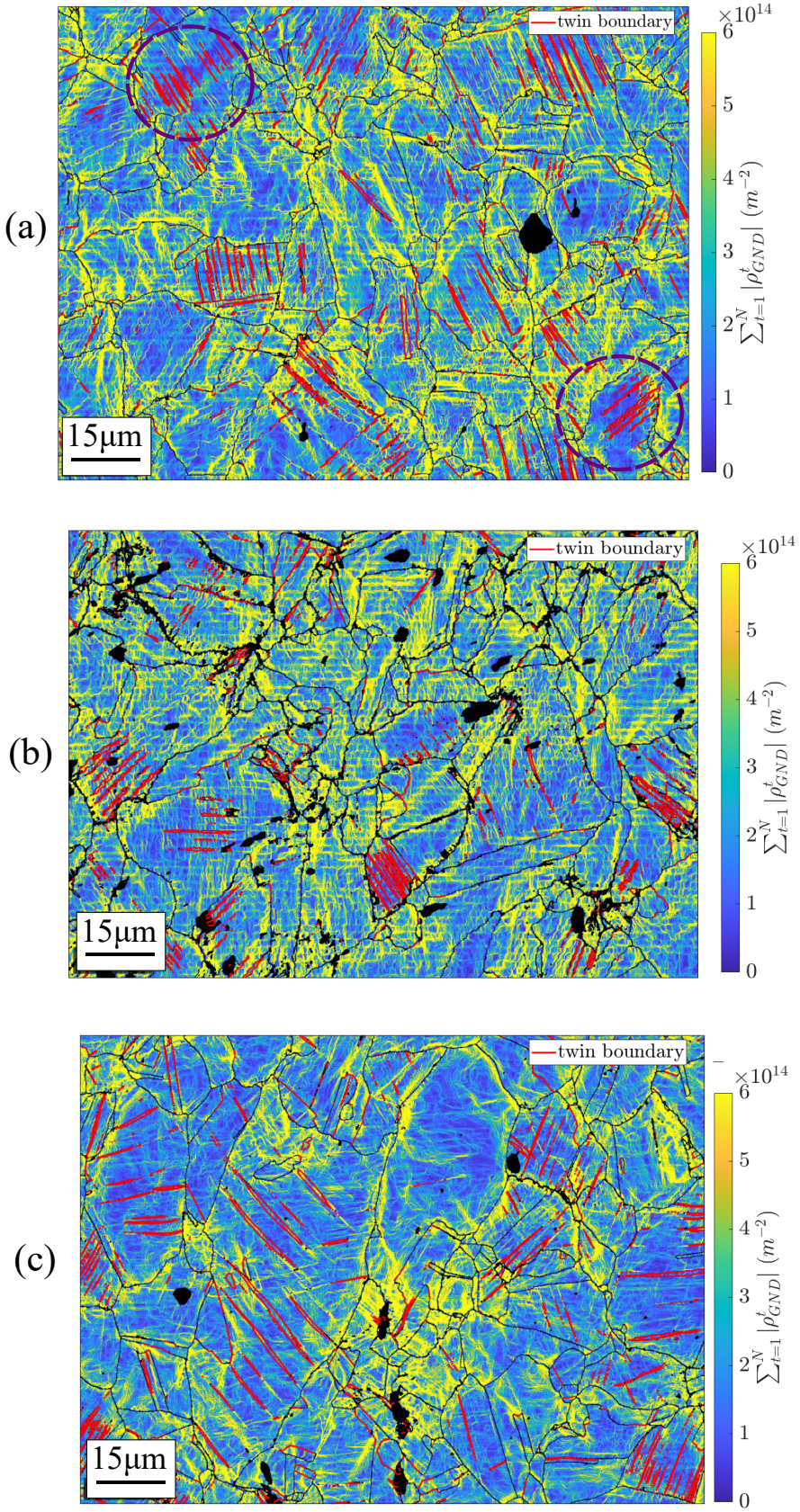

Figure 5.17: GND density maps for the (a) UN ($\varepsilon_{VM} = 12.81\%$), (b) UN F1-UN F2 ($\varepsilon_{VM} = 11.92\%$) and (c) EQ-UN ($\varepsilon_{VM} = 6.89\%$) strain paths.

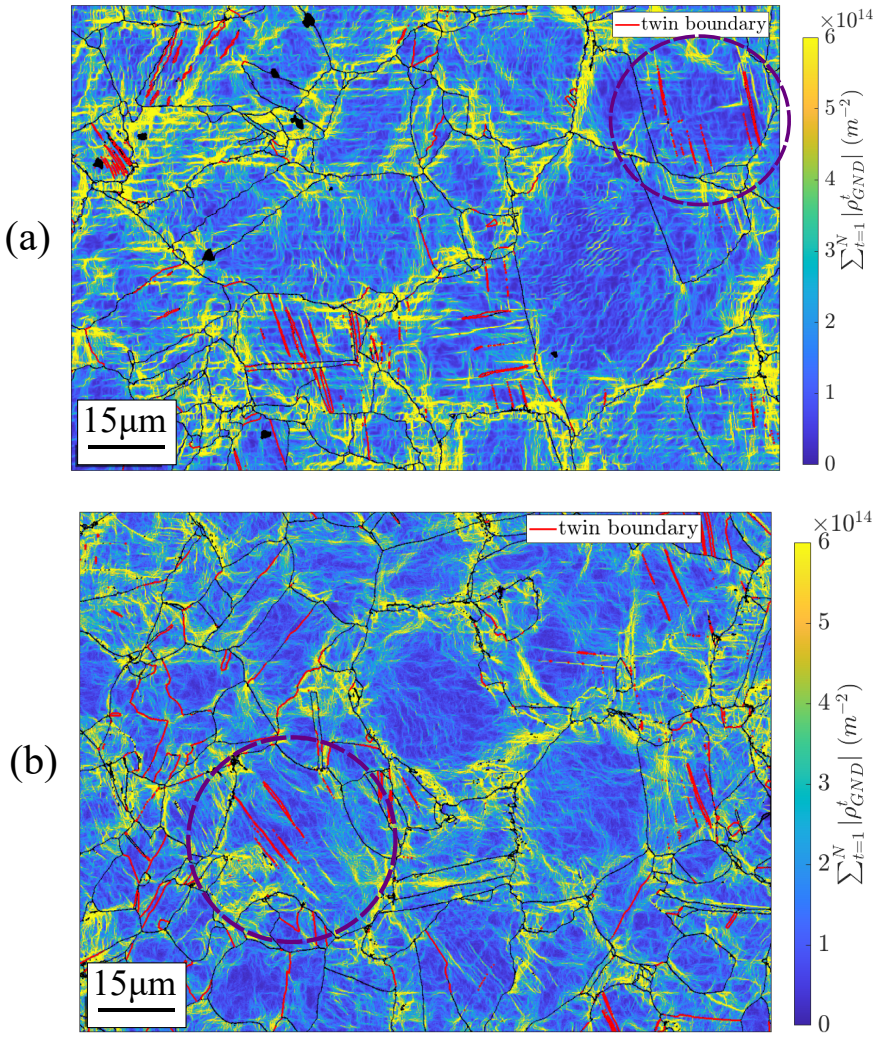

Figure 5.18: GND density maps for the (a) EQ ($\varepsilon_{VM} = 8.71\%$) and (b) UN-EQ ($\varepsilon_{VM} = 7.10\%$) strain paths.

5.5 Discussion

5.5.1 Twinning activity and grain orientation

The EBSD results revealed a strong dependence of twinning on grain orientation, an effect that is more pronounced for equibiaxial strain paths. Strengthening of the [011] ‖ND fibre, which was observed here for equibiaxial deformation (see Fig. 5.16) has been previously described in other works [68, 70]. According to the aforementioned works, this fibre has been also associated with a decreased twinning activity, which is aligned with the findings presented in the current thesis. An investigation of the effect of grain orientation dependence on twinning was conducted using the Taylor factor [36]. Taylor's theory assumes that each crystal in a polycrystalline specimen undergoes the same amount of stress as the specimen as a whole. It also assumes, that all slip systems require the same amount of shear stress to be activated and for those activated, result in the minimisation of deformation energy dissipated from each crystal. This way, Taylor factor can be used as a measure of deformation accommodated from each grain in a specimen under load.

The Taylor factor has been previously used for TWIP steels to indicate which grain orientations are favourable for twinning [74, 68, 146] where it was reported that a high Taylor factor is required for deformation twins to form at early stages of plastic deformation. More specifically, according to Beladi et al. [74] deformation twins were observed for grains oriented with the ⟨111⟩ ‖tensile axis, which were characterised by a Taylor factor of M≈3.67. In general, a high Taylor factor suggests that a large amount of strain has to be accommodated from the grain to facilitate lattice rotations under loading. This means, that higher dislocation densities are expected in grains with higher Taylor factors.

Here, the Taylor factor is used to investigate the influence of grain orientation on twin formation for different strain paths. The normalised strain tensors were used for the Taylor factor calculations, which were defined as follows:

$$\varepsilon_{\mathrm{UN}} = \begin{vmatrix} -\frac{g}{2} & 0 & 0 \\ 0 & g & 0 \\ 0 & 0 & -\frac{g}{2} \end{vmatrix} \tag{5.9}$$

for uniaxial, and

$$\varepsilon_{\mathrm{EQ}} = \begin{vmatrix} g & 0 & 0 \\ 0 & g & 0 \\ 0 & 0 & -2g \end{vmatrix} \tag{5.10}$$

for equibiaxial stress states, where $g = \sqrt{2/3}$ for uniaxial or $g = 1/6$ for equibiaxial loading. These tensors describe a loading process where the tensile axis is parallel to y-axis for uniaxial, and the loading directions align with the $x - y$ plane for equibiaxial strain states. Taylor factors were calculated via MTEX software, for the slip of the $\{111\}\langle 110\rangle$ perfect dislocations. Fig. 5.19 shows the orientation dependence of the Taylor factor for (a,b) uniaxial and (c,d) equibiaxial deformation as calculated for $\approx$ 2000 random orientations. Here, y-axis (loading axis) and z-axis (ND) inverse pole figures are presented. Uniaxial deformation results in higher Taylor factor values for $[\bar{1}11]$ ||loading axis and [011] ||loading axis, while the lowest values are observed for [001] ||loading axis. This is in good agreement with the literature [74, 146, 117]. Equibiaxial deformation, leads in similar tendencies, however, the differences of Taylor factor values between the different orientations are smaller. Looking at the y-axis (|| to one of the loading axes) inverse pole figure, one can observe that the fraction of orientations with high Taylor factor issmaller than the one for uniaxial deformation (for the same inverse pole figure). According to Mishra et al. [68], the [011] ||ND fibre is characterised by the lowest Taylor factor for biaxial

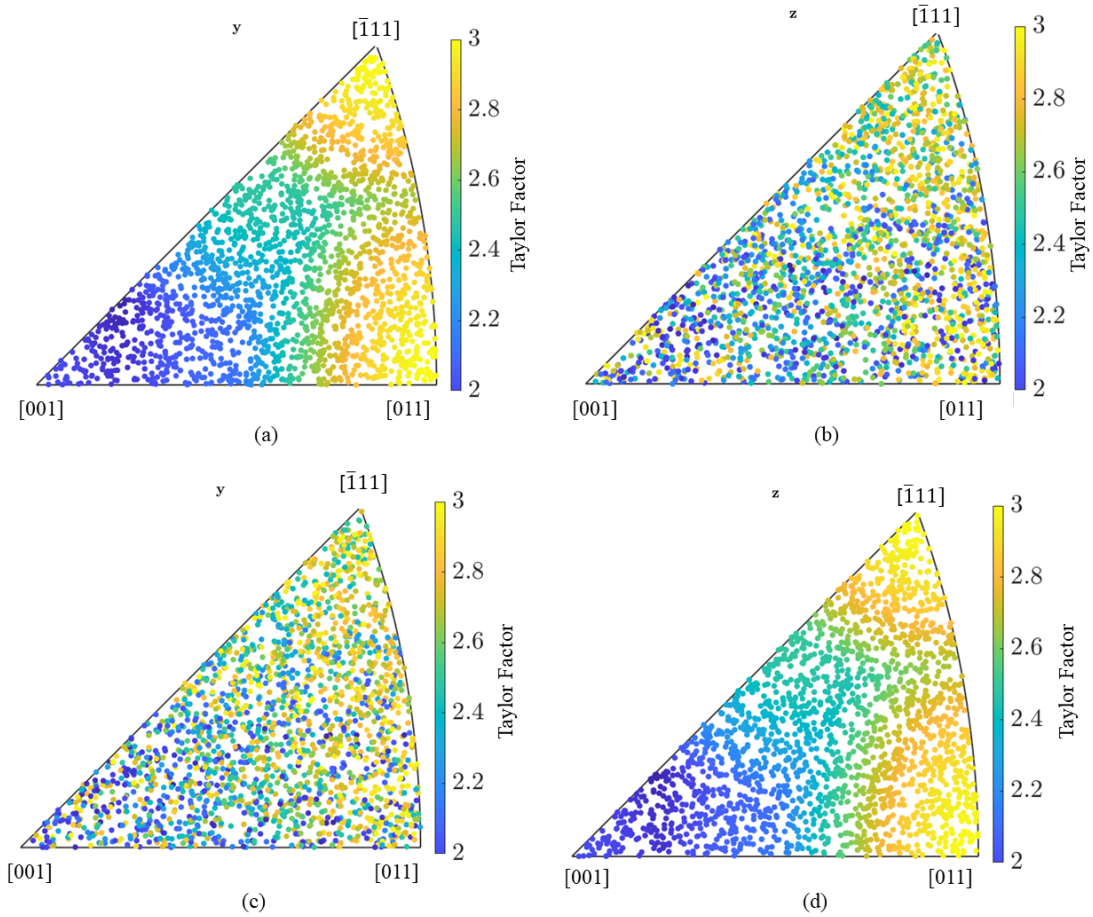

Figure 5.19: Taylor factor distributions plotted on y-axis (loading axis) and z-axis (ND) for (a,b) uniaxial and (c,d) equibiaxial deformation.

deformation, however, this contradicts the results shown in Fig. 5.19d. Our results are in better agreement with [147], where the [011] ‖ND is characterised by a high Taylor factor.

To investigate the grain orientation influence on twin formation, Taylor factor maps were plotted for all strain paths. The maps are shown in Fig. 5.20 and 5.21, for uniaxial and equibiaxial strain paths respectively. As already discussed in the EBSD results section, twinning activity is more prominent for the UN strain path, and most grains contain deformation twins regardless the Taylor factor, while a greater orientation dependence on Taylor factor is observed for equibiaxial strain

paths. This becomes apparent via a comparison of UN and EQ strain paths (Fig. 5.20a and 5.21a). One reason behind this result is the higher von Mises strain of the UN strain path ($\varepsilon_{\mathrm{VM}} = 12.81\%$ for UN vs $\varepsilon_{\mathrm{VM}} = 8.71\%$ for EQ). Interestingly, for the UN strain path twins appear in a few grains with the lowest Taylor factors while simultaneously, other grains with higher Taylor factors do not contain twins. This effect is much more pronounced for equibiaxial strain paths. For the EQ and the UN-EQ strain paths, deformation twins are observed only in grains with low Taylor factors. This unexpected result contradicts prior studies, which associate a high Taylor factor with deformation twin generation [74, 68, 146]. The exact reason behind that effect is unclear, however, some speculations can be made. According to Fig. 5.19 higher Taylor factor values are observed for orientations close to [001] ‖loading axis for the EQ strain path in comparison to UN strain path. This can mean that, orientations which are in other cases unfavourable for twin generation, are less unfavourable in the case for equibiaxial deformation. Additionally, Taylor factor analysis has been extensively used to describe orientation dependence of deformation twinning for uniaxial strain paths, however, its application to study this effect for equibiaxial deformation is very limited. Mishra et al. [68] showed that grains with high Taylor factors are favourable for deformation twinning, however, the orientations characterised by lowest Taylor factor ($\langle 101 \rangle$ ‖ND) are in not in agreement with the findings of the current thesis.

The above analysis indicates that the simple assumption that deformation twinning will take place in grains where easy slip is inhibited, is not true for the examined system. Even though twins appear preferably on grains of the [001]‖ND orientation for equibiaxial deformation, which is in good agreement with literature [68, 148], association of the Taylor factor with the twin generation does not well capture this effect. One has to consider that applying Taylor analysis assumes a random texture, however, texture rapidly develops during deformation, at it was shown in Fig. 5.16,

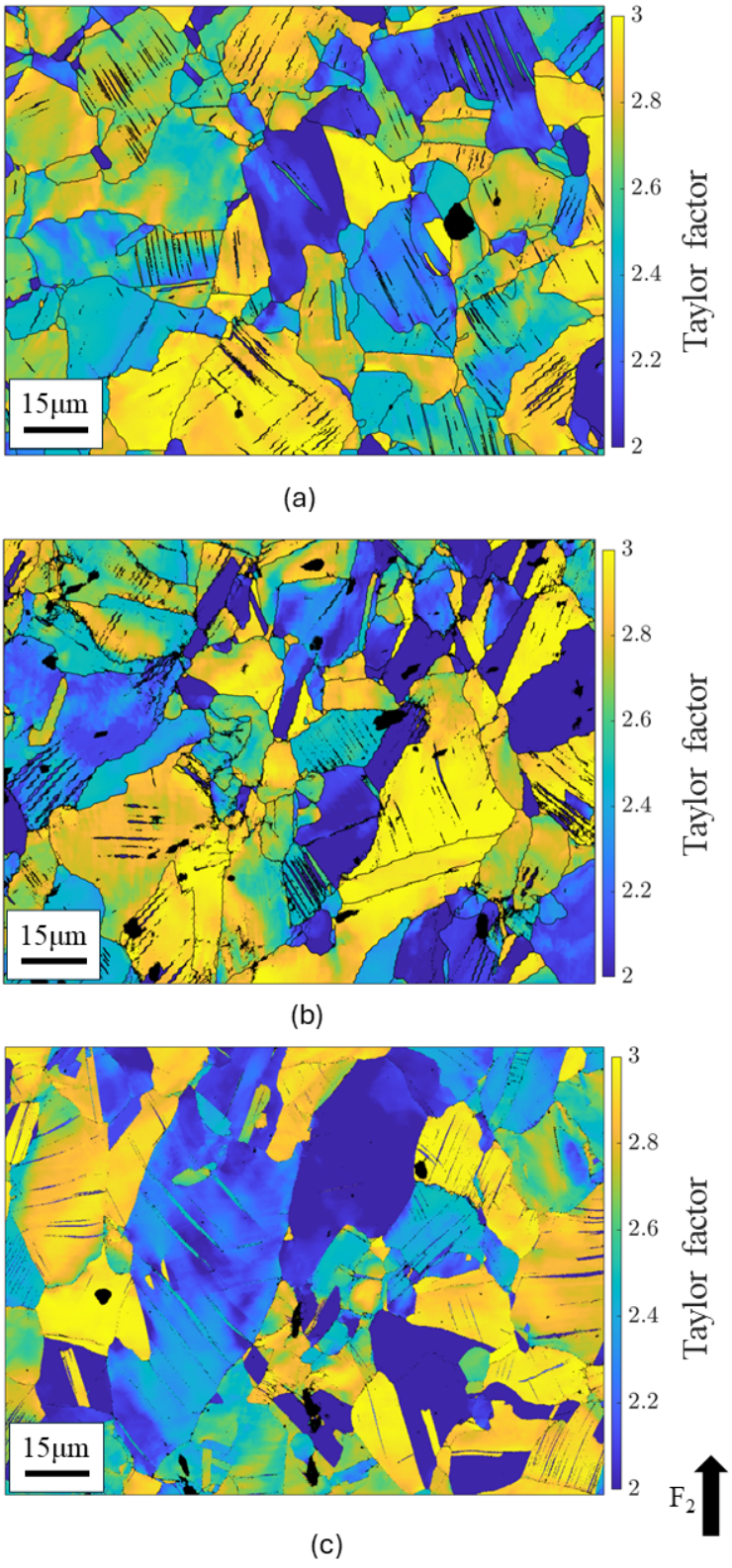

Figure 5.20: Taylor factor maps for the (a) UN ($\varepsilon_{\mathrm{VM}} = 12.81\%$), (b) UN F1-UN F2 ($\varepsilon_{VM} = 11.92\%$) and (c) EQ-UN ($\varepsilon_{\mathrm{VM}} = 6.89\%$) strain paths. The uniaxial loading direction is indicated at bottom right of the figure.

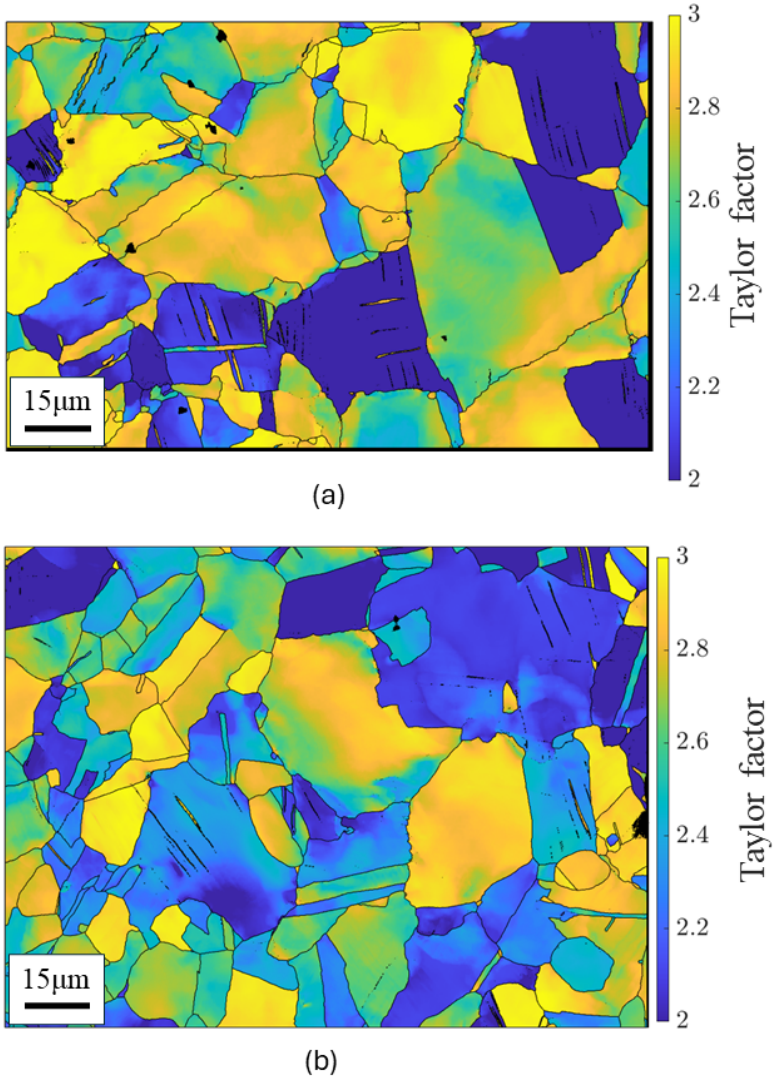

Figure 5.21: Taylor factor maps for the (a) EQ ($\varepsilon_{\mathrm{VM}} = 8.71\%$) and (b) UN-EQ ($\varepsilon_{\mathrm{VM}} = 7.10\%$) strain paths.

which can influence the accuracy of the analysis. Furthermore, the above Taylor factor was calculated here for the $\{111\}\langle 110\rangle$ slip system, to indicate the ease of dislocation slip, using the assumption that deformation twins will form where slip is unfavourable. However, in the case of twinning, Schmid analysis may be more appropriate due to the nature of the twinning mechanism. As described in Chapter 2, deformation twins will form when the $\frac{1}{2}\langle 110\rangle$ dislocation dissociates to $\frac{1}{6}\langle 211\rangle$ and $\frac{1}{6}\langle 12\bar{1}\rangle$ partial dislocations. Polatidis et al. [148] used the Schmid factor to predict the ease of martensite formation in a TRIP steel, by assuming that, for example in tension, the leading partial dislocation should have a higher Schmid factor than the trailing partial dislocation for the martensitic twin to form. A similar methodology may be more appropriate for the TWIP steel examined here.

5.5.2 Strain path sensitivity

Load vs Von Mises strain diagrams presented in Fig. 5.7 revealed small but characteristic differences between the mechanical response of the TWIP steel specimens subjected to five different strain paths: (a) UN, (b) UN F1-UN F2, (c) EQ-UN, (d) EQ and (e) UN-EQ. In all cases of non-proportional deformation, the yield load was increased compared to the yield load of the corresponding proportional strain paths. The UN F1-UN F2 strain path had the lowest influence in the yield load and almost no influence in the work hardening rate. This aligns with the results obtained from the microstructure examination, which showed only insignificant differences between UN F1-UN F2 and the UN strain paths. This is also the strain path with the least abrupt SPC, so results are in good agreement with the results of the previous chapters of non-abrupt SPCs.

Between the UN and EQ strain paths, the latter exhibited a slightly higher yield load and work hardening rate. As twinning is expected to initiate after a critical

plastic strain level has been reached [49, 50, 51], this increase in the yield load can only be related to dislocation activity, which is expected to be higher for the EQ strain path. This strain path also resulted in a higher broadening at $\varepsilon_{\mathrm{VM}} = 9.42\%$ compared to the UN strain path at $\varepsilon_{\mathrm{VM}} = 10.74\%$. From EBSD results it was shown that twinning activity was limited for the EQ strain path compared to the UN strain path. One could argue that this could be an effect of the difference in the final Von Mises strains of the corresponding specimens ($\varepsilon_{\mathrm{VM}} = 8.71\%$ for EQ vs $\varepsilon_{\mathrm{VM}} = 12.81\%$ for UN), however via comparison of the twinning activity of the EQ-UN ($\varepsilon_{\mathrm{VM}} = 6.89\%$) and UN-EQ ($\varepsilon_{\mathrm{VM}} = 7.10\%$), where the final strains are similar, one can see that twinning is remarkably more pronounced for EQ-UN strain path. Given that for the low strains introduced during the pre-straining step twinning activity is expected to be limited, most of the twins have to be generated during the second deformation step. The above results indicate that increased broadening of EQ strain path can only be associated with higher dislocation densities in the corresponding specimens. This result is also supported by the Taylor factor analysis presented in the previous section. Even though the Taylor factor alone fails to predict the grain orientations favourable for twin generation, it is a good indicator for identifying the crystal orientations where a high GND accumulation is expected. As shown in Fig. 5.19, a [011] ‖ND fibre is characterised by a high Taylor factor, while at the same time, equibiaxial deformation leads to strengthening of this texture. Hence, a higher GND accumulation is expected for the equibiaxial deformation.

For the non-proportional strain paths, the GND densities measured after an equibiaxial pre-strain are higher than the GND densities measured for uniaxial pre-strain (EQ-UN vs UN-EQ), as it can be seen in Fig. 5.17 and 5.18. The discussion above postulates that equibiaxial pre-straining leads to higher GND densities than are present after uniaxial pre-straining. However, during re-loading, the GND increase which is expected for equibiaxial deformation in the UN-EQ strain path, does

not happen. In contrast, high GND densities for the EQ-UN strain path are observed. The reason behind this result is not clear, however, the scanned area is quite small to allow generalised assumptions, and high GND densities area in Fig. 5.18b are localised. Grains for rest of the map around this area are characterised by high GND densities at the grain boundaries, but not in the intragranular area. This could indicate that an area of high residual elastic stresses, remnant from prior processing, is present. For future studies, alternative characterisation methods should be used to quantify their presence, if any.

5.6 Summary

This chapter aimed to reveal the effect of strain path and SPC on the mechanical properties and the microstructure development at the early stages of plastic deformation. The TWIP steel examined exhibited two deformation mechanisms up to $\varepsilon_{\mathrm{VM}} \approx 13\%$, comrpising twinning and slip. No martensitic transformation was observed up to this strain level. Load-strain results showed that the yield strength and the work hardening show considerable strain path sensitivity, with equibiaxial proportional deformation being characterised by a higher yield stress and work hardening rate over uniaxial proportional deformation. This was mainly associated with dislocation accumulation rather than deformation twinning. The abruptness of SPC plays a big role in the macroscopic and microscopic effects, corroborating the findings in previous chapters. Here, UN F1 - UN F2 strain path which is the least abrupt strain path, has only a very small effect on the properties of the material. Contrariwise, the effect is more significant for the more abrupt strain paths, EQ-UN and UN-EQ. Between the two, the EQ-UN strain path appeared to have the biggest influence on the work hardening due to a combination of higher dislocation density which is expected to be obtained during equibiaxial pre-straining followed

by a pronounced twin generation during the subsequent uniaxial loading.

Multiple fine deformation twins were formed in most grains during uniaxial deformation. The effect of grain orientation on twinning activity for uniaxial deformation is insignificant. In contrast, twin generation was unfavourable for the [011] ||ND orientations during equibiaxial deformation, however, twin growth occurs at a lower plastic strain compared to the uniaxial strain paths. This effect is evident not only in the orientation maps captured via EBSD but is also recorded as a stagnation in the peak broadening for {111} and {220} planes at $\varepsilon_{\mathrm{VM}} \approx 7.5\%$. Such stagnation is not observed during uniaxial deformation.

Chapter 6

Conclusions and future work

This thesis investigated the role of non-proportional deformation on the macroscopic and microscopic characteristics of two high-formability steels: a DX54 low carbon steel and a high Mn TWIP steel. The effect of strain path and SPCs on the microstructure was examined via SXRD, EBSD and neutron diffraction, aiming to provide a better understanding of the microstructure configuration at the meso- and microscale.

The micromechanics of the DX54 steel were investigated for specimens subjected to a cold rolling $\rightarrow$ uniaxial tension sequence, for a variety of pre-strain magnitudes and two perpendicular pre-strain directions. It was found that the often overlooked effect of the initial sheet texture plays an important role on the developing texture and microstructure during pre-straining. More specifically, for a relatively low pre-strain level (e_0 =14%) high GND densities developed for specimens rolled perpendicular to the initial rolling direction of the examined sheets, as a result of the large texture changes the material underwent. Those high GND densities and large texture changes resulted in a decrease of the lattice strains and a saturation of lattice

strain hardening rates during the second deformation step, when the uniaxial tension direction was perpendicular to the pre-straining direction. Overall, abrupt SPCs led in a highly deformed microstructure and a remarkable reduction in ductility.

The same effects were then investigated for a TWIP steel under a variety of strain paths and SPCs, via a miniaturised test rig, replicating the Marciniak test. Specimens were subjected to five different strain paths: 1) near-uniaxial, 2) plane strain, 3) equibiaxial, 4) cold rolling $\rightarrow$ equibiaxial and 5) uniaxial $\rightarrow$ equibiaxial. Measurements obtained via the miniaturised test rig exhibited good repeatability, especially for the equibiaxial and plane strain conditions. Deviations were observed for the uniaxial strain specimens, which were attributed to the effect of the small specimen size. Microstructure examination proved more challenging for the miniaturised specimens due to charging originating in the mounting method. However, EBSD results showed that cold rolling (equivalent to plane strain) resulted in significantly higher GND densities, compared to uniaxial and equibiaxial deformation and was also characterised by higher twinning activity. The effects of microstructure development during cold rolling were directly associated to the subsequent load-displacement behaviour of the equibiaxially deformed specimens. Uniaxial pre-strain did not lead to significant GND accumulation, hence the subsequent yield strength of the uniaxially pre-strained sample remained almost unchanged to a non-prestrained specimen. Twinning activity was also lower for uniaxial pre-strain. A ductility and tensile strength reduction was also observed for uniaxially pre-strained specimens, which could not be associated with the microstructure configuration of these specimens. Further work on this strain path was conducted on the last part of this work to clarify this effect.

In-situ neutron diffraction and ex-situ EBSD were utilised in the last part of this thesis to further investigate the microstructure characteristics of TWIP steel specimens under uniaxial and equibiaxial, proportional and non proportional defor-

mation. It was found that non-proportional deformation in all cases resulted in a higher yield strength in the second deformation step. The smallest influence was observed for a uniaxial-to-uniaxial strain path change, where the two tensile axes were perpendicular. The highest influence was obtained for equibiaxial pre-strain followed by uniaxial deformation. The yield strength and hardening rate was the highest for this strain path. The effects of equibiaxial pre-straining were attributed to the dislocation density development rather than twining, due to the low pre-strain magnitudes. Twinning activity was found to be lower and more sensitive to grain orientation, in equibiaxially deformed specimens compared to uniaxially deformed specimens. For [011]‖ND orientations, which was shown to be the developing fibre for equibiaxial deformation, were proven to be the least favourable for twin development. However, a faster twin growth was observed for equibiaxial deformation in comparison to uniaxial deformation, an argument supported by both EBSD and FWHM measurements. The influence of the as-received sheet texture was much less significant for the TWIP steel in comparison to the DX54 steel. However, this is due to the very weak initial texture of the former compared to the latter material.

6.1 Future work

The current investigation of the DX54 low carbon steel alloy confirmed the detrimental effect of abrupt SPCs on the properties of the material, and it highlighted the often overlooked effect of texture changes in the microstructure development and macroscopic material response. The hardening behaviour of this material under non-proportional strain paths has been previously examined [16, 149] via SXRD and crystal plasticity modeling, in a work that highlighted the important role of texture and the influence of GND densities in the hardening of this material. The GND density vs distance from grain boundary distribution as well as the lattice strain

hardening saturation observed for highly pre-strained specimens and abrupt SPCs can be used to further inform the aforementioned model.

Within this thesis, strain path sensitivity of a TWIP steel was investigated at low to intermediate plastic strains, where primary twinning systems are mostly active [22]. Further work is required to provide a better understanding of deformation characteristics of the examined TWIP steel at higher strain levels. Such examination can incorporate in-situ or ex-situ interrupted testing along with microstructure examination. In any case, it is important to take into account the high strain hardening rate which can lead to limitations due to the rig load capacity. Additionally, it was shown that employing Taylor factor analysis and assuming that a high Taylor factor will lead to deformation twin generation is not valid for the examined alloy. A different analysis using crystallographic orientations is proposed to be used to examine twinning favourability of different orientations, similar to the one employed by [148], to describe strain path sensitivity of martensitic transformation. Furthermore, the effect of sub-grain strain fields and residual stresses on the GND and twin development was not examined within this work. Additional investigation of such effect is required so that a better understanding of the material properties is obtained. Finally, information regarding the influence of non-proportional deformation on TWIP steels is very limited. Results obtained from this work can be utilised within CPFE or VPSC models to better describe the hardening response of this alloy family under non-proportional deformation.

It is known that composition and hence SFE controls the work hardening via the ratio between slip and twinning deformation mechanisms in TWIP steels [150]. A suggested test matrix would include testing of three TWIP steel alloys with different SFEs; a low, an intermediate and a high SFE. Interrupted or in-situ tests during uniaxial deformation and microstructure examination could reveal twinning vs dislocation density development. The investigation could then be extended to the

material behaviour in other strain paths, proportional, and non-proportional. Additionally, the effect of the pre-strain magnitude in TWIP steel properties is a subject that has not been yet investigated. Given that twinning vs dislocation activity varies depending on the work hardening stage [50, 54, 55, 151], different pre-strains could be used and the material behaviour after an SPC could be examined.

The miniaturised testing method employed in Chapter 4 was proven as a good alternative to the standard sized Marciniak test. Further optimisation of this method is required so that better repeatability is achieved. Results of this work advised that the 10 mm overall specimen diameter may lead to deviations in the load-displacement measurement especially for the narrowest specimen gauges (e.g. the ones used for uniaxial deformation). It is suggested that the diameter is increased to at least 20 mm and a larger thickness of 0.5 mm, so that the number of grains within the gauge region at least doubles. Additionally, a dual camera system can be utilised for strain measurement, which can accurately record strains even for out-of plane displacement. Regardless, the issues that arose from the use of the miniaturised testing method, with further optimisation, could be an excellent alternative to the conventional sized biaxial testing methods. Conventional tests use large material volumes, which inevitably limits the number of tests that could be feasibly carried out in a laboratory environment. For developmental alloys, where only small material volumes are likely to be produced (< 100 g), the miniaturised testing method would offer an efficient use of material for mechanical testing under multiaxial loading.

Bibliography

[1] B. De Cooman, K. Chin, and J. Kim, "High mn twip steels for automotive applications," *New trends and developments in automotive system engineering*, no. 1, pp. 101–128, 2011.

[2] O. Bouaziz, S. Allain, C. P. Scott, P. Cugy, and D. Barbier, "High manganese austenitic twinning induced plasticity steels: A review of the microstructure properties relationships," *Current Opinion in Solid State and Materials Science*, vol. 15, no. 4, pp. 141–168, 2011.

[3] S. Panda, J. Li, V. Hernandez, Y. Zhou, and F. Goodwin, "Effect of weld location, orientation, and strain path on forming behavior of ahss tailor welded blanks," *Journal of engineering Materials and technology*, vol. 132, no. 4, 2010.

[4] N. Gajjar, B. Modi, and R. K. Digavalli, "Improvement in accuracy of failure prediction in sheet hydroforming of square cups using stress-based forming limit diagram," *Journal of Failure Analysis and Prevention*, vol. 19, no. 6, pp. 1792–1800, 2019.

[5] R. Abbaschian and R. E. Reed-Hill, *Physical metallurgy principles-SI version*. Cengage Learning, 2009.

[6] A. G. Guy, "Essentials of materials sciences," 1976.

[7] S. Kibey, J. Liu, D. Johnson, and H. Sehitoglu, "Predicting twinning stress in

fcc metals: Linking twin-energy pathways to twin nucleation," *Acta materialia*, vol. 55, no. 20, pp. 6843–6851, 2007.

[8] M. Bettayeb, V. Maurice, L. H. Klein, L. Lapeire, K. Verbeken, and P. Marcus, "Nanoscale intergranular corrosion and relation with grain boundary character as studied in situ on copper," *Journal of The Electrochemical Society*, vol. 165, no. 11, p. C835, 2018.

[9] H. Bhadeshia and R. Honeycombe, *Steels: microstructure and properties*. Butterworth-Heinemann, 2017.

[10] B. De Cooman, "10 - phase transformations in high manganese twinning-induced plasticity (twip) steels," in *Phase Transformations in Steels* (E. Pereloma and D. V. Edmonds, eds.), vol. 2 of *Woodhead Publishing Series in Metals and Surface Engineering*, pp. 295–331, Woodhead Publishing, 2012.

[11] Z. Shao, Q. Bai, N. Li, J. Lin, Z. Shi, M. Stanton, D. Watson, and T. Dean, "Experimental investigation of forming limit curves and deformation features in warm forming of an aluminium alloy," *Proceedings of the Institution of Mechanical Engineers, Part B: Journal of Engineering Manufacture*, vol. 232, no. 3, pp. 465–474, 2018.

[12] E. Hsu, J. E. Carsley, and R. Verma, "Development of forming limit diagrams of aluminum and magnesium sheet alloys at elevated temperatures," in *Journal of Materials Engineering and Performance*, vol. 17, pp. 288–296, Springer Science and Business Media, LLC, 2008.

[13] T. Kuwabara, S. Ikeda, and K. Kuroda, "Measurement and analysis of differential work hardening in cold-rolled steel sheet under biaxial tension," *Journal of Materials Processing Technology*, vol. 80, pp. 517–523, 1998.

[14] D. Banerjee, M. Iadicola, A. Creuziger, and T. Foecke, "An experimental and numerical study of deformation behavior of steels in biaxial tensile tests," in

TMS 2015 144 th Annual Meeting & Exhibition: Supplemental Proceedings, pp. 279–288, Springer, 2016.

[15] M. Upadhyay, S. Van Petegem, T. Panzner, R. Lebensohn, and H. Van Swygenhoven, "Study of lattice strain evolution during biaxial deformation of stainless steel using a finite element and fast fourier transform based multi-scale approach," *Acta Materialia*, vol. 118, pp. 28–43, 2016.

[16] D. M. Collins, T. Erinosho, F. P. Dunne, R. I. Todd, T. Connolley, M. Mostafavi, H. Kupfer, and A. J. Wilkinson, "A synchrotron X-ray diffraction study of non-proportional strain-path effects," *Acta Materialia*, vol. 124, pp. 290–304, 2017.

[17] ASTM International,, "Standard Test Method for Small Punch Testing of Metallic Materials," pp. 1–12, 2020.

[18] E. Lucon, J. T. Benzing, N. Derimow, and N. Hrabe, "Small punch testing to estimate the tensile and fracture properties of additively manufactured ti-6al-4v," *Journal of Materials Engineering and Performance*, vol. 30, no. 7, pp. 5039–5049, 2021.

[19] S. Arunkumar, "Overview of small punch test," *Metals and Materials International*, vol. 26, no. 6, pp. 719–738, 2020.

[20] A. Vrettou, H. Kitaguchi, B. Cai, T. Connolley, and D. M. Collins, "Mechanisms controlling ductility loss from abrupt strain path changes in a low carbon steel," *Materials Science and Engineering: A*, vol. 843, p. 143091, 2022.

[21] C. Trager-Cowan, A. Alasmari, W. Avis, J. Bruckbauer, P. R. Edwards, G. Ferenczi, B. Hourahine, A. Kotzai, S. Kraeusel, G. Kusch, *et al.*, "Structural and luminescence imaging and characterisation of semiconductors in the scanning electron microscope," *Semiconductor Science and Technology*, vol. 35, no. 5, p. 054001, 2020.

[22] B. C. De Cooman, Y. Estrin, and S. K. Kim, "Twinning-induced plasticity (TWIP) steels," *Acta Materialia*, vol. 142, pp. 283–362, 2018.

[23] S. Van Petegem, J. Wagner, T. Panzner, M. Upadhyay, T. Trang, and H. Van Swygenhoven, "In-situ neutron diffraction during biaxial deformation," *Acta Materialia*, vol. 105, pp. 404–416, 2016.

[24] D. M. Collins, M. Mostafavi, R. I. Todd, T. Connolley, and A. J. Wilkinson, "A synchrotron X-ray diffraction study of in situ biaxial deformation," *Acta Mater.*, 2015.

[25] A. T. Mayyas, A. Qattawi, A. R. Mayyas, and M. A. Omar, "Life cycle assessment-based selection for a sustainable lightweight body-in-white design," *Energy*, vol. 39, no. 1, pp. 412–425, 2012.

[26] G. Davies, *Materials for automobile bodies*. Butterworth-Heinemann, 2012.

[27] M. E. McHenry and D. E. Laughlin, "Magnetic properties of metals and alloys," in *Physical Metallurgy*, pp. 1881–2008, Elsevier, 2014.

[28] N. Fonstein, "Chapter 7 - dual-phase steels.," in *Automotive Steels* (R. Rana and S. B. Singh, eds.), pp. 169–216, Woodhead Publishing, 2017.

[29] B. De Cooman, "Chapter 11 - high mn twip steel and medium mn steel," in *Automotive Steels* (R. Rana and S. B. Singh, eds.), pp. 317–385, Woodhead Publishing, 2017.

[30] Y. Strauven and E. Aernoudt, "Directional strain softening in ferritic steel," *Acta. Metall.*, vol. 35, no. 5, pp. 1029–1036, 1987.

[31] E. Rauch and J.-H. Schmitt, "Dislocation substructures in mild steel deformed in simple shear," *Mater. Sci. Eng.: A*, vol. 113, pp. 441–448, 1989.

[32] D. Wilson and P. Bate, "Influences of cell walls and grain boundaries on transient responses of an if steel to changes in strain path," *Acta. Metall. et materialia*, vol. 42, no. 4, pp. 1099–1111, 1994.

[33] E. Nesterova, B. Bacroix, and C. Teodosiu, "Experimental observation of microstructure evolution under strain-path changes in low-carbon if steel," *Mater. Sci. Eng.: A*, vol. 309, pp. 495–499, 2001.

[34] J. Bauschinger, "On the change of the elastic limit and the strength of iron and steel, by drawing out, by heating and cooling, and by repetition of loading (summary)," *Minutes of Proceedings of the Institution of Civil Engineers with Other Selected and Abstracted Papers*, vol. 87, p. 463, 1886.

[35] D. Hull and D. Bacon, "Introduction to dislocations 3rd edition," 1985.

[36] G. I. Taylor, "Plastic strain in metals," *J. Inst. Metals*, vol. 62, pp. 307–324, 1938.

[37] H. Bunge, "Some applications of the taylor theory of polycrystal plasticity," *Kristall und Technik*, vol. 5, no. 1, pp. 145–175, 1970.

[38] J. F. Nye, "Some geometrical relations in dislocated crystals," *Acta. Metall.*, vol. 1, no. 2, pp. 153–162, 1953.

[39] R. Cahn, "The preparation of alpha-uranium crystals," *Acta Metallurgica*, vol. 1, no. 2, pp. 176–184, 1953.

[40] L. A. Kestens and H. Pirgazi, "Texture formation in metal alloys with cubic crystal structures," *Mater. Sci. Tech. (United Kingdom)*, vol. 32, no. 13, pp. 1303–1315, 2016.

[41] A. Saeed-Akbari, J. Imlau, U. Prahl, and W. Bleck, "Derivation and variation in composition-dependent stacking fault energy maps based on subregular so-

lution model in high-manganese steels," *Metallurgical and Materials Transactions A*, vol. 40, no. 13, pp. 3076–3090, 2009.

[42] J.-E. Jin and Y.-K. Lee, "Effects of al on microstructure and tensile properties of c-bearing high mn twip steel," *Acta Materialia*, vol. 60, no. 4, pp. 1680–1688, 2012.

[43] K.-G. Chin, C.-Y. Kang, S. Y. Shin, S. Hong, S. Lee, H. S. Kim, K.-h. Kim, and N. J. Kim, "Effects of al addition on deformation and fracture mechanisms in two high manganese twip steels," *Materials Science and Engineering: A*, vol. 528, no. 6, pp. 2922–2928, 2011.

[44] S. Hong, S. Y. Shin, H. S. Kim, S. Lee, S.-K. Kim, K.-G. Chin, and N. J. Kim, "Effects of aluminum addition on tensile and cup forming properties of three twinning induced plasticity steels," *Metallurgical and Materials Transactions A*, vol. 43, no. 6, pp. 1870–1883, 2012.

[45] K. Jeong, J.-E. Jin, Y.-S. Jung, S. Kang, and Y.-K. Lee, "The effects of si on the mechanical twinning and strain hardening of fe–18mn–0.6 c twinning-induced plasticity steel," *Acta Materialia*, vol. 61, no. 9, pp. 3399–3410, 2013.

[46] X. Tian and Y. Zhang, "Effect of si content on the stacking fault energy in γ-fe–mn–si–c alloys: Part i. x-ray diffraction line profile analysis," *Materials Science and Engineering: A*, vol. 516, no. 1-2, pp. 73–77, 2009.

[47] A. Dumay, J.-P. Chateau, S. Allain, S. Migot, and O. Bouaziz, "Influence of addition elements on the stacking-fault energy and mechanical properties of an austenitic fe–mn–c steel," *Materials Science and Engineering: A*, vol. 483, pp. 184–187, 2008.

[48] J. W. Christian and S. Mahajan, "Deformation twinning," *Progress in materials science*, vol. 39, no. 1-2, pp. 1–157, 1995.

[49] S. R. Kalidindi, "Modeling the strain hardening response of low sfe fcc alloys," *International Journal of Plasticity*, vol. 14, no. 12, pp. 1265–1277, 1998.

[50] D. Barbier, N. Gey, S. Allain, N. Bozzolo, and M. Humbert, "Analysis of the tensile behavior of a twip steel based on the texture and microstructure evolutions," *Materials Science and Engineering: A*, vol. 500, no. 1-2, pp. 196–206, 2009.

[51] H. Idrissi, K. Renard, L. Ryelandt, D. Schryvers, and P. Jacques, "On the mechanism of twin formation in fe–mn–c twip steels," *Acta Materialia*, vol. 58, no. 7, pp. 2464–2476, 2010.

[52] K. Rahman, N. Jones, and D. Dye, "Micromechanics of twinning in a twip steel," *Materials Science and Engineering: A*, vol. 635, pp. 133–142, 2015.

[53] A. A. Saleh and A. A. Gazder, "A re-evaluation of "the micromechanics of twinning in a twip steel"," *Materials Science and Engineering: A*, vol. 649, pp. 184–189, 2016.

[54] I. Gutierrez-Urrutia and D. Raabe, "Dislocation and twin substructure evolution during strain hardening of an fe–22 wt.% mn–0.6 wt.% c twip steel observed by electron channeling contrast imaging," *Acta materialia*, vol. 59, no. 16, pp. 6449–6462, 2011.

[55] K. Renard and P. Jacques, "On the relationship between work hardening and twinning rate in twip steels," *Materials Science and Engineering: A*, vol. 542, pp. 8–14, 2012.

[56] P. Zhou and M. X. Huang, "On the mechanisms of different work-hardening stages in twinning-induced plasticity steels," *Metallurgical and Materials Transactions A*, vol. 46, pp. 5080–5090, 2015.

[57] A. K. Ghosh and W. A. Backofen, "Strain hardening and instability in biaxially streched sheets," *Metall. Trans.*, vol. 4, no. 4, pp. 1113–1123, 1973.

[58] J. V. Laukonis and A. K. Ghosh, "Effects of strain path changes on the formability of sheet metals," *Metall. Trans. A*, vol. 9, no. 12, pp. 1849–1856, 1978.

[59] M. Zandrahimi, S. Platias, D. Frice, D. Barrett, P. S. Bate, and W. T. Roberts, "Effects of changes in strain path on work hardening in cubic metals," *Metall. Trans. A*, vol. 20, no. 11, pp. 2471–2482, 1989.

[60] G. Vincze, E. Rauch, J. Gracio, F. Barlat, and A. Lopes, "A comparison of the mechanical behaviour of an aa1050 and a low carbon steel deformed upon strain reversal," *Acta Materialia*, vol. 53, no. 4, pp. 1005–1013, 2005.

[61] Z. Li, G. Winther, and N. Hansen, "Anisotropy in rolled metals induced by dislocation structure," *Acta materialia*, vol. 54, no. 2, pp. 401–410, 2006.

[62] S. Thuillier and E. F. Rauch, "Development of microbands in mild steel during cross loading," *Acta. Metall. Mater.*, vol. 42, no. 6, pp. 1973–1983, 1994.

[63] T. Erinosho, A. Cocks, and F. Dunne, "Texture, hardening and non-proportionality of strain in bcc polycrystal deformation," *Int. J. Plast.*, vol. 50, pp. 170–192, 2013.

[64] K. Kitayama, C. N. Tomé, E. Rauch, J. Gracio, and F. Barlat, "A crystallographic dislocation model for describing hardening of polycrystals during strain path changes. application to low carbon steels," *International Journal of Plasticity*, vol. 46, pp. 54–69, 2013.

[65] W. Wen, M. Borodachenkova, C. Tomé, G. Vincze, E. Rauch, F. Barlat, and J. Grácio, "Mechanical behavior of low carbon steel subjected to strain path changes: Experiments and modeling," *Acta Materialia*, vol. 111, pp. 305–314, 2016.

[66] Y. Shen, W. Xue, Y. Wang, Y. Liu, and L. Zuo, "Tensile behaviors of if steel with different cold-rolling reductions," *Mater. Sci. Eng.: A*, vol. 496, no. 1-2, pp. 383–388, 2008.

[67] S. Mishra, K. Narasimhan, and I. Samajdar, "Deformation twinning in aisi 316l austenitic stainless steel: role of strain and strain path," *Materials Science and Technology*, vol. 23, no. 9, pp. 1118–1126, 2007.

[68] S. K. Mishra, S. M. Tiwari, A. M. Kumar, and L. G. Hector, "Effect of strain and strain path on texture and twin development in austenitic steel with twinning-induced plasticity," *Metallurgical and Materials Transactions A*, vol. 43, pp. 1598–1609, 2012.

[69] R. Lapovok, I. Timokhina, A. Mester, M. Weiss, and A. Shekhter, "Influence of the strain history on twip steel deformation mechanisms in the deep-drawing process," *Metallurgical and Materials Transactions A*, vol. 49, pp. 2069–2083, 2018.

[70] E. Polatidis, M. Šmíd, W.-N. Hsu, M. Kubenova, J. Capek, T. Panzner, and H. Van Swygenhoven, "The interplay between deformation mechanisms in austenitic 304 steel during uniaxial and equibiaxial loading," *Materials Science and Engineering: A*, vol. 764, p. 138222, 2019.

[71] M. Weiss, K. Mester, A. Taylor, and N. Stanford, "A critical assessment of deformation twinning and epsilon martensite formation in austenitic alloys during complex forming operations," *Materials Characterization*, vol. 145, pp. 423–434, 2018.

[72] P. Yang, Q. Xie, L. Meng, H. Ding, and Z. Tang, "Dependence of deformation twinning on grain orientation in a high manganese steel," *Scripta Materialia*, vol. 55, no. 7, pp. 629–631, 2006.

[73] I. Gutierrez-Urrutia, S. Zaefferer, and D. Raabe, "The effect of grain size and grain orientation on deformation twinning in a fe–22 wt.% mn–0.6 wt.% c twip steel," *Materials Science and Engineering: A*, vol. 527, no. 15, pp. 3552–3560, 2010.

[74] H. Beladi, I. Timokhina, Y. Estrin, J. Kim, B. De Cooman, and S. Kim, "Orientation dependence of twinning and strain hardening behaviour of a high manganese twinning induced plasticity steel with polycrystalline structure," *Acta materialia*, vol. 59, no. 20, pp. 7787–7799, 2011.

[75] M. L. Young, J. D. Almer, M. R. Daymond, D. R. Haeffner, and D. C. Dunand, "Load partitioning between ferrite and cementite during elasto-plastic deformation of an ultrahigh-carbon steel," *Acta Mater.*, vol. 55, no. 6, pp. 1999–2011, 2007.

[76] H. Mecking, U. Kocks, and C. Hartig, "Taylor factors in materials with many deformation modes," *Scripta materialia*, vol. 35, no. 4, 1996.

[77] O. Bouaziz, S. Allain, and C. Scott, "Effect of grain and twin boundaries on the hardening mechanisms of twinning-induced plasticity steels," *Scripta Materialia*, vol. 58, no. 6, pp. 484–487, 2008.

[78] K. Rahman, V. Vorontsov, and D. Dye, "The effect of grain size on the twin initiation stress in a twip steel," *Acta Materialia*, vol. 89, pp. 247–257, 2015.

[79] S.-I. Lee, S.-Y. Lee, J. Han, and B. Hwang, "Deformation behavior and tensile properties of an austenitic fe-24mn-4cr-0.5 c high-manganese steel: Effect of grain size," *Materials Science and Engineering: A*, vol. 742, pp. 334–343, 2019.

[80] J. Chen, F.-t. Dong, Z.-y. Liu, and G.-d. Wang, "Grain size dependence of twinning behaviors and resultant cryogenic impact toughness in high manganese austenitic steel," *Journal of Materials Research and Technology*, vol. 10, pp. 175–187, 2021.

[81] Y. Zhu, X. Liao, X. Wu, and J. Narayan, "Grain size effect on deformation twinning and detwinning," *Journal of Materials Science*, vol. 48, pp. 4467–4475, 2013.

[82] A. A. Saleh, E. V. Pereloma, B. Clausen, D. W. Brown, C. N. Tomé, and A. A. Gazder, "On the evolution and modelling of lattice strains during the cyclic loading of twip steel," *Acta materialia*, vol. 61, no. 14, pp. 5247–5262, 2013.

[83] S. J. McCormack, W. Wen, E. V. Pereloma, C. N. Tomé, A. A. Gazder, and A. A. Saleh, "On the first direct observation of de-twinning in a twinning-induced plasticity steel," *Acta Materialia*, vol. 156, pp. 172–182, 2018.

[84] C. d'Hondt, V. Doquet, and J. Couzinié, "Direct monitoring of twinning/detwinning in a twip steel under reversed cyclic loading," *Materials Science and Engineering: A*, vol. 814, p. 141250, 2021.

[85] A. B. Pereira, F. A. Fernandes, and B. Filipe, "Effect of deformation path on the microstructure and mechanical behavior of twip980 steel," *Journal of Manufacturing and Materials Processing*, vol. 3, no. 1, p. 12, 2019.

[86] J.-K. Hwang, "Correlation of strain path, texture, twinning, and mechanical properties in twinning-induced plasticity steel during wire drawing," *Materials*, vol. 13, no. 10, p. 2250, 2020.

[87] S. P. Keeler, *Plastic instability and fracture in sheets stretched over rigid punches*. PhD thesis, Massachusetts Institute of Technology, 1961.

[88] ASTM International, "Standard Test Method for Determining Forming Limit Curves," *ASTM Book of Standards*, vol. i, no. Reapproved, pp. 1–15, 2015.

[89] Z. Deng and J. P. McGuire, "Development of novel forming limit curve testing method," in *IOP Conference Series: Materials Science and Engineering*, vol. 418, Institute of Physics Publishing, 9 2018.

[90] X. Kong, X. Chu, C. Chen, Y. Wang, P. Liu, and Z. Wang, "Comparative investigation of the experimental determination of aa5086 flcs under different necking criteria," *Materials*, vol. 14, no. 13, p. 3685, 2021.

[91] K. Achineethongkham and V. Uthaisangsuk, "Analysis of forming limit behaviour of high strength steels under non-linear strain paths using a micromechanics damage modelling," *International Journal of Mechanical Sciences*, vol. 183, p. 105828, 2020.

[92] J. Lian, W. Liu, X. Gastañares, R. Juan, and J. Mendiguren, "Plasticity evolution of an aluminum-magnesium alloy under abrupt strain path changes," *International Journal of Material Forming*, vol. 15, no. 3, p. 40, 2022.

[93] R. Sharma, D. Sargeant, S. Daroju, M. Knezevic, M. P. Miles, and D. T. Fullwood, "Multi-strain path deformation behavior of aa6016-t4: Experiments and crystal plasticity modeling," *International Journal of Solids and Structures*, vol. 244, p. 111536, 2022.

[94] T. Foecke, M. A. Iadicola, A. Lin, and S. Banovic, "A method for direct measurement of multiaxial stress-strain curves in sheet metal," *Metallurgical and Materials Transactions A*, vol. 38, pp. 306–313, 2007.

[95] M. Iadicola, T. Foecke, and S. W. Banovic, "Experimental observations of evolving yield loci in biaxially strained aa5754-o," *International Journal of Plasticity*, vol. 24, no. 11, pp. 2084–2101, 2008.

[96] Y. Jeong, M. A. Iadicola, T. Gnäupel-Herold, and A. Creuziger, "Multiaxial constitutive behavior of an interstitial-free steel: Measurements through x-ray and digital image correlation," *Acta materialia*, vol. 112, pp. 84–93, 2016.

[97] L. Leotoing and D. Guines, "Investigations of the effect of strain path changes on forming limit curves using an in-plane biaxial tensile test," *International Journal of Mechanical Sciences*, vol. 99, pp. 21–28, 2015.

[98] R. Xiao, X.-X. Li, L.-H. Lang, Q. Song, and K.-N. Liu, "Forming limit in thermal cruciform biaxial tensile testing of titanium alloy," *Journal of Materials Processing Technology*, vol. 240, pp. 354–361, 2017.

[99] S. Van Petegem, J. Wagner, T. Panzner, M. V. Upadhyay, T. T. Trang, and H. Van Swygenhoven, "In-situ neutron diffraction during biaxial deformation," *Acta Mater.*, vol. 105, pp. 404–416, 2016.

[100] M. V. Upadhyay, J. Capek, T. Panzner, and H. Van Swygenhoven, "Microstructure evolution of stainless steel subjected to biaxial load path changes: In-situ neutron diffraction and multi-scale modeling," *International Journal of Plasticity*, vol. 122, pp. 49–72, 2019.

[101] E. Polatidis, M. Morgano, F. Malamud, M. Bacak, T. Panzner, H. Van Swygenhoven, and M. Strobl, "Neutron diffraction and diffraction contrast imaging for mapping the trip effect under load path change," *Materials*, vol. 13, no. 6, p. 1450, 2020.

[102] K. Kiriyama, S. Zhang, H. Hayashida, J.-i. Suzuki, and T. Kuwabara, "Development of a biaxial tensile testing machine for pulsed neutron experiments," *MethodsX*, vol. 6, pp. 2166–2175, 2019.

[103] S. Dhara, S. Taylor, B. Shollock, S. Hazra, *et al.*, "A novel experimental set-up for in-situ microstructural characterization during continuous strain path change," in *IOP Conference Series: Mater. Sci. Eng.*, vol. 967, p. 012007, IOP Publishing, 2020.

[104] M. P. Manahan, *The development of a miniaturized disk bend test for the determination of post-irradiation mechanical behavior.* PhD thesis, Massachusetts Institute of Technology, 1982.

[105] X. Mao and H. Takahashi, "DEVELOPMENT OF A FURTHER-

MINIATURIZED SPECIMEN OF 3 mm DIAMETER FOR TJZM DISK (0 3 mm) SMALL PUNCH TESTS," tech. rep., 1987.

[106] T. E. García, C. Rodríguez, F. J. Belzunce, and C. Suárez, "Estimation of the mechanical properties of metallic materials by means of the small punch test," *Journal of Alloys and Compounds*, vol. 582, pp. 708–717, 2014.

[107] E. Fleury and J. S. Ha, "Small punch tests to estimate the mechanical properties of steels for steam power plant: I. Mechanical strength," tech. rep.

[108] E. Altstadt, H. E. Ge, V. Kuksenko, M. Serrano, M. Houska, M. Lasan, M. Bruchhausen, J. M. Lapetite, and Y. Dai, "Critical evaluation of the small punch test as a screening procedure for mechanical properties," *Journal of Nuclear Materials*, vol. 472, pp. 186–195, 4 2016.

[109] G. Williamson and W. Hall, "X-ray line broadening from filed aluminium and wolfram," *Acta metallurgica*, vol. 1, no. 1, pp. 22–31, 1953.

[110] B. D. Cullity, *Elements of X-ray Diffraction*. Addison-Wesley Publishing, 1956.

[111] B. B. Hutchinson, "Deformation Microstructures and Mechanisms," pp. 1471–1485, 1999.

[112] F. Bachmann, R. Hielscher, and H. Schaeben, "Texture analysis with mtex–free and open source software toolbox," in *Solid State Phenomena*, vol. 160, pp. 63–68, Trans Tech Publ, 2010.

[113] W. Pantleon, "Resolving the geometrically necessary dislocation content by conventional electron backscattering diffraction," *Scr. Mater.*, vol. 58, no. 11, pp. 994–997, 2008.

[114] J. F. Nye, "Some geometrical relations in dislocated crystals," *Acta. Metall.*, vol. 1, no. 2, pp. 153–162, 1953.

[115] J. Jiang, T. B. Britton, and A. J. Wilkinson, "Accumulation of geometrically necessary dislocations near grain boundaries in deformed copper," *Phil. Mag. Letters*, vol. 92, no. 11, pp. 580–588, 2012.

[116] M. Drakopoulos, T. Connolley, C. Reinhard, R. Atwood, O. Magdysyuk, N. Vo, M. Hart, L. Connor, B. Humphreys, G. Howell, *et al.*, "I12: the joint engineering, environment and processing (jeep) beamline at diamond light source," *J. Synchrotron Radiat.*, vol. 22, no. 3, pp. 828–838, 2015.

[117] M. L. Hart, M. Drakopoulos, C. Reinhard, and T. Connolley, "Complete elliptical ring geometry provides energy and instrument calibration for synchrotron-based two-dimensional x-ray diffraction," *J. Appl. Crystallogr.*, vol. 46, no. 5, pp. 1249–1260, 2013.

[118] A. Doucet and R. Wagoner, "Plane-strain work hardening and transient behavior of interstitial-free steel," *Metall. Trans. A*, vol. 18, no. 12, pp. 2129–2134, 1987.

[119] R. Ray, J. J. Jonas, and R. Hook, "Cold rolling and annealing textures in low carbon and extra low carbon steels," *Int. Mater. Rev.*, vol. 39, no. 4, pp. 129–172, 1994.

[120] A. Lopes, E. Rauch, and J. Gracio, "Textural vs structural plastic instabilities in sheet metal forming," *Acta Mater.*, vol. 47, no. 3, pp. 859–866, 1999.

[121] J. Schmitt, J. Fernandes, J. Gracio, and M. Vieira, "Plastic behaviour of copper sheets during sequential tension tests," *Mater. Sci. Eng.: A*, vol. 147, no. 2, pp. 143–154, 1991.

[122] X.-x. Huang and G. Winther, "Dislocation structures. part i. grain orientation dependence," *Phil. Mag.*, vol. 87, no. 33, pp. 5189–5214, 2007.

[123] ASTM International,, "Standard Test Methods for Tension Testing of Metallic Materials," pp. 1–31, 2022.

[124] A. A. Vasilyev, A. I. Rudskoy, P. A. Glukhov, S. F. Sokolov, and N. G. Kolbasnikov, "Estimation of the degree of recrystallization upon annealing of cold-rolled automobile body sheet steels using EBSD analysis and hardness measurements," *Russian Metallurgy (Metally)*, vol. 2018, no. 10, pp. 973–979, 2018.

[125] ASTM International, "Standard Test Methods for Determining Average Grain Size," pp. 1–29, 2021.

[126] I. Gutierrez-Urrutia and D. Raabe, "Grain size effect on strain hardening in twinning-induced plasticity steels," *Scripta Materialia*, vol. 66, no. 12, pp. 992–996, 2012.

[127] S. Kang, J.-G. Jung, M. Kang, W. Woo, and Y.-K. Lee, "The effects of grain size on yielding, strain hardening, and mechanical twinning in fe–18mn–0.6 c–1.5 al twinning-induced plasticity steel," *Materials Science and Engineering: A*, vol. 652, pp. 212–220, 2016.

[128] Z. Marciniak and K. Kuczyński, "Limit strains in the processes of stretch-forming sheet metal," *International journal of mechanical sciences*, vol. 9, no. 9, pp. 609–620, 1967.

[129] A. M. Sadegh and W. M. Worek, *Marks' Standard Handbook for Mechanical Engineers*. McGraw-Hill Education, 2018.

[130] J. Klepaczko and C. Chiem, "On rate sensitivity of fcc metals, instantaneous rate sensitivity and rate sensitivity of strain hardening," *Journal of the Mechanics and Physics of Solids*, vol. 34, no. 1, pp. 29–54, 1986.

[131] J. E. Gutierrez, J. Noder, and C. Butcher, "Experimental characterization and deterministic prediction of in-plane formability of 3rd generation advanced high strength steels," *Metals*, vol. 10, no. 7, p. 902, 2020.

[132] A. Hijazi, N. Yardi, and V. Madhavan, "Determination of forming limit curves using 3d digital image correlation and in-situ observation," *Proceedings of SAMPE*, pp. 16–20, 2004.

[133] M. E. Leonard, F. Ugo, M. Stout, and J. W. Signorelli, "A miniaturized device for the measurement of sheet-metal formability using digital image correlation," *Review of Scientific Instruments*, vol. 89, no. 8, 2018.

[134] V. D. Vijayanand, M. Mokhtarishirazabad, J. Peng, Y. Wang, M. Gorley, D. M. Knowles, and M. Mostafavi, "A novel methodology for estimating tensile properties in a small punch test employing in-situ DIC based deflection mapping," *Journal of Nuclear Materials*, vol. 538, p. 152260, 2020.

[135] J. Blaber, B. Adair, and A. Antoniou, "Ncorr: open-source 2d digital image correlation matlab software," *Experimental Mechanics*, vol. 55, no. 6, pp. 1105–1122, 2015.

[136] MATLAB, *version 9.10 (R2021a)*. Natick, Massachusetts: The MathWorks Inc., 2021.

[137] M. A. Sutton, J. Yan, V. Tiwari, H. Schreier, and J.-J. Orteu, "The effect of out-of-plane motion on 2d and 3d digital image correlation measurements," *Optics and Lasers in Engineering*, vol. 46, no. 10, pp. 746–757, 2008.

[138] A. Agha, "Effectiveness of 2d digital image correlation in capturing the fracture behavior of sheet metal alloys," *SAE Int. J. Mater. Manf*, vol. 16, no. 2, p. 2023, 2022.

[139] R. Mohammadzadeh, "Deformation characteristics of nanocrystalline twip steel under uniaxial tension and compression," *Mechanics of Materials*, vol. 138, p. 103147, 2019.

[140] S. H. Akbarian, A. Zarei-Hanzaki, A. S. Anoushe, H. R. Abedi, R. Unnikrishnan, and G. Cios, "Step-by-step texture modification through strain path change toward improvement of the hardening capacity in a twinning-induced-plasticity steel," *Mater. Sci. Eng. A*, vol. 799, no. August 2020, p. 140269, 2021.

[141] Y. Lü, M. Bruhis, and J. McDermid, "Effect of strain path on the microstructural evolution of a fe-22mn-0.6 c alloy," in *AIST Int Symposium on New Developments in AHSS. Vail, Colo*, pp. 113–118, 2013.

[142] T. Ungár and A. Borbély, "The effect of dislocation contrast on x-ray line broadening: A new approach to line profile analysis," *Applied Physics Letters*, vol. 69, no. 21, pp. 3173–3175, 1996.

[143] T. Ungár, S. Ott, P. Sanders, A. Borbély, and J. Weertman, "Dislocations, grain size and planar faults in nanostructured copper determined by high resolution x-ray diffraction and a new procedure of peak profile analysis," *Acta materialia*, vol. 46, no. 10, pp. 3693–3699, 1998.

[144] T. Ungár, I. Dragomir, Á. Révész, and A. Borbély, "The contrast factors of dislocations in cubic crystals: the dislocation model of strain anisotropy in practice," *Journal of applied crystallography*, vol. 32, no. 5, pp. 992–1002, 1999.

[145] D. Pierce, K. Nowag, A. Montagne, J. Jiménez, J. Wittig, and R. Ghisleni, "Single crystal elastic constants of high-manganese transformation-and twinning-induced plasticity steels determined by a new method utilizing

nanoindentation," *Materials Science and Engineering: A*, vol. 578, pp. 134–139, 2013.

[146] X. Duan, D. Wang, K. Wang, and F. Han, "Twinning behaviour of twip steel studied by taylor factor analysis," *Philosophical magazine letters*, vol. 93, no. 5, pp. 316–321, 2013.

[147] R. Rakshit, A. Sarkar, S. K. Panda, and S. Mandal, "Influence of out-of-plane stretch forming induced different strain paths on micro-texture evolution, slip system activity and taylor factor distribution in al–li alloy," *Materials Science and Engineering: A*, vol. 830, p. 142267, 2022.

[148] E. Polatidis, W.-N. Hsu, M. Šmíd, T. Panzner, S. Chakrabarty, P. Pant, and H. Van Swygenhoven, "Suppressed martensitic transformation under biaxial loading in low stacking fault energy metastable austenitic steels," *Scripta Materialia*, vol. 147, pp. 27–32, 2018.

[149] T. Erinosho, D. Collins, A. Wilkinson, R. Todd, and F. Dunne, "Assessment of x-ray diffraction and crystal plasticity lattice strain evolutions under biaxial loading," *International Journal of Plasticity*, vol. 83, pp. 1–18, 2016.

[150] D. T. Pierce, J. A. Jiménez, J. Bentley, D. Raabe, and J. E. Wittig, "The influence of stacking fault energy on the microstructural and strain-hardening evolution of fe–mn–al–si steels during tensile deformation," *Acta Materialia*, vol. 100, pp. 178–190, 2015.

[151] H. Ding, H. Ding, D. Song, Z. Tang, and P. Yang, "Strain hardening behavior of a trip/twip steel with 18.8% mn," *Materials Science and Engineering: A*, vol. 528, no. 3, pp. 868–873, 2011.